

Lehrstuhl für Elektrische Antriebssysteme und Leistungselektronik  
der Technischen Universität München

# Mitigation of Sub-synchronous Resonance caused by wind power and Series Compensation

Bin Li

Vollständiger Abdruck der von der Fakultät für Elektrotechnik und Informationstechnik der Technischen Universität München zur Erlangung des akademischen Grades eines

Doktor-Ingenieurs

genehmigten Dissertation.

Vorsitzender: Prof. Dr.-Ing. Rolf Witzmann

Prüfer der Dissertation:

1. Prof. Dr.-Ing. Dr. h. c. Ralph Kennel
2. Prof. Dr. ir. Dr. h. c. Rik W. De Doncker  
(RWTH Aachen Universität)

Die Dissertation wurde am 16.11.2018 bei der Technischen Universität München eingereicht und durch die Fakultät für Elektrotechnik und Informationstechnik am 03.06.2019 angenommen.



## PREFACE

This research has been carried out in the Chair of Electrical Drive Systems and Power Electronics at Technical University of Munich. With this dissertation I have finally finished my Doctor of Philosophy (PhD). Thinking the past several years, there is a lot of things in my memories.

First of all, I would like to thank Prof. Ralph M. Kennel. As my doctor father, he gave me a lot of help, which is not only from technical side, but also from spirit point of view. With his help, I found the proper research direction. Under his supervision, my dissertation was progressed little by little. During this process, he encouraged me many times, which gave me sufficient confidence and power to go on with my research. Only with his encouragement, I could finish my PhD successfully. Meanwhile, his research resources also help me a lot. In one word, my PhD has been strongly benefitted from his help.

At the same time, I also want to thank my family. My wife, Lijuan Xu, has helped me continuing my dissertation. When I had some issues in my research, she urged me to get over the difficulties. When I lost my confidence, she talked to me and made me feel encouraged. Besides, she offered me a perfect daily care. It was really helpful.

In the flowing, I also want to thank Prof. Dr. -Ing. Rik W. De Doncker from RWTH Aachen University. As the second examiner, he provided me a lot of interesting inspirations and proposed many heuristic questions. From him I knew what an expert was.

At the end, many thanks must be given to my colleagues in the Chair of Electrical Drive Systems and Power Electronics at Technical University of Munich. They have assisted me during the work of this PhD thesis and I really enjoyed the time with them.

## CONTENTS

<b>PREFACE</b> .....	<b>1-3</b>
<b>CONTENTS</b> .....	<b>1-4</b>
<b>1 INTRODUCTION</b> .....	<b>1-7</b>
1.1 BACKGROUND .....	1-7
1.2 OVERVIEW OF SOLUTIONS TO MITIGATE SSR IN PRESENCE OF DFIG AND SC .....	1-8
1.3 REPORT STRUCTURE .....	1-9
<b>2 SUB-SYNCHRONOUS RESONANCE CHARACTERISTICS</b> .....	<b>2-10</b>
2.1 MODELING OF DFIG.....	2-10
2.2 DERIVATION OF TRANSFER FUNCTIONS.....	2-12
2.2.1 Derivation of transfer functions of system at nominal frequency.....	2-15
2.2.2 Derivation of transfer functions of system at sub-synchronous frequency .....	2-27
2.2.3 Grid-side converter .....	2-28
2.2.4 Rotor-side converter .....	2-28
2.3 ANALYSIS OF SSR CHARACTERISTICS .....	2-34
2.3.1 SSR mitigation by addition of voltage magnitude control loop to grid-side converter....	2-42
2.3.2 SSR mitigation by damping control of grid-side converter .....	2-50
2.3.3 Summary .....	2-57
2.4 CONCLUSIONS.....	2-57
2.4.1 Main conclusions on SSR characteristics .....	2-57
2.4.2 Main conclusions on SSR mitigation by DFIG control modification .....	2-58
<b>3 MODELING OF INVESTIGATED NETWORK AND SUB-SYNCHRONOUS RESONANCE RISK EVALUATION</b> .....	<b>3-59</b>
3.1 MODELING OF INVESTIGATED NETWORK .....	3-59
3.2 EVALUATION OF SSR RISK IN THE SYSTEM.....	3-61
3.2.1 DFIG controllers with larger gain.....	3-61
3.2.2 DFIG controllers with smaller gain .....	3-61
<b>4 SUBSYNCHRONOUS RESONANCE MITIGATION BY TEMPORAL BYPASS OF SERIES COMPENSATION</b> .....	<b>4-63</b>
4.1 CONTROL ALGORITHM 1 .....	4-63
4.1.1 Bypassing SC .....	4-63
4.1.2 Reinserting SC .....	4-65
4.1.3 Signal process .....	4-66
4.1.4 Validation of algorithm 1 .....	4-67
4.1.5 Effectiveness evaluation .....	4-69
4.2 CONTROL ALGORITHM 2 - WITH PREDICTION ABILITY .....	4-72
4.3 SUMMARY .....	4-74
<b>5 SUB-SYNCHRONOUS RESONANCE MITIGATION BY WF-STATCOM</b> .....	<b>5-76</b>
5.1 MODEL DESCRIPTION .....	5-76
5.2 SOLUTION USING GENERATOR SPEED AS CONTROL INPUT .....	5-78
5.2.1 Controller design .....	5-79
5.2.2 Controller evaluation.....	5-80
5.3 SOLUTION BASED ON ACTIVE POWER.....	5-85
5.3.1 Controller structure .....	5-86
5.3.2 Controller Effectiveness verification .....	5-89

5.3.3	Minimized StatCom capacity.....	5-93
5.4	SUMMARY .....	5-95
<b>6</b>	<b>SUB-SYNCHRONOUS RESONANCE MITIGATION BY WIND FARM STATIC VAR COMPENSATOR.....</b>	<b>6-96</b>
6.1	MODELING OF SVC AND ITS VOLTAGE CONTROL SYSTEM.....	6-96
6.2	DESIGN OF SSR DAMPING CONTROLLER .....	6-98
6.2.1	Control architecture .....	6-98
6.2.2	Controller design .....	6-99
6.2.3	Gain adaptation .....	6-103
6.3	VALIDATION OF DEVELOPED SSR DAMPING CONTROLLER .....	6-104
6.3.1	Effectiveness for SSR damping .....	6-104
6.3.2	Effectiveness for the whole wind generation level range.....	6-105
6.3.3	Effectiveness for different compensation levels .....	6-106
6.3.4	Effectiveness for DFIGs with different control parameters and operating at different generation levels .....	6-109
6.3.5	Required rating .....	6-110
6.4	SUMMARY .....	6-110
<b>7</b>	<b>SUB-SYNCHRONOUS RESONANCE MITIGATION BY THYRISTOR-CONTROLLED SERIES CAPACITOR .....</b>	<b>7-112</b>
7.1	INTRODUCTION TO TCSC AND ITS CONTROL SYSTEM .....	7-112
7.1.1	TCSC main circuit.....	7-112
7.1.2	TCSC control system.....	7-113
7.2	PSCAD MODEL AND TRANSFER FUNCTION MODEL OF TCSC AND THE COMPENSATED SYSTEM.....	7-114
7.2.1	Modeling of TCSC in PSCAD .....	7-114
7.2.2	Investigated system with TCSC connected.....	7-114
7.2.3	Transfer function model of the investigated system .....	7-115
7.2.4	Connection between TCSC control system and DFIG control system.....	7-117
7.3	INVESTIGATION ON SYSTEM COMPENSATED BY PURE TCSC .....	7-118
7.3.1	Issues identified.....	7-118
7.3.2	Analysis of interaction between DFIG and TCSC control systems .....	7-118
7.3.3	Elimination of control interaction by adding damping control to TCSC control system .....	7-126
7.4	INVESTIGATION ON SYSTEM COMPENSATED BY COMBINED TCSC AND FIXED CAPACITOR .....	7-130
7.4.1	Evaluation of SSR risk in system with DFIG and TCSC+FC .....	7-130
7.4.2	Investigation on impact of boost factor and TCSC inductance on SSR .....	7-143
7.4.3	Development of SSR damping control for system with DFIG and TCSC+FC .....	7-146
7.5	CONCLUSIONS .....	7-156
<b>8</b>	<b>COMPARISON OF DIFFERENT MITIGATION SOLUTIONS.....</b>	<b>8-158</b>
8.1	COMPARISON REGARDING APPLICABLE SCENARIOS.....	8-158
8.2	COMPARISON REGARDING SSR DAMPING PERFORMANCE.....	8-158
<b>9</b>	<b>CONCLUSIONS.....</b>	<b>9-161</b>
	<b>LIST OF FIGURES .....</b>	<b>9-163</b>
	<b>LIST OF TABLES.....</b>	<b>9-167</b>
	<b>REFERENCES .....</b>	<b>9-168</b>



# 1 INTRODUCTION

## 1.1 Background

Wind power has been growing rapidly in recent years. The world total installed capacity will shoot up from 591 GW in 2018 to 908 GW in 2023 [1]. China has now become the largest market, followed by USA. In the past years China has demonstrated its fast growth. The installed capacity has been doubled in four consecutive years from 2011 to 2014 and increased by 42% from 23.2 GW in 2014 to 33.0 GW in 2015. It is estimated the number will reach 35 GW in 2020.

There are several characteristics of the wind power development in China. The first one is that the wind resources are mainly distributed in the northern region, especially the northwest, which is far away from the load centers. Second, the wind power is mainly on-shore. The third characteristic is the concentrated development mode. The wind energy development in USA also has similar characteristics.

With the above mentioned characteristics, transmission of bulk wind energy is inevitable. Several alternative solutions exist, namely UHVAC (ultra-high voltage alternate current) transmission, LCC (line commuted converter) HVDC (High Voltage Direct Current), and VSC (voltage source converter) HVDC. For on-shore wind power, UHV ac transmission is cheaper compared to dc solutions within a certain transmission distance. It's easier to handle wind power fluctuation with ac transmission. Compared to point-to-point dc transmission, it's easier to deliver wind power to different regional grids through substations along the ac corridor. However, ac transmission requires more corridor space and incurs high power losses. The transmission capability is also limited to a certain transmission distance. Nevertheless, UHVAC transmission is still a promising solution.

Series Compensation (SC) is an effective way to increase power transmission capability of ac lines. By inserting series capacitors in the ac line, the electrical length of the line is shortened. However, if the ac lines are compensated by fixed capacitors, there is a resonance frequency in sub-synchronous range in the system, which might cause SSR (sub synchronous resonance) problems [2, 3, 4]. Generally, SSR might happen in the following forms: induction generator effect (IGE), torsional interaction (TI), and torque amplification (TA).

Both TI and TA are related to the generator shaft system. It has been well known that thermal power plants are vulnerable to these types of SSR. If the mechanical resonance frequency of the shaft system and the electrical resonance frequency are complementary (i.e., the sum of them equals to system nominal frequency), SSR will happen. In severe cases, the generator shaft systems can be destroyed. TI is triggered by torsional swing of the shaft system whereas TA is triggered by disturbances in the electrical system

IGE is caused by self-excitation of induction generators. For induction machines connected at the end of a series compensated lines, the resonance may happen if the resistance of the combined impedance (combination of the impedance of the induction machine, line impedance, and the impedance of the series compensation capacitor) is smaller than or equal to zero at frequencies where the reactance is zero (resonance frequencies) [5, 6]. The presence of non-positive resistance is due to the negative equivalent resistance of the rotor circuit looked from the stator side at frequencies lower than the rotor rotating frequency.

Although self-excitation of induction machines has been well addressed, SSR with doubly-fed induction generator (DFIG) is relatively a new phenomenon which is drawing more and more attention. SSR in wind power with series compensated ac transmission lines has been observed

in the wind energy integration studies. It has also been occurred in reality in wind farms in Texas, USA in 2009 [7]. Most wind turbines lost the grid connection and the system stability was threatened by the accident.

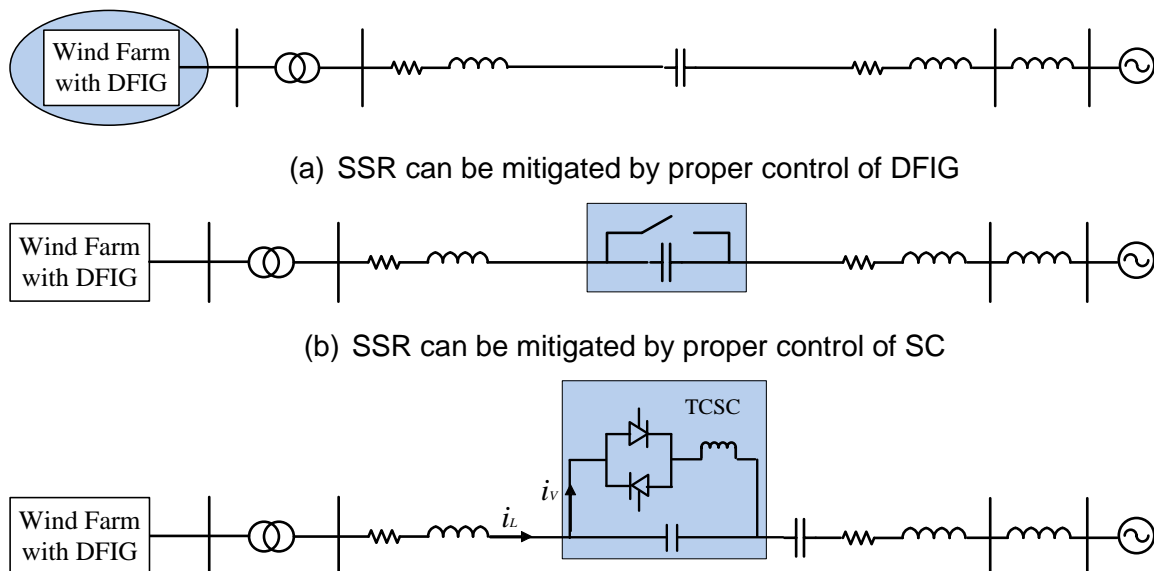
The mechanism of SSR in case of DFIG can be explained briefly as follows: SSR is caused by the electrical interaction between DFIG and series capacitor. The series capacitor and the combined inductance in the system (including line inductance, source inductance, lumped DFIG inductance, etc.) determine a resonance frequency which is in sub-synchronous range. The DFIG rotor winding presents a negative resistance at the resonance frequency. The negative resistance is a combined effect of the negative slip and DFIG control system. If the combined resistance of the system (including the negative rotor resistance and other lumped system resistance) is smaller than zero at the resonance frequency, there will be a negative damping in the system, causing oscillations at the resonance frequency.

DFIG is one of the commonly used types of wind power generator (WTG). In America and Europe 75%~80% of wind turbines are DFIG and 70% in China [8]. Even though full power converter (FPC) type WTGs are getting popular nowadays, DFIGs will still take a main market share in the future. Therefore, the SSR phenomenon in presence of wind power and SC is worth investigating.

## 1.2 Overview of solutions to mitigate SSR in presence of DFIG and SC

Since SSR is caused by interaction between DFIG and SC, it is possible to solve the problem by proper control of either DFIG or SC. In addition, SSR problem can also be solved by FACTS (Flexible Alternative Current Transmission Systems) devices such as TCSC, StatCom or SVC. In this dissertation, the investigated solutions related to StatCom or SVC are assumed to be implemented in the StatCom or SVC installed at the wind farm terminal for reactive power support. SSR mitigation is an added function to the reactive power support function in wind farms. They are referred to as WF-StatCom and WF-SVC respectively.

Various solutions have been investigated, developed and presented in the dissertation. Fig. 1-1 gives an overall picture how SSR can be mitigated by various devices in the system.



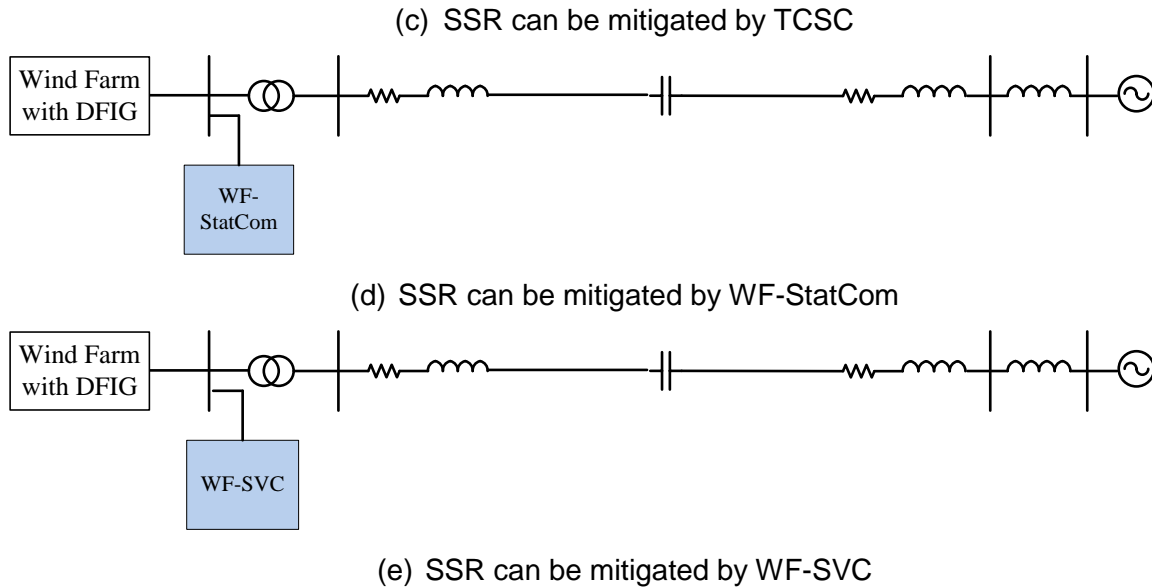


Fig. 1-1. Overview of various solutions to SSR mitigation

### 1.3 Report structure

The dissertation is structured as following:

- Chapter 2 analyzes the SSR characteristics in detail. Furthermore, the solution based on modifying DFIG converter control is investigated.
- Chapter 3 describes the research network and its modeling method. The research network is analyzed for the investigation of SSR mitigation solutions by proper control of SC, TCSC, WF-StatCom and WF-SVC.
- Chapter 4 presents SSR mitigation solutions by proper control of SC.
- Chapter 5 and Chapter 6 present SSR mitigation solution by WF-StatCom and WF-SVC respectively.
- Chapter 7 describes SSR mitigation solutions by TCSC.
- In Chapter 8, various solutions are compared.
- Conclusions are drawn in Chapter 9.

## 2 SUB-SYNCHRONOUS RESONANCE CHARACTERISTICS

In this thesis, the DFIG (double-feed induction generator) model used in the study is described. Transfer functions for both nominal frequency and sub-synchronous frequency are derived and verified. SSR (sub-synchronous resonance) characteristics in presence of SC (series compensation) and wind farm with DFIG have been investigated with identified main factors affecting SSR. Methods of SSR mitigation by DFIG control modification have been investigated and their effectiveness evaluated.

### 2.1 Modeling of DFIG

Fig. 2-1 shows the diagram of a DFIG. The stator is connected directly to the power system and the rotor is connected to the system through two back-to-back ac/dc converters named grid-side converter and rotor-side converter.

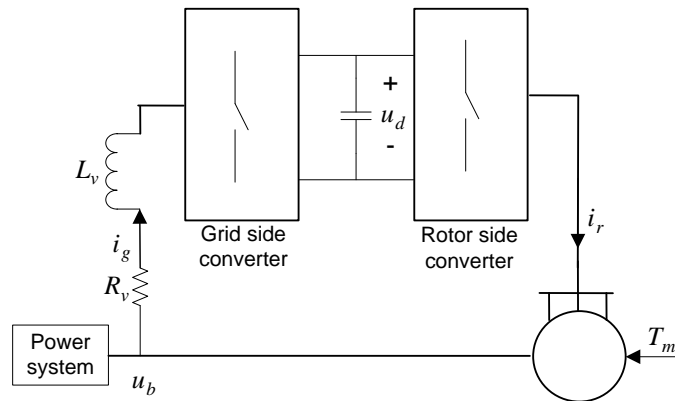


Fig. 2-1 DFIG diagram

In the averaged model, the two converters are represented as two controllable voltage sources as shown in Fig. 2-2. It is assumed that the converters can always provide the required reference voltages, which are calculated through the control systems for grid-side converter and rotor-side converter respectively. On the dc side, the capacitor is represented as an integration block which integrates the current calculated from the ac active power flowing through the two converters, using the principle of active power balance. The dc voltage is generated internally through the integration block.

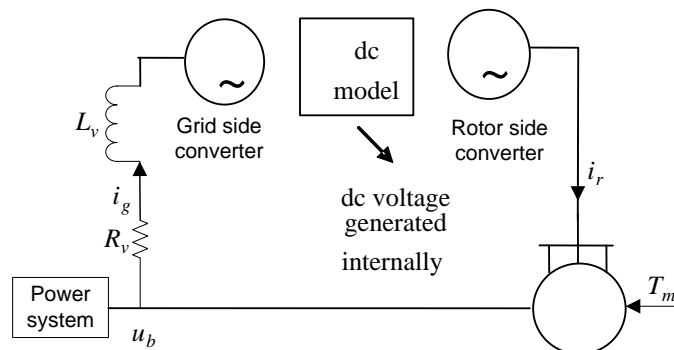


Fig. 2-2 Schematic diagram of the DFIG model

The control structure of the grid side converter is depicted in Fig. 2-3. A phase-locked-loop (PLL) is applied to the DFIG terminal voltage such that the vector is aligned with the d axis in the dq frame. The dc side voltage is controlled at a pre-set value by a PI controller. The output of this PI controller gives the reference for the active current of the converter. The reactive current reference is set to zero. The converter current is transformed into dq frame using the angle from the PLL. The references and the measured current and voltage components are then delivered to the block named 'Reference voltage calculation'. The detailed structure of this block will be shown in next section.

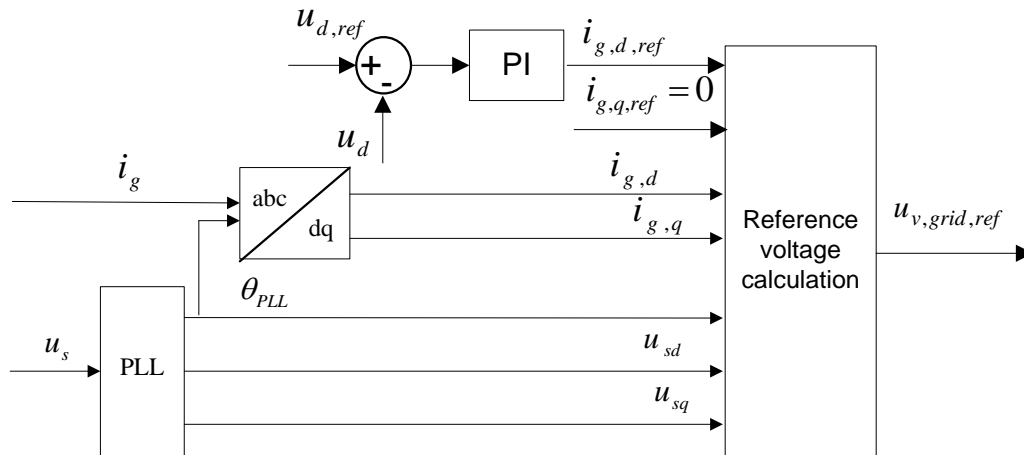


Fig. 2-3. Control structure of the grid side converter

Fig. 2-4 shows the control structure of the rotor side converter. There are two loops in the control system. In the outer loop, the generator is controlled to generate the maximum possible active power at a given wind speed using maximum power following method. The reference rotor angular speed obtained by this method is then compared with the actual rotor speed. A PI controller is employed to control the rotor speed. The output of this PI controller gives the reference for electrical torque, which is then converted into the reference for the converter active current. Also in the outer loop there is a reactive power PI controller and the output of this controller gives the reference for the converter reactive current. The converter current (reactive and active current) is controlled in the inner loop.

The converter current is transformed into dq reference frame using a reference angle that represents the relative position of the stator voltage vector and the rotor voltage vector. This reference angle is the difference between the angle from the PLL and the rotor angle.

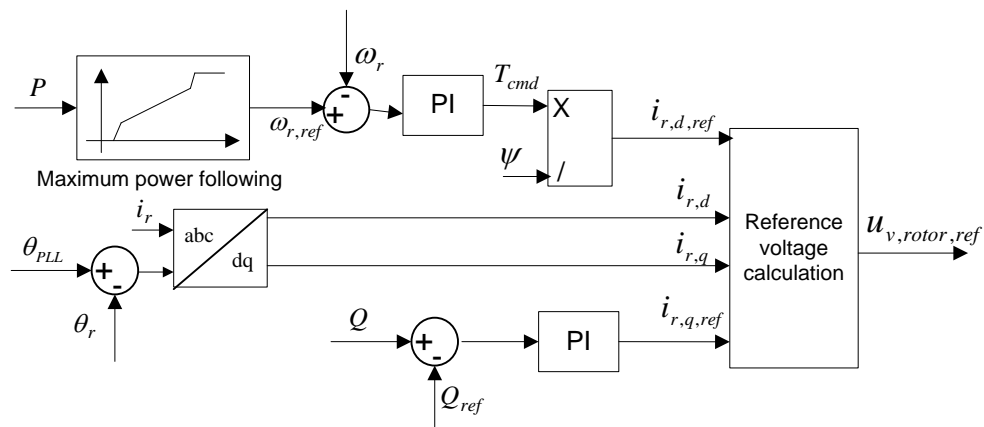


Fig. 2-4 Control structure of the rotor side converter

The converter current components and their references are delivered to the block named 'Reference voltage calculation'. The detailed structure of this block will be described in the next section.

The mechanical torque input to the DFIG is generated through mathematic models of a wind turbine and a drive train, as shown in Fig. 2-5. The drive train contains two masses. The inputs to the mathematic models are wind speed and pitch angle. Wind speed is set manually. The pitch angle is adjusted through a proportional controller on rotor speed and a PI controller on the output active power of the DFIG.

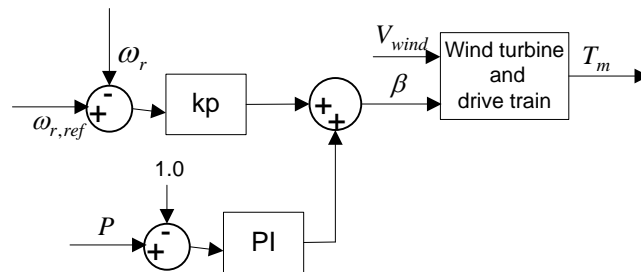


Fig. 2-5 Pitch control and mechanical torque calculation

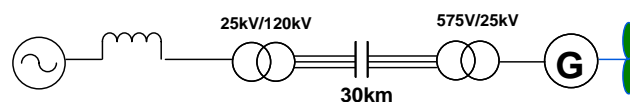
The information above gives a description of whole control structure. The rotor speed reference and the mechanical torque produced by the wind turbine are considered to be constant. This assumption is justified since the focus of the study is on SSR phenomenon related to electrical interaction between the electrical system of the DFIG and the SC. The mechanical system has much slower dynamics.

## 2.2 Derivation of transfer functions

The system used for analysis is depicted in Fig. 2-6. A simplified model of the system is shown in Fig. 2-7. The power system is simplified as an infinite voltage source with lumped inductance  $L_{sys}$  and resistance  $R_{sys}$ .  $C_{SC}$  is the capacitance of the SC capacitor. The wind farm is represented by a lumped DFIG WTG.

The specifications of the system parameters are listed in Table 2-1. It should be pointed out the voltage level and power rating of the system, especially the voltage level of the series compensation, is not realistic. However, the whole system can be seen as scaled-down from a large-scale, high-voltage level and long transmission line system. Since the analysis is performed on a per unit base, the results should be also valid for realistic voltage levels. Hence, the values in Fig. 2-7 Simplified model of the system

are all in pu value with the DFIG nominal power as the base power.



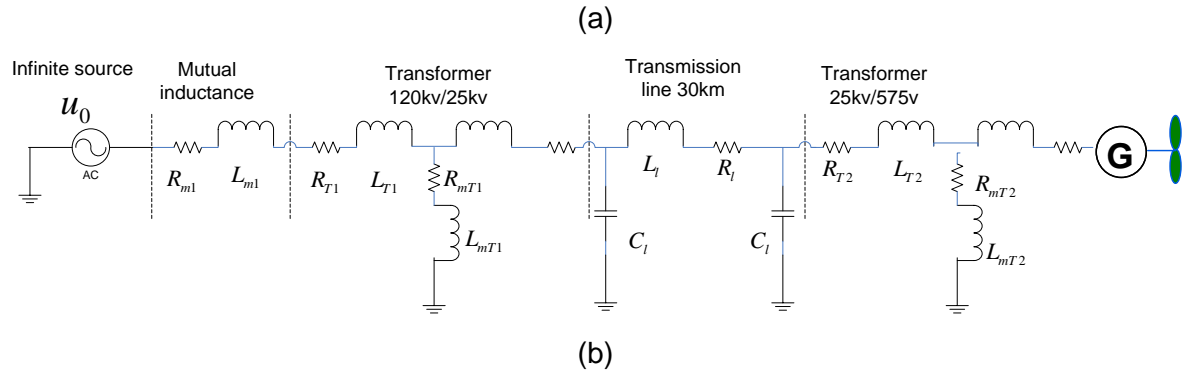


Fig. 2-6 System used for analysis

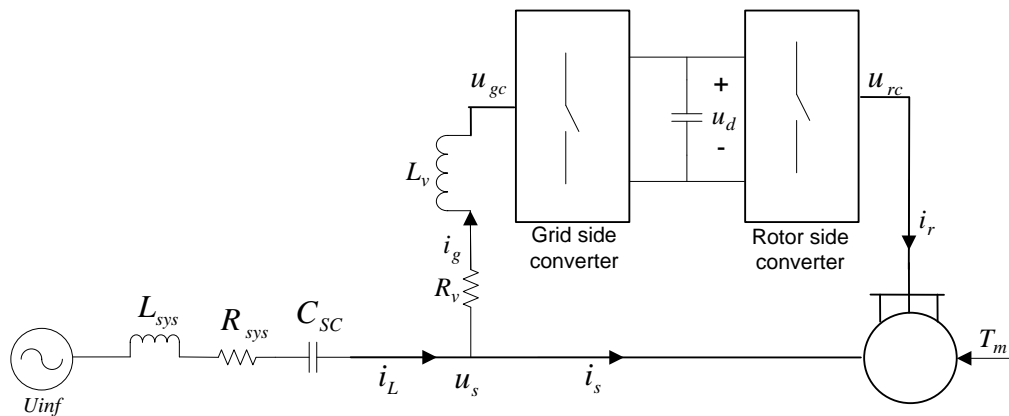


Fig. 2-7 Simplified model of the system

Table 2-1 System specifications

Parameter	Value (pu)
$R_{sys}$ (lumped system resistance)	0.0584 (of which, 0.0553 is line resistance)
$L_{sys}$ (lumped system inductance)	0.276 at nominal frequency (of which, 0.19 is line reactance)
$R_v$ (resistance of grid-side converter phase reactor)	0.003
$L_v$ (inductance of grid-side converter phase reactor)	0.003 at nominal frequency
$R_s$ (DFIG stator resistance)	0.0023
$L_{ls}$ (DFIG stator leakage inductance)	0.018 at nominal frequency
$R_r$ (DFIG rotor resistance)	0.0016
$L_{lr}$ (DFIG rotor leakage inductance)	0.016 at nominal frequency
$L_m$ (DFIG magnetizing inductance)	2.9 at nominal frequency

The equivalent circuit of the above system can be drawn in Fig. 2-8. In the figure,  $u_{gc}$  and  $u_{rc}$  are the voltages produced at the terminals of the grid-side and rotor-side converter respectively. Both of the two voltages are controllable.

Assume that the voltages and currents in the system contain a component of nominal frequency  $f_n$  and a component of sub-synchronous frequency  $f_{ss}$ . These quantities in  $\alpha\beta$  plane can be expressed as

$$\left\{ \begin{array}{l} \overline{i_s^{\alpha\beta}} = \overline{i_{sn}^{\alpha\beta}} + \overline{i_{sss}^{\alpha\beta}} = \overline{i_{sn}^{dq}} e^{j\omega_n t} + \overline{i_{sss}^{dq}} e^{j\omega_{ss} t} \\ \overline{u_s^{\alpha\beta}} = \overline{u_{sn}^{\alpha\beta}} + \overline{u_{sss}^{\alpha\beta}} = \overline{u_{sn}^{dq}} e^{j\omega_n t} + \overline{u_{sss}^{dq}} e^{j\omega_{ss} t} \\ \overline{i_r^{\alpha\beta}} = \overline{i_{rn}^{\alpha\beta}} + \overline{i_{r_{ss}}^{\alpha\beta}} = \overline{i_{rn}^{dq}} e^{j(\omega_n - \omega_r)t} + \overline{i_{r_{ss}}^{dq}} e^{j(\omega_{ss} - \omega_r)t} \\ \overline{u_{rc}^{\alpha\beta}} = \overline{u_{rcn}^{\alpha\beta}} + \overline{u_{rc_{ss}}^{\alpha\beta}} = \overline{u_{rcn}^{dq}} e^{j(\omega_n - \omega_r)t} + \overline{u_{rc_{ss}}^{dq}} e^{j(\omega_{ss} - \omega_r)t} \\ \overline{i_g^{\alpha\beta}} = \overline{i_{gn}^{\alpha\beta}} + \overline{i_{g_{ss}}^{\alpha\beta}} = \overline{i_{gn}^{dq}} e^{j\omega_n t} + \overline{i_{g_{ss}}^{dq}} e^{j\omega_{ss} t} \end{array} \right. \quad (2-1)$$

In the above equations, the subscriptions refer to:

s: stator

sn: nominal frequency component of stator quantities

sss: sub-synchronous component of stator quantities

r: rotor

rc: rotor converter

r(c)n: rotor quantities induced by nominal frequency component of air-gap flux

r(c)ss: rotor quantities induced by sub-synchronous component of air-gap flux

g: grid-side converter

gn: nominal frequency component of grid-side converter quantities

gss: sub-synchronous component of grid-side converter quantities

According to superimpose principle, the equivalent circuit can be split into two circuits with frequencies  $f_n$  and  $f_{ss}$  respectively, as shown in Fig. 2-9 and Fig. 2-10. The system can be seen as the sum of these two circuits.

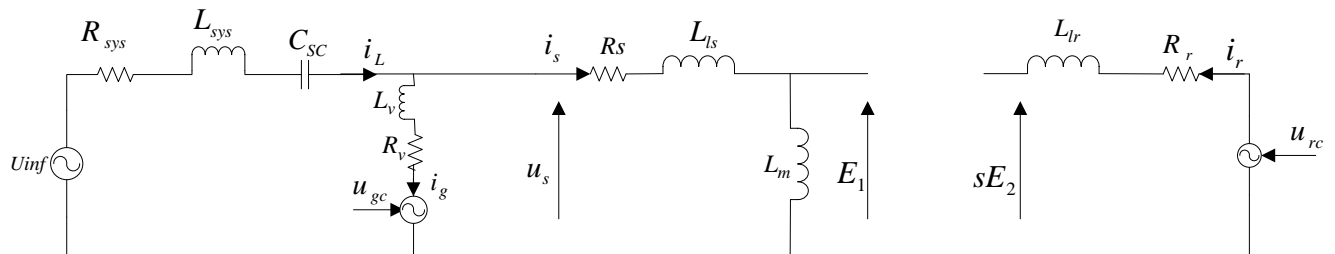


Fig. 2-8 System equivalent circuit

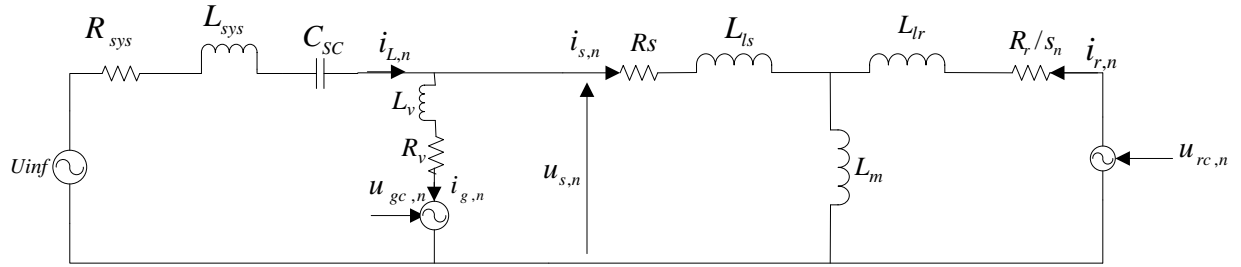
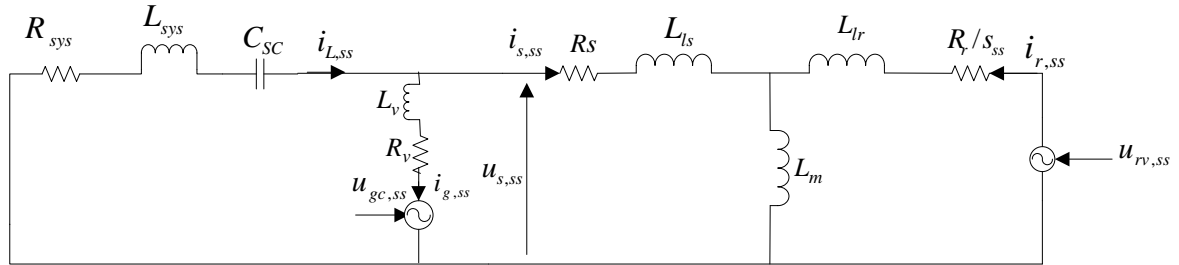


Fig. 2-9 system equivalent circuit of nominal frequency

Fig. 2-10 system equivalent circuit of frequency  $f_{ss}$ 

where

$$E_1 = sE_2$$

$$s = \frac{N_{stator}}{N_{rotor}} \quad (\text{turns ratio})$$

In the following sections, the transfer functions of the system with frequency  $f_n$  and  $f_{ss}$  will be derived respectively. It should be pointed out that delays due to measurement filters/transducers are not considered in the modeling.

## 2.2.1 Derivation of transfer functions of system at nominal frequency

### 2.2.1.1 Grid-side converter

As described in Section 2.1, there are two control loops in the grid-side converter control system. The control system together with the plants is depicted in Fig. 2-11. The outer loop controls the dc link voltage and gives the reference of the active current of the converter. The inner loop controls the active current to follow the reference value. The reactive current of the converter is also controlled in the inner loop. Its reference can either be set directly or be given by an outer loop. Depending on control target, the outer loop can control, for example, the reactive power or terminal voltage. However, the grid-side converter is mainly used for active power delivery during normal operation, especially when the generator is running with large slip. Moreover, the power rating is usually 20-30% of the DFIG power rating. Therefore, usually the grid-side converter is not controlled to provide reactive power support during normal operation. Hence, in the SSR characteristic studies the reference of the reactive current is set directly to zero.

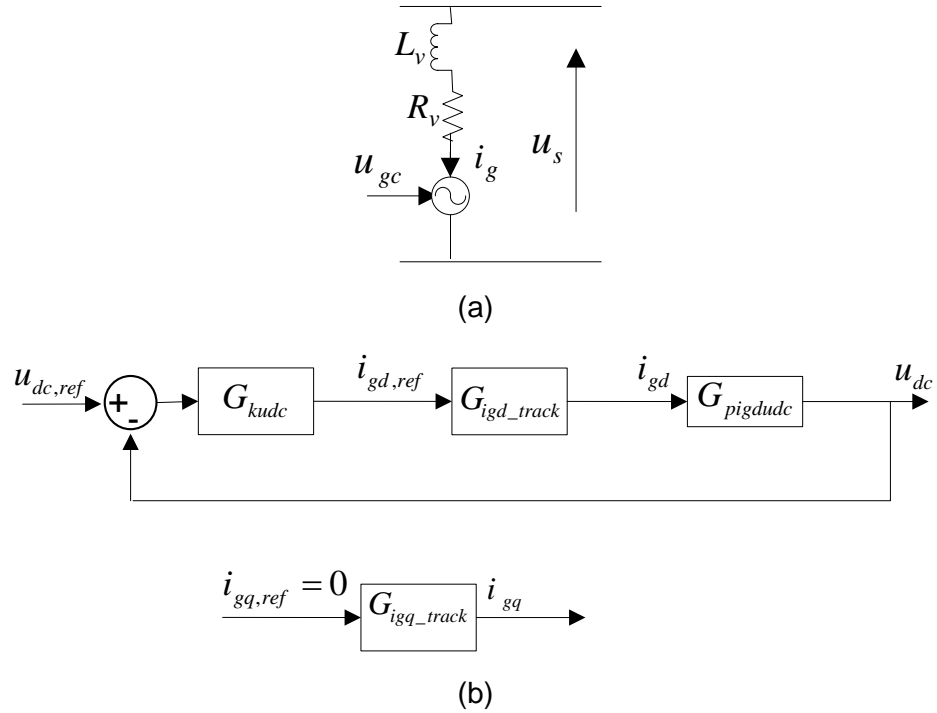


Fig. 2-11 Control system of the grid-side converter

### 2.2.1.1.1 Inner current control loop

In the control system, the DFIG stator voltage  $u_s$  is measured and transformed into  $\alpha\beta$  coordinate system as  $u_s^{\alpha\beta}$ . Voltage equation of the grid-side converter can be written as

$$\vec{u}_{gc}^{\alpha\beta} = \vec{u}_s^{\alpha\beta} - R_v \vec{i}_g^{\alpha\beta} - L_v \frac{d\vec{i}_g^{\alpha\beta}}{dt} \quad (2-2)$$

After transform into rotating dq coordinate system, (2-2) becomes:

$$\begin{cases} \vec{u}_{gcd} = \vec{u}_{sd} - R_v \vec{i}_{gd} - L_v \frac{d\vec{i}_{gd}}{dt} + \omega L_v \vec{i}_{gq} \\ \vec{u}_{gcq} = \vec{u}_{sq} - R_v \vec{i}_{gq} - L_v \frac{d\vec{i}_{gq}}{dt} - \omega L_v \vec{i}_{gd} \end{cases} \quad (2-3)$$

Since the PLL works on stator voltage, it can be assumed that  $u_{sq} \approx 0$ .

(2-3) can be re-arranged as

$$\begin{cases} \vec{u}_{gcd} - \vec{u}_{sd} - \omega L_v \vec{i}_{gq} = -R_v \vec{i}_{gd} - L_v \frac{d\vec{i}_{gd}}{dt} = \vec{u}'_{gcd} \\ \vec{u}_{gcq} - \vec{u}_{sq} + \omega L_v \vec{i}_{gd} = -R_v \vec{i}_{gq} - L_v \frac{d\vec{i}_{gq}}{dt} = \vec{u}'_{gcq} \end{cases} \quad (2-4)$$

Apply Laplace transform to (2-4) gives the following transfer function:

$$G_{pugcig}(s) = \frac{i_{gd}(s)}{-u'_{gcd}(s)} = \frac{i_{gq}(s)}{-u'_{gcq}(s)} = \frac{1}{sL_v + R_v} \quad (2-5)$$

The diagram of the inner control loop is depicted in detail in Fig. 2-12. In order to eliminate the coupling between d and q components, the control system takes the references of the coupled current components as feed-forward signals. The measured terminal voltage is also taken as a feed-forward signal. The reference value of converter voltage is calculated by

$$\begin{cases} u_{gcd,ref} = u_{sd} + \omega L_v i_{gq,ref} - R_v i_{gd,ref} - V'_{gcd} \\ u_{gcq,ref} = u_{sq} - \omega L_v i_{gd,ref} - R_v i_{gq,ref} - V'_{gcq} \end{cases} \quad (2-6)$$

where  $V'_{gcd}$  and  $V'_{gcq}$  are the outputs from the current controllers. In the equations, the first three items on the right side are the feed-forward items.

If the difference between the feed-forward signals and their respective real value is negligible, the inner control system can be simplified as shown in Fig. 2-13.

Therefore, the closed-loop transfer function of grid-side current control system can be written as:

$$G_{ig\_cl}(s) = G_{igd\_track}(s) = G_{igq\_track}(s) = \frac{G_{pugcig}(s)(R_v + G_{kig}(s))}{1 + G_{pugcig}(s)G_{kig}(s)} \quad (2-7)$$

where  $G_{pugcig}(s) = \frac{1}{sL_v + R_v}$  is the plant model of the current control loop.

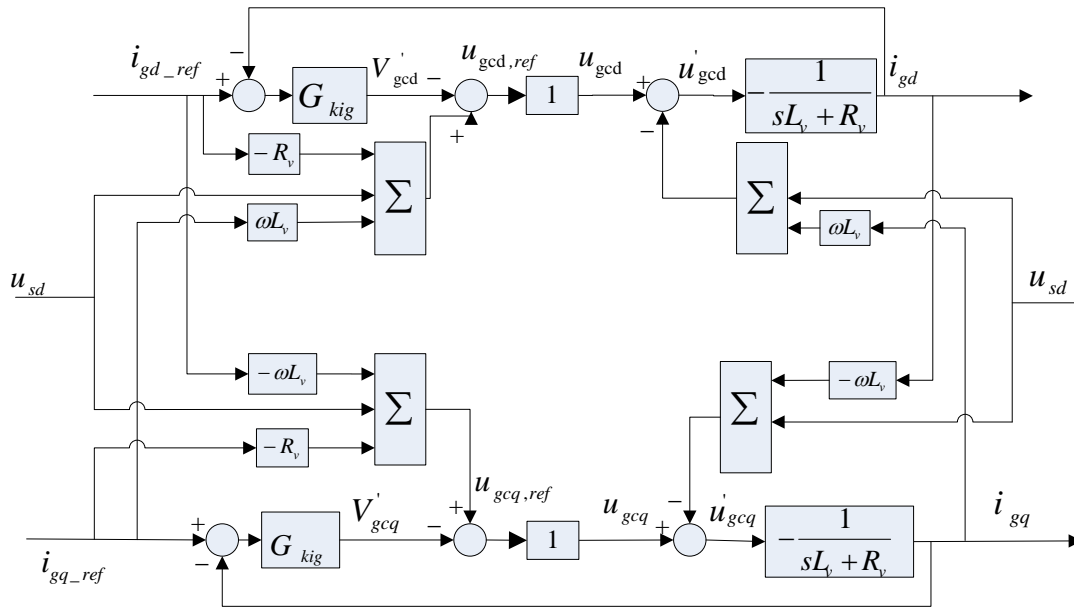


Fig. 2-12 Inner control loop of the grid-side converter

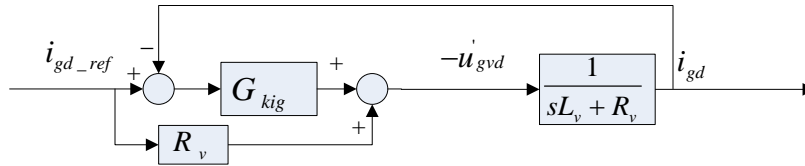


Fig. 2-13 Simplified inner active current control loop of grid-side converter

### 2.2.1.1.2 Outer control loop

As stated above, the dc link voltage is controlled in the outer loop. The dc link voltage is governed by

$$\frac{d(\frac{1}{2}Cu_{dc}^2)}{dt} = P_{ac,gc} - P_{ac,rc} \quad (2-8)$$

where  $P_{ac,gc} = u_{gd}i_{gd} + u_{gq}i_{gq} \approx u_{gd}i_{gd}$  is the power flowing from the the grid-side converter to the dc link and  $P_{ac,rc}$  is the power flowing from the dc link to the rotor-side converter. In a DFIG, there is always an active power flow  $P_{ac,rc}$  and it can be positive or negative depending on

whether the generator is operating at sub-synchronous or super-synchronous speed. The control system of the grid-side converter will adjust its active current (thus the active power) accordingly so that the dc link voltage is kept at the reference value. Therefore,  $P_{ac,rc}$  can be seen as a disturbance to the plant, as shown in Fig. 2-14. The plant model can be derived as following.

Let the transfer function of the plant and disturbance model be

$$G_{pigdudc}(s) = \frac{u_{dc}(s)}{i_{gd}(s)} \quad \text{and} \quad G_{dprcudc}(s) = \frac{u_{dc}(s)}{P_{ac,rc}(s)}$$

Then we have

$$u_{dc}(s) = G_{pigdudc}(s)i_{gd}(s) + G_{dprcudc}(s)P_{ac,rc}(s) \quad (2-9)$$

By discarding the disturbance term, (2-8) can be re-written as

$$\frac{d(\frac{1}{2}Cu_{dc}^2)}{dt} = u_{gd}i_{gd} \quad (2-10)$$

The plant is non-linear due to the presence of the square term. There are two ways to achieve linear control. One way is to control the energy stored in the dc-link capacitor, i.e.,  $\frac{1}{2}Cu_{dc}^2$ . Another way is to linearize the plant around the operation point  $u_{dc0}$ . Here, the latter method is used. By using Taylor expansion around  $u_{dc0}$ ,  $u_{dc}^2$  can be approximated as

$$u_{dc}^2 \approx u_{dc0}^2 + 2u_{dc0}(u_{dc} - u_{dc0}) = 2u_{dc0}u_{dc} - u_{dc0}^2 \quad (2-11)$$

Therefore, (2-10) can be approximated as:

$$Cu_{dc0} \frac{d(u_{dc})}{dt} = u_{gd}i_{gd} \quad (2-12)$$

This gives the plant model:

$$G_{pigdudc}(s) = \frac{u_{dc}(s)}{i_{gd}(s)} = \frac{u_{gd}}{sCu_{dc0}} \quad (2-13)$$

Similarly, the disturbance model can be obtained as

$$G_{dprcudc}(s) = \frac{u_{dc}(s)}{P_{ac,rc}(s)} = \frac{1}{sCu_{dc0}} \quad (2-14)$$

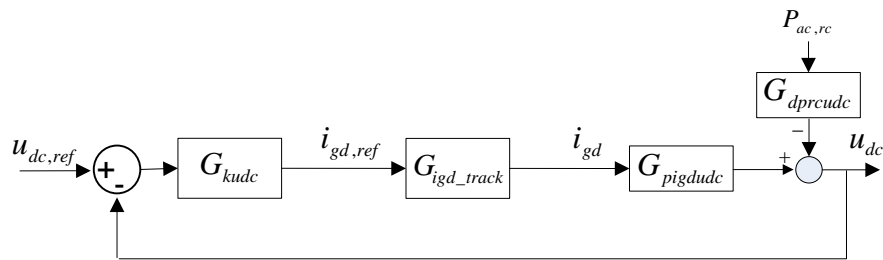


Fig. 2-14 Grid-side converter control system

The closed-loop transfer functions for reference tracking and disturbance rejection are:

$$G_{udc\_track}(s) = \frac{u_{dc}(s)}{u_{dc,ref}(s)} = \frac{G_{kudc}(s)G_{igd\_track}(s)G_{pigdudc}(s)}{1+G_{kudc}(s)G_{igd\_track}(s)G_{pigdudc}(s)} \quad (2-15)$$

$$G_{udc\_d}(s) = \frac{u_{dc}(s)}{P_{ac,rc}(s)} = \frac{G_{dprcudc}(s)}{1+G_{kudc}(s)G_{igd\_track}(s)G_{pigdudc}(s)} \quad (2-16)$$

### 2.2.1.1.3 Selection of controller parameters

The dc link voltage during normal operation is chosen as 1150 V. With the parameter shown in Table 2-2 controller parameters for grid-side converter, the two plant models are determined.

The PI controllers are described with the following transfer function:

$$G_{PI}(s) = kp * \left( \frac{s-zero_{PI}}{s} \right) \quad (2-17)$$

In selecting controller gains, the inner loop should be faster than outer loop, usually 5 times faster [24]. With the parameters selected as in Table 2-2, the bandwidths for inner and outer loop are 2016 rad/s and 526 rad/s respectively.

Table 2-2 controller parameters for grid-side converter

	PI controller zero	Kp	Ti	Bandwidth (rad/s)
Ig	6	1.6	0.104	2016
Udc	50	3	0.0067	520

#### 2.2.1.1.4 Validation of the derived transfer functions

Simulations have been performed in Matlab to validate the above derived transfer functions.

Fig. 2-15 shows the step response of the active current control system with DFIG model and with transfer function respectively. The difference between these two results is mainly because that the difference between the feed-forward signal  $i_{gq,ref}$  and its real value  $i_{gq}$  is neglected in derivation of the transfer function. If the real value is used as the feed-forward signal instead of the reference in the DFIG simulation, the responses get closer, as shown in Fig. 2-16.

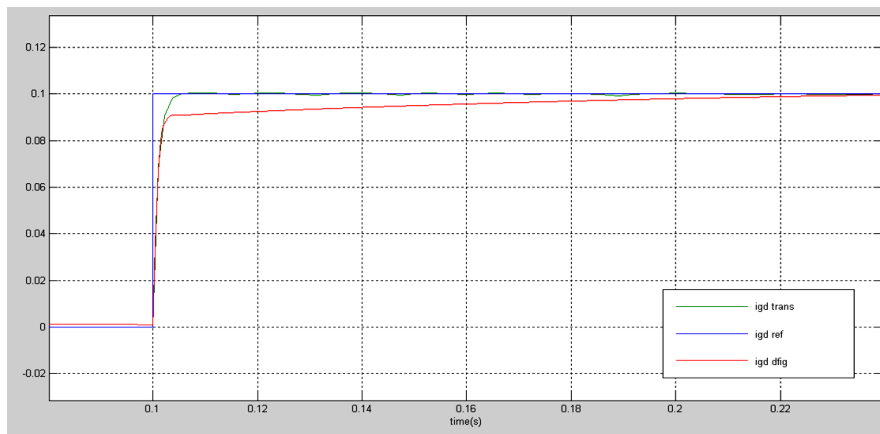


Fig. 2-15 Step response of the inner current control system (red: simulation with DFIG model, green: simulation with transfer function)

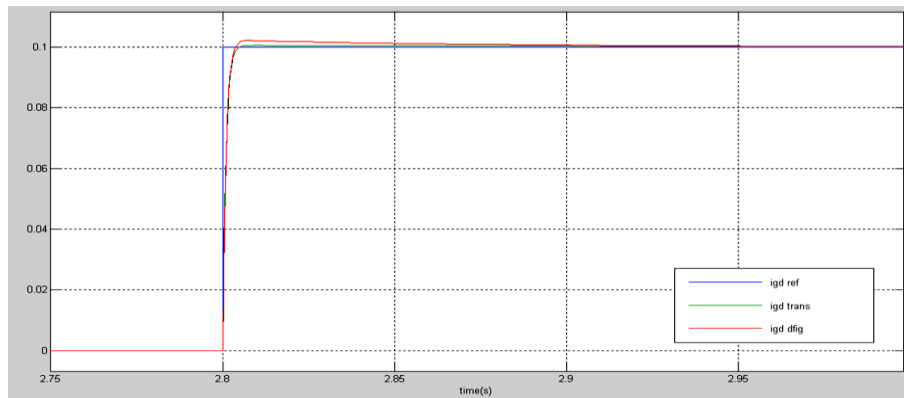


Fig. 2-16 Step response of the inner current control system (red: DFIG model; green: transfer function)

The step response of the dc voltage control system is shown in Fig. 2-17. Fig. 2-18 shows the dc voltage response to a unit step change in the active power from the rotor-side converter.

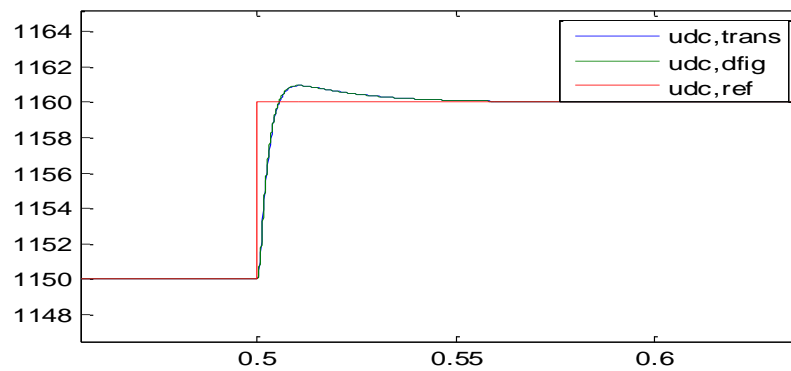


Fig. 2-17 Step response of the dc voltage control system (red: reference; green: DFIG model; blue: transfer function)

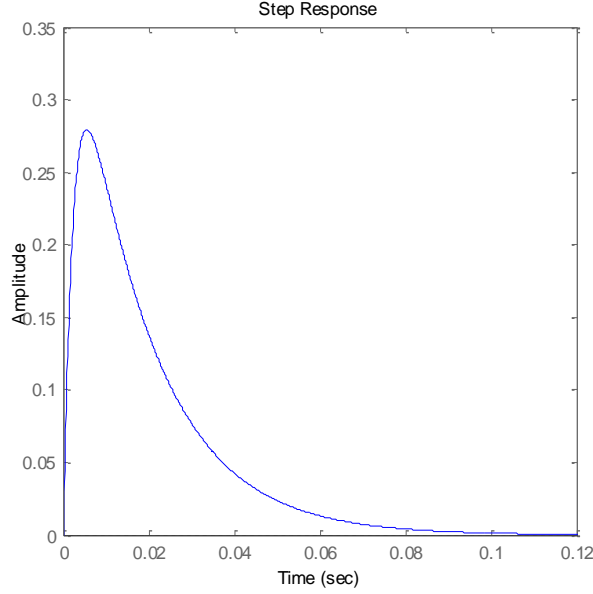


Fig. 2-18 Response of dc voltage to step change in active power from rotor converter

## 2.2.1.2 Rotor-side converter

### 2.2.1.2.1 Inner current control loop

The rotor circuit equation in  $\alpha\beta$  plane is:

$$\overrightarrow{u_{rn}^{\alpha\beta}} = R_r \overrightarrow{i_{rn}^{\alpha\beta}} + L_{lr} \frac{d\overrightarrow{i_{rn}^{\alpha\beta}}}{dt} + L_m \frac{d(\overrightarrow{i_{sn}^{\alpha\beta}} + \overrightarrow{i_{rn}^{\alpha\beta}})}{dt} = R_r \overrightarrow{i_{rn}^{\alpha\beta}} + L_r \frac{d\overrightarrow{i_{rn}^{\alpha\beta}}}{dt} + L_m \frac{d\overrightarrow{i_{sn}^{\alpha\beta}}}{dt} \quad (2-18)$$

where  $L_r = L_{lr} + L_m$ . In the equation, the rotor voltage and current the vectors in the above equation are rotating at slip frequency  $\omega_{sn} = \omega_n - \omega_r$ . However, since the rotor is rotating at a frequency of  $\omega_r$ , the net effect is that these vectors are rotating at nominal frequency in the air gap of the machine.

The angle used for dq transform of rotor current and voltage is obtained by:

$$\theta_{rs} = \theta_{PLL} - \theta_r, \text{ where } \theta_r \text{ is the rotor angle.}$$

After transform into rotating dq plane using angle  $\theta_r$ , the equation becomes:

$$\begin{cases} \overrightarrow{u_{rnd}} = R_r \overrightarrow{i_{rnd}} + L_r \frac{d\overrightarrow{i_{rnd}}}{dt} + L_m \frac{d\overrightarrow{i_{snd}}}{dt} - (\omega_n - \omega_r) L_m \overrightarrow{i_{snq}} - (\omega_n - \omega_r) L_r \overrightarrow{i_{rnq}} \\ \overrightarrow{u_{rnq}} = R_r \overrightarrow{i_{rnq}} + L_r \frac{d\overrightarrow{i_{rnq}}}{dt} + L_m \frac{d\overrightarrow{i_{snq}}}{dt} + (\omega_n - \omega_r) L_m \overrightarrow{i_{snd}} + (\omega_n - \omega_r) L_r \overrightarrow{i_{rnd}} \end{cases} \quad (2-19)$$

Define new variables

$$\begin{cases} \overrightarrow{u'_{rnd}} = \overrightarrow{u_{rnd}} + (\omega_n - \omega_r) L_m \overrightarrow{i_{snq}} + (\omega_n - \omega_r) L_r \overrightarrow{i_{rnq}} \\ \overrightarrow{u'_{rnq}} = \overrightarrow{u_{rnq}} - (\omega_n - \omega_r) L_m \overrightarrow{i_{snd}} - (\omega_n - \omega_r) L_r \overrightarrow{i_{rnd}} \end{cases} \quad (2-20)$$

(2-19) can be re-written as

$$\begin{cases} \overrightarrow{u'_{rnd}} = R_r \overrightarrow{i_{rnd}} + L_r \frac{d\overrightarrow{i_{rnd}}}{dt} + L_m \frac{d\overrightarrow{i_{snd}}}{dt} \\ \overrightarrow{u'_{rnq}} = R_r \overrightarrow{i_{rnq}} + L_r \frac{d\overrightarrow{i_{rnq}}}{dt} + L_m \frac{d\overrightarrow{i_{snq}}}{dt} \end{cases} \quad (2-21)$$

Applying Laplace transform to (2-21) gives:

$$\begin{cases} u'_{rnd}(s) = (R_r + sL_r)i_{rnd}(s) + sL_m i_{sna}(s) \\ u'_{rnq}(s) = (R_r + sL_r)i_{rnq}(s) + sL_m i_{snq}(s) \end{cases} \quad (2-22)$$

In order to eliminate stator current components from the above equation, the stator circuit equation is written as:

$$\overrightarrow{u_{sn}^{\alpha\beta}} = R_s \overrightarrow{i_{sn}^{\alpha\beta}} + L_{ls} \frac{d\overrightarrow{i_{sn}^{\alpha\beta}}}{dt} + L_m \frac{d(\overrightarrow{i_{sn}^{\alpha\beta}} + \overrightarrow{i_{rn}^{\alpha\beta}})}{dt} = R_s \overrightarrow{i_{sn}^{\alpha\beta}} + L_s \frac{d\overrightarrow{i_{sn}^{\alpha\beta}}}{dt} + L_m \frac{d\overrightarrow{i_{rn}^{\alpha\beta}}}{dt} \quad (2-23)$$

where  $L_s = L_{ls} + L_m$ .

After transform into rotating dq plane, the equation becomes:

$$\begin{cases} \overrightarrow{u_{sna}} = R_s \overrightarrow{i_{sna}} + L_s \frac{d\overrightarrow{i_{sna}}}{dt} + L_m \frac{d\overrightarrow{i_{rna}}}{dt} - \omega L_s \overrightarrow{i_{snq}} - \omega L_m \overrightarrow{i_{rnq}} = u_{sna} \\ \overrightarrow{u_{snq}} = R_s \overrightarrow{i_{snq}} + L_s \frac{d\overrightarrow{i_{snq}}}{dt} + L_m \frac{d\overrightarrow{i_{rnq}}}{dt} + \omega L_s \overrightarrow{i_{sna}} + \omega L_m \overrightarrow{i_{rna}} = 0 \end{cases} \quad (2-24)$$

With some manipulation, the following can be obtained:

$$\begin{cases} L_s^2 \frac{d^2 \overrightarrow{i_{sna}}}{dt^2} + 2R_s L_s \frac{d\overrightarrow{i_{sna}}}{dt} + (R_s^2 + \omega^2 L_s^2) \overrightarrow{i_{sna}} \\ = \overrightarrow{u_{sna}} R_s + L_s \frac{d\overrightarrow{u_{sna}}}{dt} + \omega L_s \overrightarrow{u_{snq}} + \omega L_m R_s \overrightarrow{i_{rnq}} - (L_m L_s \frac{d^2 \overrightarrow{i_{rna}}}{dt^2} + L_m R_s \frac{d\overrightarrow{i_{rna}}}{dt} + \omega^2 L_s L_m \overrightarrow{i_{rna}}) \\ L_s^2 \frac{d^2 \overrightarrow{i_{snq}}}{dt^2} + 2R_s L_s \frac{d\overrightarrow{i_{snq}}}{dt} + (R_s^2 + \omega^2 L_s^2) \overrightarrow{i_{snq}} \\ = \overrightarrow{u_{snq}} R_s + L_s \frac{d\overrightarrow{u_{snq}}}{dt} - \omega L_s \overrightarrow{u_{sna}} - \omega L_m R_s \overrightarrow{i_{rna}} - (L_m L_s \frac{d^2 \overrightarrow{i_{rnq}}}{dt^2} + L_m R_s \frac{d\overrightarrow{i_{rnq}}}{dt} + \omega^2 L_s L_m \overrightarrow{i_{rnq}}) \end{cases} \quad (2-25)$$

Laplace transformation of (2-25) gives:

$$\begin{cases} i_{sna}(s) = \frac{(R_s + sL_s)u_{sna}(s) + \omega L_s u_{snq}(s) - (s^2 L_m L_s + sL_m R_s + \omega^2 L_s L_m)i_{rna}(s) + \omega L_m R_s i_{rnq}(s)}{s^2 L_s^2 + 2sR_s L_s + R_s^2 + \omega^2 L_s^2} \\ i_{snq}(s) = \frac{(R_s + sL_s)u_{snq}(s) - \omega L_s u_{sna}(s) - (s^2 L_m L_s + sL_m R_s + \omega^2 L_s L_m)i_{rnq}(s) - \omega L_m R_s i_{rna}(s)}{s^2 L_s^2 + 2sR_s L_s + R_s^2 + \omega^2 L_s^2} \end{cases} \quad (2-26)$$

which can be re-written as

$$\begin{cases} i_{sna}(s) = G_{usndisna}(s)u_{sna}(s) + G_{irna}(s)i_{rnq}(s) + G_{irndisna}(s)i_{rna}(s) \\ i_{snq}(s) = G_{usndisnq}(s)u_{sna}(s) + G_{irndisnq}(s)i_{rnq}(s) + G_{irna}(s)i_{rna}(s) \end{cases} \quad (2-27)$$

In the equations

$$\begin{cases} G_{usndisna}(s) = \frac{i_{sna}(s)}{u_{sna}(s)} = \frac{R_s + sL_s}{s^2 L_s^2 + 2sR_s L_s + R_s^2 + \omega^2 L_s^2} \\ G_{irndisna}(s) = \frac{i_{sna}(s)}{i_{rna}(s)} = -\frac{s^2 L_m L_s + sL_m R_s + \omega^2 L_s L_m}{s^2 L_s^2 + 2sR_s L_s + R_s^2 + \omega^2 L_s^2} \\ G_{irna}(s) = \frac{i_{sna}(s)}{i_{rnq}(s)} = \frac{\omega L_m R_s}{s^2 L_s^2 + 2sR_s L_s + R_s^2 + \omega^2 L_s^2} \\ G_{usndisnq}(s) = \frac{i_{snq}(s)}{u_{snq}(s)} = \frac{-\omega L_s}{s^2 L_s^2 + 2sR_s L_s + R_s^2 + \omega^2 L_s^2} \\ G_{irna}(s) = \frac{i_{snq}(s)}{i_{rnq}(s)} = -\frac{s^2 L_m L_s + sL_m R_s + \omega^2 L_s L_m}{s^2 L_s^2 + 2sR_s L_s + R_s^2 + \omega^2 L_s^2} = G_{irndisna}(s) \\ G_{irndisnq}(s) = \frac{i_{snq}(s)}{i_{rna}(s)} = -\frac{\omega L_m R_s}{s^2 L_s^2 + 2sR_s L_s + R_s^2 + \omega^2 L_s^2} = -G_{irna}(s) \end{cases} \quad (2-28)$$

where  $u_{snq} \approx 0$  is considered.

Similar to the feed-forward method used in grid-side converter control system, the rotor current control system takes the coupled current components as the feed-forward signals to eliminate

the cross coupling between d and q components. The inner control system is depicted in Fig. 2-19. For nominal frequency component, the converter reference voltages are calculated as:

$$\begin{cases} u_{rcnd,ref} = R_r i_{rnd,ref} + V'_{rcnd} - (\omega_n - \omega_r) L_r i_{rnq,ref} - (\omega_n - \omega_r) L_m i_{snq,est} \\ u_{rcnq,ref} = R_r i_{rnq,ref} + V'_{rcnq} + (\omega_n - \omega_r) L_r i_{rnd,ref} + (\omega_n - \omega_r) L_m i_{srd,est} \end{cases} \quad (2-29)$$

Where  $i_{srd,est}$  and  $i_{snq,est}$  are the estimated d and q components of the stator current. If the difference between the references ( $i_{rnd,ref}$ ,  $i_{rnq,ref}$ ) and their real values, and the difference between the estimated ( $i_{srd,est}$ ,  $i_{snq,est}$ ) and the real value of stator current are negligible, the diagram of the inner current control system of the rotor converter can be simplified as in Fig.2-20 Simplified inner current control system of the rotor converter.

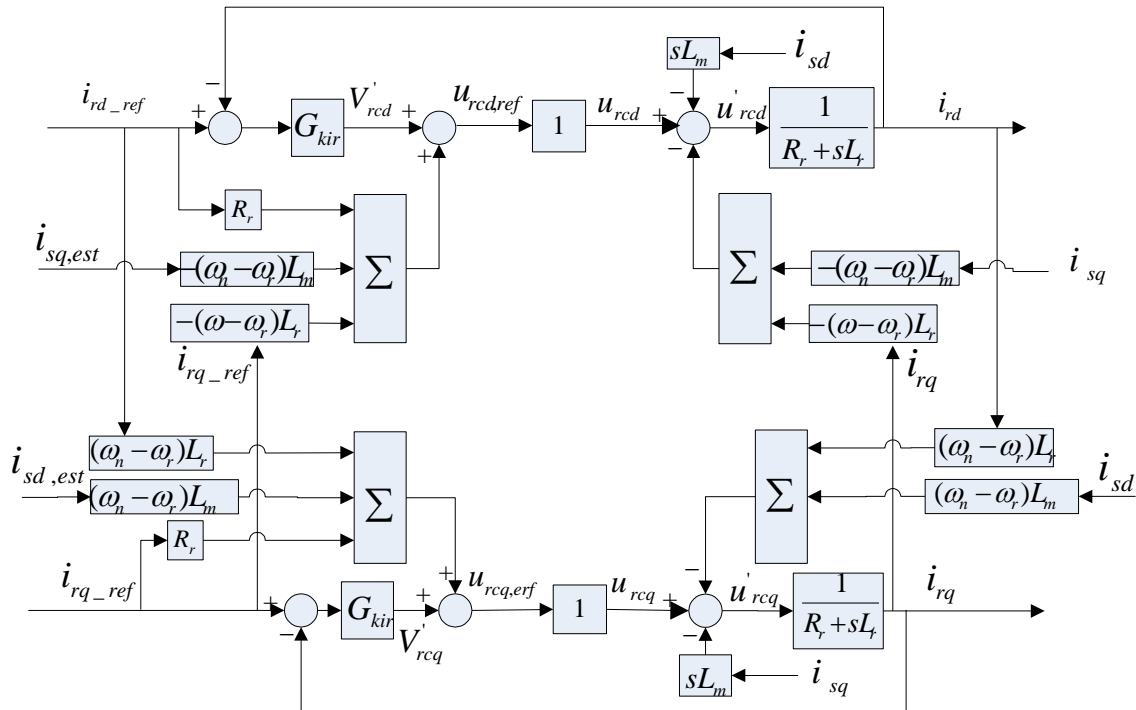


Fig. 2-19 Inner current control system of the rotor converter

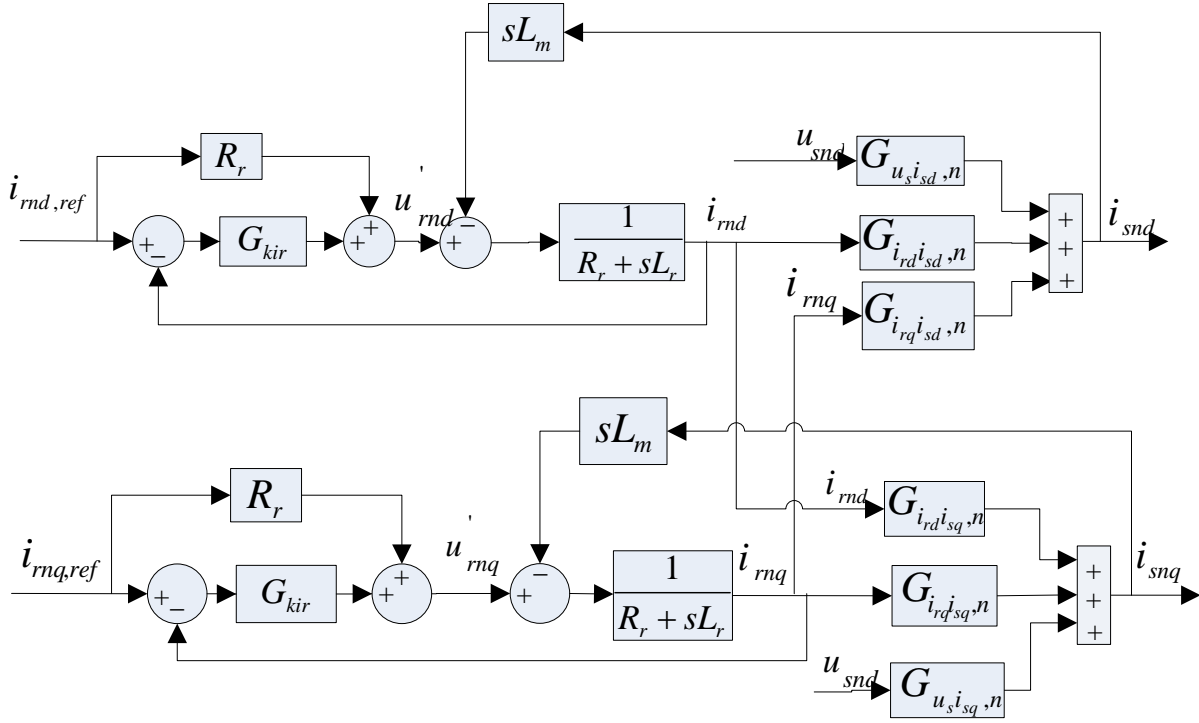


Fig.2-20 Simplified inner current control system of the rotor converter

If  $u_{snd}$  is seen as a disturbance to the plant, the system can be further simplified as shown in Fig. 2-21 Simplified inner current control system of the rotor converter.

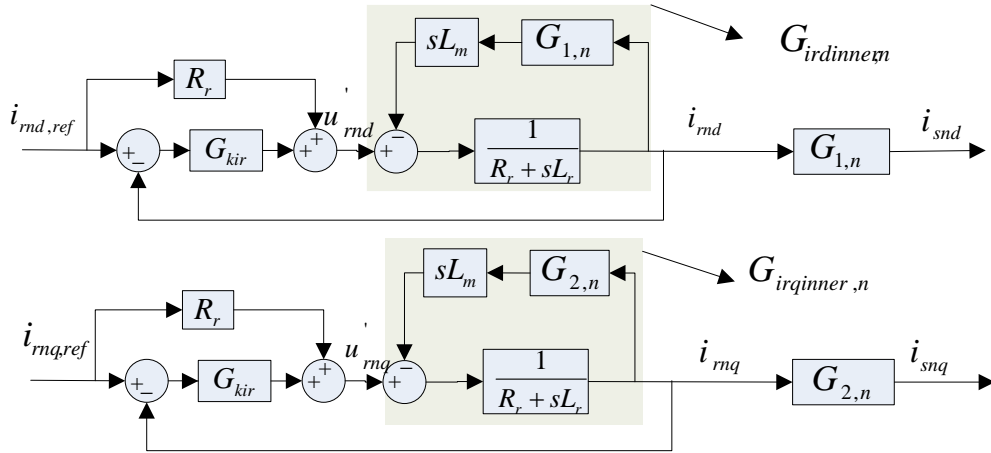


Fig. 2-21 Simplified inner current control system of the rotor converter

In the figure,

$$\begin{cases}
 G_{1,n}(s) = G_{irdis,n}(s) + G_{irdir,qn}(s)G_{irqis,d,n}(s) \\
 G_{2,n}(s) = G_{irqis,qn}(s) + G_{irqird,n}(s)G_{irdis,qn}(s) \\
 G_{irdinner,n}(s) = \frac{1}{R_r + sL_r + sL_m G_{1,n}} \\
 G_{irqinner,n}(s) = \frac{1}{R_r + sL_r + sL_m G_{2,n}}
 \end{cases} \quad (2-30)$$

where  $G_{irdir,qn}(s)$  and  $G_{irqird,n}(s)$  represent the coupling between d and q components of rotor current due to the coupling between rotor and stator currents.

Then, the transfer function of the inner current loop can be derived:

$$\begin{cases} G_{ird\_track,n}(s) = \frac{(R_r + G_{kir}(s))G_{irdinner,n}(s)}{1 + G_{kir}(s)G_{irdinner,n}(s)} = \frac{(R_r + G_{kir}(s))}{R_r + sL_r + sL_m G_{1,n}(s) + G_{kir}(s)} \\ G_{irq\_track,n}(s) = \frac{(R_r + G_{kir}(s))G_{irqinner,n}(s)}{1 + G_{kir}(s)G_{irqinner,n}(s)} = \frac{(R_r + G_{kir}(s))}{R_r + sL_r + sL_m G_{2,n}(s) + G_{kir}(s)} \end{cases} \quad (2-31)$$

### 2.2.1.2.2 Outer control loop

Reactive power control

The reactive power control structure is depicted in Fig. 2-22.

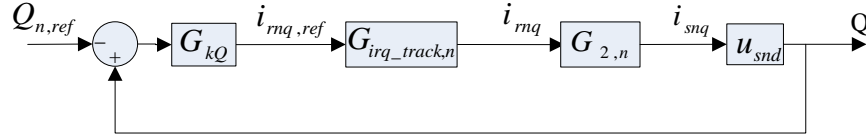


Fig. 2-22 Structure of reactive power control

Since the reactive current from the grid-side converter is controlled to zero, the reactive power from the DFIG equals to the reactive power from the stator, which is given by (2-32) in pu system:

$$Q_{pu} = u_{snd}i_{snq} - u_{snq}i_{snd} \approx u_{snd}i_{snq} \quad (2-32)$$

Therefore, the closed-loop transfer function of reactive power tracking can be obtained:

$$G_{Q\_track}(s) = -\frac{G_{kQ}(s)G_{irq\_track,n}(s)G_{2,n}(s)u_{snd}}{1 + G_{kQ}(s)G_{irq\_track,n}(s)G_{2,n}(s)u_{snd}} \quad (2-33)$$

The structure of the rotor speed control system is depicted in Fig. 2-23.

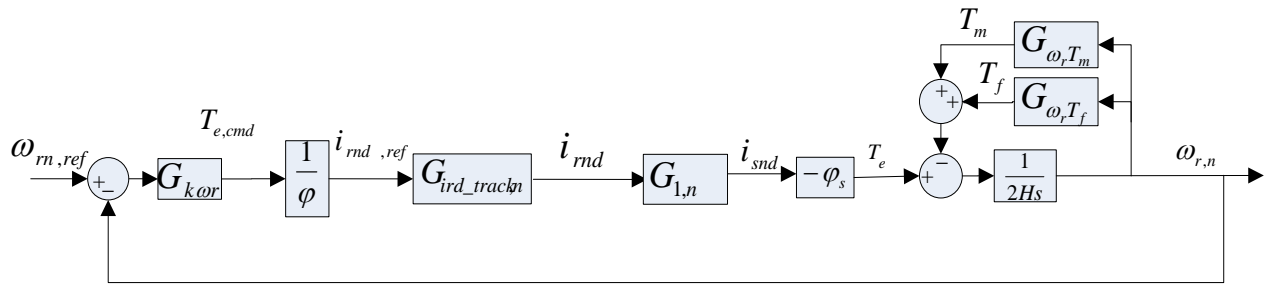


Fig. 2-23 Structure of the rotor speed control system

The output of the speed controller gives the reference for electrical torque that should be produced by the generator. Divided by the estimated flux magnitude, the torque command is translated into the reference for the active rotor current. Through the inner current tracking loop, the desired rotor current can be obtained. Accordingly, the electrical torque can be obtained in the per unit system:

$$T_e = \varphi_{snd}i_{snq} + \varphi_{snq}i_{snd} \approx \varphi_{snq}i_{snd} \quad (2-34)$$

where  $\varphi_{snq}$  is the q component of the stator flux. Since the PLL works on the stator voltage with  $u_{snq} = 0$ ,  $\varphi_{snd}$  is close to zero considering that the stator resistance is very small (the derivative part is neglected), as derived from (2-24).

The mechanical system can be described as:

$$\frac{d\omega_{rn}}{dt} = \frac{1}{2H} (T_e - F\omega_{rn} - T_m) \quad (2-35)$$

where  $H$  is the inertia of the generator,  $F$  is the friction factor, and  $T_m$  is the mechanical torque delivered by the wind turbine via shaft system. The shaft system is represented by

$$\begin{cases} \frac{d\omega_{WT}}{dt} = \frac{1}{2H_{WT}} (T_{WT} - T_m) \\ T_m = (\omega_{WT} - \omega_r) D_{mut} + T_{m1} \\ \frac{dT_{m1}}{dt} = K_{sh} (\omega_{WT} - \omega_r) \end{cases} \quad (2-36)$$

where  $K_{sh}$  is the shaft stiffness,  $D_{mut}$  is the mutual damping between generator and wind turbine;  $\omega_{WT}$ ,  $H_{WT}$ , and  $T_{WT}$  are the rotating speed, inertia and the produced torque of the wind turbine,  $T_{m1}$  is the torque produced by the shaft.  $T_{WT}$  is considered to be dependent only on wind speed in the study. The transfer function of the above mechanical system can be obtained as:

$$G_{wrTm}(s) = \frac{T_m(s)}{\omega_r(s)} = \frac{2H_{WT}s(D_{mut}s + K_{sh}\omega_n)}{2H_{WT}s^2 + D_{mut}s + K_{sh}\omega_n} \quad (2-37)$$

Thus, the transfer function of the total mechanical system of the DFIG is given by:

$$G_{Te\omega_r}(s) = \frac{\frac{1}{2Hs+F}}{1 + \frac{1}{2Hs+F} G_{wrTm}(s)} = \frac{1}{2Hs+F + G_{wrTm}(s)} \quad (2-38)$$

Finally, the closed-loop transfer function of the rotor speed control system can be written as:

$$G_{\omega_r\_track,n}(s) = \frac{G_{kor}(s)G_{ird\_track,n}(s)G_{1,n}(s)G_{Tewr}(s)}{1 + G_{kor}(s)G_{ird\_track,n}(s)G_{1,n}(s)G_{Tewr}(s)} \quad (2-39)$$

### 2.2.1.2.3 Validation of the derived transfer function

Simulations have been performed to verify the above derived transfer functions. In the simulation, the mechanical power is kept constant. In addition, the active current is kept constant for reactive power step simulation and the reactive current is kept constant for speed step simulation. The figure shows good agreement between the derived transfer function and the DFIG model.



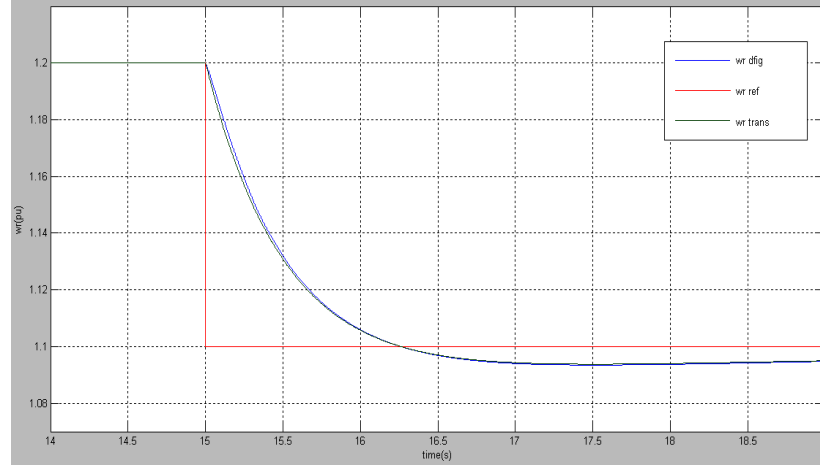


Fig. 2-24 Step response of the inner current control system (top: reactive power; bottom: rotor speed; blue: reference; red: DFIG model; green: transfer function)

#### 2.2.1.2.4 Selection of controller parameters

The controller parameters can be chosen as listed in Table 2-3. In the table, the corresponding bandwidths of the inner and outer control loops are also listed.

Table 2-3 Parameters for rotor converter control system

Controller	PI controller zero	Kp	Ti	Bandwidth (rad/s)
Ir	15	0.3	0.22	358
Wr	5	24	0.0083	4.5
Q	50	1.5	0.013	67

#### 2.2.2 Derivation of transfer functions of system at sub-synchronous frequency

The sub-synchronous component of the stator current has a frequency of  $f_{ss}$ . The current vector rotates with an angular frequency of  $\omega_{ss}$  in the  $\alpha\beta$  plane. In the control system, the coordinate transform of the stator quantities from  $\alpha\beta$  to dq plane uses the angle  $\theta_{PLL} = j\omega_n t$  from PLL. After transformation, the dq components ( $\overline{i_s^{dq}}$ ) will contain a dc component ( $\overline{i_{sn}^{dq}}$ , corresponding to the nominal frequency component) and a sinusoidal component ( $\overline{i_{ssn}^{dq}}$ , corresponding to the sub-synchronous component). The above analysis applies to stator voltage and grid-side current.

$$\begin{cases} \overline{i_s^{dq}} = \overline{i_s^{\alpha\beta}} e^{-j\omega_n t} = \overline{i_{sn}^{dq}} + \overline{i_{ssn}^{dq}} e^{j(\omega_{ss}-\omega_n)t} = \overline{i_{sn}^{dq}} + \overline{i_{ssn}^{dq}} \\ \overline{u_s^{dq}} = \overline{u_s^{\alpha\beta}} e^{-j\omega_n t} = \overline{u_{sn}^{dq}} + \overline{u_{ssn}^{dq}} e^{j(\omega_{ss}-\omega_n)t} = \overline{u_{sn}^{dq}} + \overline{u_{ssn}^{dq}} \\ \overline{i_g^{dq}} = \overline{i_g^{\alpha\beta}} e^{-j\omega_n t} = \overline{i_{gn}^{dq}} + \overline{i_{gss}^{dq}} e^{j(\omega_{ss}-\omega_n)t} = \overline{i_{gn}^{dq}} + \overline{i_{gss}^{dq}} \end{cases} \quad (2-40)$$

As stated earlier, the rotor current contains a component induced by nominal frequency component of the air-gap flux and a component induced by sub-synchronous frequency

component of the air-gap flux. In the control system, the angle used for coordinate transform of the rotor quantities from  $\alpha\beta$  to dq plane is

$$\theta_{rs} = \theta_{PLL} - \theta_r = j(\omega_n - \omega_r)t \quad (2-41)$$

where  $\theta_r$  is the rotor angle.

After transformation, the dq components ( $\overline{l_r^{dq}}$ ) will contain a dc component ( $\overline{l_{rn}^{dq}}$ , corresponding to the component induced by nominal frequency flux component) and a sinusoidal component ( $\overline{l_{rssh}^{dq}}$ , corresponding to the component induced by sub-synchronous flux component). The above analysis applies to rotor voltage.

$$\begin{cases} \overline{l_r^{dq}} = \overline{l_r^{\alpha\beta}} e^{-j(\omega_n - \omega_r)t} = \overline{l_{rn}^{dq}} + \overline{l_{rssh}^{dq}} e^{j(\omega_{ss} - \omega_n)t} = \overline{l_{rn}^{dq}} + \overline{l_{rssh}^{dq}} \\ \overline{u_{rc}^{dq}} = \overline{u_{rc}^{\alpha\beta}} e^{-j(\omega_n - \omega_r)t} = \overline{u_{rcn}^{dq}} + \overline{u_{rcss}^{dq}} e^{j(\omega_{ss} - \omega_n)t} = \overline{u_{rcn}^{dq}} + \overline{u_{rcss}^{dq}} \end{cases} \quad (2-42)$$

## 2.2.3 Grid-side converter

The derivation of the transfer function at nominal frequency in Section 2.2.1.1 is valid for both nominal frequency and sub-synchronous frequency.

## 2.2.4 Rotor-side converter

### 2.2.4.1 Derivation of the transfer functions

The circuit equation for sub-synchronous frequency can be written as:

$$\overline{u_{rcss}^{\alpha\beta}} = \overline{u_{rcssn}^{dq}} e^{j(\omega_n - \omega_r)t} = R_r \overline{l_{rssh}^{dq}} e^{j(\omega_n - \omega_r)t} + L_r \frac{d(\overline{l_{rssh}^{dq}} e^{j(\omega_n - \omega_r)t})}{dt} + L_m \frac{d(\overline{l_{sssn}^{dq}} e^{j(\omega_n - \omega_r)t})}{dt} \quad (2-43)$$

Multiplying both sides with  $e^{-j(\omega_n - \omega_r)t}$  yields:

$$\overline{u_{rcssn}^{dq}} = R_r \overline{l_{rssh}^{dq}} + L_r \frac{d(\overline{l_{rssh}^{dq}})}{dt} + j(\omega_n - \omega_r) L_r \overline{l_{rssh}^{dq}} + L_m \frac{d(\overline{l_{sssn}^{dq}})}{dt} + j(\omega_n - \omega_r) L_m \overline{l_{sssn}^{dq}} \quad (2-44)$$

This gives equations for the individual d and q components:

$$\begin{cases} \overline{u_{rcssnd}} = R_r \overline{l_{rsshnd}} + L_r \frac{d\overline{l_{rsshnd}}}{dt} + L_m \frac{d\overline{l_{sssnd}}}{dt} - (\omega_n - \omega_r) L_m \overline{l_{sssnq}} - (\omega_n - \omega_r) L_r \overline{l_{rsshnq}} \\ \overline{u_{rcssnq}} = R_r \overline{l_{rsshnq}} + L_r \frac{d\overline{l_{rsshnq}}}{dt} + L_m \frac{d\overline{l_{sssnq}}}{dt} + (\omega_n - \omega_r) L_m \overline{l_{sssnd}} + (\omega_n - \omega_r) L_r \overline{l_{rsshnd}} \end{cases} \quad (2-45)$$

The control system calculates the reference voltage as:

$$\begin{cases} u_{rcssd,ref} = R_r i_{rsshnd,ref} + V'_{rssd} - (\omega_n - \omega_r) L_r i_{rsshnq,ref} - (\omega_n - \omega_r) L_m i_{sssnq,est} \\ u_{rcssq,ref} = R_r i_{rsshnq,ref} + V'_{rssq} + (\omega_n - \omega_r) L_r i_{rsshnd,ref} + (\omega_n - \omega_r) L_m i_{sssnd,est} \end{cases} \quad (2-46)$$

where  $V'_{rssd}$  and  $V'_{rssq}$  are the outputs from the corresponding current controllers.

In derivation of the transfer functions, there are two main differences between sub-synchronous frequency and nominal frequency system.

1. The first difference is that the infinite source presents only in the nominal frequency circuit. The presence of the infinite source and the PLL system justify the assumption that the impact of the system impedance on the stator terminal voltage at nominal frequency is insignificant. As a result, the control system of grid-side converter and rotor-side converter can be assumed

to be independent to each other. Due to the absence of the infinite source at sub-synchronous frequency, the system impedances ( $R_{sys}$ ,  $L_{sys}$ ,  $C_{SC}$ ) have to be taken into consideration in deriving the relation between stator current and rotor current at sub-synchronous frequency.

For sub-synchronous frequency circuit, the following equations hold

$$\begin{cases} \overline{u_{SSSn}^{dq}} e^{j\omega_n t} = -R_{sys} \overline{i_{LSSn}^{dq}} e^{j\omega_n t} - L_{sys} \frac{d(\overline{i_{LSSn}^{dq}} e^{j\omega_n t})}{dt} - \overline{u_{CSSn}^{dq}} e^{j\omega_n t} \\ \overline{i_{LSSn}^{dq}} e^{j\omega_n t} = C_{SC} \frac{d(\overline{u_{CSSn}^{dq}} e^{j\omega_n t})}{dt} \\ \overline{i_{LSSn}^{dq}} e^{j\omega_n t} = \overline{i_{SSSn}^{dq}} e^{j\omega_n t} + \overline{i_{gSSn}^{dq}} e^{j\omega_n t} \end{cases} \quad (2-47)$$

where  $\overline{i_{LSSn}^{dq}}$  is the line current vector in dq plane.

Apply Laplace transform and with some manipulations, the following can be obtained:

$$\begin{cases} u_{SSSn}^d(s) = -\left(R_{sys} + sL_{sys} + \frac{s}{C_{SC}(s^2 + \omega_n^2)}\right) i_{SSSn}^d(s) + \left(\omega_n L_{sys} - \frac{\omega_n}{C_{SC}(s^2 + \omega_n^2)}\right) i_{SSSn}^q(s) \\ \quad - \left(R_{sys} + sL_{sys} + \frac{s}{C_{SC}(s^2 + \omega_n^2)}\right) i_{gSSn}^d(s) + \left(\omega_n L_{sys} - \frac{\omega_n}{C_{SC}(s^2 + \omega_n^2)}\right) i_{gSSn}^q(s) \\ u_{SSSn}^q(s) = -\left(R_{sys} + sL_{sys} + \frac{s}{C_{SC}(s^2 + \omega_n^2)}\right) i_{SSSn}^q(s) - \left(\omega_n L_{sys} - \frac{\omega_n}{C_{SC}(s^2 + \omega_n^2)}\right) i_{SSSn}^d(s) \\ \quad - \left(R_{sys} + sL_{sys} + \frac{s}{C_{SC}(s^2 + \omega_n^2)}\right) i_{gSSn}^q(s) - \left(\omega_n L_{sys} - \frac{\omega_n}{C_{SC}(s^2 + \omega_n^2)}\right) i_{gSSn}^d(s) \end{cases} \quad (2-48)$$

The generator stator circuit equations are

$$\begin{cases} u_{SSSn}^d(s) = R_s i_{SSSn}^d(s) + L_s s i_{SSSn}^d(s) + L_m s i_{rSSn}^d(s) - \omega_n L_s i_{SSSn}^q(s) - \omega_n L_m i_{rSSn}^q(s) \\ u_{SSSn}^q(s) = R_s i_{SSSn}^q(s) + L_s s i_{SSSn}^q(s) + L_m s i_{rSSn}^q(s) + \omega_n L_s i_{SSSn}^d(s) + \omega_n L_m i_{rSSn}^d(s) \end{cases} \quad (2-49)$$

From the two sets of equations above, the relation between the stator current and the rotor current as well as the grid-side converter current can be resolved.

$$\begin{cases} i_{SSSn}^d(s) = i_{rSSn}^d(s) G_{irdisd,ss}(s) + i_{rSSn}^q(s) G_{irqisd,ss}(s) + i_{gSSn}^d(s) G_{igdisd,ss}(s) + i_{gSSn}^q(s) G_{igqisd,ss}(s) \\ i_{SSSn}^q(s) = i_{rSSn}^q(s) G_{irqisq,ss}(s) + i_{rSSn}^d(s) G_{irdisq,ss}(s) + i_{gSSn}^d(s) G_{igdisq,ss}(s) + i_{gSSn}^q(s) G_{igqisq,ss}(s) \end{cases} \quad (2-50)$$

In case there is no outer loop for reactive current of the grid-side converter ( $i_{gSSn}^q = 0$ ). Existence of the outer loop for active current of the grid-side converter,  $i_{gSSn}^d$  is non-zero and is determined by the rotor current  $i_{rSSn}^d$ . This can be expressed as:

$$i_{gSSn}^d(s) = i_{rSSn}^d(s) G_{irdigd,ss}(s) \quad (2-51)$$

$G_{irdigd,ss}(s)$  can be derived from the diagram as shown below:

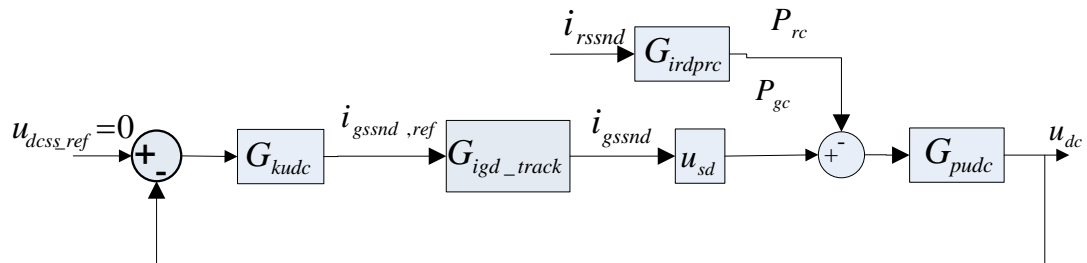


Fig. 2-25 Simplified DC voltage control loop

In the figure,  $G_{irdpre}(s)$  can be approximated as:

$$G_{irdpre}(s) = \frac{P_{rc}(s)}{i_{rssnd}(s)} \approx \frac{X_m}{X_s} * u_{snd} \quad (2-52)$$

2. The second difference is that the difference between the reference current or estimated current and their real values is not negligible for sub-synchronous frequency.

In the control system, the stator current is estimated using the following equation:

$$\begin{cases} i_{sd,est} = \frac{R_s u_{sd} - \omega^2 L_s L_m i_{rnd,ref} - \omega L_m R_s i_{rnq,ref}}{R_s^2 + \omega^2 L_s^2} \\ i_{snq,est} = \frac{-\omega L_s u_{sd} - \omega^2 L_s L_m i_{rnq,ref} - \omega L_m R_s i_{rnd,ref}}{R_s^2 + \omega^2 L_s^2} \end{cases} \quad (2-53)$$

Considering  $u_{sssnd}$  is small and  $R_s \ll \omega L_s$ , the estimated sub-synchronous frequency stator current is

$$\begin{cases} i_{sssnd,est} \approx -\frac{L_m}{L_s} i_{rssnd,ref} \\ i_{sssnq,est} \approx -\frac{L_m}{L_s} i_{rssnq,ref} \end{cases} \quad (2-54)$$

Therefore, the control system, including the impact of grid-side converter control on rotor-side converter control, together with the plants for sub-synchronous frequency can be depicted in the following figure. As shown in the figure, the calculation of torque and reactive power of sub-synchronous frequency contains only one item. Actually, the sub-synchronous frequency torque and reactive power equations should be:

$$\begin{cases} T_{e,ss} \approx \varphi_{snq} i_{sssnd} + \varphi_{sssnd} i_{snq} + \varphi_{sssnq} i_{snd} \\ Q_{ss} \approx u_{snd} i_{sssnq} + u_{sssnq} i_{snd} + u_{sssnd} i_{snq} \end{cases} \quad (2-55)$$

where  $\varphi_{snd} \approx 0$  and  $u_{snq} \approx 0$  are considered.

However, since  $\varphi_{sssnd}$  and  $\varphi_{sssnq}$  are much smaller than  $\varphi_{snq}$ , these two items in the torque calculation are neglected. Similarly, the last two items in the reactive power calculation are also neglected.

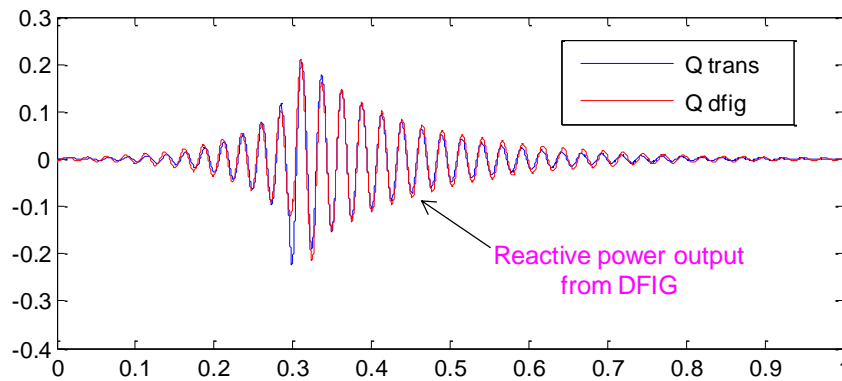
The computation of the transfer functions are performed in Matlab. The detailed steps will not be shown in this report.



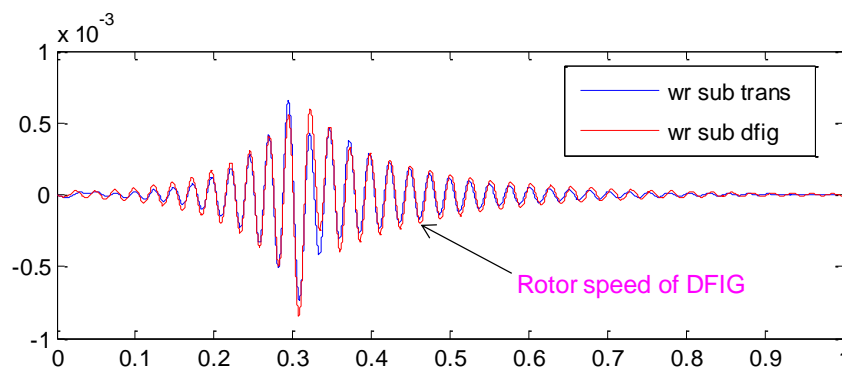
### 2.2.4.1.1 Validation of the derived transfer functions

#### (1). Validation 1

Simulations have been performed in Simulink with the DFIG model system and the transfer function system. Fig.2-27 shows the DFIG reactive power and rotor speed response. In the simulation with transfer function model, the impact of grid-side converter is neglected for simplicity. The simulations started from steady state. Then SSR was stimulated by increasing rotor converter current controller gain. At 0.3s, the current controller gain was reduced and the oscillations were damped out. The results show good agreement between the DFIG model and the derived transfer functions except the differences in the peak amplitude of the response. The oscillation frequency is about 39 Hz, which is the complimentary frequency of 21 Hz in the 60 Hz system. Fig. 2-28 shows the impedance characteristics of the whole system at sub-synchronous frequency as shown in Fig. 2-10 but with the grid-side converter branch neglected. Here the compensation degree is set to be 40% of the line reactance. It can be seen there are two resonance frequencies. One is 9.2 Hz representing resonance between the series capacitor and the sum of  $L_{sys}$ ,  $L_{ls}$ , and  $L_m$ . The other one is 21 Hz representing resonance between the series capacitor and the sum of  $L_{sys}$ ,  $L_{ls}$ , and  $L_{lr}$ .

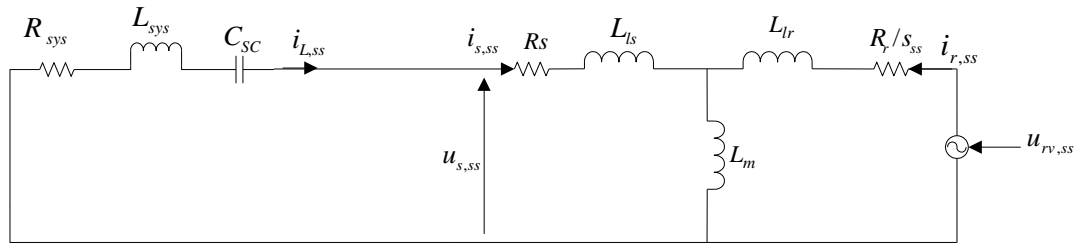


(a)

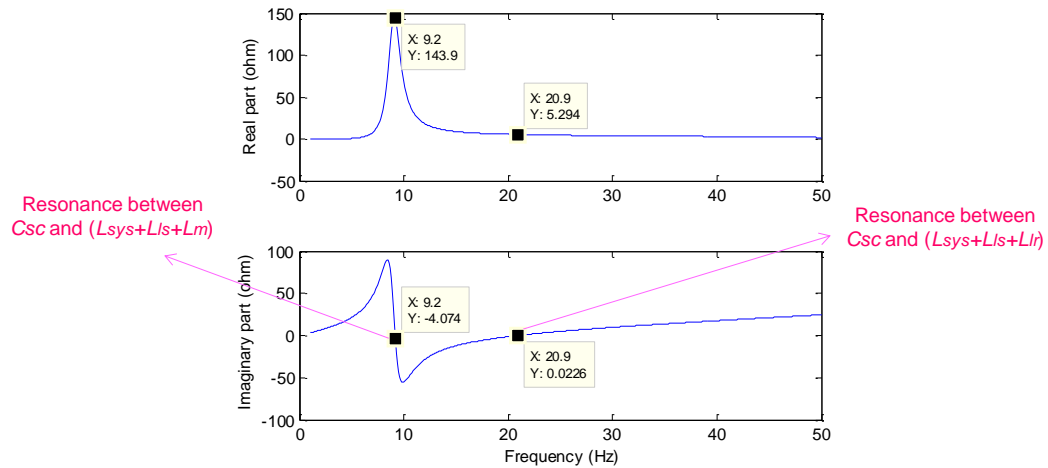


(b)

Fig.2-27 Comparison between DFIG model and the derived transfer functions in case of SSR (top: reactive power from DFIG, bottom: DFIG rotor speed; blue: results from system built with transfer functions, red: results from system with DFIG model)



(a)



(b)

Fig. 2-28 Impedance Characteristics of the system at sub-synchronous frequencies

## (2). Validation 2

The second validation has been made by comparing the critical gain of the rotor current controller in DFIG model and in the mathematic calculation in Matlab. From the simulations with DFIG model, for the same set of controller parameters except the rotor current controller gain, increasing the current controller gain to 0.149 will stimulate SSR. Fig. 2-29 shows the pole-zero map of the closed-loop transfer function of the inner current control loop of the rotor-side converter. In this comparison, the outer loops are disconnected in DFIG model and are disregarded in the transfer function calculation. The critical value of current controller gain is 0.151, which is slightly larger than the value obtained from the DFIG model.

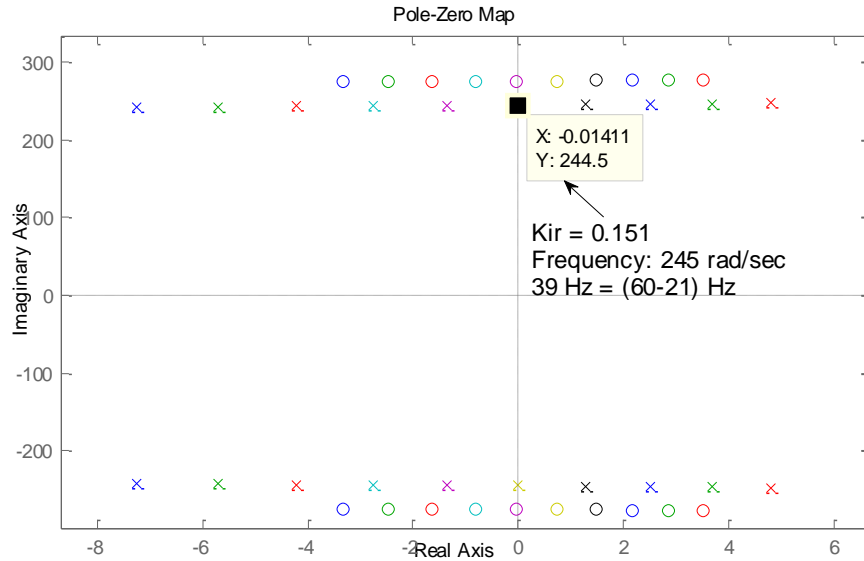


Fig. 2-29 Pole-zero map of the closed inner current control loop of the rotor-side converter

### 2.3 Analysis of SSR characteristics

Based on the derived transfer function, the SSR characteristics will be investigated by studying the pole-zero maps of the closed-loop transfer function of the rotor speed control system. The transfer function studied is the one from disturbances in stator current to the rotor speed  $G_{disor}(s)$ . The variables used in the study are listed in Table 2-4 with their values for base case and varying ranges.

Table 2-4 Variables used in study of closed-loop transfer functions

Variable	Base case value	Varying range
Compensation degree	40%	10% - 70% of line reactance
Rotor speed (steady state) $w_r$	1.2 pu	0.8 – 1.2 pu
$R_r$	0.016 pu	0 - 0.1 pu
$k_{ig}$	1.6	0.5 – 5
$k_{udc}$	3	0 – 10
$k_{ir}$	0.15	0.1 – 0.4
$k_{wr}$	24	0 – 50
$k_Q$	0.75	0.4 – 1.6

Fig. 2-30 to Fig. 2-38 show how the poles of  $G_{disor}$  change with the variables. In each figure, only one variable is varied and others are set to their base-case values.

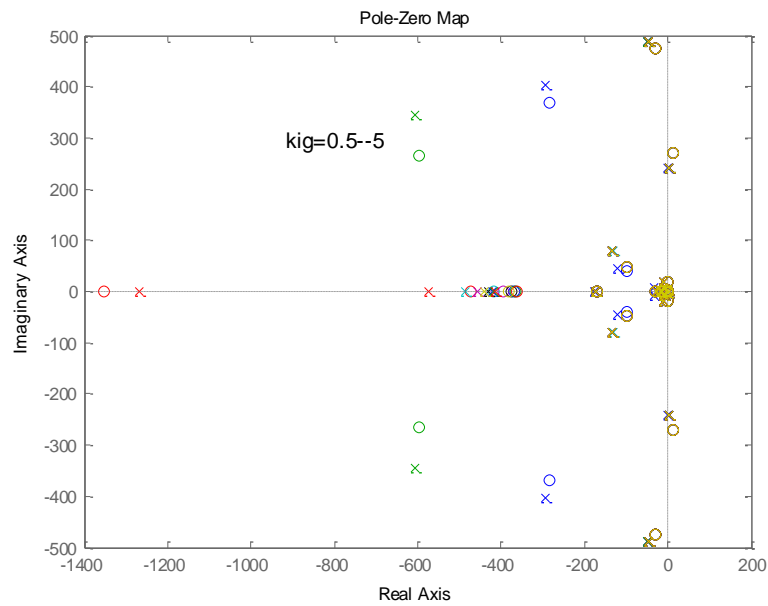


Fig. 2-30 Pole-zero map of closed loop transfer functions of rotor speed in response to stator current disturbances with  $k_{ig}$  varying from 0.5 to 5

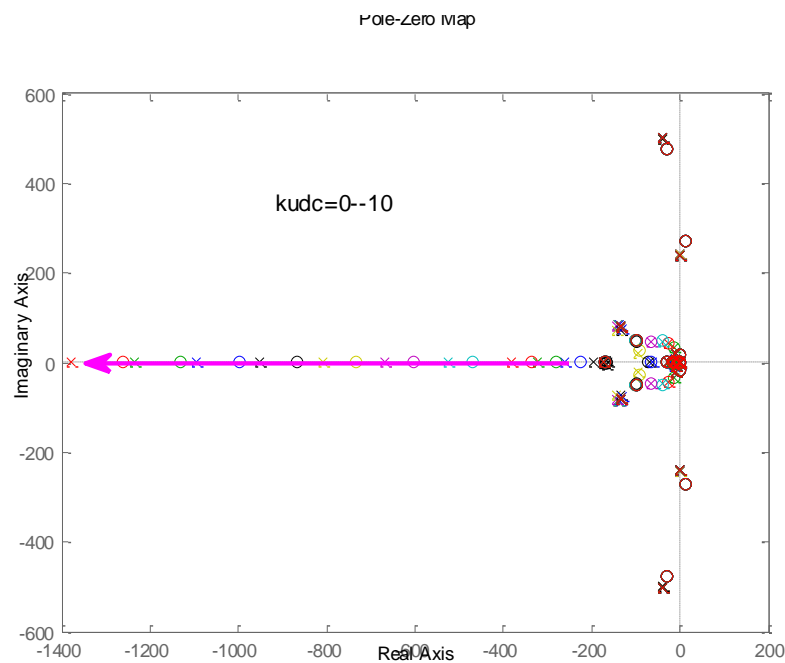


Fig. 2-31 Pole-zero map of closed loop transfer functions of rotor speed in response to stator current disturbances with  $k_{udc}$  varying from 0 to 10

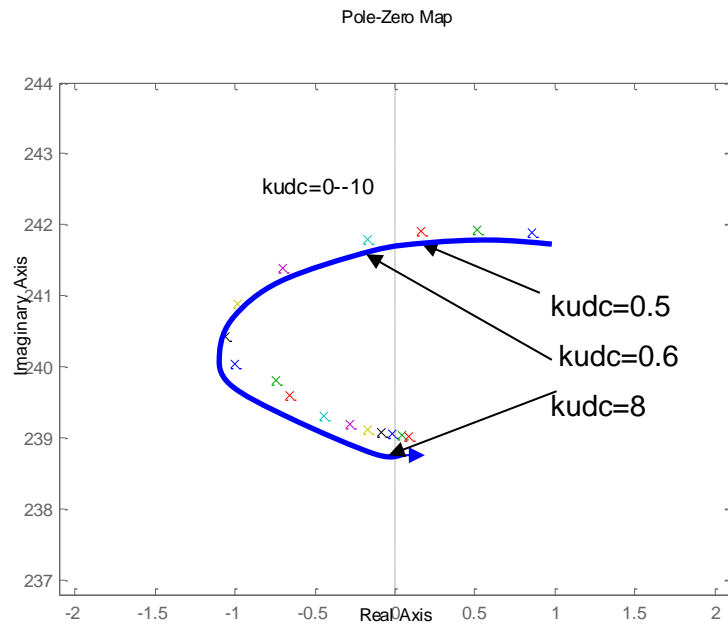


Fig. 2-32 Pole-zero map of closed loop transfer functions of rotor speed in response to stator current disturbances with  $k_{udc}$  varying from 0 to 10 (zoomed)

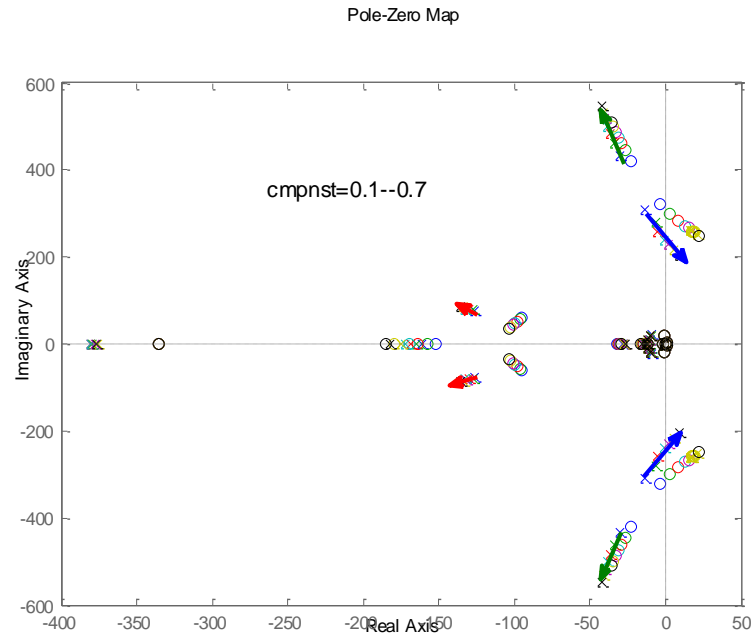


Fig. 2-33 Pole-zero map of closed loop transfer functions of rotor speed in response to stator current disturbances with compensation degree varying from 10% to 70%

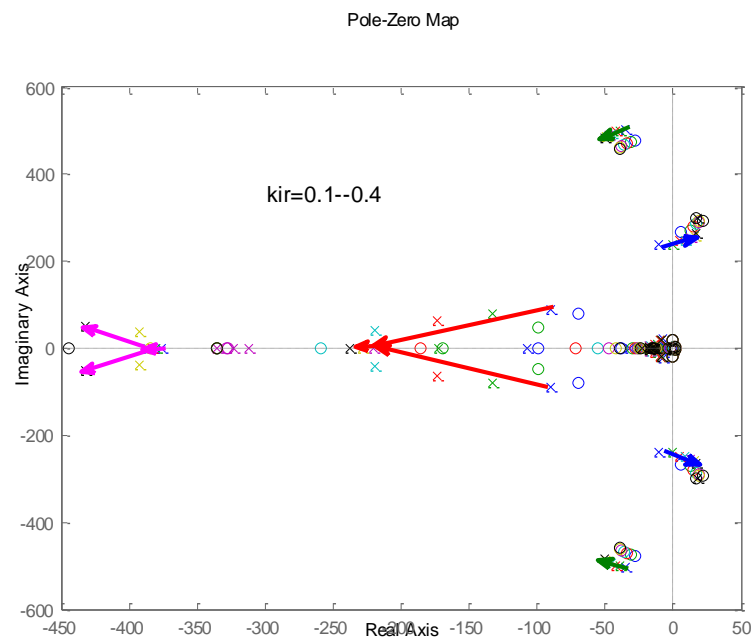


Fig. 2-34 Pole-zero map of closed loop transfer functions of rotor speed in response to stator current disturbances with kir varying from 0.1 to 0.4

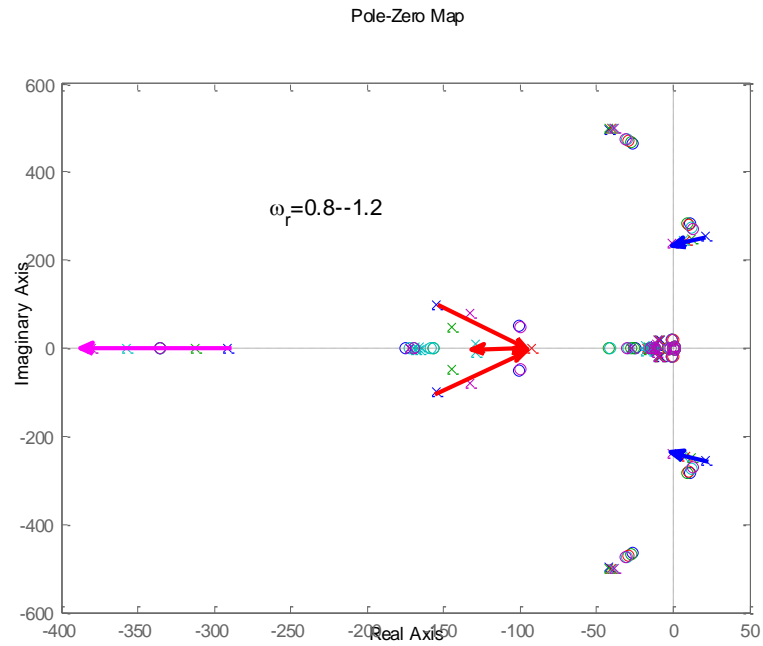


Fig. 2-35 Pole-zero map of closed loop transfer functions of rotor speed in response to stator current disturbances with  $\omega_r$  varying from 0.8 pu to 1.2 pu

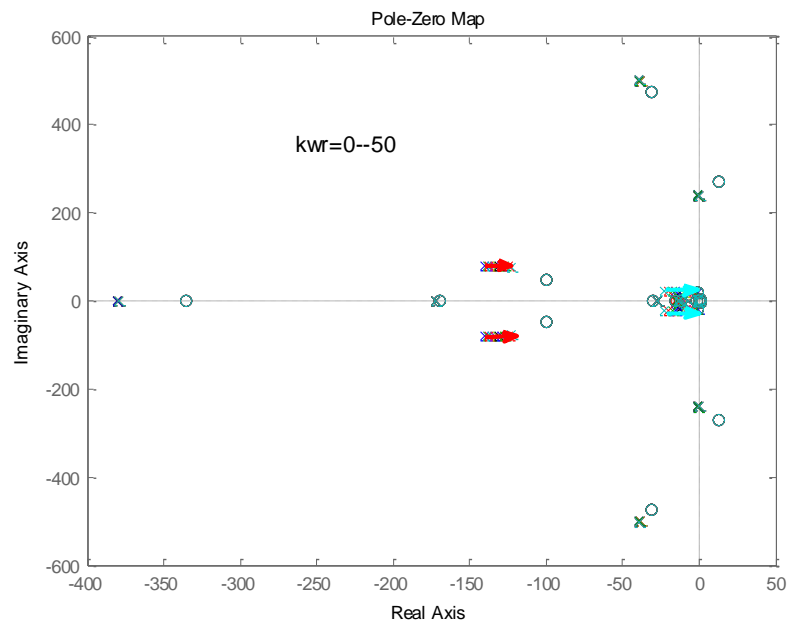


Fig. 2-36 Pole-zero map of closed loop transfer functions of rotor speed in response to stator current disturbances with  $k_{\omega r}$  varying from 0 to 50

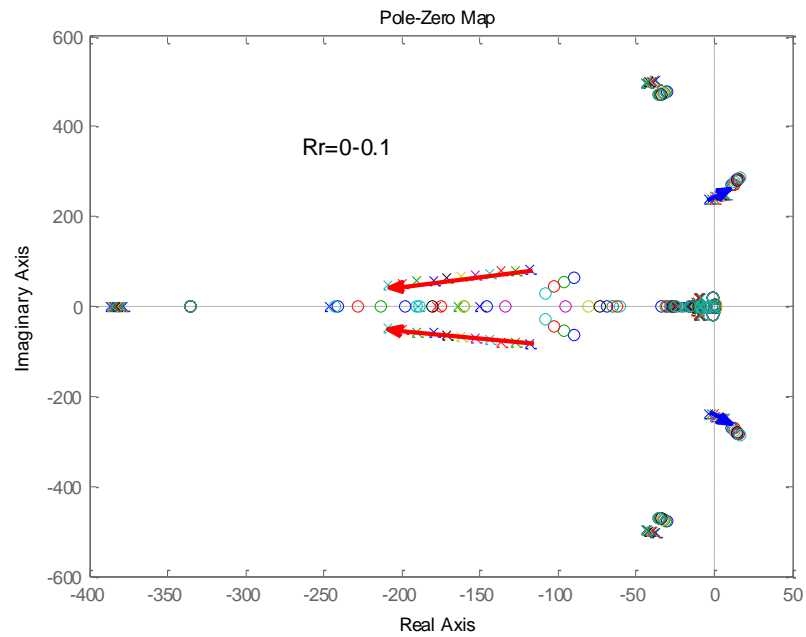


Fig. 2-37 Pole-zero map of closed loop transfer functions of rotor speed in response to stator current disturbances with  $R_r$  varying from 0 to 0.1 pu

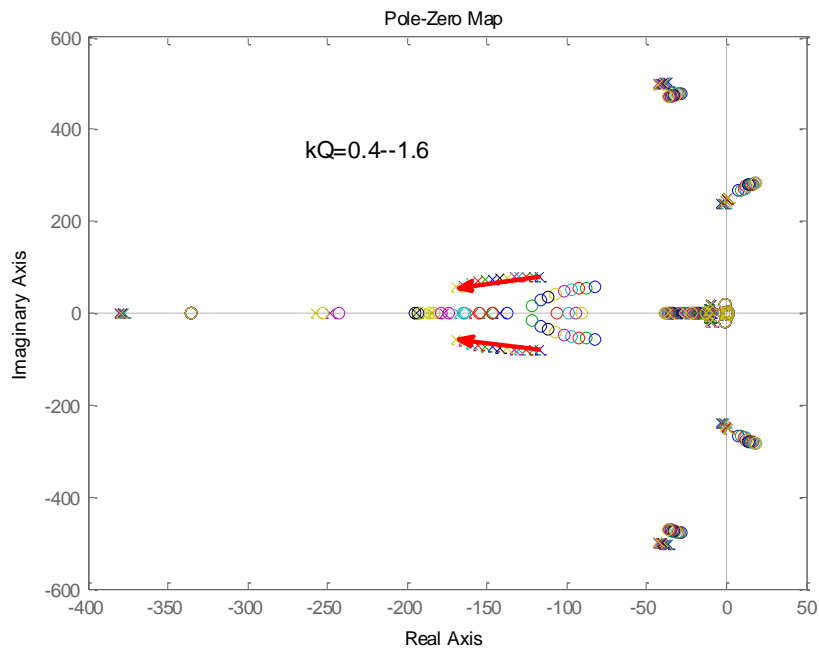


Fig. 2-38 Pole-zero map of closed loop transfer functions of rotor speed in response to stator current disturbances with  $K_Q$  varying from 0.4 to 1.6

From the above figures, the impact of the variables on SSR can be summarized.

Table 2-5. Impact of variables on SSR

Variable	Impact
Compensation degree	SSR risk <i>higher</i> with <i>higher</i> compensation degree
$\omega_r$ Rotor speed (steady state)	SSR risk <i>higher</i> with <i>lower</i> generation level
$R_r$ (rotor winding resistance)	SSR risk <i>higher</i> with <i>higher</i> resistance
$K_{ir}$ (rotor-side converter current controller gain)	SSR risk <i>higher</i> with <i>larger</i> controller gains
$k_Q$ (rotor-side converter reactive power controller gain)	insignificant impact
$K_{\omega r}$ (rotor-side converter rotor speed controller gain)	Almost no impact
$K_{ig}$ (grid-side converter current controller gain)	Almost no impact
$K_{udc}$ (grid-side converter dc voltage controller gain)	Almost no impact

In addition, the following points can be observed from the figures.

1. The poles can be identified to be related to different modes. Taking Fig. 2-33 for example, which is re-plotted in Fig. 2-39. There are five pairs of poles and they can be identified as related to super-synchronous mode, sub-synchronous mode, mechanical system (including generator and shaft), dc voltage control loop, dq coupling of rotor and stator current.
2. Rotor speed control loop has little impact on SSR. However, increasing controller gain will reduce damping of the mechanical mode, as shown in Fig. 2-36. All the other variables have no impact on the mechanical mode.
3. The SSR frequency changes slightly with the change of variables even the system physical configuration is the same.

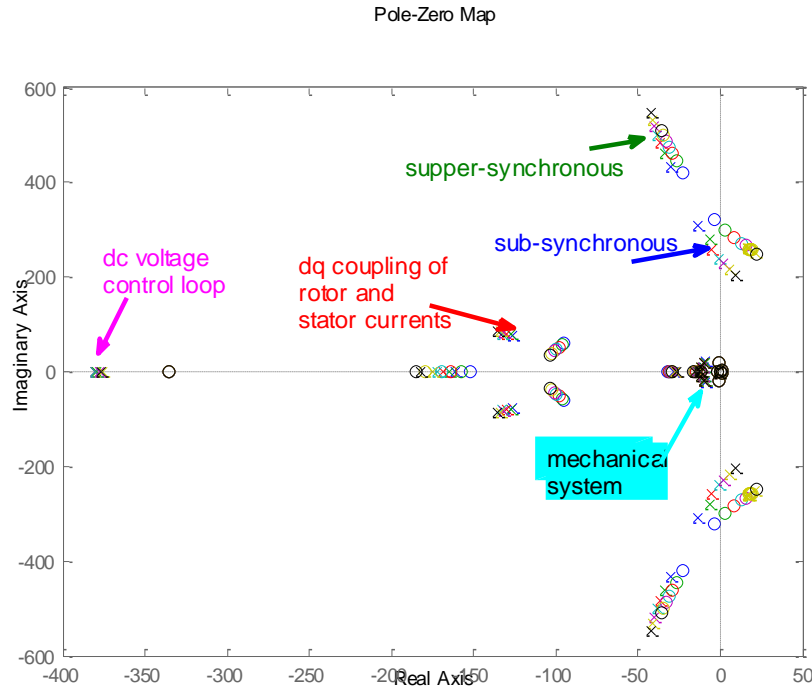


Fig. 2-39 Identification of the closed-loop poles

From the analysis above, current controller gain of the rotor-side converter has big impact on SSR. Fig. 2-34 shows increasing this gain will push the poles related to SSR towards the right half plane. This implies that SSR could be eliminated by reducing this gain.

The pole-zero map in Fig. 2-40 shows that the maximum current controller gain that can be selected is 0.036 in order to avoid SSR. This value in the simulation with DFIG model in PSCAD is 0.038. It should be noted that the reactive power controller gain is also reduced to keep proper dynamic separation of the inner and outer loop. With this set of controller gains, the bandwidths for nominal frequency system control are 70 rad/s, 15.7 rad/s, 4.6 rad/s respectively for inner current loop, reactive power control loop and speed control loop.

Therefore, reducing controller gains can eliminate SSR. However, the response of nominal frequency system control is very slow.

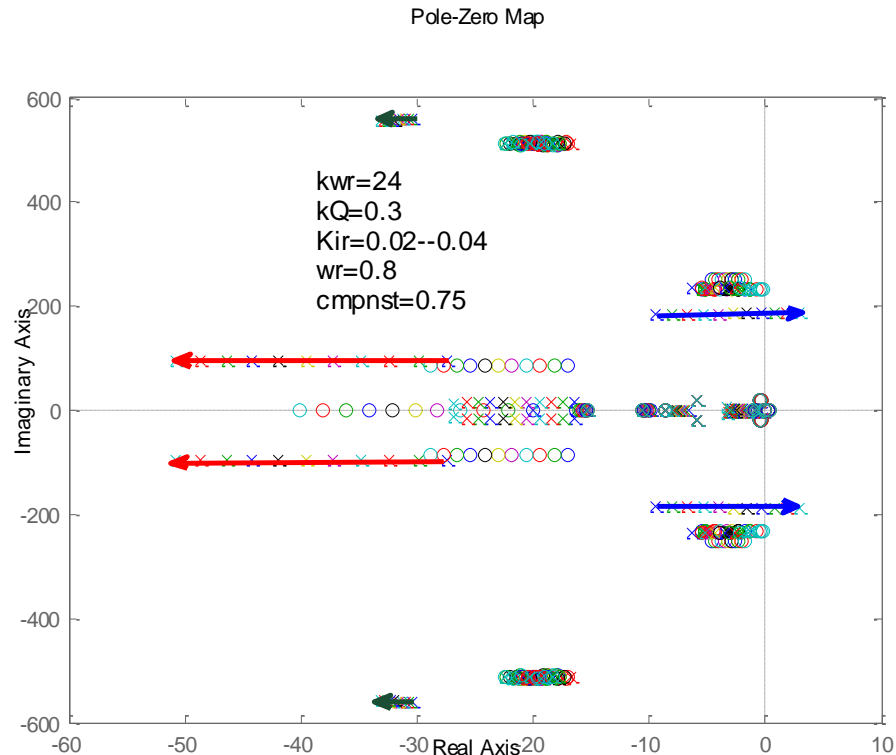


Fig. 2-40 Pole-zero map with varying kir for system with 75% compensation and 0.8pu rotor speed

### 2.3.1 SSR mitigation by addition of voltage magnitude control loop to grid-side converter

#### 2.3.1.1 Addition of voltage magnitude control loop

As stated earlier, the reactive current reference is set to zero in the model. This is a commonly used control method due to the following reason. The grid-side converter is usually designed to have only 25-30% of the DFIG rating. It's mainly used for delivering active power either from the rotor to the grid (at super-synchronous rotor speed) or from the grid to the rotor (at sub-synchronous rotor speed). Usually it is not required for the grid-side converter to provide reactive power during normal operation.

However, if a voltage magnitude control loop is added to the grid-side converter control system as shown in Fig. 2-41, the SSR problem can get mitigated as shown in the following:

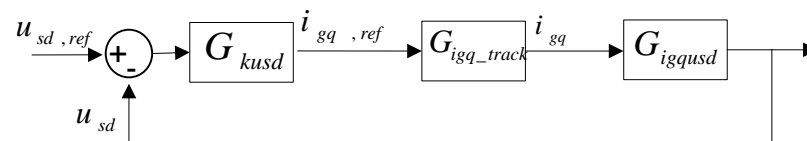


Fig. 2-41 Addition of voltage magnitude control loop

Since the PLL works on the stator voltage  $u_{snq} \approx 0$ ,  $u_{snd}$  can be taken as the control signal. In presence of sub-synchronous frequency component in the stator voltage, the control signal is actually  $u_{sd} = u_{snd} + u_{ssnd}$ .





### 2.3.1.2 Analysis of the closed-loop system with added voltage control loop

In this section, the closed-loop system with added voltage control loop will be analyzed. Due to addition of the voltage magnitude control loop, the coupling relation between d and q components of the rotor and stator current is changed. The closed loop transfer function from stator current disturbance to rotor speed has been derived. However, with the complete model shown in Fig. 2-43, the order of the transfer function derived is too high to make any clear analysis. Therefore, the following simplifications are made:

- Impact of the dc voltage control loop of the grid-side converter on rotor-side converter control system is neglected, considering dc voltage controller has little impact on SSR.
- In deriving the coupling between d and q components ( $i_{rq}$  and  $i_{sq}$  induced by  $i_{rd}$ ,  $i_{sd}$  and  $igq\_damp$ ), the outer control loops (Q and  $w_r$ ) are disconnected. This simplification is justified considering the response of the outer loops is much slower than the inner loops.

Fig. 2-44 shows that with increasing of voltage magnitude controller gain, the poles related to SSR are pushed toward the left half plane.

Simulation in PSCAD has been performed to verify the analysis. With the new control system, it's possible to use high controller gains for rotor converter control system. With a current controller gain of 0.2 and a proper voltage magnitude controller gain, the system can remain stable in case of disturbance created by changing the compensation degree from 40% to 75% at a rotor speed of 0.8 pu.

The boundary value of voltage controller gain is 2.5 in PSCAD. However, Fig. 2-44 shows a boundary value of 0.8. The reason for the discrepancy might be the simplification in deriving the transfer functions. Nevertheless, the tendency of reducing SSR risk by increasing voltage controller gain is the same.

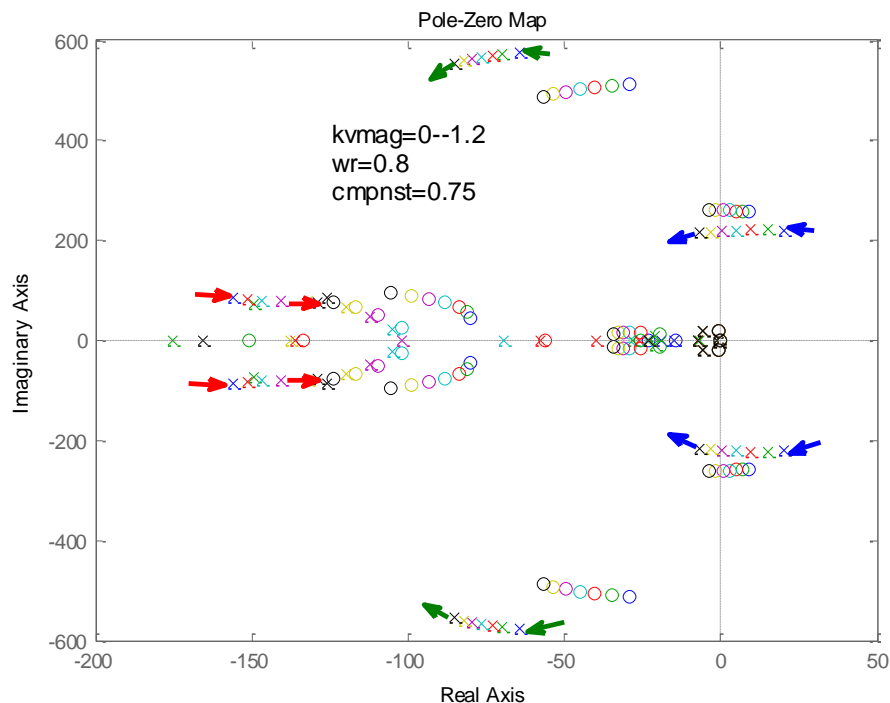
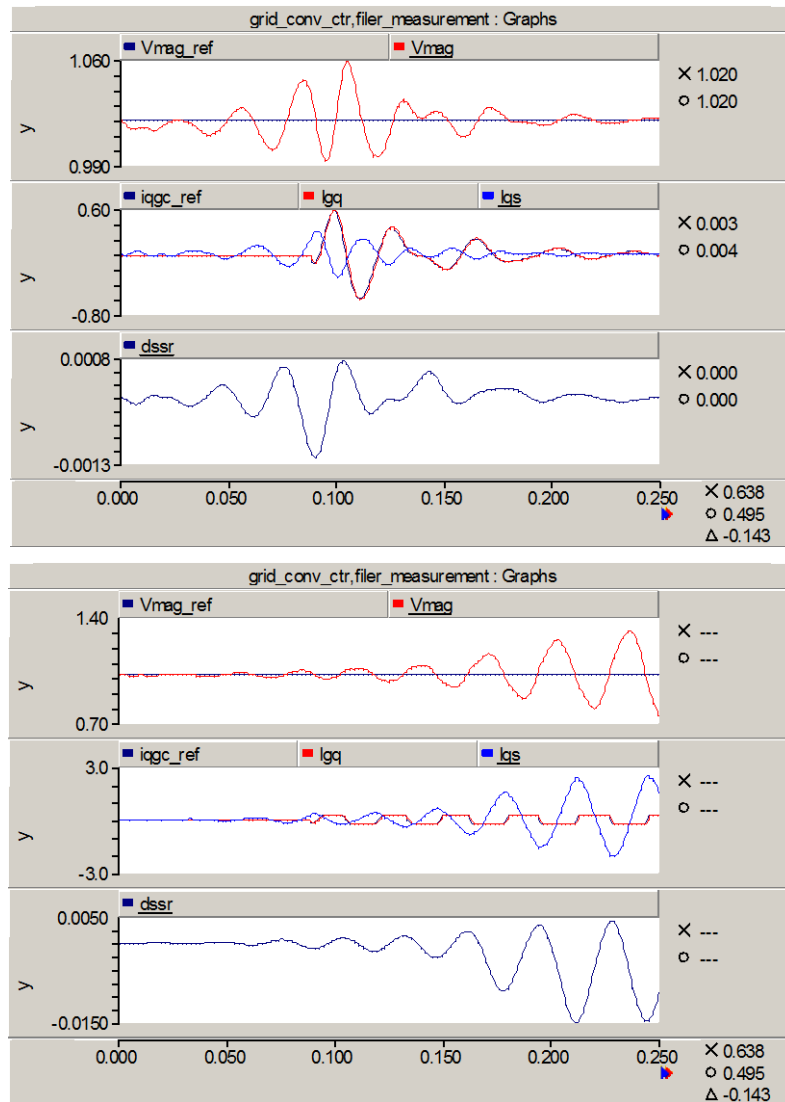


Fig. 2-44 Pole-zero map of closed loop transfer function with varying voltage magnitude controller gain

**2.3.1.3 Effectiveness of the method**

Simulations show, if the voltage magnitude controller is enabled, the system can remain stable in case of disturbances created by increase of compensation degree even for the following set of controller gains: 0.3 for current controller, 1.5 for reactive power controller, 24 for speed controller. The corresponding bandwidths for these three control system are 358 rad/s, 67 rad/s, and 4.5 rad/s.

However, if the controller is disabled from the beginning of the disturbance, this method does not always work.



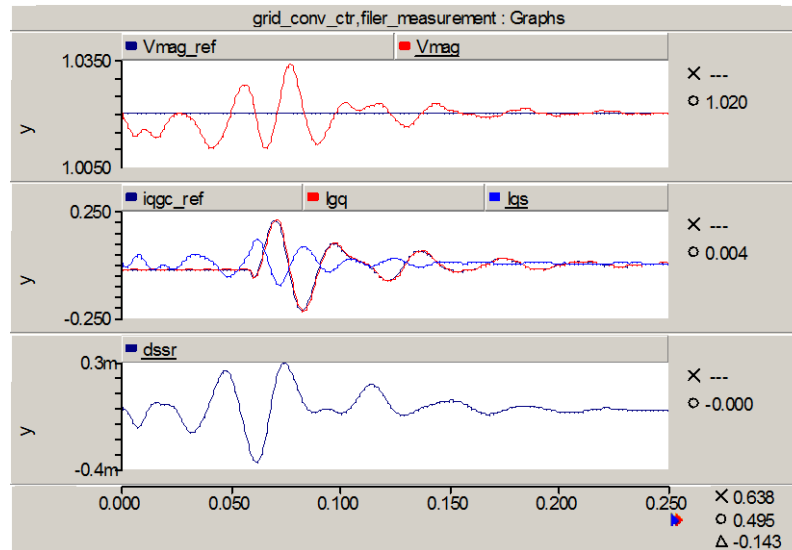


Fig. 2-45 SSR damping by enabling voltage magnitude control (top: current rating 0.8 pu, enabled at 0.085 s; middle: current rating 0.25 pu, enabled at 0.085 s; bottom: current rating 0.25 pu, enabled at 0.059 s)

If the oscillation has not grown to a certain magnitude, the voltage controller can produce a current to oppose the sub-synchronous frequency component in the stator current (as shown in the top and bottom graphs of Fig. 2-45). The net effect is that the grid-side converter provides a temporary path for the sub-synchronous current in the stator. However, this ability is limited by the current rating of the grid-side converter. If the controller is enabled after the oscillation grows beyond a certain magnitude, the oscillations cannot be damped out, as shown in the middle graphs of Fig. 2-45.

At generation level corresponding to the slip of DFIG, the grid-side converter delivers considerable active power either from the rotor to power system or from power system to the rotor. This means available current rating for reactive current is limited. Thus, once the SSR grows to a certain magnitude, the grid-side converter cannot provide enough damping current to damp out the SSR.

In the DFIG control system, there are many saturation blocks (for example, the current order, the modulation index, etc.). These saturation blocks make the system extremely non-linear. Therefore, it's hard to make theoretical analysis. Due to the limitations, the SSR will grow to a certain magnitude and then the oscillations are sustained. Usually the magnitude of the sustained oscillation is much larger than the current rating of the grid-side converter considering the grid-side converter is usually designed to be 25% -30% of the DFIG power rating. Therefore, the effectiveness of this method is limited by the current rating of the grid-side converter to some extent.

Moreover, the gain of voltage magnitude controller is limited. Fig. 2-46 shows the root locus of the closed-loop system of the voltage magnitude control (with 40% compensation level). There is one pair of branches starting from the open loop pole at 377 rad/s and ending at the open loop zero at 261 rad/s on the imaginary axis. This branch is zoomed in in Fig. 2-47. For system with a compensation degree of 75%, the maximum damping can be achieved is 0.178 with a gain of 1.51. If the damping should be larger than 0.05, the corresponding gain should be in the range of 0.272 – 9.34. If the damping should be larger than 0.105, the corresponding gain should be in

the range of 0.58 – 4.53. With a gain of 4, the damping ratio is 0.112 and the frequency is 274 rad/s (44 Hz).

To verify the analysis above, simulation has been done in PSCAD. As shown in Fig. 2-48, the SSR was stimulated by increasing the compensation degree. Shortly, the voltage magnitude controller was enabled. However, the oscillation could not be damped out and the rotor speed dropped to zero. After a while, oscillations in stator voltage magnitude appeared again, but the frequency changed. As shown in Fig. 2-49, the oscillation frequency during 0.3s~0.4s is 31 Hz, but about 46 Hz during 4.3s~4.4s.

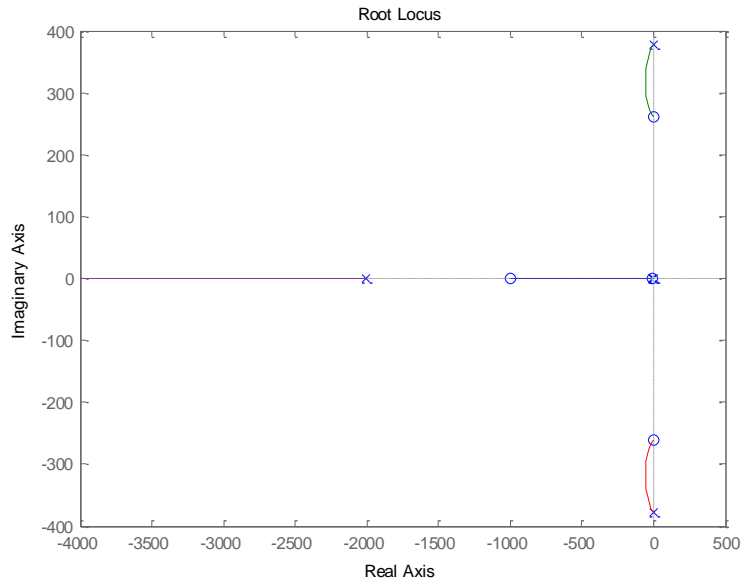


Fig. 2-46 Root locus of the closed-loop voltage magnitude control

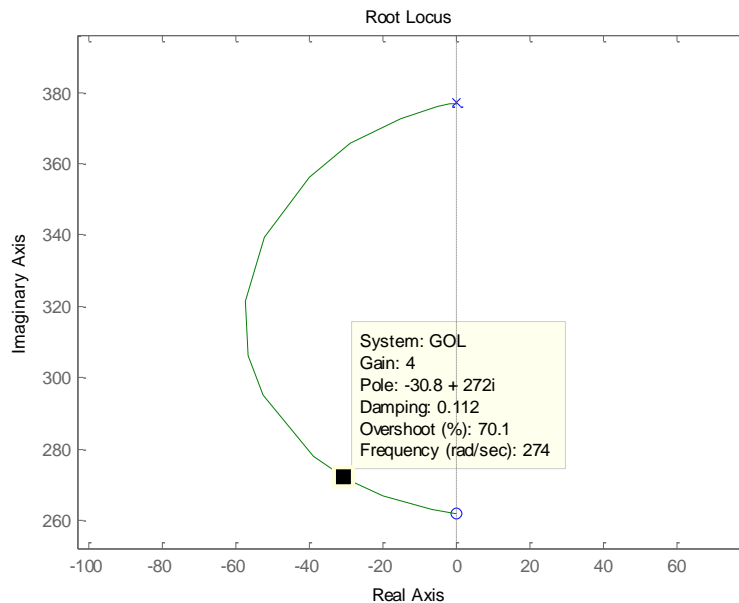


Fig. 2-47 Root locus of the closed-loop voltage magnitude control (zoomed in)

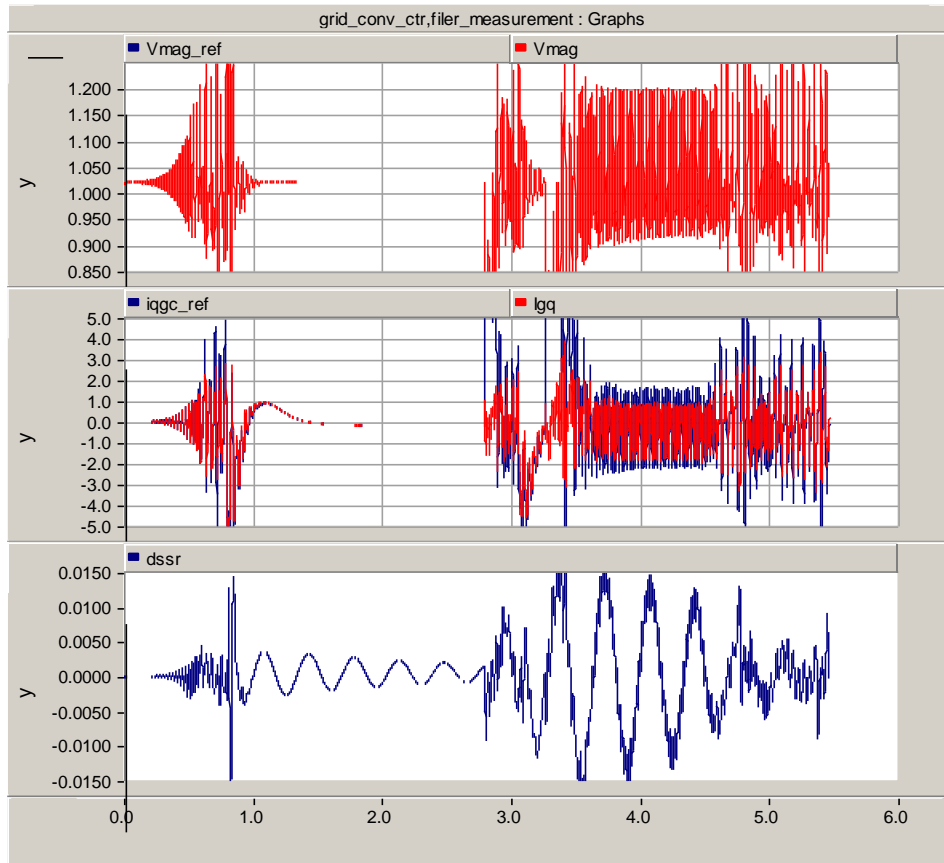


Fig. 2-48 Change of oscillation frequency

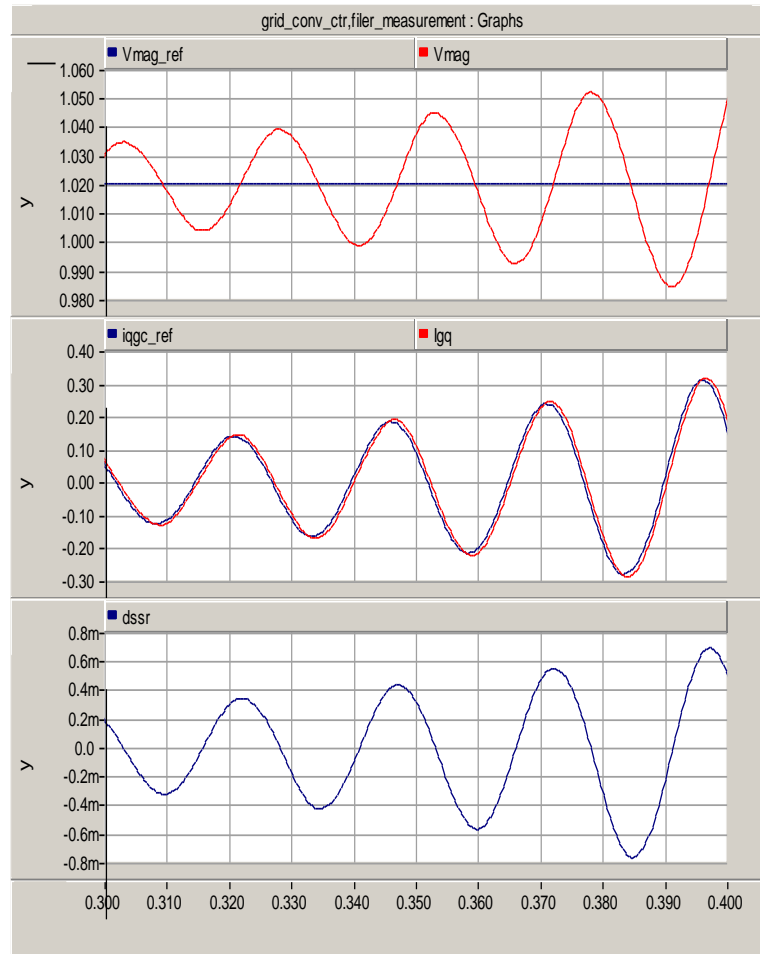


Fig. 2-49 Simulation results (zoomed in)

The conclusion is drawn that the method of eliminating SSR through voltage magnitude control loop of grid-side converter is effective only if the damping current is injected into the grid before the oscillation in the stator current grows to a magnitude beyond the current capability of the grid-side converter. Moreover, there is a poorly damped pair of poles in the voltage magnitude control system, raising a risk of oscillations in the voltage.

## 2.3.2 SSR mitigation by damping control of grid-side converter

### 2.3.2.1 Addition of damping control to grid-side converter control system

The damping control is added on top of the voltage magnitude control loop as shown in Fig. 2-50. The rotor speed is taken as the control signal. After passing through a high pass filter (HPF), the oscillatory rotor speed is multiplied by a factor. This signal is then subtracted from the voltage magnitude reference. By modulating the voltage reference, an additional current component is injected from the grid-side converter to oppose the sub-synchronous component in the stator current. The whole control system with the damping control loop is depicted in Fig. 2-51. The newly added damping control is highlighted in pink.

The HPF used in the study has the following form and its time constant is 0.016s.

$$G_{HPF} = \frac{sT_{HPF}}{1 + sT_{HPF}}$$

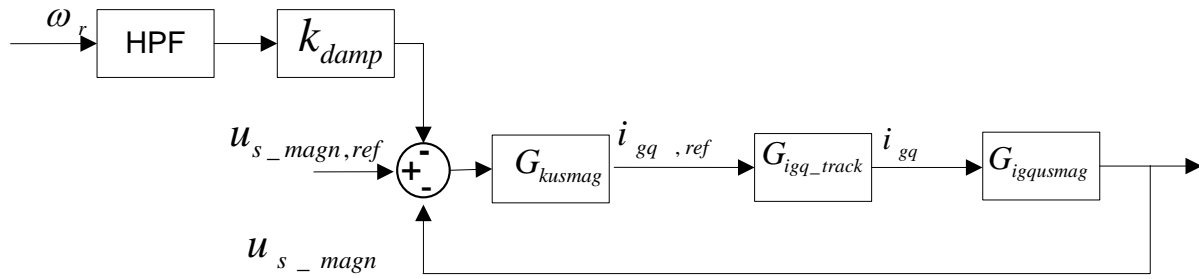


Fig. 2-50 Damping controller



### 2.3.2.2 Analysis of the closed-loop control system with damping control

The closed-loop poles are plotted in Fig. 2-52 with varying damping factor. In the computation, the gains for rotor current, reactive power and voltage magnitude are set to 0.2, 1, and 1 respectively. It can be seen that with increasing damping factor, the poles related to SSR are pushed toward the left half plane, resulting increase of the SSR damping mode. However, the damping effect of another pair of poles is reduced. I.e., the damping factor should be selected with cautions.

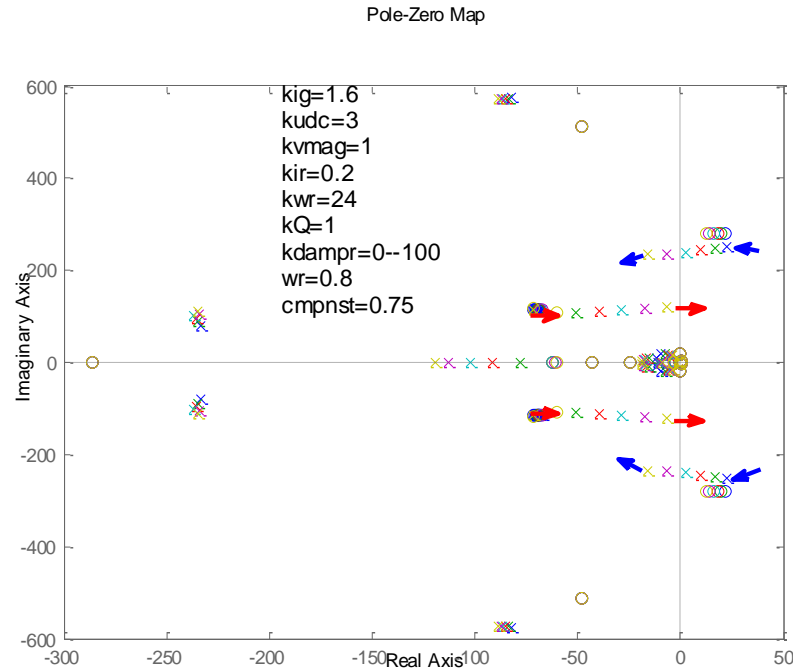


Fig. 2-52 Pole-zero map with varying damping factor

Simulation in PSCAD has been performed to verify the analysis. With a current controller gain of 0.2, a voltage magnitude controller gain of 1 and a damping factor larger than 68, the system can remain stable in case the compensation degree changes from 40% to 75% at a rotor speed of 0.8 pu. The boundary value of voltage controller gain is 68 in PSCAD. Fig. 2-44 shows a boundary value of 66.

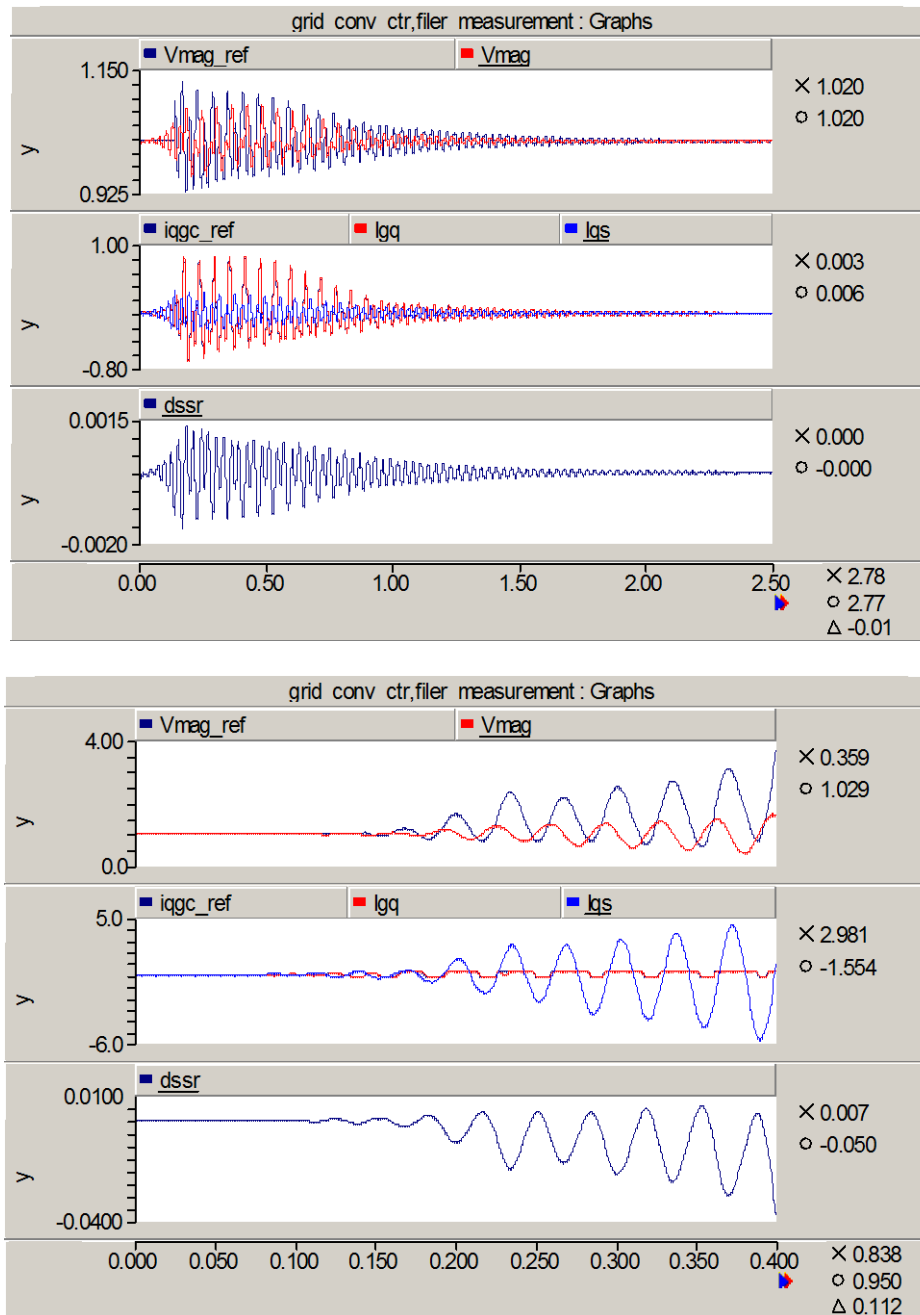
### 2.3.2.3 Effectiveness of the damping control

Similar to the analysis with method 2, simulations in PSCAD have been analyzed. The simulation results are plotted in Fig. 2-53. Similar conclusions have been drawn. The method of mitigating SSR through damping control loop of grid-side converter is effective only if the damping current is injected to the grid before the oscillation in the stator current grows to a magnitude beyond the current capability of the grid-side converter.

Similarly, if the SSR cannot be damped out, the rotor speed dropped to zero and oscillation in voltage magnitude with another frequency appeared, as shown in Fig. 2-54.

Simulations have also been performed to investigate the effectiveness of the damping method with multi-DFIG system. In the investigation, the wind farm is split into three DFIGs instead of single DFIG in previous analysis. A droop is added to the voltage magnitude control system of the grid-side converter. The current rating of the grid-side converter was set to 0.8 pu, which is

comparable to DFIG rating. Two cases were simulated. In case 1 the three DFIGs were operated at the same generation level. In case 2, they were operated at different generation levels, the corresponding rotor speeds are 1.2 pu, 1.08 pu, and 0.856 pu respectively. SSR were stimulated by increasing the compensation degree from 40% to 75%. In all these two cases, SSR could be damped out by the damping controller. The simulation results from the case 2 are plotted in Fig. 2-55. It is verified further that the damping controller can be effective to damping out SSR by proper selection of the control parameters in case that the current rating of the grid-side converter is sufficiently large.



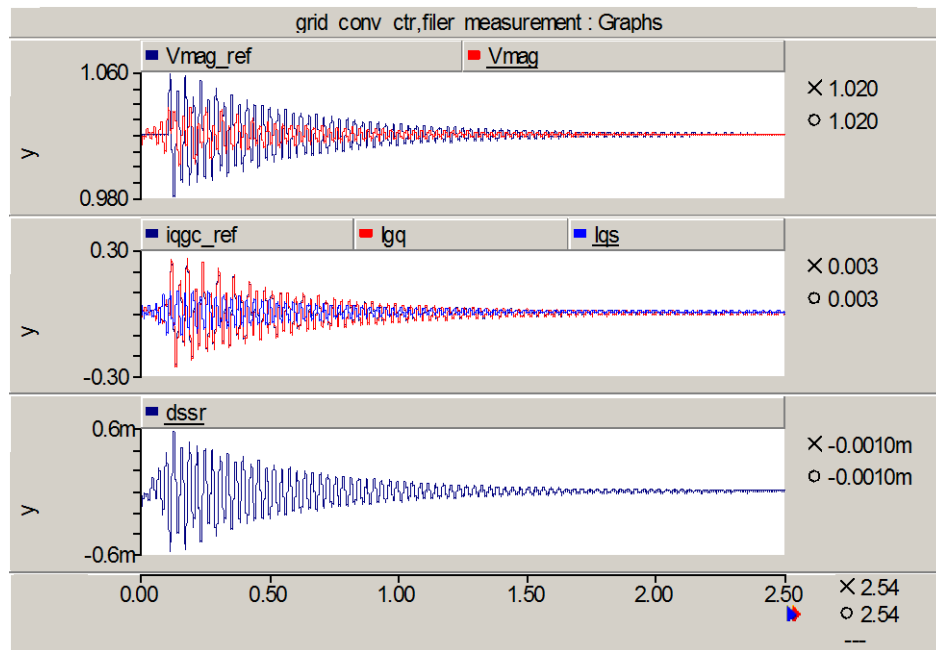


Fig. 2-53 SSR damping by damping control (top: current rating 0.8 pu, enabled at 0.14s; middle: current rating 0.25 pu, enabled at 0.14 s; bottom: current rating 0.25 pu, enabled at 0.1s)

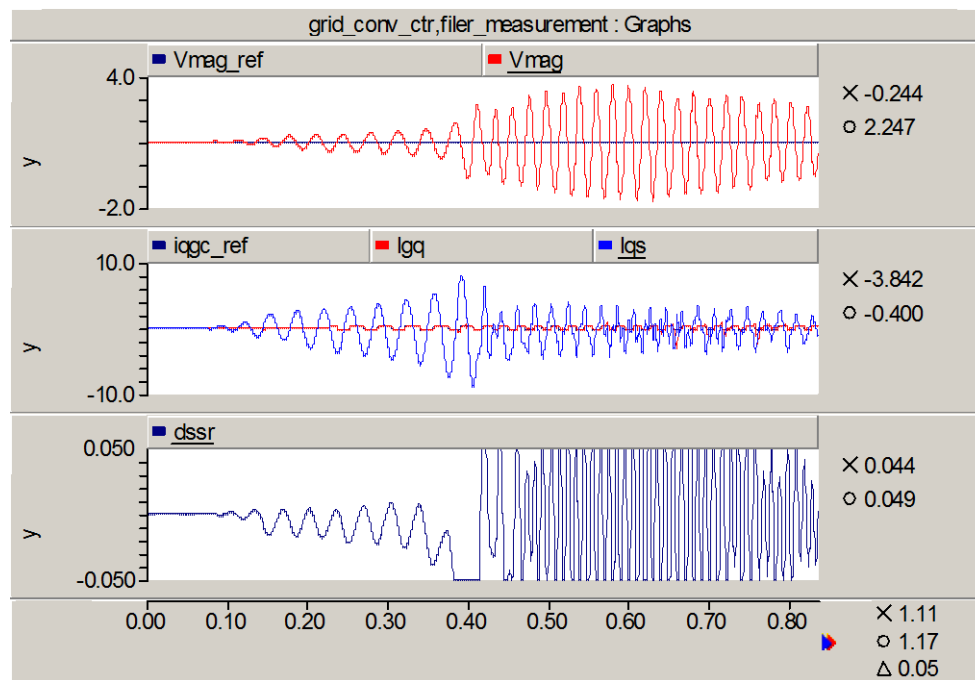


Fig. 2-54 Change of oscillation frequency



Fig. 2-55 SSR mitigation by damping controller with a three-DFIG system and single DFIG system (from top to bottom: DFIG terminal voltage, DFIG output current, DFIG output reactive power and active power, DFIG rotor speed, DFIG reactive current from grid-side converter)

### 2.3.3 Summary

SSR can be mitigated by modifying DFIG control system. Three methods have been investigated.

1. Reducing controller gains. This method is effective. However, the drawback is that the response of nominal frequency system control is very slow.
2. Add voltage control loop to the grid-side converter control system. The method is effective under two conditions:
  - Voltage control system responses fast enough, before the oscillations grow beyond the current capability of the grid-side converter.
  - The current rating of the grid-side converter is sufficiently large.
 The drawback is that the control system becomes more complicated and poorly damped poles are introduced. There is a risk of oscillations other than the original SSR mode.
3. Add damping control to the voltage control loop of the grid-side converter (added in method 2). The effectiveness of this method is similar to method 2. The drawback is that the control system becomes more complicated and there is a risk of oscillations other than the original SSR mode.

The exact rating of grid-side converter required for SSR damping has not been investigated. However, considering the rating of the grid-side converter is only 25-30% of the DFIG rating and it is mainly for active power delivery between the rotor and the grid, the effectiveness is limited to some extent.

## 2.4 Conclusions

In this report, the DFIG model used in the study is described. Transfer functions for both nominal frequency and sub-synchronous frequency are derived and verified. SSR characteristics in presence of SC and wind farm with DFIG have been investigated with main factors affecting SSR identified. Methods of SSR mitigation by DFIG control modification have been investigated and their effectiveness evaluated.

### 2.4.1 Main conclusions on SSR characteristics

Impacts of variables on SSR are summarized as below:

Variable	Impact
Compensation degree	SSR risk higher with higher compensation degree
$\omega_r$ Rotor speed (steady state)	SSR risk higher with lower generation level
$R_r$ (rotor winding resistance)	SSR risk higher with higher resistance
$K_{ir}$ (rotor-side converter current controller gain)	SSR risk higher with larger controller gains
$k_Q$ (rotor-side converter reactive power controller gain)	insignificant impact
$K_{wr}$ (rotor-side converter rotor speed controller gain)	Almost no impact
$K_{ig}$ (grid-side converter current controller gain)	Almost no impact

Kudc (grid-side converter dc voltage controller gain)	Almost no impact
---	------------------

### 2.4.2 Main conclusions on SSR mitigation by DFIG control modification

SSR can be mitigated by modifying DFIG control system. Three methods have been investigated.

1. Reducing controller gains. This method is effective. However, the drawback is that the response of nominal frequency system control is very slow.
2. Add voltage control loop to the grid-side converter control system. The method is effective under two conditions:
  - Voltage control system responses fast enough, before the oscillations grow beyond the current capability of the grid-side converter.
  - The current rating of the grid-side converter is sufficiently large.
 The drawback is that the control system becomes more complicated and poorly damped poles are introduced. There is a risk of oscillations other than the original SSR mode.
3. Add damping control to the voltage control loop of the grid-side converter (added in method 2). The effectiveness of this method is similar to method 2. The drawback is that the control system becomes more complicated and there is a risk of oscillations other than the original SSR mode.

The exact rating of grid-side converter required for SSR damping has not been investigated. However, considering the rating of the grid-side converter is only 25-30% of the DFIG rating and it is mainly for active power delivery between the rotor and the grid, the effectiveness is limited to some extent.

### 3 MODELING OF INVESTIGATED NETWORK AND SUB-SYNCHRONOUS RESONANCE RISK EVALUATION

#### 3.1 Modeling of investigated network

The research network that will be used in the investigation is the IEEE (first) benchmark model [9] for computer simulation of SSR (sub-synchronous resonance) as shown in Fig. 3-1. The nominal power is 892.4 MW and the nominal voltage is 500 kV. The transmission line reactance and resistance are 0.5 pu and 0.02 pu of the base impedance respectively. The source impedance is 0.06 pu of the base impedance. The transmission line is assumed to be compensated with 40% of the line reactance nominally, unless otherwise stated.

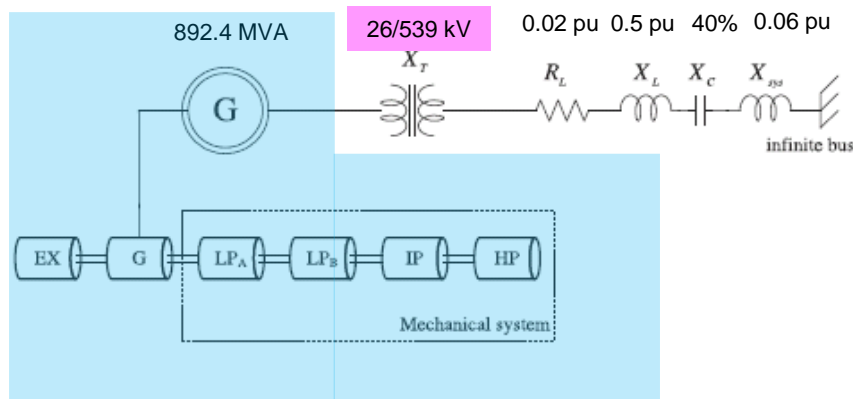


Fig. 3-1. Sketch map of the research network in the project - IEEE (first) benchmark model for computer simulation of SSR

This model is aimed for investigation of SSR caused by interaction of the shaft system of a synchronous generator in a thermal power plant and the series capacitor. In order to use it for the investigation of wind power related SSR, the model should be adapted. The synchronous generator together with its shaft system is replaced with a wind farm cluster as shown in Fig. 3-2. The voltage level on the low voltage side of the transformer is set to 35 kV, which is a typical voltage level for wind farm collection system. The transmission line voltage is set to 525 kV. The wind farm cluster consists of three wind farms and each wind farm is modeled as a lumped DFIG together with a  $\pi$ -line representing the collection network and the step up transformer inside the wind farm. The model of the wind farm cluster is depicted in Fig. 3-3. The installed capacity of each wind farm is 408 MW, the corresponding nominal power is 450 MVA. This gives a total installed capacity of 1224 MW. For wind farm clusters with such a scale, the maximum output power is typically 65-75% of the installed capacity [10]. Let's assume the maximum output is 892.4 MW (same as the nominal power of the synchronous generator in the benchmark model), corresponding to 73% of the installed capacity.

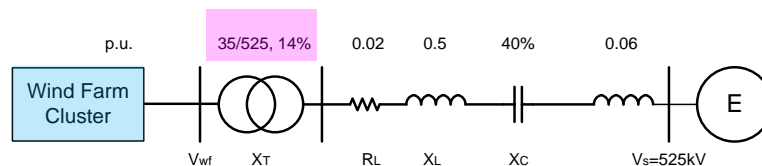


Fig. 3-2. Research network adapted from IEEE (first) benchmark model for computer simulation of SSR

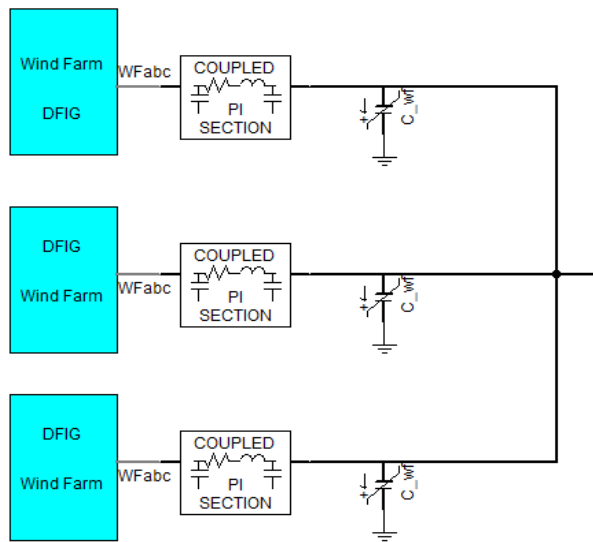


Fig. 3-3. Modeling of wind farm cluster

The DFIG model is developed in the last chapter. Each phase of the series compensation system is modeled as depicted in Fig. 3-4.

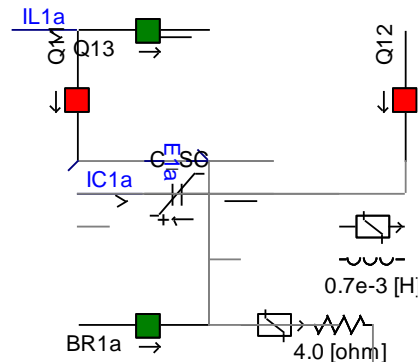


Fig. 3-4 Modeling of each phase of the series compensation system

The system parameters are listed in Table 3-1.

Table 3-1 System Parameters

Parameter	Real value
System nominal power in IEEE benchmark model	892.4 MW
System nominal voltage in IEEE benchmark model	500 kV
Base impedance in IEEE benchmark model	280 $\Omega$

Voltage source reactance	54 mH (With reactance of 0.06 pu of the base impedance in IEEE benchmark model)
Transmission line inductance	446 mH (With reactance of 0.4 pu of the base impedance in IEEE benchmark model)
Transmission line resistance	5.6 $\Omega$ (0.02 pu of the base impedance in IEEE benchmark model)
Transformer voltage	35 kV/525 kV
Wind farm total installed capacity	1224 MW
Wind farm maximum output	892.4 MW
Series capacitor	57 $\mu$ F (with reactance of 40% of the line reactance) nominally, unless otherwise stated

### 3.2 Evaluation of SSR risk in the system

As stated in Chapter 2, control parameters of DFIG rotor-side converter have big impact on SSR risk. Larger gains result in higher SSR risk. SSR risk in the system shown in Fig. 3-2 is evaluated with respect to different control speeds of DFIG.

#### 3.2.1 DFIG controllers with larger gain

Larger gains result in a fast control of DFIG, which is desired in general to achieve a better control performance. However, SSR risk will be high in this case. Simulations show the following result: if the control parameters for rotor-side converter are set to a big value [ $k_{ir}=0.3$ ,  $k_Q=1.5$ ,  $k_w=24$ ], SSR will occur even when the wind generation level is the highest.

#### 3.2.2 DFIG controllers with smaller gain

Smaller gains result in a slow control of DFIG. But SSR risk will be low. Simulations with the control parameters for rotor-side converter set to [ $k_{ir}=0.1$ ,  $k_Q=0.5$ ,  $k_w=8$ ] have been carried out to evaluate SSR risk. Table 3-2 lists the simulation results to check whether SSR oscillation occurs or not.

Table 3-2. Evaluation of SSR risk with slower DFIG control

Scenario	Vw in 3 wind farms (m/s)	Minimal $\omega_r$ (p.u.)	Total Pwf (MW)	SSR
1	10.59/10.59/10.59	1.145	779	No
2	10.59/10.59/6	0.7	570	No
3	10.59/6/6	0.75 (Osc. starts)	385	Yes
4	6/6/6	0.80 (Osc. starts)	220	Yes
5	8.2/8.2/8.2	0.83	386	No

From the table, following points can be concluded:

- SSR risk is higher if more DFIGs operate at low generation level (based on scenario 1, 2, 3, and 4).

- With the same total wind generation, SSR risk is higher if the DFIGs operate at different generation level (based on scenario 3 and 5)

## 4 SUBSYNCHRONOUS RESONANCE MITIGATION BY TEMPORAL BYPASS OF SERIES COMPENSATION

In previous chapter, the SSR (sub-synchronous resonance) risk in the investigated system has been evaluated. The results show that with moderate or slow DFIG control speed the system is very likely to suffer SSR when wind speed is low enough. If the DFIG control speed is fast, the system will suffer SSR even at high wind speed. Therefore, it is necessary to find solutions to eliminate or avoid SSR in the system. This chapter investigates the feasibility to eliminate SSR by proper control of SC (series compensation).

Research shows the system has a high SSR risk if the power generation level is low. In case of low wind speed, the SC is not absolutely necessary for the transmission line since the power transmitted is relative low. This characteristic provides the possibility to bypass the SC temporally to avoid SSR. If the wind speed goes high again, it is necessary to reinsert SC. The bypassing and reinserting processes are the fundamental of the idea to mitigate SSR. In this chapter, a solution employing current and voltage of transmission line is developed. Those signals are easy to be measured locally. In order to realize the purpose of SSR mitigation, SC control algorithm must consider the following aspects:

- Select feasible variable as the control input to determine the best time to bypass the series capacitor in case SSR occurs or in case of high SSR risk.
- Select feasible variable as the control input to decide the optimized time to reinsert SC.
- Avoid the unnecessary bypass or reinserting of SC due to the transients after SC's action and other transients.

In the following, two developed control algorithms will be presented. The DFIG control speed is slow with control parameters for rotor-side converter set to [kir=0.1, kQ=0.5, kw=8].

### 4.1 Control algorithm 1

The control algorithm takes measured current through the transmission line and the voltage at the low-voltage side of the series capacitor as the input signals. These signals are indicated in Fig. 4-1. The developed solution consists of two integrated control functions: bypass control and reinsertion control, which will be described in detail in the following sections.

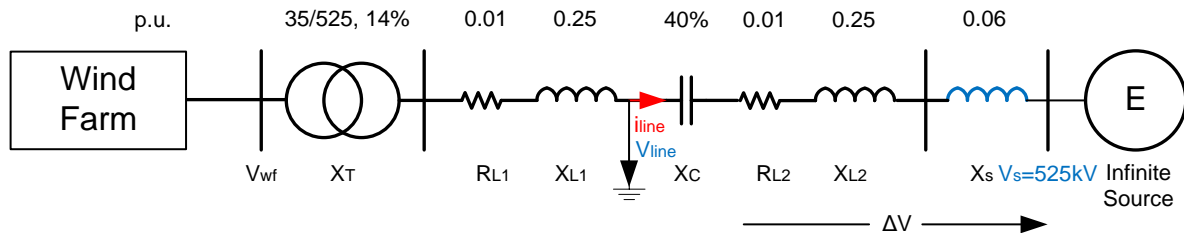


Fig. 4-1 Model used for solution based on proper SC control

#### 4.1.1 Bypassing SC

The current through transmission line is employed as the input signal for bypassing control. The control block diagram is depicted in Fig. 4-2.

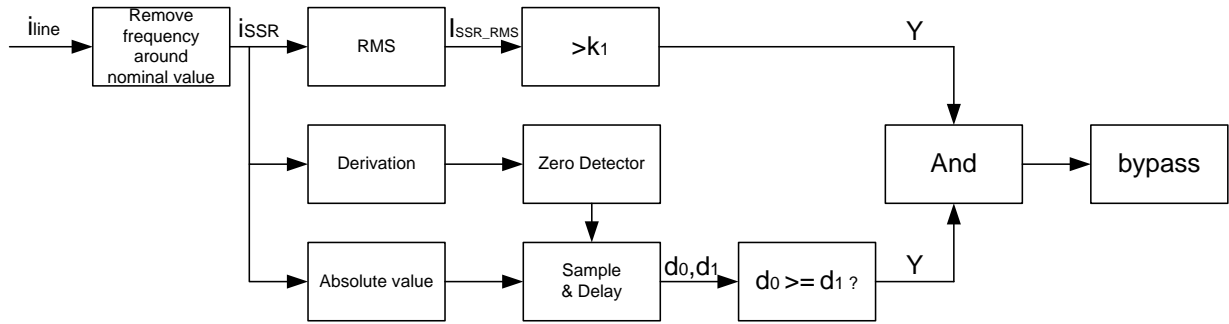


Fig. 4-2 Block diagram of bypass control

The parameters used in Fig. 4-2 are listed as follows:

- $i_{line}$  : measured current through transmission line;
- $i_{SSR}$  : sub-synchronous component in  $i_{line}$ ;
- $I_{SSR\_RMS}$  : amplitude of  $i_{SSR}$ ;
- $k_1$  : threshold value for SSR detection.
- $d_0$  : sampled peak value of  $i_{SSR}$  at present
- $d_1$  : sampled peak value of  $i_{SSR}$  with one sample delay

The bypass command is controlled by an “AND” logic, which have two input signals.

The first one is to check whether SSR appears in the system. The line current  $i_{line}$  is measured. The sub-synchronous frequency component  $i_{SSR}$  is obtained by removing the frequencies around 50 Hz. The RMS value of  $i_{SSR}$  is calculated and compared with a preset value  $k_1$ .  $k_1$  is selected to be slightly larger than zero so that unnecessary action due to transients can be avoided. If  $I_{SSR\_RMS}$  is larger than  $k_1$ , the control system deems that SSR occurs.

The second signal to the AND logic is to check whether SSR is decaying or growing. Sub-synchronous oscillations can be stimulated due to disturbances in the system, for example, re-insertion of SC, change of operation conditions or other transients. However, in some cases the oscillations can decay by themselves due to system damping. Inclusion of this criterion for SSR detection can avoid unnecessary bypass action in these cases. Signal  $i_{SSR}$  is further processed to get the sampled absolute values of the present and previous peak of  $i_{SSR}$ . Every time when the derivative of  $i_{SSR}$  crosses zero, a sample pulse is sent out to sample the absolute value of  $i_{SSR}$ . The sampled value is held until next peak is sampled. If the present peak  $d_0$  is large than or equal to the previous peak  $d_1$ , the control system deems that the oscillation is not being damped.

When both of the criteria are met, the control system will give the “bypass” command to SC.

When SC is bypassed, the power system operates without any series compensation. Therefore, the transmission capability of the system decreases. However, research studies have proved that SSR usually happens when power generation level is low. Therefore, at the time point of bypassing the power through the transmission lines is also low. So the power system without SC should work without any problem as long as the system is well planned.

It is important to note that the input signal ' $i_{line}$ ' here could also be replaced by other signals, such as  $V_{SC}$  (voltage across SC),  $P_{line}$  (power through transmission line) since those parameters

are related. As the signal ' $i_{line}$ ' is available in SC control system of normal product, it is selected as the input signal for bypass control.

#### 4.1.2 Reinserting SC

During the period when SC is out of service, the wind speed may become high and power generation level will go up. Consequently, voltage drop along the transmission line will increase. If the voltage drop becomes significant, it is necessary to reinsert the SC. The proposed control system is shown in Fig. 4-3. The system monitors the voltage  $u_{line}$  at the low voltage bus of the SC. The voltage magnitude  $V_{line}$  is then obtained. When the voltage drops to a pre-defined level (e.g. 0.95 pu), the control system will check if there is a fault in the system. If not, a re-insertion command will be sent out to the SC.

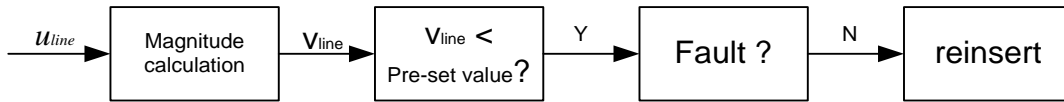


Fig. 4-3 Structure of reinserting process

For the proposed solution, it will be perfect from economic point of view if  $i_{line}$  could also be used as the source signal for reinserting SC. This section will analyze the advantage of both signals and try to make sure which could be better for application.

At the beginning, it is important to make clear the only criterion to reinsert the SC is to keep line voltage magnitude  $V_{line}$  no less than the pre-defined value, no matter the measured parameter is ' $u_{line}$ ' or ' $i_{line}$ '. The reason is that the permitted minimal voltage is defined clearly in grid code in all countries. In the following, vector is used to demonstrate the evaluation, of which the symbol is " $\vec{\quad}$ ".

If there is only pure wind power with constant capacity, the following equation is valid.

$$\vec{V}_{line} = \vec{V}_s + \Delta\vec{V} + \vec{I}_{line} * jX_c = \vec{V}_s + \vec{I}_{line} * (R_{L2} + jX_{L2} + jX_S) + \vec{I}_{line} * jX_c$$

It could be assumed  $\vec{V}_s$  is constant. If  $(R_{L2} + jX_{L2} + jX_S)$  and  $jX_c$  are constant, it is possible to derive  $\vec{V}_{line}$  based on the measured  $\vec{I}_{line}$ . Then the derived  $\vec{V}_{line}$  can be used to determine if  $\vec{V}_{line}$  magnitude is smaller than the pre-set value. If yes, the SC should be re-inserted. In this way line current can be used as the input signal for re-insertion control.

However, if the system changes (e.g.  $X_s$  becomes bigger), the solution based on ' $i_{line}$ ' measurement is not valid any more. It has to change the parameter in control algorithms, which is not desired. Unfortunately, change of  $X_s$  is very common in system operation, e.g. load change. Moreover, the power angle also has a significant influence on the  $\vec{V}_{line}$  calculation that is based on signal ' $i_{line}$ '. If there are more sources installed at 35 kV or 500 kV bus, power angle of  $\vec{I}_{line}$  ( $\vec{V}_{line}$  as reference) could be different from the value before. In this case, it is very difficult to give the reinsert signal exactly when  $\vec{V}_{line}$  is smaller than pre-defined value.

The control algorithms based on ' $u_{line}$ ' measurement is system independent. It is still valid if  $X_s$  changes or other sources are added to the system. That is because the only criterion to reinsert SC is ' $V_{line} < \text{pre-defined value}$ '. Of course, this solution needs extra measurement device, which is not perfect from economy point of view.

To summarize, ' $i_{line}$ ' should be selected to make sure the developed system could work without any problem.

### 4.1.3 Signal process

In order to understand the solution better, the employed signals used in Fig. 4-2 are illustrated in Fig. 4-4.

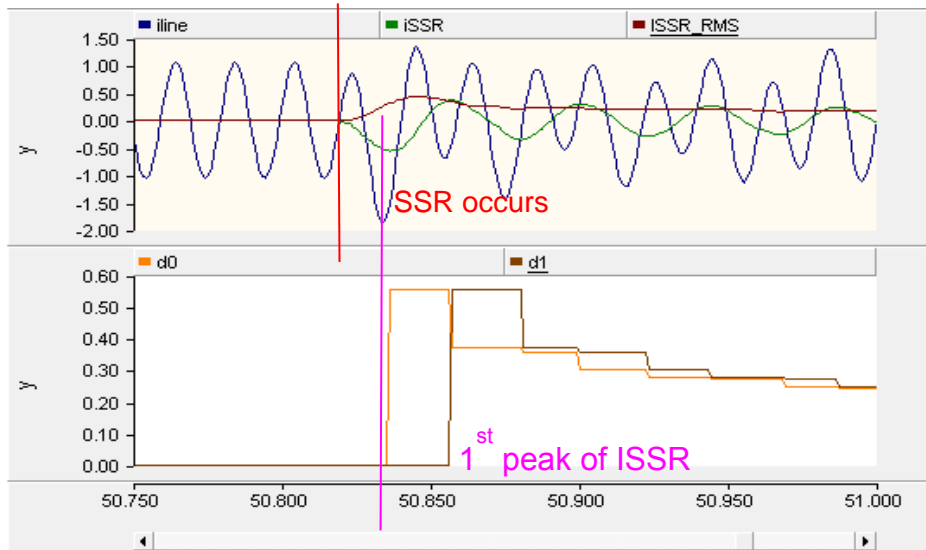


Fig. 4-4 Signal process in bypass control

As shown in Fig. 4-4, SSR occurs at  $t = 50.82$  s. Signal  $i_{line}$  consists of a sinusoidal component with a frequency of 50 Hz and another sinusoidal component with a frequency of 22 Hz (SSR). Signal  $i_{SSR}$  is a sinusoidal component with only a frequency of 22 Hz (The frequencies around nominal frequency are removed).  $i_{SSR\_RMS}$  demonstrates the RMS value of  $i_{SSR}$ . On the bottom graph, sequence  $d_0$  represents the sampled peak value of  $i_{SSR}$  and sequence  $d_1$  is one cycle delayed than  $d_0$ .

It is important to note that the system must be locked between the time point of SSR first appearing and the second peak value of  $i_{SSR}$ , as shown in Fig. 4-5. Without this lock unit, the system could have a problem of correctly judging whether SSR could be damped out. Because during  $t_1$  (time of the 1<sup>st</sup> peak value) and  $t_2$  (time of the 2<sup>nd</sup> peak value)  $d_0$  is always bigger than  $d_1$ . As shown in Fig. 4-5, the signal is decaying. That is, SC should not be bypassed. But without such a lock unit, SC will be bypassed immediately at the first peak.

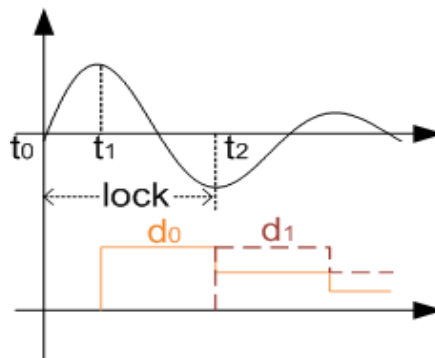


Fig. 4-5 Lock period of the system

#### 4.1.4 Validation of algorithm 1

Based on the discussion above, the proposed solution is implemented in the investigated system in PSCAD for validation. The simulation results are shown in Fig. 4-6. At the beginning of the simulation, wind speed is 10.59 m/s and the system is in a steady state with wind farm output power  $P_{wf} = 779$  MW (0.64 pu). At  $t = 8$  s, the wind speed varies from 10.59 m/s to 6 m/s, the output power starts decreasing. At  $t = 28$  s, SSR occurs due to low power generation level. The developed control system detects the growing oscillations and bypasses the SC. Here  $Q13 = 0$  means SC is out of operation. Since the transmitted power is low ( $P_{wf} = 230$  MW), the system doesn't have any problem for operation without SC, as expected.

Fig. 4-7 illustrates detailed information at the time point of bypass. As shown in Fig. 4-7, before  $t = 28.07$  s system suffers SSR and the amplitude of SSR becomes bigger and bigger. After SC is bypassed at  $t = 28.07$  s, SSR is damped out very fast. Therefore, bypass SC can eliminate SSR effectively.

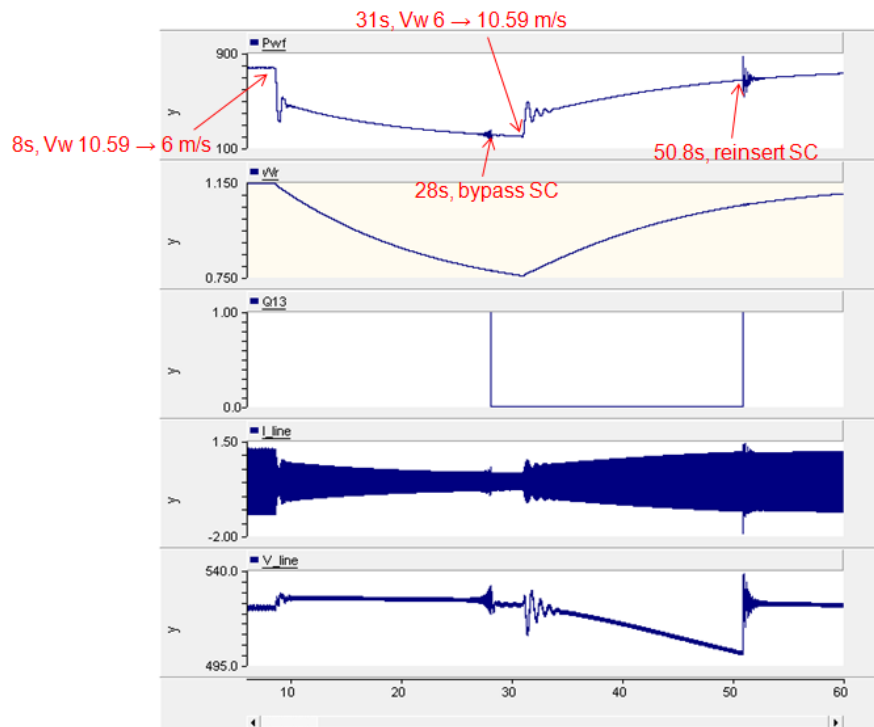


Fig. 4-6 simulation results of temporarily bypass SC

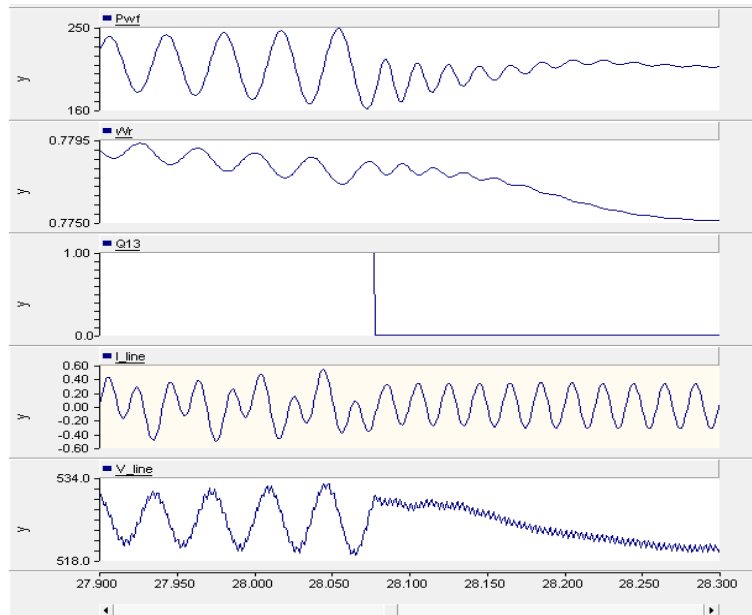


Fig. 4-7 bypass process

At  $t=31$  s, wind speed jumps from 6 m/s back to 10.59 m/s, output power of wind farm increases and the line voltage magnitude  $V_{line}$  begins to decrease. When  $t=50.8$  s,  $V_{line}$  reaches its threshold value and the system reinserts SC to meet the system operation requirement. Fig. 4-8 presents the time point of reinserting process. As observed in the figure, reinserting SC improves the line voltage significantly.

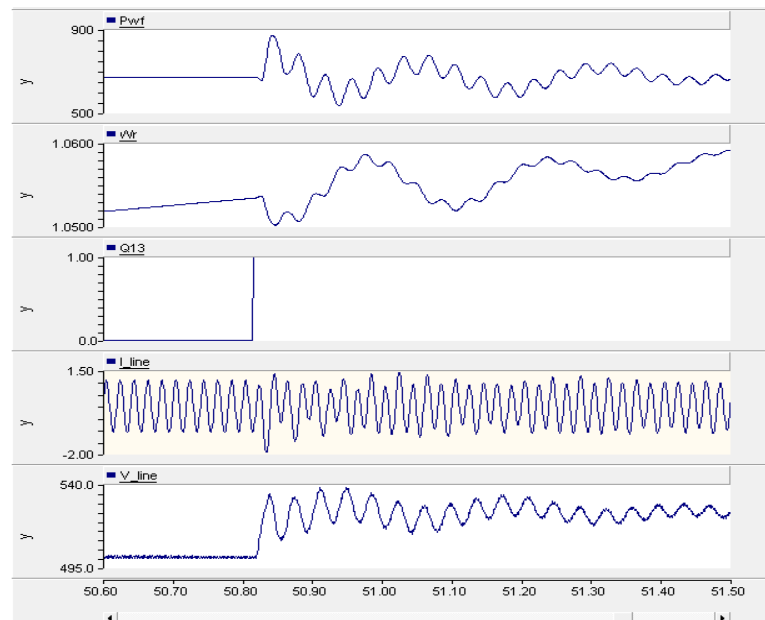


Fig. 4-8 reinserting process

When re-inserting the SC, it is possible that this transient will cause the control system to bypass the SC by mistake. Here 'by mistake' it means that the new steady state condition after the transient will not have SSR, i.e., the transient oscillation is going to disappear after the short transient. In this case, the system should let SC in operation instead of sending bypass signal to SC. The smart system developed in this project can detect that SSR is going to be eliminated by the system itself and make the judgment that SC should keep in operation, as shown in Fig. 4-8

(Q13). This is a big advance compared to existing solution of bypassing SC, which can only detect SSR appearance and then bypass SC no matter SSR will be damped out or become severe.

From Fig. 4-6 it is clear the integrated bypass and reinserting control is effective to mitigate SSR. There is no mis-action of SC. If SSR occurs and will not disappear automatically, the developed system sends bypass signal to SC. When the line voltage is too low to meet the voltage requirement, SC is reinserted into the system.

#### 4.1.5 Effectiveness evaluation

There might be a concern whether SSR will come back after reinserting SC. If that happens, it will lead to re-bypass of SC and further lead to repeated bypass-insertion of SC. In the following section, the possibility of this phenomenon will be investigated. Besides, the effectiveness will also be evaluated for the case with three DFIGs operating at different generation levels and with different network strengths.

##### 4.1.5.1 Possibility of SSR coming back

To investigate the possibility of SSR coming back after reinserting SC, it is important to find out the operation conditions at the instant when bypass and reinsertion happen. From Fig. 4-6 those value are recorded and listed in Table 4-1.

Table 4-1 value for bypass and reinserting SC

	$\Omega_r$	Pwf	l <sub>line</sub>	v <sub>line</sub>
Bypass value	0.778 p.u.	220 MW	0.4 kA	530 kV
Reinserting value	1.05 p.u.	670 MW	1.33 kA	500 kV

From Table it is clear that the SC will be reinserted when Pwf = 670 MW while from Table 3-2 (scenario 5) it is observed there is not SSR risk even when Pwf is as low as 386 MW. In Chapter 3 it has been proved that the SSR risk is high when power generation level is low. It could be concluded that there is no possibility for the investigated system to have re-bypass problem after reinserting SC. When applying the control algorithm to other systems, comprehensive system study should be performed to evaluate the risk of SSR being brought back by re-insertion of SC.

This conclusion is also valid when wind speeds in three wind farms are different, which is proved by scenario 2 in Table 3-2. The re-bypass possibility is considered to be the biggest when the wind generation has the following characteristics: low generation in one wind farm but with high total output power. This could be considered as the scenario that two of the three wind farms have the same high wind speed and the third one has a low wind speed, as shown in scenarios 2. Since under the worst operation conditions (scenario 2) the system doesn't suffer SSR, it could be concluded the proposed solution is valid for the investigated system.

##### 4.1.5.2 Effectiveness for system with different strength

Based on the discussion above, it is clear the proposed solution is valid for different operation conditions. The section will investigate the solution's effectiveness for system with different strength.

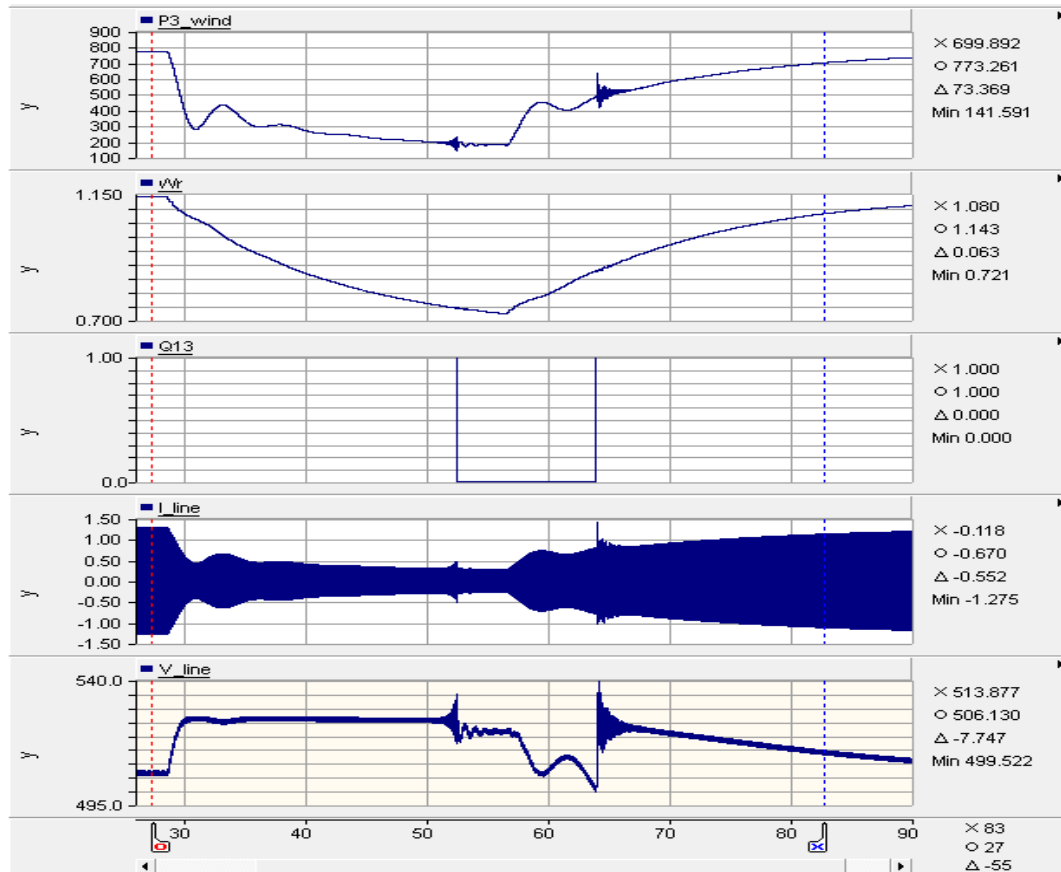


Fig. 4-9 system with  $X_{line}=0.75$  pu instead of 0.5 pu

For this simulation studies above, the series compensation level keeps at 40% and all the wind farms have the same wind speed. All the parameters shown in Fig. 4-1 are constant. In this section line reactance  $X_{line}$  is variable. For the first simulation case,  $X_{line}$  is 0.75 pu. The sequence of the events happened in Fig. 4-9 is the same as the one in Fig. 4-6 except the time when these events happened. From Fig. 4-9 it is clear the line voltage before wind speed change is 506 V in comparison with 522 V in Fig. 4-6. At reinserting time point the active power is 500 MW in comparison with 670 MW in Fig. 4-6. Therefore, there is also not the possibility that the SSR comes back after reinserting SC (386 MW as the threshold value).

The same simulation study has been performed in case of  $X_{line}=0.25$  pu. The proposed solution also works well, as shown in Fig. 4-10. The voltage is never below 0.95 pu even with high power generation level. In fact, this system is so strong that it could work without SC.

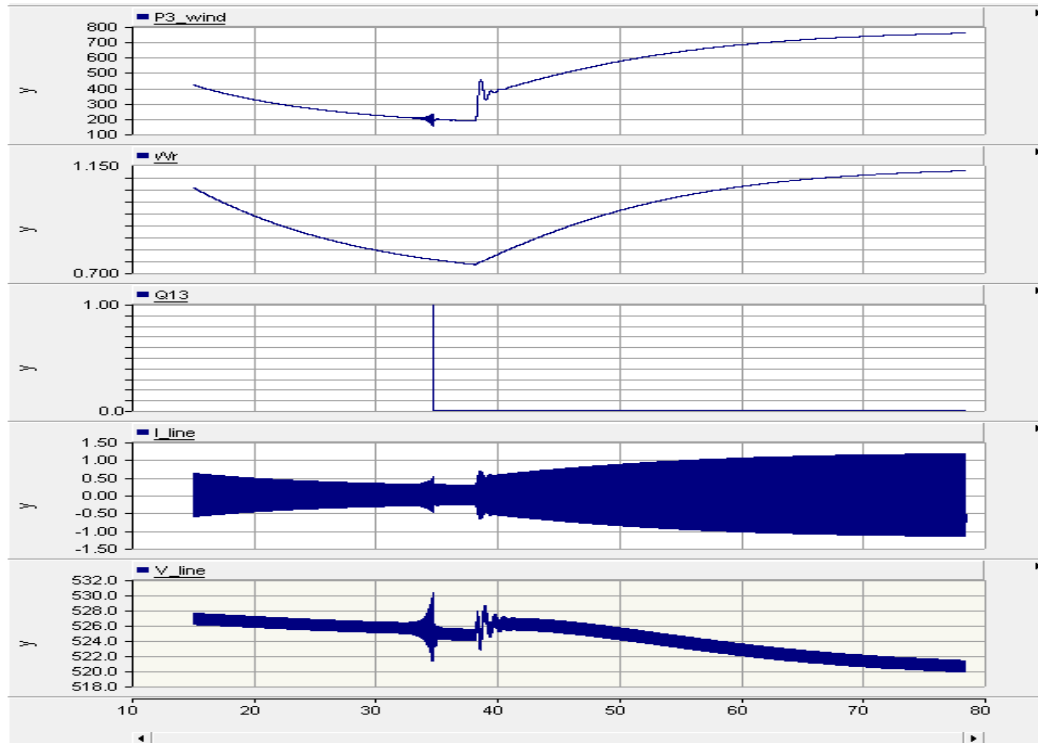


Fig. 4-10 system with  $X_{line}=0.25$  pu

Based on the simulation studies in this section it could be concluded that the temporally bypassing and re-inserting control algorithm works for different network strength. But for weak system, the risk of bring SSR back after reinserting SC is relative high.

#### 4.1.5.3 Effectiveness in case DFIGs operating at different generation levels

Compared scenario 3 with scenario 5 in Table 3-2, it is observed the difference of wind speed could also influence SSR risk. For both scenarios, total output power is the same. However, the wind farms with the same wind speed don't have SSR appearance while wind farms with different wind speeds do. Since scenario 3 is considered to have the highest SSR risk, it is selected to prove its effectiveness in case DFIGs operating at different generation levels. The results are shown in Fig. 4-11.

As shown in the figure, before 22s three wind farms have the same wind speed 10.59 m/s. At 22s two of the three are changed to 6 m/s. As the wind power decreases, SSR occurs at 50 s and the SC is bypassed at 52 s. At 60 s, the wind speed of all wind farms is set to be 10.59 m/s. The voltage is below pre-defined value at 62.5s and the control algorithm reinserts SC. The results prove that the developed solution is valid for the case of DFIGs operating at different generation levels.

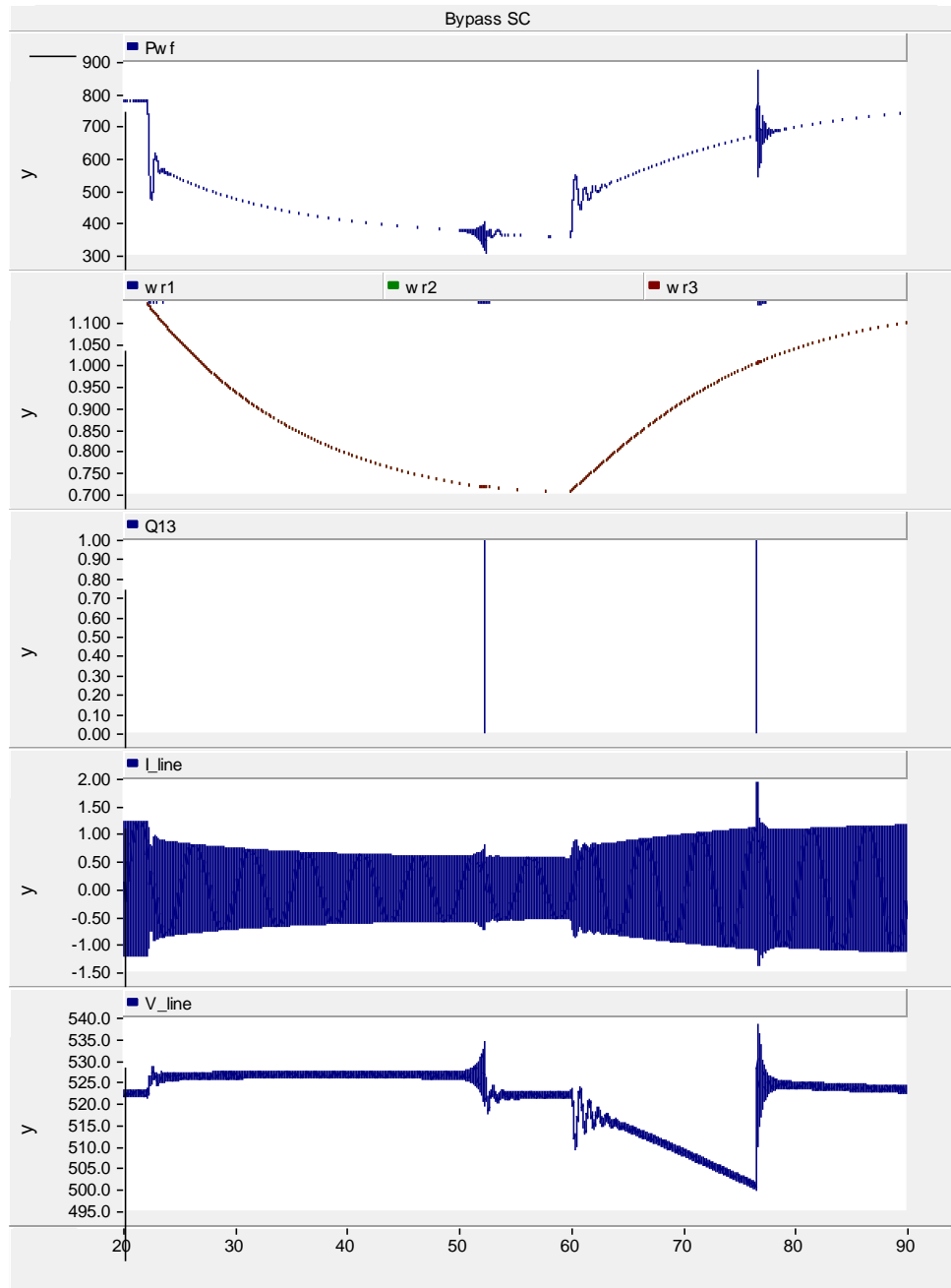


Fig. 4-11 Effectiveness in case DFIGs operating at different generation levels

#### 4.2 Control algorithm 2 - with prediction ability

The solution discussed above is based on detecting SSR, in which SSR has already occurred in the system. In this section, a solution of temporarily bypassing SC with prediction ability is proposed. This solution is able to predict the appearance of SSR and bypass the SC in advance. In this case it is possible to avoid the appearance of SSR instead of damping SSR after its appearance.

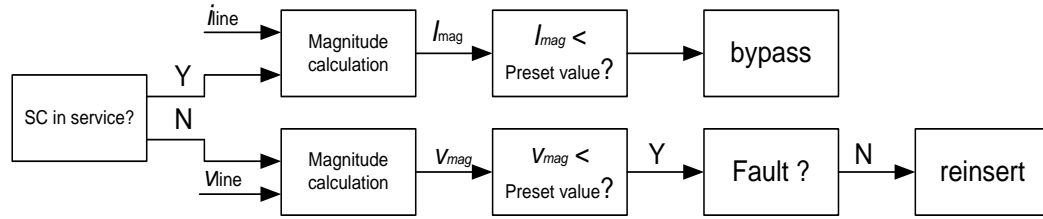


Fig. 4-12 SSR mitigation solution with prediction ability

The control algorithm is shown in Fig. 4-12. In comparison with control algorithm 1, the reinserting process is the same. Only the bypassing process differs. As the unique judgment criteria, SC is bypassed only if the current  $i_{line}$  is smaller than the pre-defined value. Obviously this pre-defined value should be related to the threshold current value with which the system is very likely to suffer SSR. Therefore, it is important to define this threshold value. According to Table 3-2, it is clear that the maximal possible active power at which SSR occurs is 385 MW. Therefore, the threshold value should be the current related to this maximal possible active power. Considering the security margin, this threshold value is multiplied by a coefficient which is slightly bigger than 1 (e.g.1.05).

Based on the idea described above, the control algorithm is applied in the investigated system and Fig. 4-13 shows the result. As illustrated in the figure, the wind speed varies from 10.59 m/s to 7 m/s at 16 s. As a result, the rotor speed goes down. At 38 s, SC is controlled to be bypassed since the control algorithms predicts the SSR risk is high. Therefore, before bypassing SC there is no SSR occurring in the system. Through this way the disturbance to the system is reduced. Since the reinserting control algorithm of the alternative solution is the same as in control algorithm 1, it is unnecessary to discuss more on this point.

This alternative solution could avoid SSR appearance as much as possible to reduce the disturbances to the system. However, the application area of the predictive solution is restricted to the system with pure wind power source.

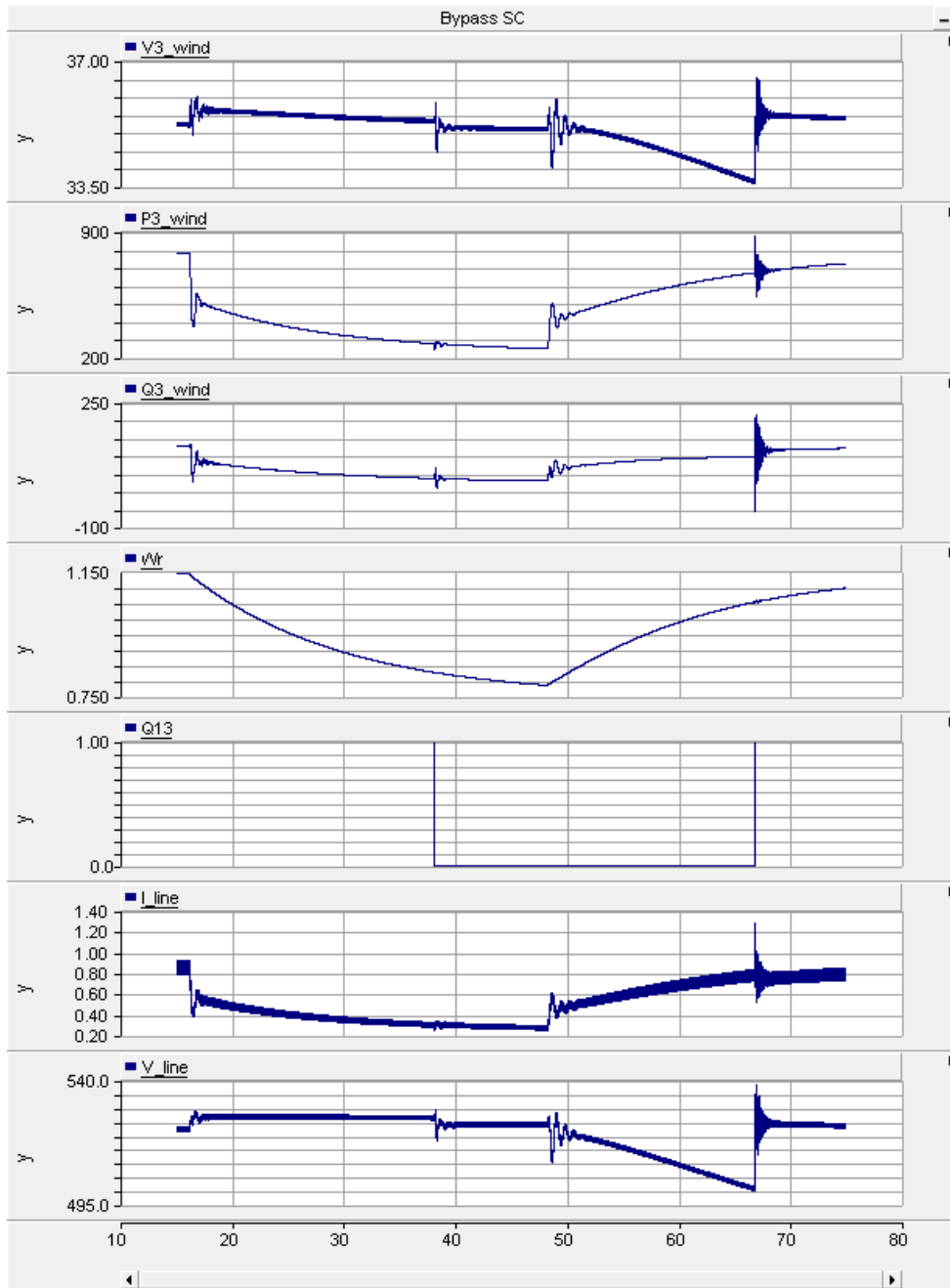


Fig. 4-13 bypass SC without SSR appearance

### 4.3 Summary

From technical and economic point of view it is feasible to bypass the SC upon SSR occurrence or when SSR risk is predicted to be high (corresponding to low wind power generation level) and reinsert the SC when wind power is high enough. The solution developed in this section employs the current through the transmission line and the voltage at SC connection bus to eliminate SSR successfully. Line current signal is available in most of common SC products whereas voltage signal needs extra measurement.

It should be pointed out that the solutions cannot be applied to systems where DFIGs have very high control speed such that SSR occurs even at high generation level. Otherwise, SC will be

bypassed due to SSR oscillation while it is needed for high power transmission. SSR in such kind of system should be mitigated using FACTS solutions, which will be discussed in the following chapters.

The solutions are suitable for systems where DFIGs have moderate or slow control speed, especially where wind farms are radially connected (or become radially connected under some conditions) to the end of the AC transmission line.

## 5 SUB-SYNCHRONOUS RESONANCE MITIGATION BY WF-STATCOM

As an important FACTS (flexible alternating current transmission system) member, StatCom (Static Synchronous Compensator) has the capability to compensate the reactive power dynamically. According to the Chinese Technical Rule for Connecting Wind Farm to Power System [11], the wind farms are required to be equipped with dynamic compensation devices if possible. In other grid codes, the requirement is similar. With grid codes getting stricter and stricter, deployment of StatCom in wind farm for dynamic reactive power support will be more and more common. This provides the possibility and facility to mitigate SSR (sub-synchronous resonance) using WF-StatCom. The SSR damping function is an added value for WF-StatCom without additional cost.

In this Chapter, SSR damping solution based on StatCom is developed and its effectiveness is verified. First, system model including StatCom is described. Then the solution based on generator speed is evaluated. After that, the solution based on active power is proposed, developed and validated. Finally the main content is summarized with the drawn conclusions.

As mention in Chapter 4, the SSR mitigation solution by temporal bypass of SC cannot be applied to systems where DFIG (double-feed induction generator) control speed is fast, corresponding to high SSR risk in the system. In the following the investigation regarding SSR mitigation solutions with WF-StatCom, WF-SVC and TCSC, the DFIG control speed is fast with the controller parameter of the rotor-side converter set to big value [ $k_{ir}=0.3$ ,  $k_Q=1.5$ ,  $k_w=24$ ].

### 5.1 Model description

The StatCom can be installed either at the point of common coupling (PCC, see Fig. 5-1) or at the SC installation point. As stated at the beginning of this chapter, what we are interested is to develop SSR damping function as an added value to the StatCom installed at the wind farm terminal, whose main function is to provide dynamic reactive power support to the wind farm. Therefore, it makes sense to analyze the system with StatCom installed at PCC point of wind farm, as shown in Fig. 5-1 .

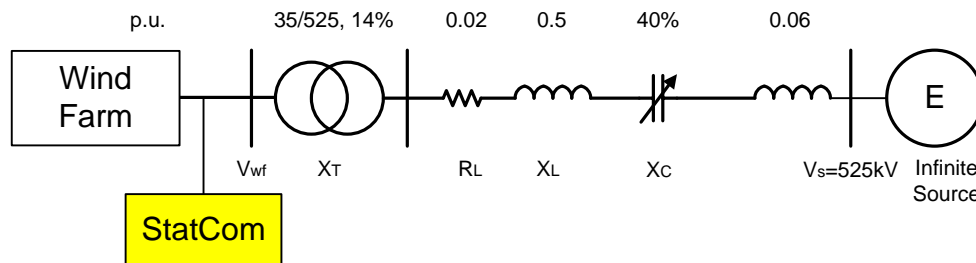


Fig. 5-1 IEEE first bench mark model for SSR research with wind farm and StatCom

The StatCom is modeled as a controllable voltage source connected to the network via a phase reactor represented by an inductor and a resistor, as shown in Fig. 5-2 . In the model, switching of the IGBTs is neglected. This will not have significant impact on the conclusions drawn from the study since the focus is sub-synchronous phenomenon, which has a much slower dynamics than IGBT switching. By modeling the StatCom in this way, it is assumed that the StatCom can always provide the required reference voltage.

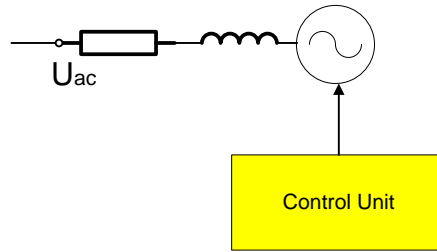


Fig. 5-2 Structure of StatCom model

The controllable voltage source is controlled by StatCom control unit, which is illustrated in Fig. 5-3 in detail. The control strategy is to regulate the DC voltage and AC bus voltage.

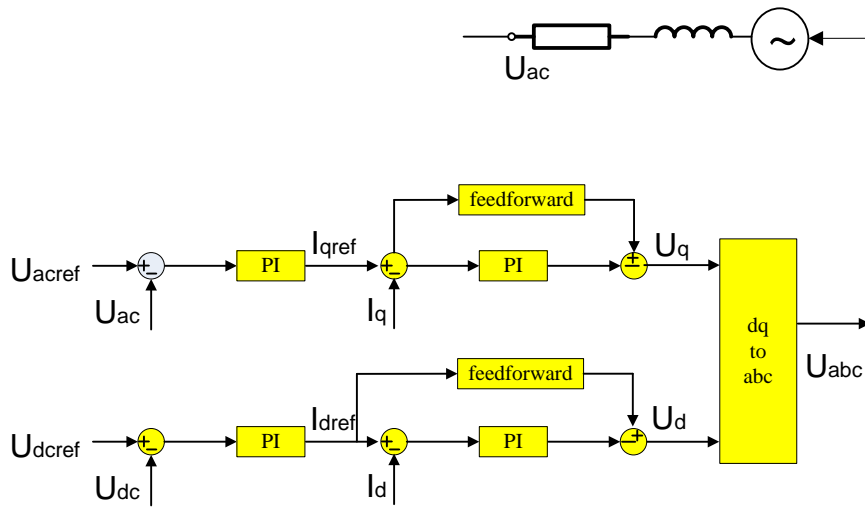


Fig. 5-3 diagram of StatCom control

The control unit adopts the widely used two-loop control structure with the current control ( $I_d$  and  $I_q$ ) in the inner loop and voltage control in the outer loop. At the beginning, the StatCom rating is assumed to very large to remove any possible limitations imposed by StatCom rating. With this idea and considering the maximum output from the wind farm is 892.4 MW, the StatCom capacity is set to 1000 MVA.

As known from the SSR characteristic study, the SSR risk is higher with lower wind generation level and with higher DFIG controller gains. Therefore, when tuning the StatCom control parameters, the DFIG controller gains are set small since the system could not reach steady state with the desired big DFIG controller parameters. The control parameters of DFIG rotor-side converter used during StatCom controller tuning are listed as follows: [ $k_{ir}=0.1$ ,  $k_Q=0.5$ ,  $k_w=8$ ]. When investigating SSR damping control later, the gains will be set back to [ $k_{ir}=0.3$ ,  $k_Q=1.5$ ,  $k_w=24$ ], corresponding to higher SSR risk.

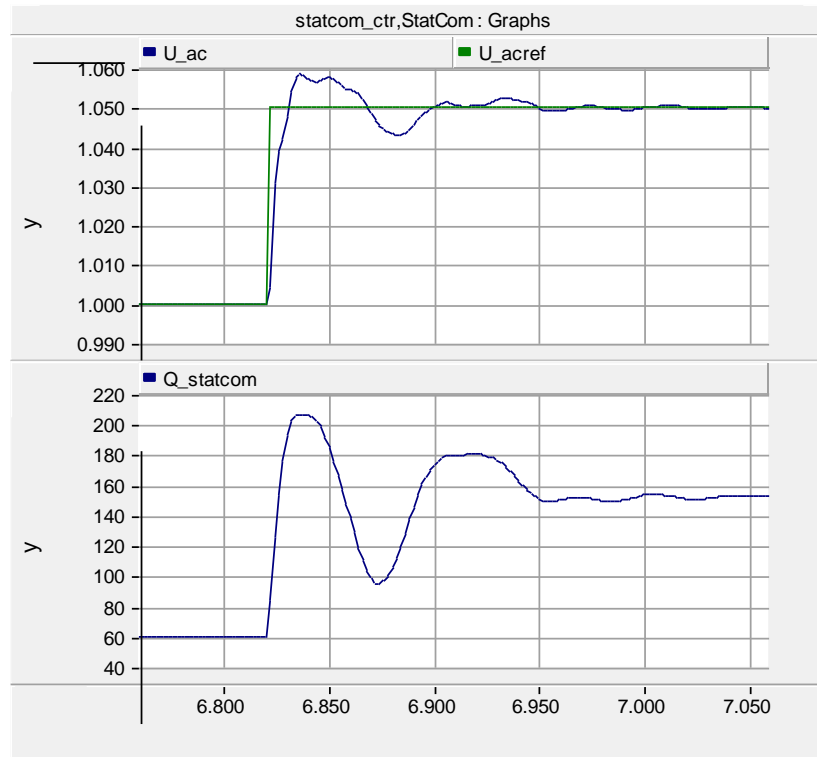


Fig. 5-4 StatCom step response

In order to tune the StatCom control parameters, step responses have been tested in the system shown in Fig. 5-1 . The result with the final tuned parameters is shown Fig. 5-4. The reference value is changed from 1.00 pu to 1.05 pu at  $t = 6.823$  s. The overshoot is 16%; the rising time of controller is 9 ms and setting time is 0.15 s. Due to the increased voltage reference, the required reactive power is changed from 60 MVar to 157 MVar to boost the voltage.

## 5.2 Solution using generator speed as control input

It is well known that StatCom could improve system stability. However, StatCom itself does not provide the essential damping to mitigate SSR as the primary task of the StatCom is to control the bus voltage [12,13,14,15,16,31,35]. In order to provide an effective damping of SSR, it is necessary to coordinate the controller of StatCom with an auxiliary SSR damping controller (SSDC). The produced signal "Umod" is sent to "Uacref" to modulate the signal of bus voltage reference, as shown in Fig. 5-5 .

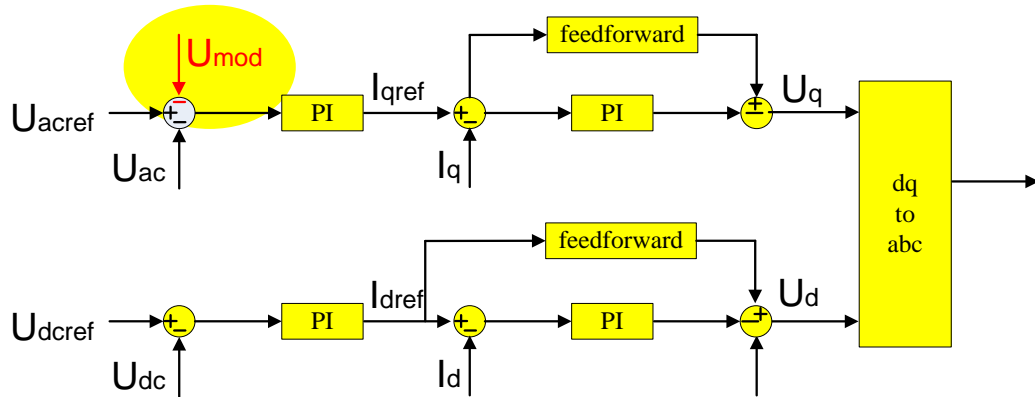


Fig. 5-5 introduced modulating signal

Now the question becomes how to generate the signal “U<sub>mod</sub>” and how to find the signals used as input signal. Generator speed is adopted to generate the modulation signal. This section will evaluate the SSR damping controller.

### 5.2.1 Controller design

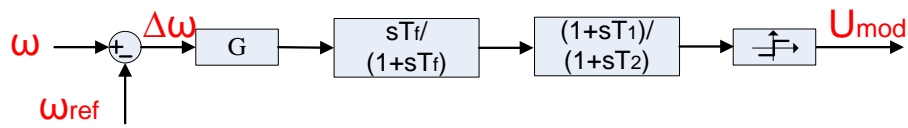


Fig. 5-6 SSDC controller structure

Fig. 5-6 displays the auxiliary SSR damping controller structure. It is composed of a gain block, a washout filter and a lead-lag compensator. It is logical to have a saturation block to limit the output of the auxiliary controller. For SSDC  $\Delta\omega$  denotes the angular frequency difference from its reference and it is adopted as the feedback input signal [2, 3, 4, 5, 6, 17].

The damping controllers are designed so as to provide an extra electrical torque in phase with the speed deviation in order to enhance the damping of oscillations. The gain setting of the damping controller is adopted so as to achieve the desired damping ratio of the electromechanical oscillations. The purpose of the washout circuit is to block the auxiliary controller from responding to the steady-state power conditions. The parameters of the lead-lag compensator are adjusted so that the phase shift between the speed deviation and the resulting electrical torque at the desired frequency is compensated.

Here, the parameters of the controller are determined through simulation studies by a trial-error method with the aim of achieving the best damping. The output of the auxiliary damping controller is used to modulate the reference settings of StatCom in order to provide the effective damping of subsynchronous oscillations [3], as depicted in Fig. 5-6. The final tuned parameters for SSDC controller are presented in Table 5-1. The Bode diagram of SSDC controller is shown in Fig. 5-7. It is observed that the controller has a high-pass characteristic and it compensates  $65^\circ$  at 38 Hz.

Table 5-1

Para	Value
G	15
Tf	0.5
T1	0.0189
T2	0.000928

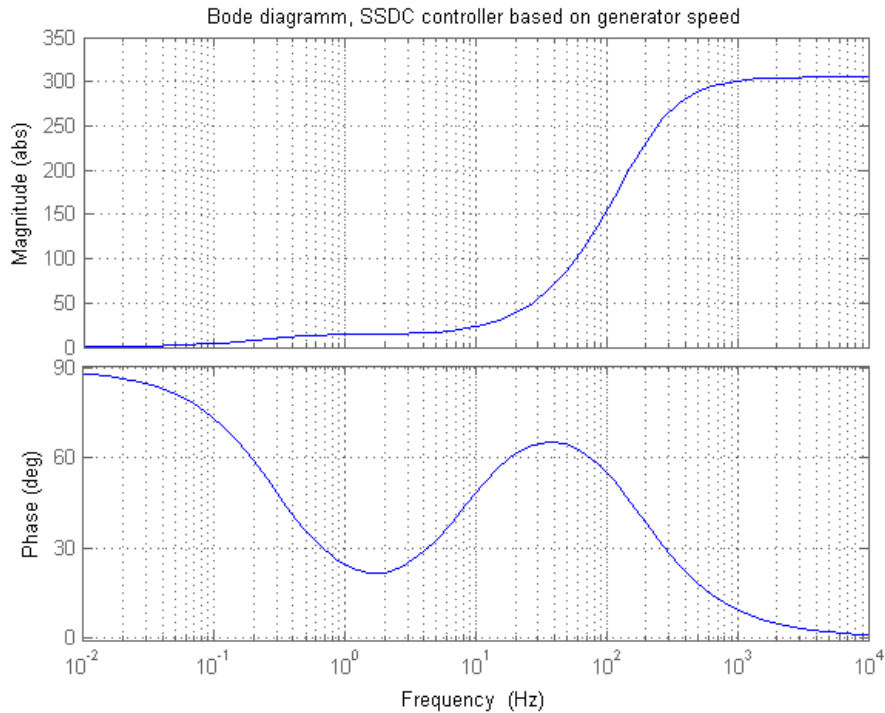


Fig. 5-7 Bode diagram of designed SSDC based on generator speed

## 5.2.2 Controller evaluation

### 5.2.2.1 effectiveness for whole wind power generation level

With the controller designed above, it is possible to verify its effectiveness over the whole power generation range. As shown in Fig. 5-8, the system is found in steady state under the condition of 40% compensation level and 10.59 m/s as wind speed. Three lumped DFIGs are assumed to have the same wind speed in this case study. Meanwhile, the reference value of bus voltage is set to 1.05 pu. At  $t = 52$  s, the wind speed is changed to 4 m/s. Of course such a big step change of wind speed is not possible in reality. The purpose to utilize a step change is to reduce the simulation time. With the wind speed reduction, the reactive power out of StatCom becomes negative (inductive) rapidly and then goes back to positive again. As the generator speed goes down, the reactive power decreases slowly until it reaches the minimal value. Over the whole power generation range, the bus voltage follows its reference value all the time except the transient state after wind speed change. The modulation signal has the similar shape to the bus voltage.

In order to prove the effectiveness of designed SSDC, the controller is tested again under the condition with the lowest wind power output, (13.4 MW, corresponding to 0.01 pu of the 1224 MW installed capacity), which results in the most severe SSR situation. The simulation results are shown in Fig. 5-9. At  $t = 1.02$  s, the SSDC is disabled. The modulation signal “U\_mod” changes to zero immediately. Shortly, SSR appears in the system and the oscillation starts growing, which could lead to the system instability. At  $t = 1.38$  s, the controller is enabled. The modulation signal starts to work and generate positive damping to SSR. Oscillations in all signals are being damped. After around 0.4 s, there is no oscillation visible in the system and the modulation signal becomes zeros again. Therefore, the designed SSDC is effective for the operation condition with the highest SSR risk from power generation point of view. It could be considered that this SSDC is valid for all the operation condition.

Based on the discussions above, it could be concluded that the developed SSDC controller is valid for the whole wind power generation range.

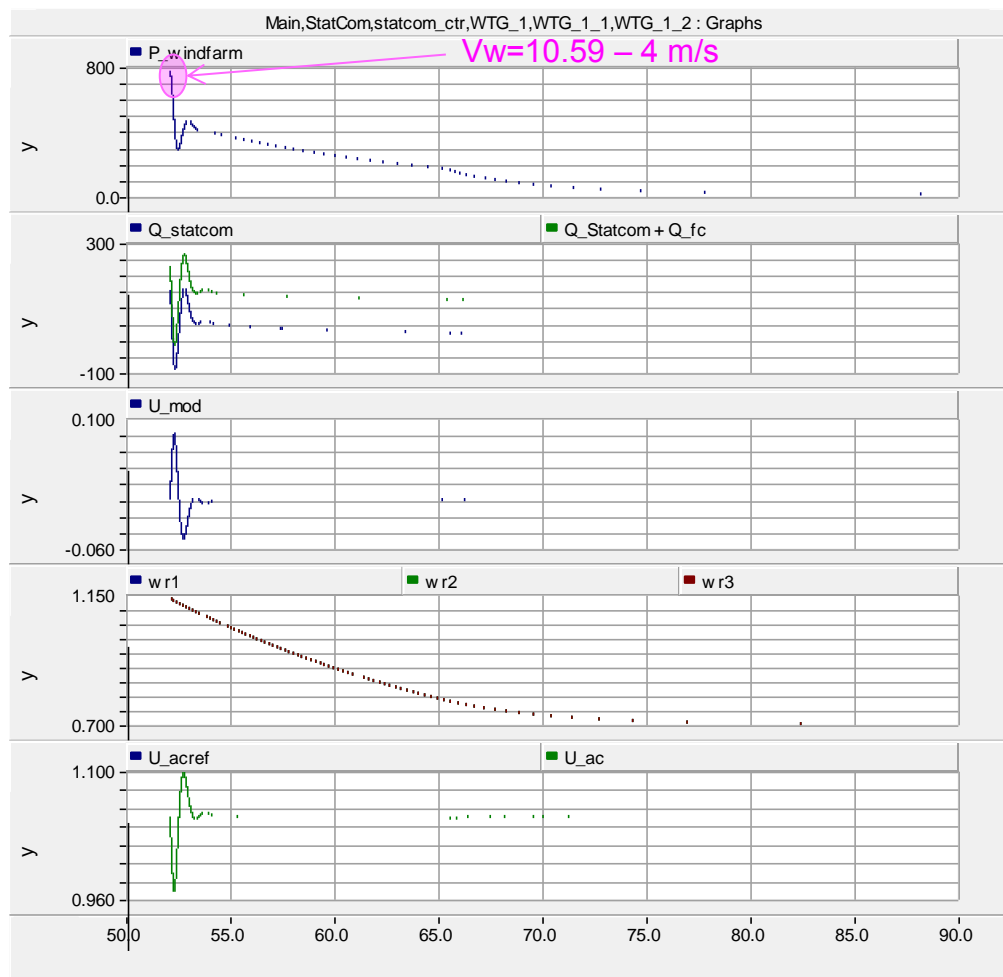


Fig. 5-8 Effectiveness of designed SSDC over whole power range

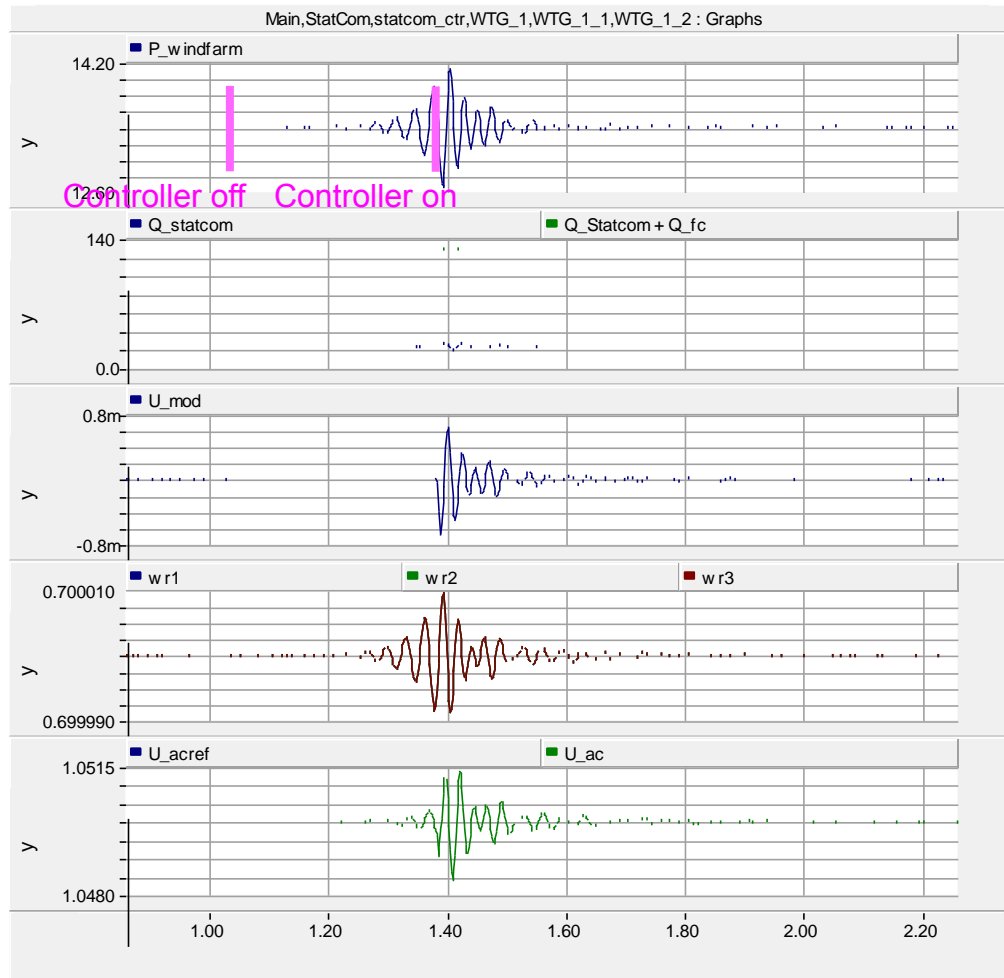


Fig. 5-9 Effectiveness of designed controller under the lowest power generation level

### 5.2.2.2 Effectiveness for different external systems

In the analysis above, the SSDC has been validated from power generation level point of view. However, it is still unknown whether the SSDC will be effective if the external system varies. The system change has different forms. But the essential difference is the variation of the equivalent impedance. As a typical form, different compensation level is selected to reflect change of system configuration. In this section, the effectiveness of the SSDC is tested under different compensation levels. Meanwhile, the power generation level is kept at the lowest level to make sure the damping effect is valid for whole wind power generation level.

The simulation results are shown in Fig. 5-10. At the beginning the system is compensated with 40% level, which is the default compensation level in this project. At  $t = 2.9$  s, the compensation level is change to 55%. It is clear that the required reactive power increased by 20 MVar. This could be explained by the increase of system compensation level. Transient oscillation is caused due to the system change but it is damped out after the transients. The figure proves that the designed controller has the SSR mitigation capability for 55% compensation level. At  $t = 5$  s, the compensation level is changed to 70%. The simulation results prove that the SSDC is also effective for system with 70%.

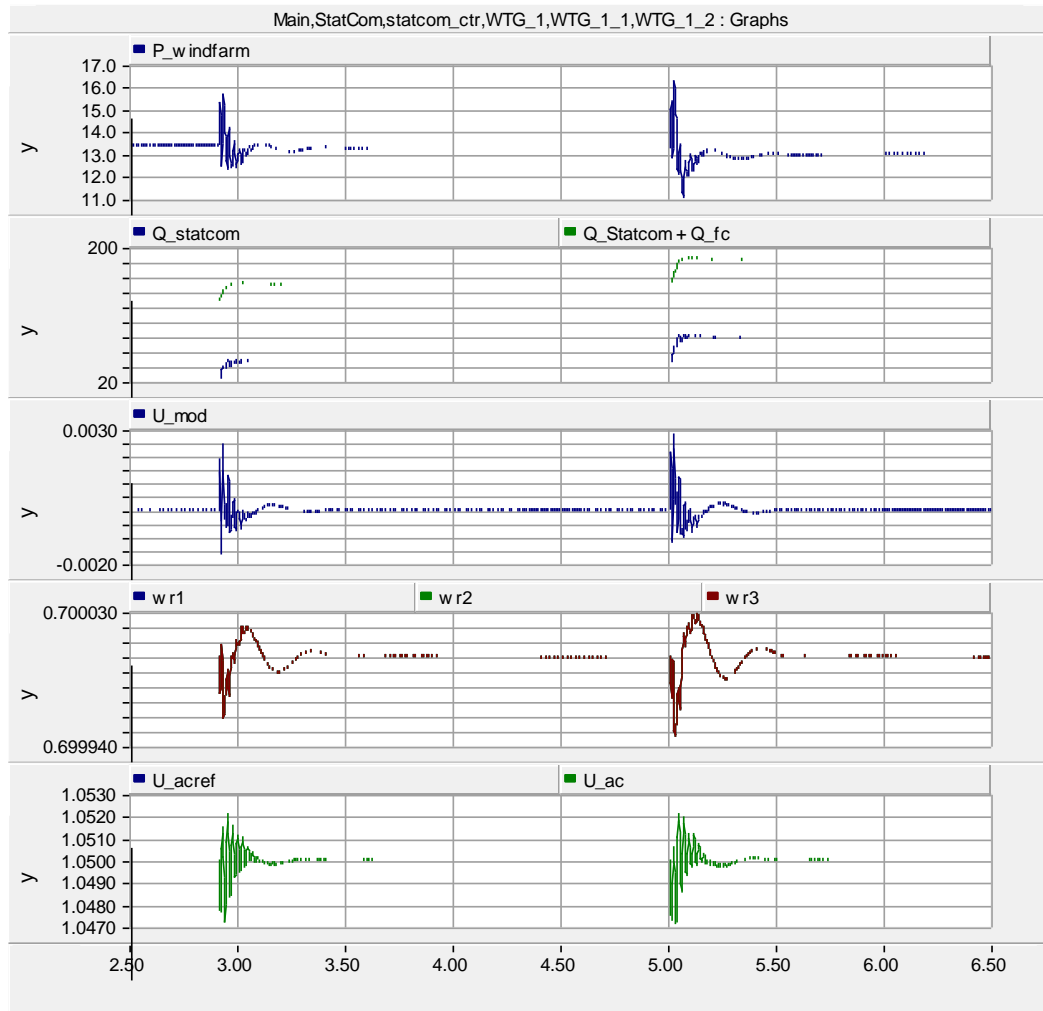


Fig. 5-10 SSSDC effectiveness under different compensation level

With the analysis above, it could be summarized that the designed SSSDC has the capability of damping SSR caused by series compensation and DFIG, no matter what the system compensation level and power generation level are. The controller gain used in the simulation is constant and it doesn't depend on the power generation level. However, it has to be kept in mind that the StatCom rating in the simulations is sufficiently large.

### 5.2.2.3 Effectiveness for DFIGs operating at different generation levels

In all the analysis above the investigation is carried out with the same wind speed in all three wind farms. However, it is a normal phenomenon that the wind farms have different wind speeds. Even in the same wind farm, the wind turbines are rotating with the different speeds. Since the designed controller needs rotor speed as the input signal, the effectiveness of SSSDC is challenged in case the wind turbines rotate with different rotor speeds. Therefore, it is necessary to be investigated.

Among all the wind turbines, it is possible to select an arbitrary rotor speed signal as the controller input. The effectiveness will be tested for two representative cases with the selected rotor speed being the maximal and minimal value among all the three turbines. If the solution with maximal

and minimal rotor speed as input signal is valid, it could be stated that the solution based on arbitrary rotor speed is also valid.

In Fig. 5-11 the wind speed in the three wind farms is 4, 5, 6 m/s respectively and the adopted rotor speed is the one in the wind farm with 4 m/s (the minimal value in all three wind farms, scenario 1). The damping controller is disabled at  $t = 11$  s and enabled at  $t = 11.5$  s again. As observed in the figure, without SSDC the SSR comes back and the system has high risk of instability. If the SSDC is added to StatCom controller unit, the sub-synchronous component is damped out due to the additional positive damping effect generated by modulation signal.

The simulation of SSDC effectiveness employing maximal wind speed (scenario 2) as input signal is also done and its result is shown in Fig. 5-12.

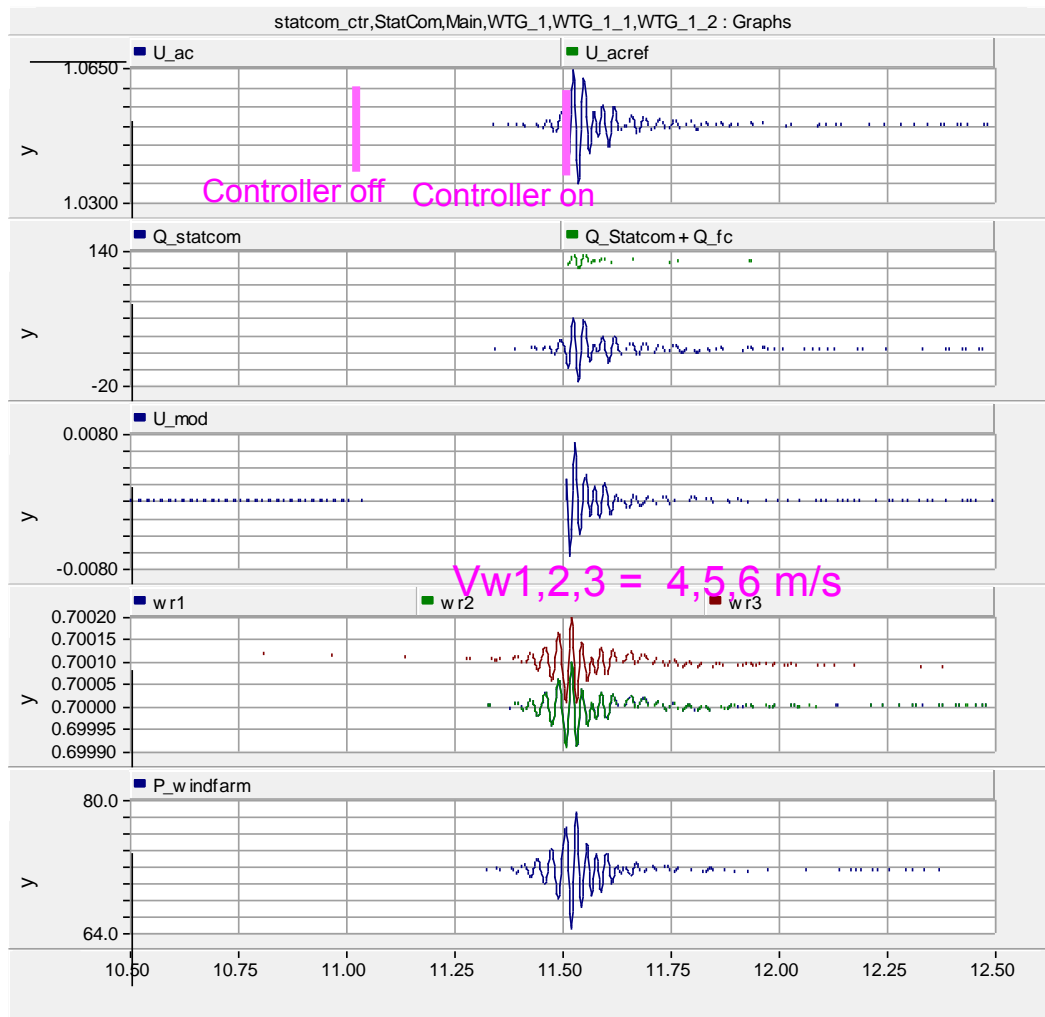


Fig. 5-11 SSDC effectiveness under different wind speed, scenario 1

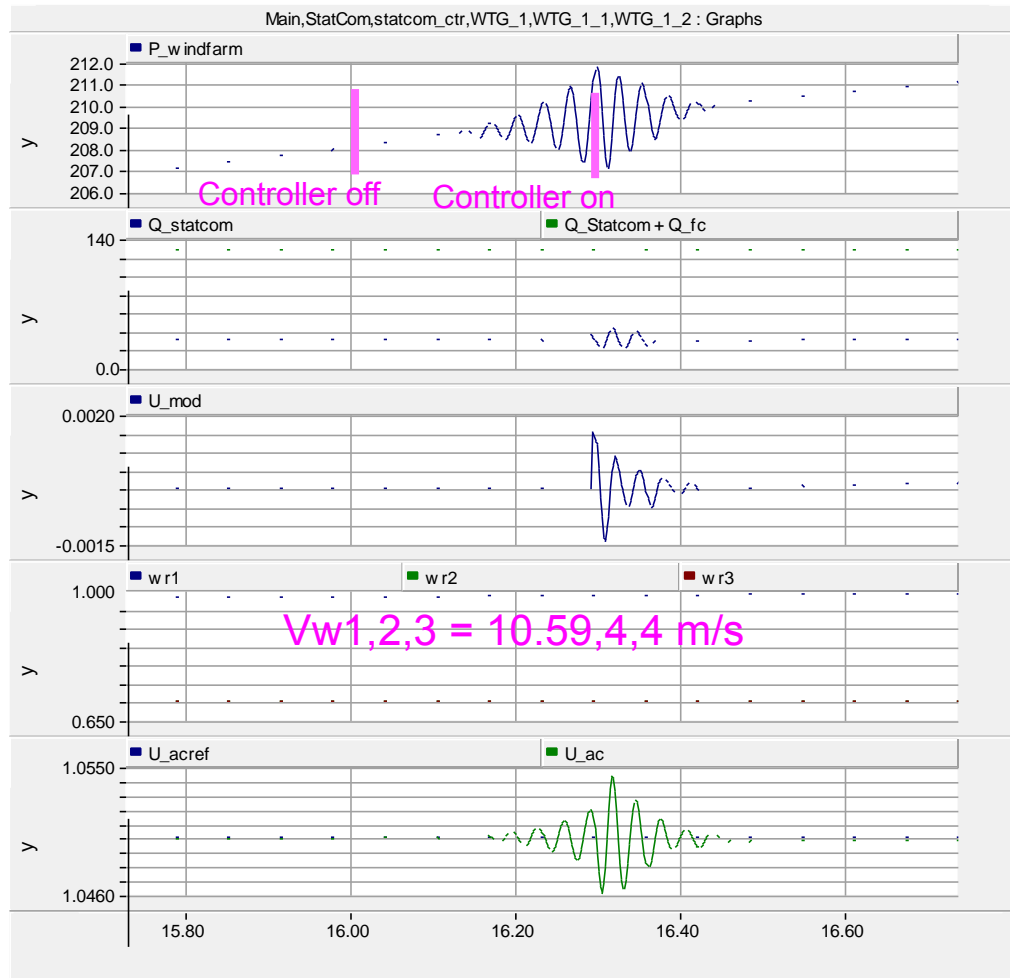


Fig. 5-12 SSSDC effectiveness under different wind speed, scenario 2

In scenario 2, the wind speed in three wind farms is 10.59, 4, 4 m/s respectively. The rotor speed in the wind farm with maximal wind speed 10.59 m/s is served as the input of SSSDC. Similar to scenario 1, the developed SSSDC is effective to damp out the sub-synchronous component. Combining with the simulation of scenario 1, it could be concluded that the developed solution could be applied in the wind farms with different wind speeds. By introducing the rotor speed of arbitrary wind turbine and giving the signal to SSSDC, the designed controller is able to damp the SSR in the system.

To summarize, the solution using rotor speed as the control input is effective for whole wind power generation range, for various compensation degrees and for DFIGs operating at different generation levels. However, it has to be kept in mind that the StatCom rating in the simulations is sufficiently large. Besides, the controller also has its drawback. Since the solution is based on a signal with some distance from the StatCom, dedicated communication is a must.

### 5.3 Solution based on active power

In previous section, the developed solution utilizes rotor speed to modulate bus voltage. Due to its dependence on signal communication, the feasibility is limited. It is necessary to find other signals which are available or at least locally measurable in StatCom control system. In this

section, a controller with active power through transmission line as input signal is developed and its effectiveness is verified.

### 5.3.1 Controller structure

The controller designed in this section has the similar structure as the one shown in Section 5.2. The differences are the input signal used and inclusion of an extra lead-lag compensator, as shown in Fig. 5-13. Since generator speed is closely related to wind power, it is logical to replace the speed signal with active power signal. In the simulation studies, it is proved there are more than one oscillation frequencies existing in the system. The extra lead-lag controller is used to damp oscillations in other frequency range.

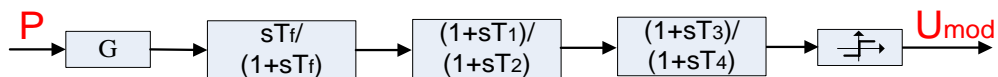


Fig. 5-13 SSDC based on reactive power

Similar to the discussion in Section 5.2, the parameters of the lead-lag compensator are adjusted so that the phase shift between the active power through the transmission line and the resulting electrical torque at the desired frequency is compensated.

In the sequel, an additional electrical damping torque output is acquired in phase with the active power. Here, the parameters of the controller are determined through the simulation studies by a trial-error method with the aim of achieving the best damping [3]. As depicted in Fig. 5-13, the output of the SSDC controller is utilized to modulate bus voltage to yield the proper damping of oscillations. The detailed data for SSDC are presented in Table 5-2.

Table 5-2 SSDC controller parameters

Parameter	Value
G	0.005
Tf	0.5
T1	0.0189
T2	0.000929
T3	0.000082
T4	0.0429

T1 and T2 are the time constants of the first lead controller, which compensate the system with 65° leading at 38 Hz. Meanwhile, the controller also provides the compensation of 85° lag at 85 Hz. With those components together, the SSDC controller is added to StatCom control unit. The results of simulation studies are shown in Fig. 5-14.

At the beginning, the system is found in a steady state. The power generation level is in a high level. At  $t = 1.5$  s, the wind speed is change from 10.59 m/s (original wind speed) to 4 m/s.

Normally the output of saturation block in Fig. 5-13 is limited to a small value (like 0.05) so that the bus voltage could not deviate too much from its reference value. But with such a SSDC the modulation signal will reach its limited value for a long time which could lead to system instability. Therefore, the limitation value is set to 1 since the system stability has the highest priority. Even with such a big value 1, the output of saturation block still reaches its threshold value for 0.8 s. During the saturated time, the bus voltage exceeds 1.5 pu, which is not permitted in power system. Moreover, SSR appears in the system. Although this SSR could be damped after the transient and the system could be in a new steady state, it is not permitted to bring such a disturbance to power system. The bus voltage increase could lead to a disaster to power system.

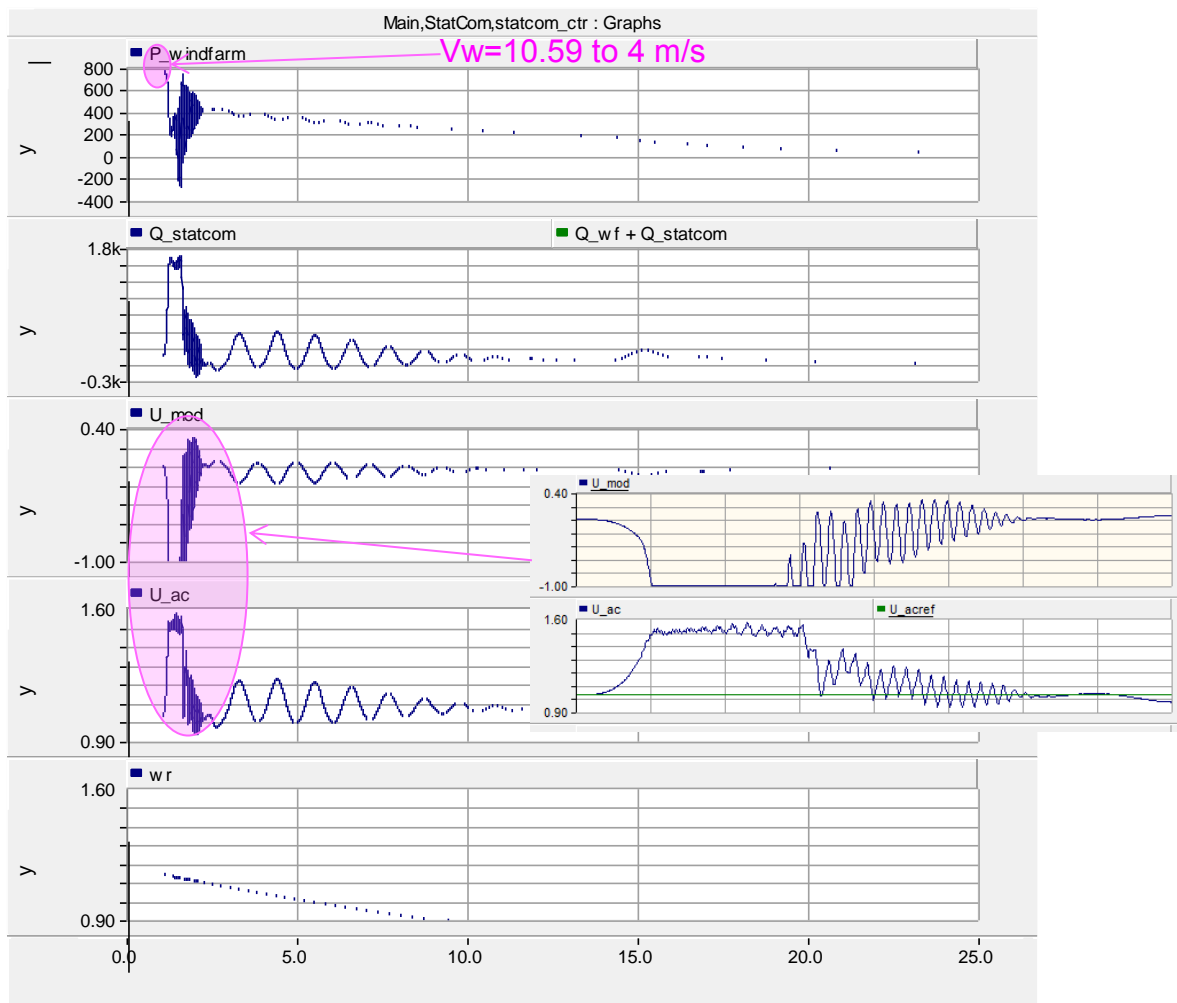


Fig. 5-14 Effectiveness of SSDC based on active power

Therefore, a solution to mitigate this disturbance or at least reduce the disturbance to an acceptable level must be developed. Introducing a time delay could meet this requirement. The improved controller is illustrated in Fig.5-15.

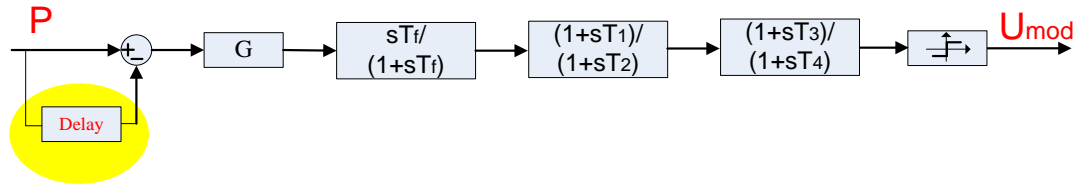


Fig. 5-15 Modified SSDC based on active power

The effect of the modified controller is checked through a small test. A signal P comprises of a sinusoidal component with a small amplitude and a DC component. The DC component is change to a small value suddenly to check the output signal of high pass filter. The comparison of the output signal of high pass filter is depicted in Fig. 5-16.

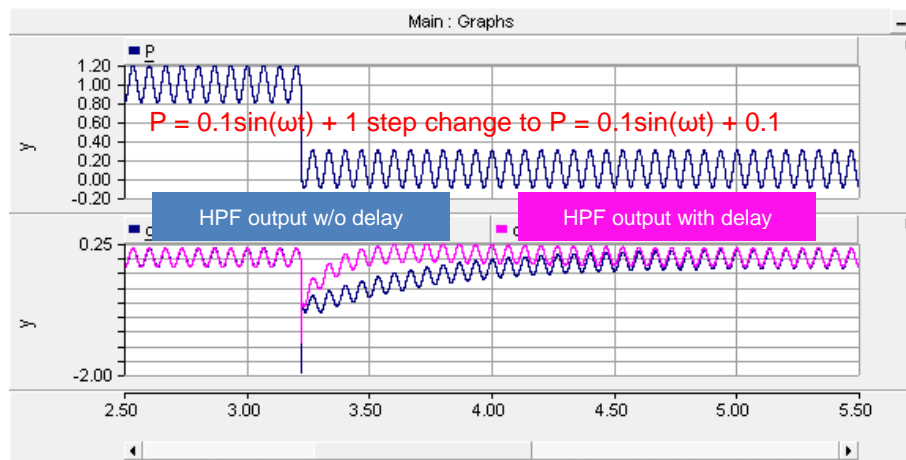


Fig. 5-16 Effect of modified SSDC

As illustrated in Fig. 5-16, with time delay the high pass filter output is reduced by a certain level and it goes back much faster to steady state value in comparison with the high pass filter output without delay. This different has a very big influence on the transient characteristic of designed controller.

Introducing the time delay has also influence on the characteristic of SSDC. Hence, it is necessary to find out a new set of control parameters, which is shown in Table 5-3. The new control has a lead-lag controller with  $20^\circ$  lag at 35 Hz. The Bode diagram is shown in Fig. 5-17. This Bode diagram depicts the frequency characteristic of the controller only including gain block, high pass filter and lead-lag controller, but no delay unit.

Table 5-3

Parameter	Value
G	0.0020
Tf	0.5
T1	0.0032
T2	0.0065
T3	0
T4	0
Delay	0.01 s

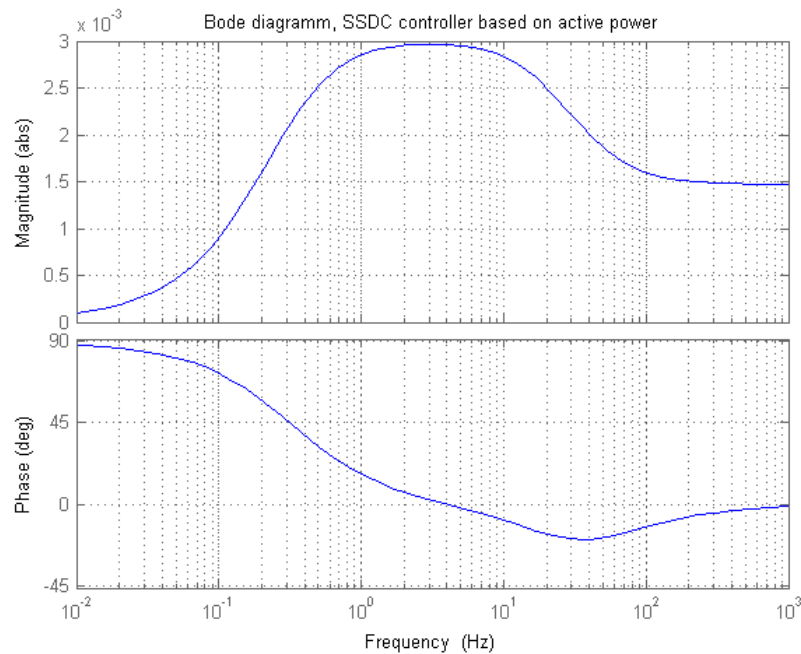


Fig. 5-17 Bode diagram of modified SSDC based on active power

## 5.3.2 Controller Effectiveness verification

### 5.3.2.1 Different power generation level

The simulation result based on the controller described in Table 5-3 is shown in Fig. 5-18. In comparison with the controller without active power delay, the modified controller doesn't lead to the big increase of bus voltage. As shown in Fig. 5-18, the maximal bus voltage is 1.0451 pu, which is much smaller than the voltage of 1.55 pu shown in Fig. 5-14. This value is also acceptable in power system. Although it leads to a small disturbance in power system, the disturbance should be very smooth in case of realistic change of wind speed. In reality, step change of wind speed is not possible. Using ramp function to represent wind speed, the transient characteristic of designed controller becomes much smaller. This is also proved by EMTDC simulation. After the transient state, the system goes into a new steady state even in case of very low power generation level. In the whole power range, there is no SSR phenomenon. It is also important to note the gain changes when the active power reaches 250 MW. From the figure, there is no visible transient due to gain change at  $t = 10$  s (the time when active power reaches the critical value).

In order to prove the SSR damping capability further, the controller is switched off to see what will happen. It is estimated that SSR component will be created in the system and go to an instability state. When the amplitude of SSR grows to a certain value, the SSDC is switched on to check, whether it could damp out the SSR. This study has been carried out with PSCAD and its results are shown in Fig. 5-19. At  $t = 2.1$  s SSDC is turned off while at  $t = 2.6$  s SSDC is turned on. As observed in the figure, losing SSDC SSR occurs in the system and the system has a risk

of instability. If the StatCom is equipped with the developed controller, the component with sub-synchronous frequency is mitigated effectively so that the system is free of SSR risk.

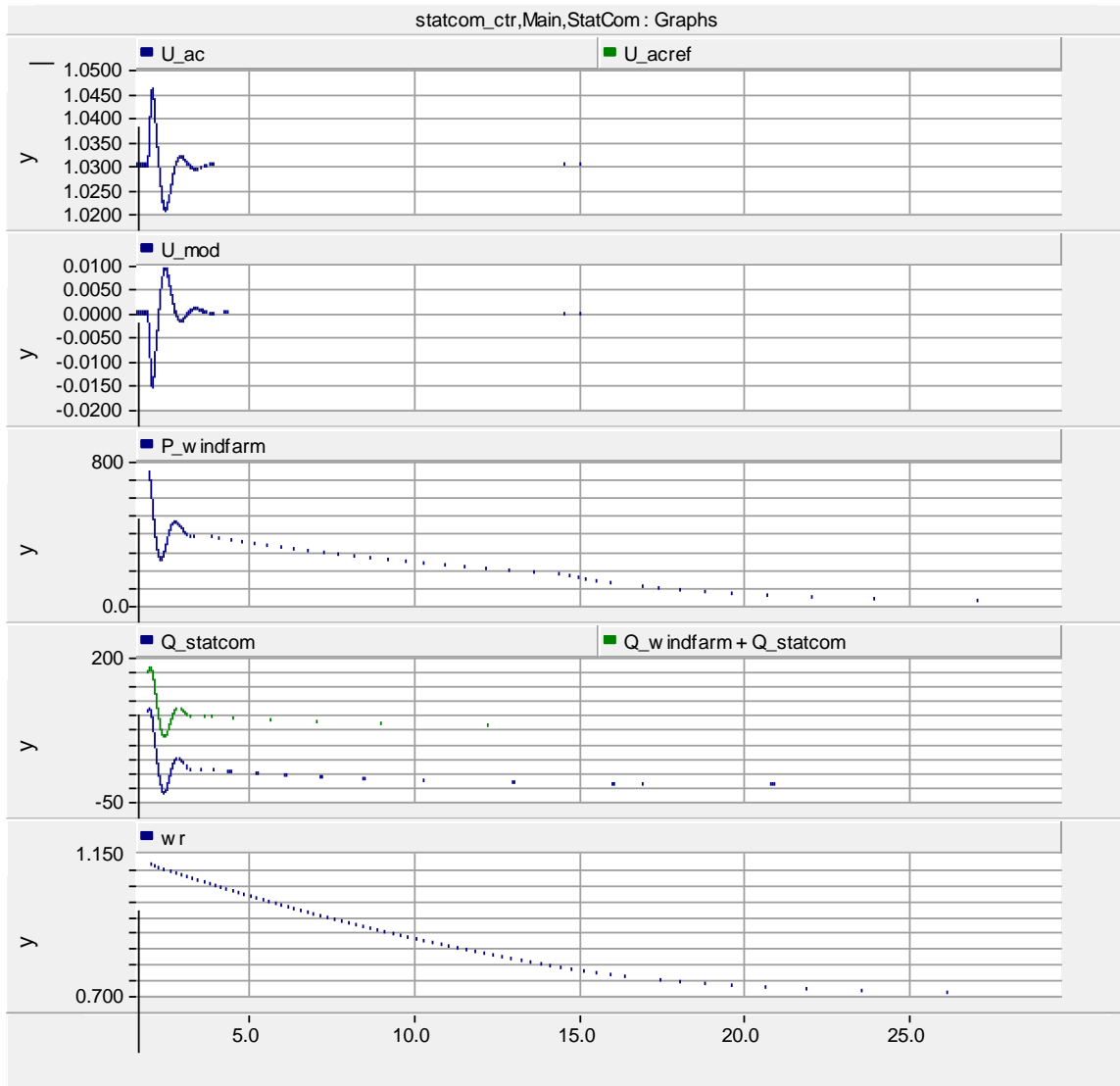


Fig. 5-18 Effectiveness of modified SSDC based on active power over whole power range

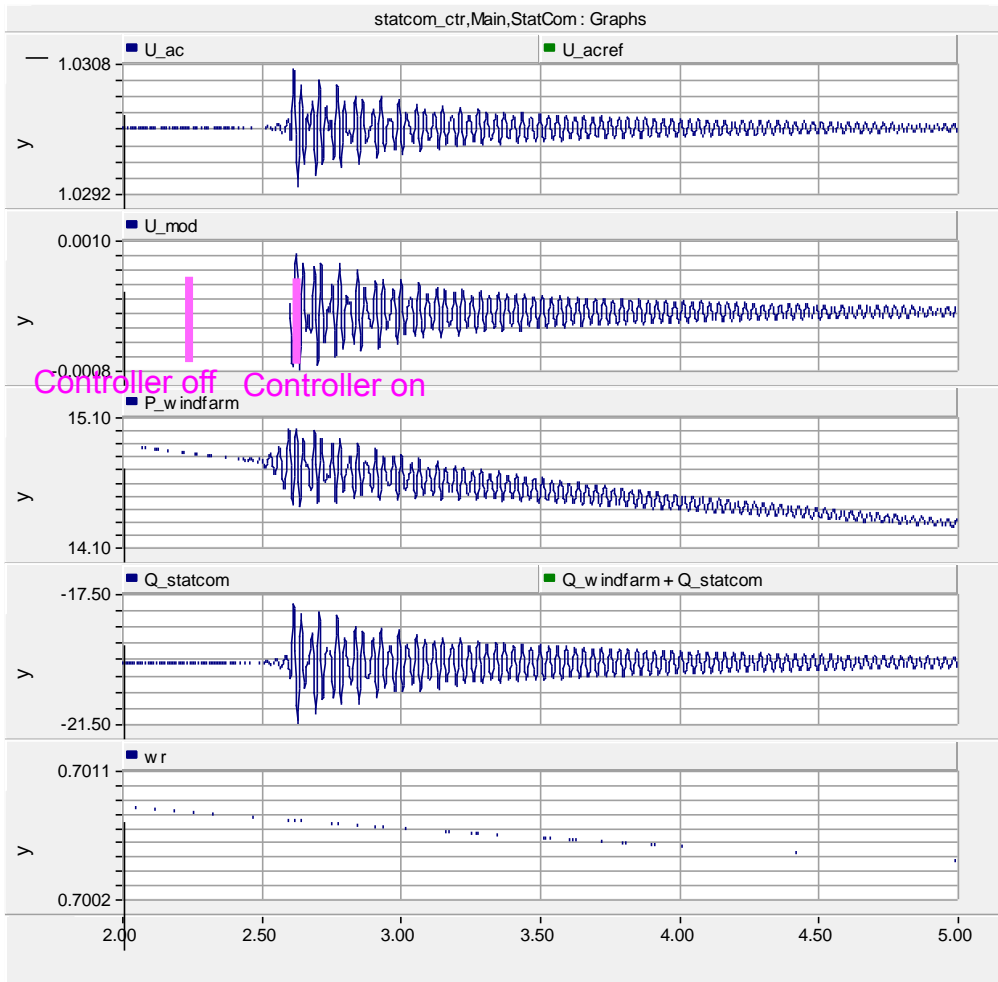


Fig. 5-19 performance of SSDC with active power delay

### 5.3.2.2 Different systems

The discussion above focuses on the different wind generation. It is also very worthy to do the investigation of influence of different system on SSR damping effect. As in real operation the system varies all the time, this work is pretty valuable for the application of the developed solution. With this idea, EMTDC test has been done with different compensation levels, which is typical form of varying system configuration. With this test, it is possible to evaluate the solution's independence on specific system.

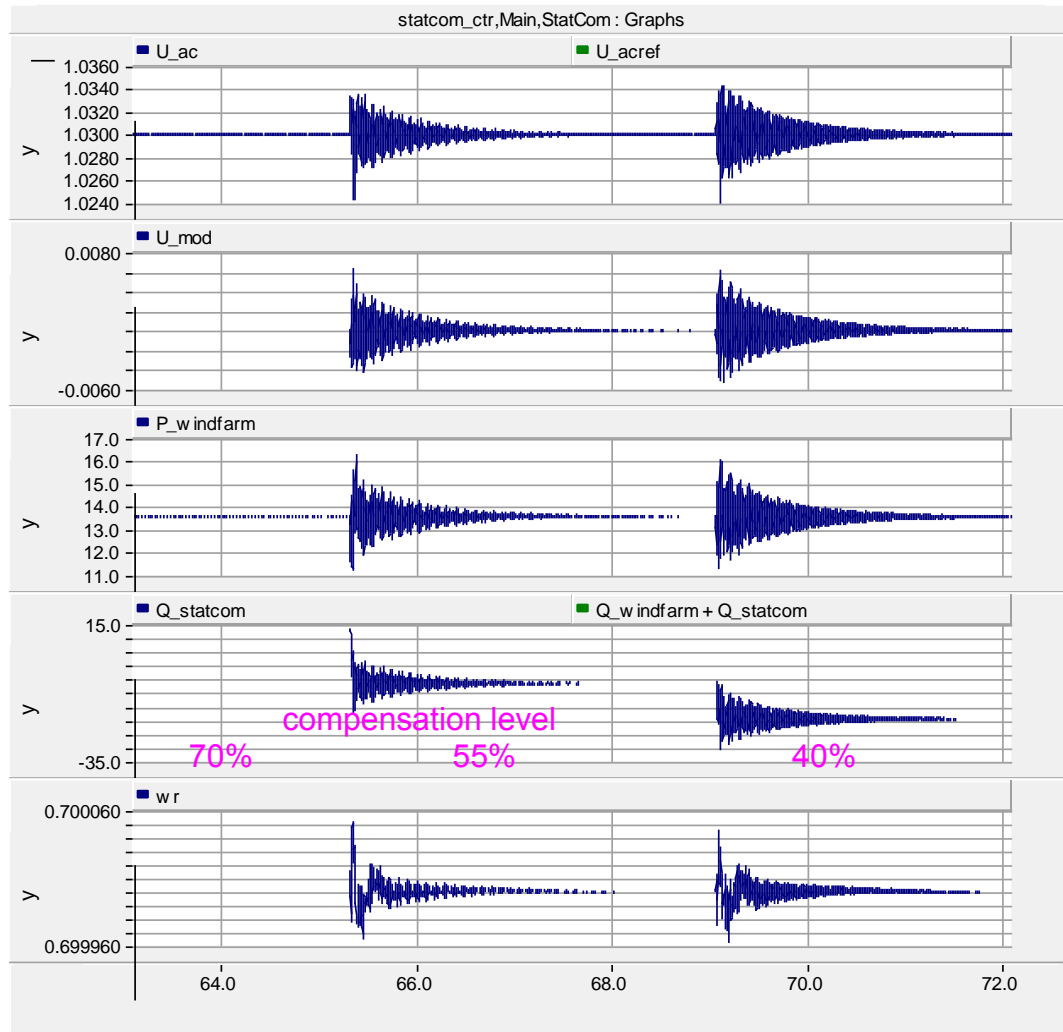


Fig. 5-20 Effectiveness of modified SSDC based on active power, different compensation level

The result of the test described above is shown in Fig. 5-20. From the figure it is observed the reactive power out of StatCom changes from 13 MVar via -6 MVar to -19 MVar as the compensation level changing from 70% via 55% to 40%. For the the system with all the involved compensation level, SSR is damped effectively with the designed controller. That is, with this modified SSDC the system SSR risk is highly reduced. The bus voltage is also regulated to its reference value.

The controller gain required for different generation levels is different. The gain required at lower generation level is larger. Although the gain required at the lowest generation level can also be used at high generation level, a smaller gain results in better performance in term of the amplitude of the ripples in the steady state signals. Nevertheless, for SSR damping purpose, the controller gain can be kept constant for the whole wind generation range in the simulation. However, it has to be kept in mind that the StatCom capacity in the investigation is sufficiently high. In case StatCom rating is small, the controller gain has to be adapted to wind generation level, which will be investigated in the next section.

### 5.3.3 Minimized StatCom capacity

The analysis above have validated the StatCom with SSDC has the potential to mitigate SSR. In the investigation above, the StatCom rating is set to be very big. From economic point of view, it is also valuable to estimate the required rating of StatCom for SSR mitigation.

The required StatCom capacity for reactive power support depends on many issues, e.g. reference value of bus voltage, fixed capacitor bank installed in the wind farm, operation point of wind turbines and system compensation level. Here, the system compensation level is set to 40%, the same as the default value. From Fig. 5-8, Fig. 5-13 and Fig. 5-18 it could be calculated that the required variable reactive power is around 135 MVar due to the different power generation level. In this investigation, the highest wind power output considered is 770 MW (0.63 pu) and the lowest is 13 MW (0.01 pu). Therefore, the fixed capacitance is set to the value so that the required positive and negative peak value of reactive power is the same. In this way the reactive power configuration is the most cost-effective. According to this strategy, the fixed capacitor bank is changed from 80  $\mu\text{F}$  to 115  $\mu\text{F}$ . The StatCom capacity is set to 70 MVar to meet the voltage requirement dynamically. With such a system configuration, a simulation is performed to check its effectiveness over the whole power generation range. The simulation result is shown in Fig. 5-21.

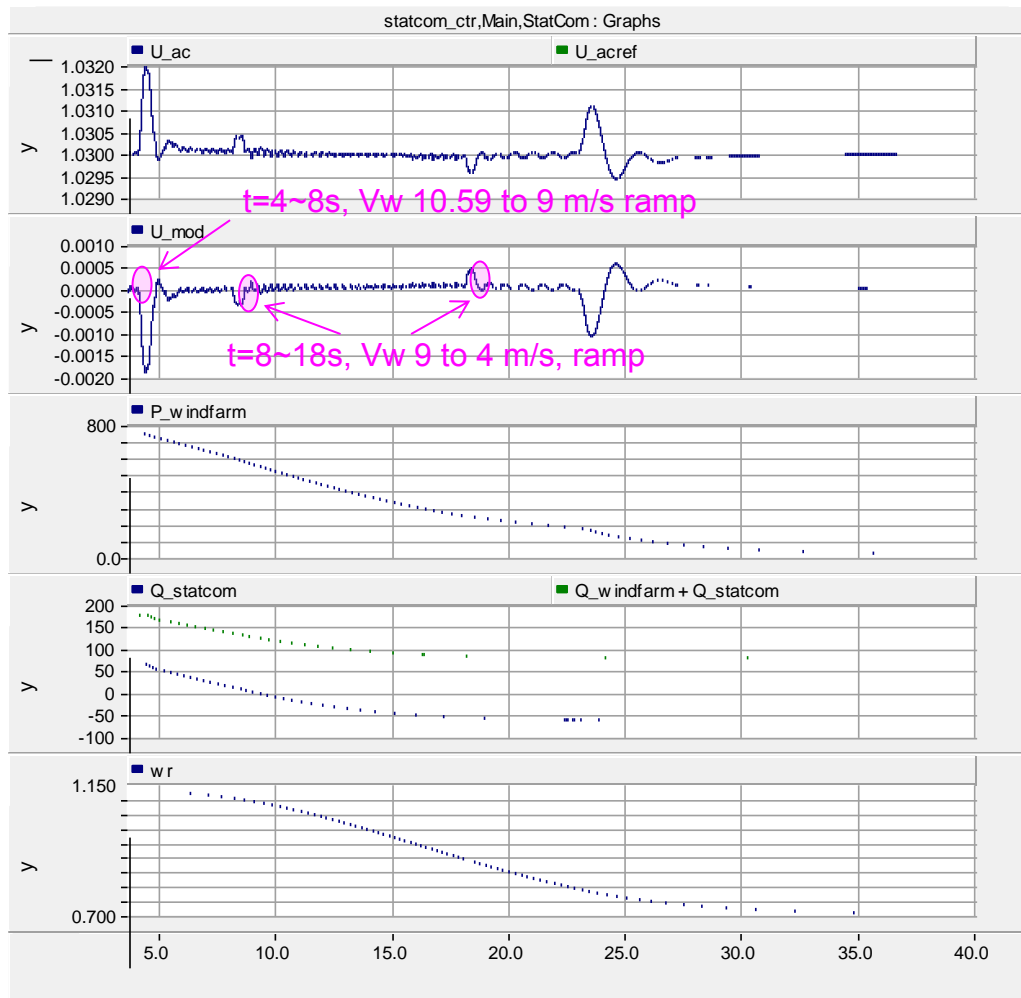


Fig. 5-21 Effectiveness of SSDC with minimized StatCom capacity

During 4 s and 8 s, wind speed is ramped from 10.59 m/s to 9 m/s. Due to the contribution of modulation signal and wind speed change, the bus voltage goes up by 0.002 pu for a short time and then goes back to its reference value quickly. During 8s and 18s, wind speed is ramped from 9 m/s to 4 m/s. The operation point is transferred to a new one without suffering SSR. The disturbance to the system is also very small (the disturbance at around 23s is due to the wind turbine control, not StatCom or wind speed), which could be neglected. From the figure it could be concluded the SSR risk of the system equipped with  $\pm 70$  MVar StatCom is mitigated.

As researched in [18] by IEEE PES Wind Plant Collector System Design Working Group, in a 200 MW wind farm the required StatCom capacity is  $-50 \sim +100$  MVar to satisfy all the requirements, like LVRT, HVRT, power factor requirement. If a wind farm is installed with such a StatCom capacity, the SSDC developed in this section is sufficient to prevent the system from SSR without any problem.

Table 5-4

Parameter	Value
G	0.0055 for $P > 250$ MW 0.0065 for $P < 250$ MW
Tf	0.5
T1	0.0038
T2	0.0046
T3	0
T4	0
Delay	0.01 s

The parameter used here is listed in Table 5-4. From the table, it is clear that the gain used here is not constant any more. It is a variable which is dependent on active power. Under the condition of low power level a big gain is required whereas under high power a small one is necessary. Otherwise, the controller could lose its effectiveness and SSR component will appear in the system. As shown in Fig. 5-22, the gain of the controller is adapted online according to the active power. With the so-called gain adaption block (in yellow in Fig. 5-22), the developed controller is powerful and valid for the whole power generation level. This kind of gain adaption is the key innovation in the research related to StatCom solution.

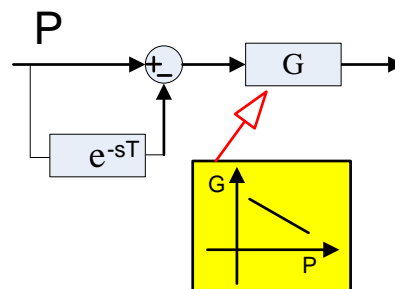


Fig. 5-22 Gain adaption

In comparison with the controller with constant gain in Table 5-3, which is used for the system with a big StatCom, the following conclusion could be drawn: for SSR mitigation purpose, the controller gain in system with a sufficiently large StatCom can be kept constant whereas it has

to be adapted to wind generation level in system with a small one. Therefore, using gain adaption could reduce the required StatCom capacity.

#### 5.4 Summary

In this chapter, the solutions to mitigate SSR by WF-StatCom are proposed, designed and validated. Simulation results have shown the developed solutions are valid for the whole wind power range and different system configurations. Since the solution based on generator speed needs external signal communication channel, the solution based on delayed active power is preferred. In order to investigate the economy of this solution, the required StatCom rating is estimated. Since the rating that meets the requirement for reactive power support is sufficient for SSR damping, it is feasible to add the developed SSDC to StatCom controller to achieve SSR mitigation purpose.

The novelty of the damping control strategy is the gain adaption in the designed controller. By introducing the adaptive concept, the developed controller could adjust the gain automatically according to wind power generation level. If the StatCom is sufficiently large, this kind of gain adaption is not absolute necessary to eliminate SSR. But if StatCom capacity is limited, a gain adaption has to be adopted in order to make sure the controller's effectiveness for whole wind power generation level. Therefore, gain adaption could help to reduce the required StatCom capacity from SSR mitigation point of view, which provide essential value for SSR mitigation in wind applications.

## 6 SUB-SYNCHRONOUS RESONANCE MITIGATION BY WIND FARM STATIC VAR COMPENSATOR

With grid codes getting stricter and stricter, deployment of dynamic reactive power support at wind farm will be more and more common. SVC (static VAR compensator) is one of the main types of reactive power compensation devices. In case that SVC is needed at the wind farm terminal for reactive power support, it will be valuable that it can provide SSR damping as an additional function. The objective of this chapter is to investigate the feasibility of SSR mitigation by WF-SVC. Since the SVC is assumed to be a WF-SVC, the diagram of the investigated system can be depicted as in Fig. 6-1. The SVC is installed at the PCC (point of common coupling) of wind farm cluster, on the low-voltage side of the step up transformer. The transmission line is series compensated by 40% of the line reactance.

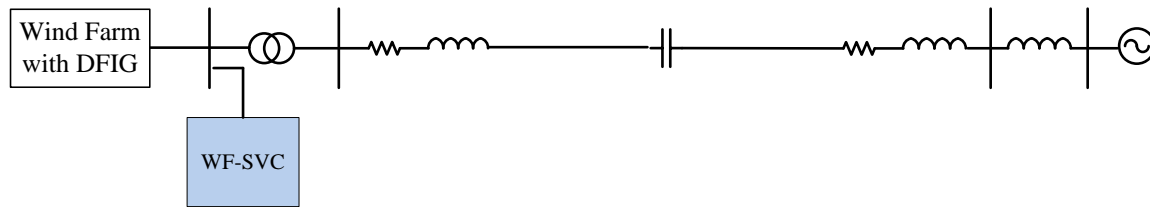


Fig. 6-1. Single line diagram of the investigated system

It is reported that by adding a damping control loop to the SVC control system, SSR (sub-synchronous resonance) caused by induction or synchronous generators and series compensated ac lines can be damped. In [19,20], synchronous generator is considered and in [21] induction generator is considered.

In these studies, the input to the damping controller is the rotor speed of the generator, although it is also mentioned in [38] that the input signal can be other signals such as line current or line power, etc. Since the WF-SVC is installed with some distance from the DFIGs/IGs. It's unlikely the speed signal will be available in WF-SVC control unit, unless dedicated communication channel is added. Moreover, a wind farm usually consists of large amount of generators, the effectiveness and reliability of the method is questionable. Although in Chapter 5, the method of using speed signal from one of the three DFIGs as input to damp out SSR is tested effective with StatCom, the speed signal has to be communicated to the WF-SVC control unit. Therefore, a damping controller with an input signal easier to be acquired will be developed in this project.

In the literature mentioned above, only one wind power generation level is considered. However, wind generation level varies from time to time and the SSR characteristics are related to wind generation level. For instance, the resonance frequency at high and low generation might differ by several hertz. Therefore, this project should develop a controller effective for the whole wind power generation range.

The objective of this chapter is to design a damping controller for WF-SVC. The controller should take an input signal easier to be accessed and be effective for the whole possible wind power generation range. As a starting point, a description about the SVC modeling and its voltage control system used in the study will be given. Then the design procedure of SSR damping controller will be presented. Finally, the designed controller is validated by computer simulations with various operation conditions considered.

### 6.1 Modeling of SVC and its voltage control system

The SVC model adopted in this project is a generic model available in PSCAD library. This model represents a 12-pulse Thyristor Switched Capacitor (TSC) / Thyristor Controlled Reactor (TCR) system, as shown in Fig. 6-2 [39]. The model includes its own transformer, which consists of a star connected primary winding and dual secondary windings (one star and a one delta connected). The user may select the limits of absorption (inductive) and production (capacitive) of the SVC, as well as, the number of TSC stages. The MVA rating of each equal stage is determined by dividing the production limit by the number of stages.

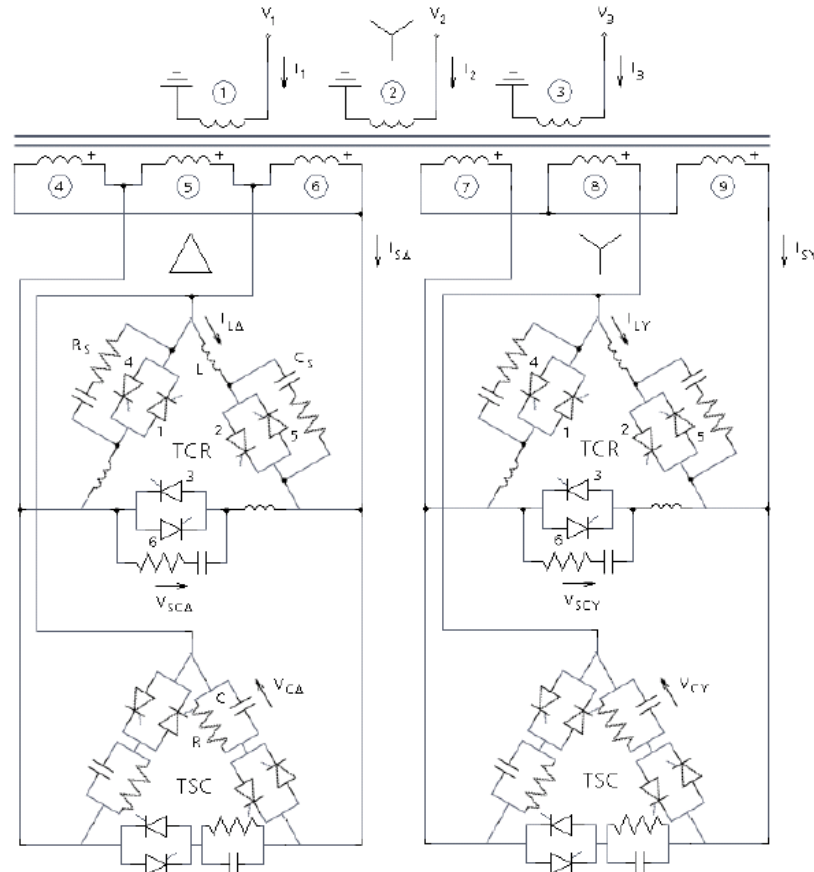


Fig. 6-2. Main circuit model of the SVC

Simulations with the SVC model and the system demonstrated in Fig. 6-1 show that the reactive power required to maintain the voltage at the SVC connection point at 1.02 pu varies from 80 MVar to 240 MVar when the wind generation level varies from 1% (10 MW, minimal value) to 73% (892 MW, maximal value). Therefore, the reactive power support is configured as 140 MVar fixed capacitor bank with -60/100 MVar SVC.

The voltage control system adopted is also a commonly used control method, which is depicted in Fig. 6-3. The RMS value of the voltage at the SVC connection point is controlled with a 3% droop. The voltage regulator is an integral controller. The output from the voltage regulator is the reference of the SVC susceptance. The 'TCR/TSC control' block distributes the susceptance between the TCR and the TSC. The block takes the reference of the SVC susceptance and the number of TSC stages currently in use as the inputs and calculates the desired non-linear susceptance of the TCR. Finally the block outputs the switching signal for TSC capacitor banks and the order of the firing angle for the TCR.

The integral gain is tuned based on the step response of the voltage at the SVC connection point in the investigated system. Fig. 6-4 shows the step response with different integral gains. The one with larger gain gives a shorter rise time (88 ms compared to 120 ms) but with bigger overshoot (16% compared to 8%) and longer settling time. In the simulation, the smaller gain (100) is chosen.

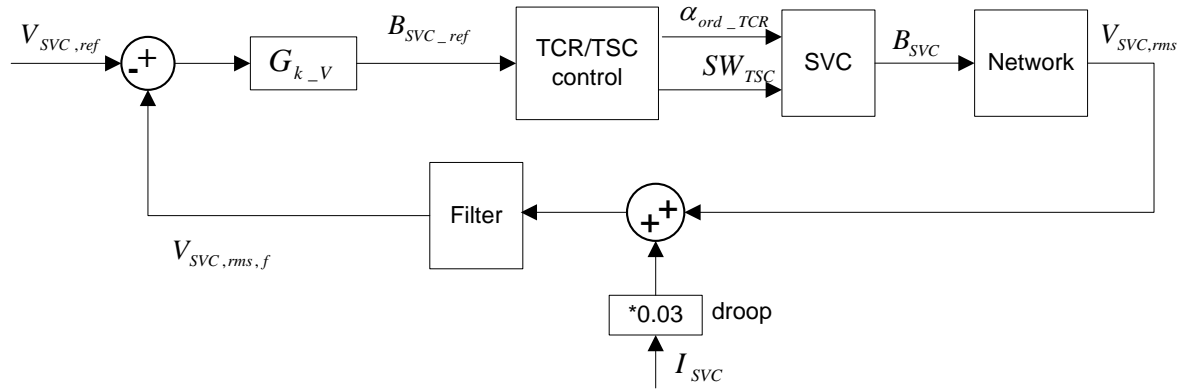


Fig. 6-3. SVC voltage control system

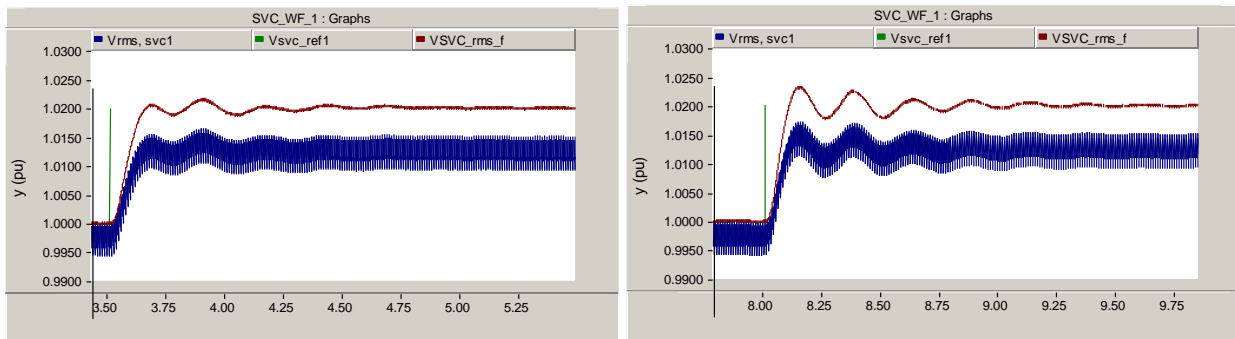


Fig. 6-4 Step responses with different integral gains: (a) 100; (b) 150. Green: voltage reference; blue: measured RMS value of the voltage; red: the filtered RMS value of the voltage with the droop considered.

## 6.2 Design of SSR damping controller

As discussed at the beginning of this chapter, the controller should take an input signal that is easier to be accessed and should be effective for the whole possible wind power generation range.

### 6.2.1 Control architecture

The input signal for the damping controller should be able to indicate the oscillations effectively and should be responsive to change in the susceptance of the SVC. Current or active power through the transmission line is a good choice. Also, the current measurement can be implemented locally in the SVC control system. In the following investigation, line power is used as an indication of oscillations and it can be calculated from the measured line current and bus voltage at the SVC connection point.

In order to extract the oscillation signals from the total line power signal, usually a HPF is employed in the damping controller. This works well if there is no sudden change in line power. In case of sudden power change, the controller will respond to the change unnecessarily due to

utilization of the HPF. In order to mitigate this adverse effect, the power signal should be processed. One optional method is to subtract a signal that is the delayed power signal as shown in Fig. 6-5.

$$\Delta P_{Line} = P_{Line} - P_{Line\_delayed} \quad (6-1)$$

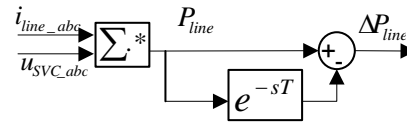


Fig. 6-5. Processing of power signal

Since the SSR oscillation frequency is around 27 Hz, a delay time of 0.00617 s is used in the controller design. As a result, the oscillatory signal in  $P_{Line}$  is passed to  $\Delta P_{Line}$  with a unity gain and about  $60^\circ$  phase in advance.

The output of the damping controller can be added either to the outer loop or to the inner loop of the SVC voltage control system. In this study, it's added to the inner loop as shown in Fig. 6-6.

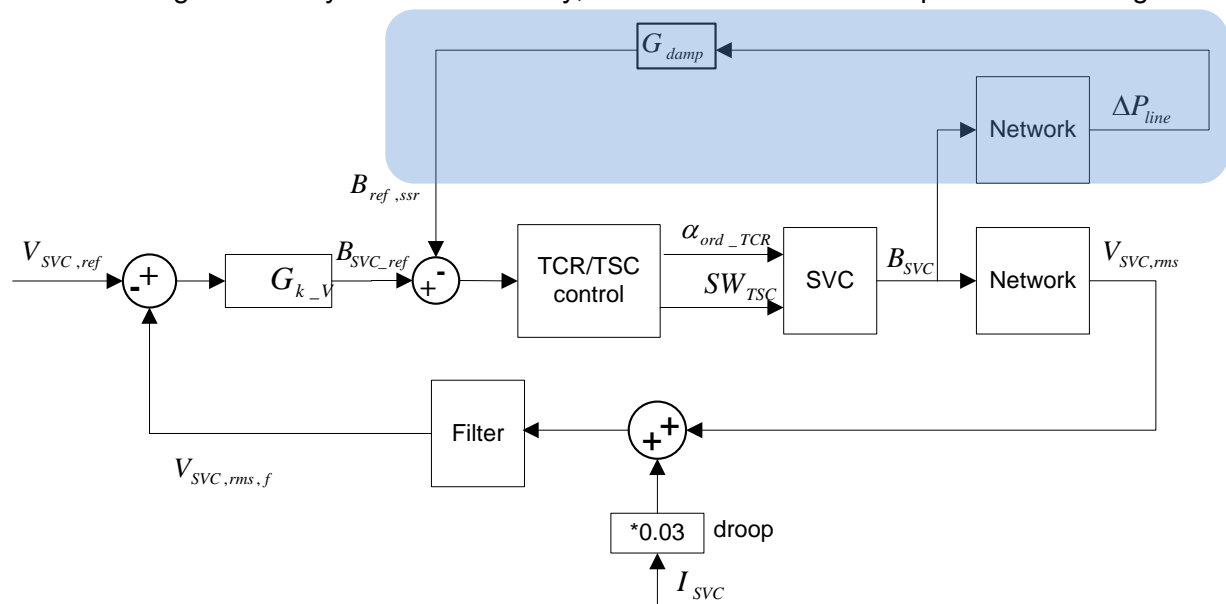


Fig. 6-6. SVC control system with the addition of damping controller

## 6.2.2 Controller design

When designing the damping controller, knowledge about the frequency characteristic of the plant, which is the frequency response of  $\Delta P_{Line}$  to SVC susceptance, will be helpful. To obtain the frequency response characteristic, sinusoidal signals with a certain magnitude and various frequencies (ranging from 1 Hz to 120 Hz) are injected to the reference signal of the SVC susceptance during normal operation, as shown in Fig. 6-7. The response of  $\Delta P_{Line}$  is recorded.

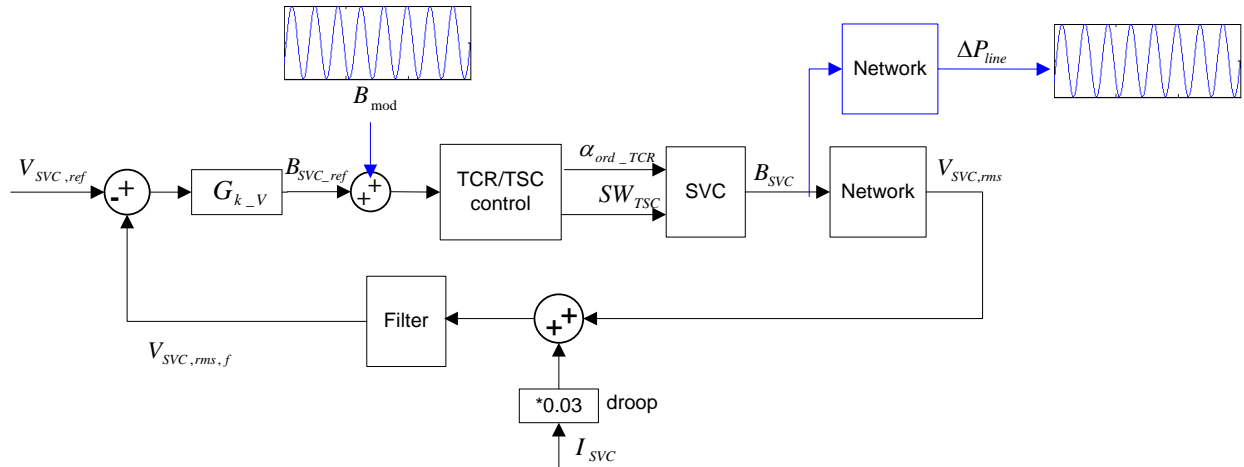


Fig. 6-7. Sinusoidal signal injection for obtaining frequency response of line power to SVC susceptance

As known from the SSR characteristic study, the SSR risk is lower with higher wind generation level and with smaller DFIG controller gains. Therefore, the sinusoidal signal injection is performed with the DFIGs operating at high power generation level (780 MW, 0.64 pu) and with smaller controller gains ( $k_{ir}=0.1$ ) for the DFIGs, so that a stable system operation can be achieved. Hence, the frequency characteristic only represents the operation condition specified above. The resonance frequency will vary slightly (by several Hertz) with varying wind generation level and DFIG controller gains, which should be taken into consideration in controller design. Nevertheless, if the SSR risk is decreased under the operation condition specified above, the risk should also be reduced under other operation conditions.

The frequency response characteristic is plotted in Fig. 6-8 (blue curves) with the system shown in Fig. 6-1. The compensation degree is 40% of the line reactance. The highest peak of the gain curve happens at 27 Hz, which is the SSR frequency.

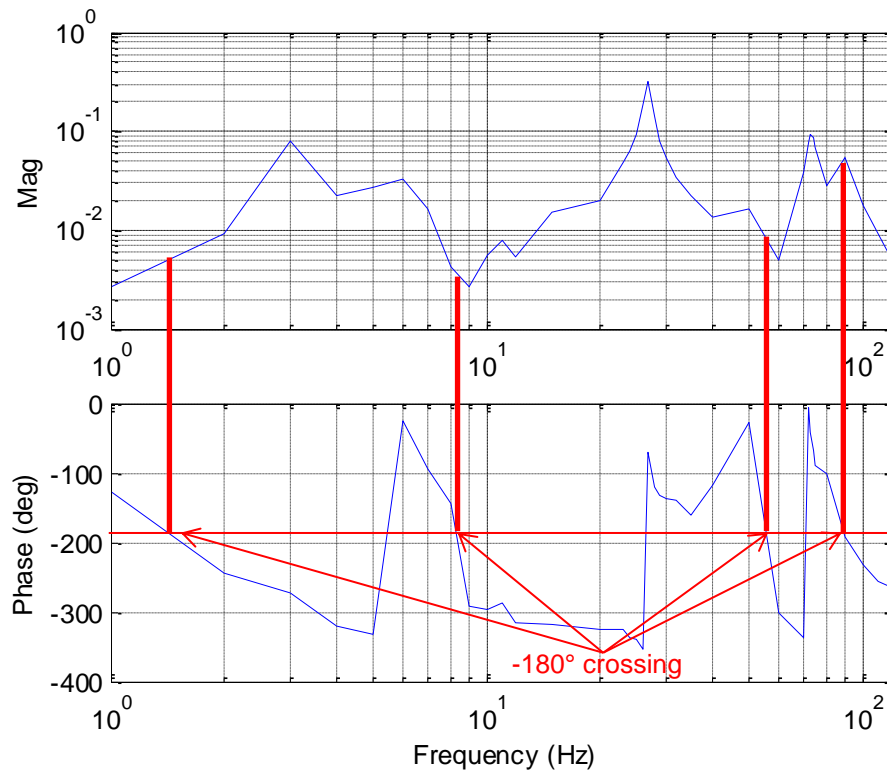


Fig. 6-8. Frequency response characteristic of line power to SVC susceptance

From damping control point of view, the control system shown in Fig. 6-6 can be re-drawn in Fig. 6-9. In the figure,  $G_{B\Delta P1} * G_{B\Delta P2}$  represents the closed-loop response of  $\Delta P_{Line}$  to the modulated reference of the SVC susceptance, which is illustrated in Fig. 6-7 and whose characteristic is depicted in Fig. 6-8. Assume there is a disturbance entering into the network, which is represented by signal 'd' in Fig. 6-9. Without damping controller, the response of  $\Delta P_{Line}$  to the disturbance will be

$$\Delta P_{Line} = G_{B\Delta P2} d \tag{6-2}$$

With the addition of the damping control, the response becomes:

$$\Delta P_{Line} = \frac{G_{B\Delta P2}}{1 + G_{B\Delta P1} G_{B\Delta P2} G_{damp}} d = \frac{G_{B\Delta P2}}{1 + G_{LP}} d \tag{6-3}$$

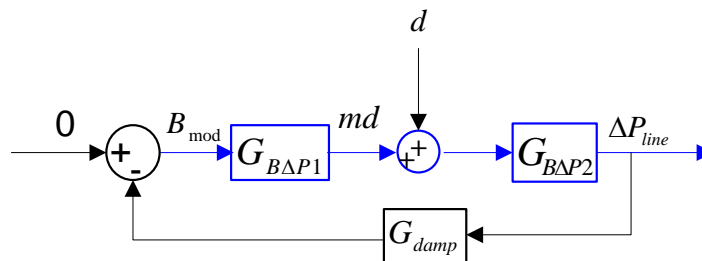


Fig. 6-9 Damping control system

It can be seen that the response to the disturbance will be attenuated if the loop gain  $|G_{LP}| = |G_{B\Delta P1} G_{B\Delta P2} G_{damp}|$  at critical frequency is large. The larger the loop gain is, the more the response will be attenuated.

Signal 'md' can be seen as produced by the damping control system to counteract the disturbance:

$$md = -\frac{G_{LP}}{1+G_{LP}} d \quad (6-4)$$

If the loop gain  $|G_{LP}| \gg 1$ , we will have  $md \approx -d$ .

For purpose of disturbance rejection, the loop gain should be as large as possible. However, as can be seen from Fig. 6-8, the phase angle curve crosses  $-180^\circ$  four times. In order to keep the system stable, the gain at each crossing should be smaller than one. Of all the four  $-180^\circ$  crossing frequencies, the gain at 90 Hz is the largest, which implies that this frequency will be the limiting factor on how much the loop gain can be increased. This is verified in the simulations in PSCAD. If the damping controller gain is too small, sub-synchronous will appear; with the increase of controller gain, the sub-synchronous oscillation will disappear; if the gain is further increased beyond a certain value, oscillations with frequency of about 90 Hz will appear.

With all the factors above taken into consideration, the damping controller can be designed. First of all, a HPF should be employed so that the steady state power is filtered out. Then lead-lag compensator will be employed to shape the loop frequency characteristic. The compensator should provide gain increase with leading phase angle around the SSR frequency. The leading phase will increase system stability. Meanwhile, the compensator should not increase the gain at frequency around 90 Hz. Therefore, a phase-lead compensator around SSR frequency together with a phase-lag compensator at frequency larger than SSR frequency will be employed, resulting in a controller as shown in (6-5)

$$G_{damp} = k_{damp} G_{HPF} G_{Lead} G_{Lag} \quad (6-5)$$

After tuning in PSCAD, the bode diagrams of the designed damping controller together with each of its three components are depicted in Fig. 6-10 with  $k_{damp} = 1$ .

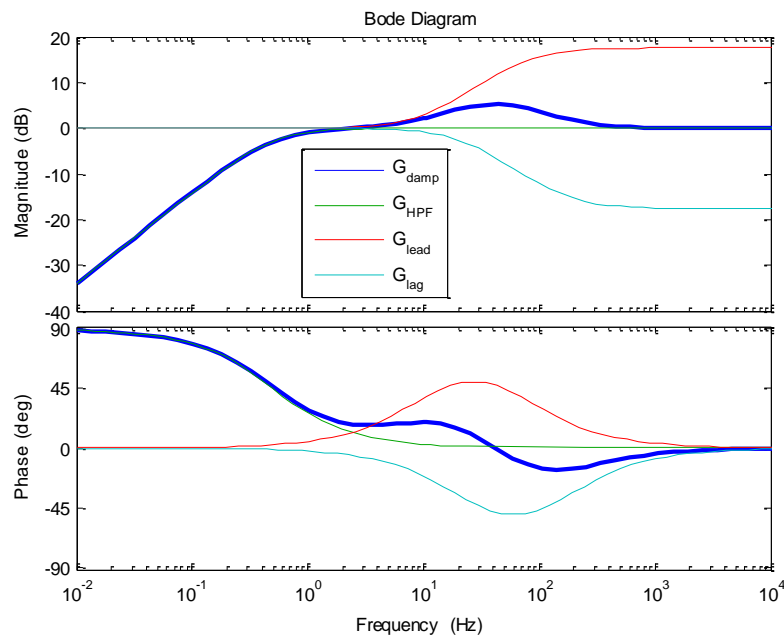


Fig. 6-10. Bode diagram of the damping controller (blue, bold) and its components ( $k_{damp} = 1$ )

The bode plot of the loop with damping controller is depicted in Fig. 6-11 with  $k_{damp} = 1$ .

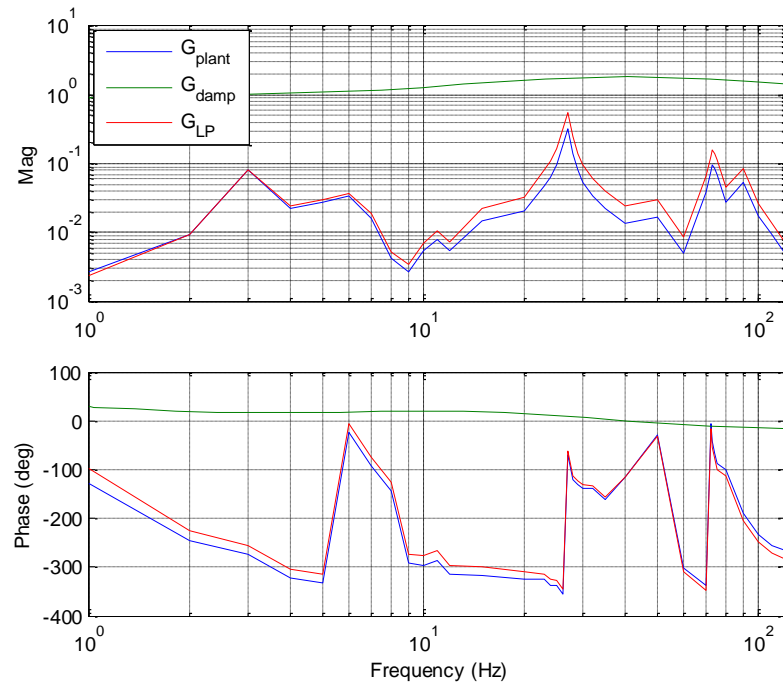


Fig. 6-11. Bode plot of loop transfer function with damping controller ( $k_{damp} = 1$ )

### 6.2.3 Gain adaptation

Due to the limiting factor on high gain employment imposed by 90 Hz response as described earlier, the controller gain is limited to a certain range. During gain tuning, it is found that the gain that is effective for SSR damping at high wind generation level might not be bigger enough for damping SSR at lower generation level. Therefore, the controller gain must be adapted to wind generation level in order to be effective for the whole possible wind generation range. This is essential for SSR damping in wind application and is a missing point in the research work reported in literature. In these research, usually only one operation point is investigated.

Gain adaptation can be done in one of the optional ways as shown in the shaded part of Fig. 6-13 and in (6-6):

$$k_{damp} = k_{damp0} + (a - P_{Line}) * b \quad (6-6)$$

This results in the following gain adaptation curve:

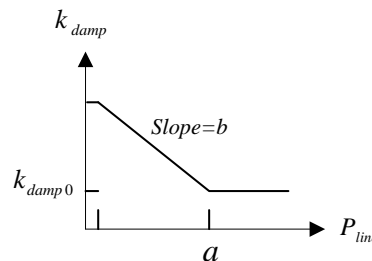


Fig. 6-12. Gain adaptation curve

Finally, the designed controller can be depicted in Fig. 6-13.

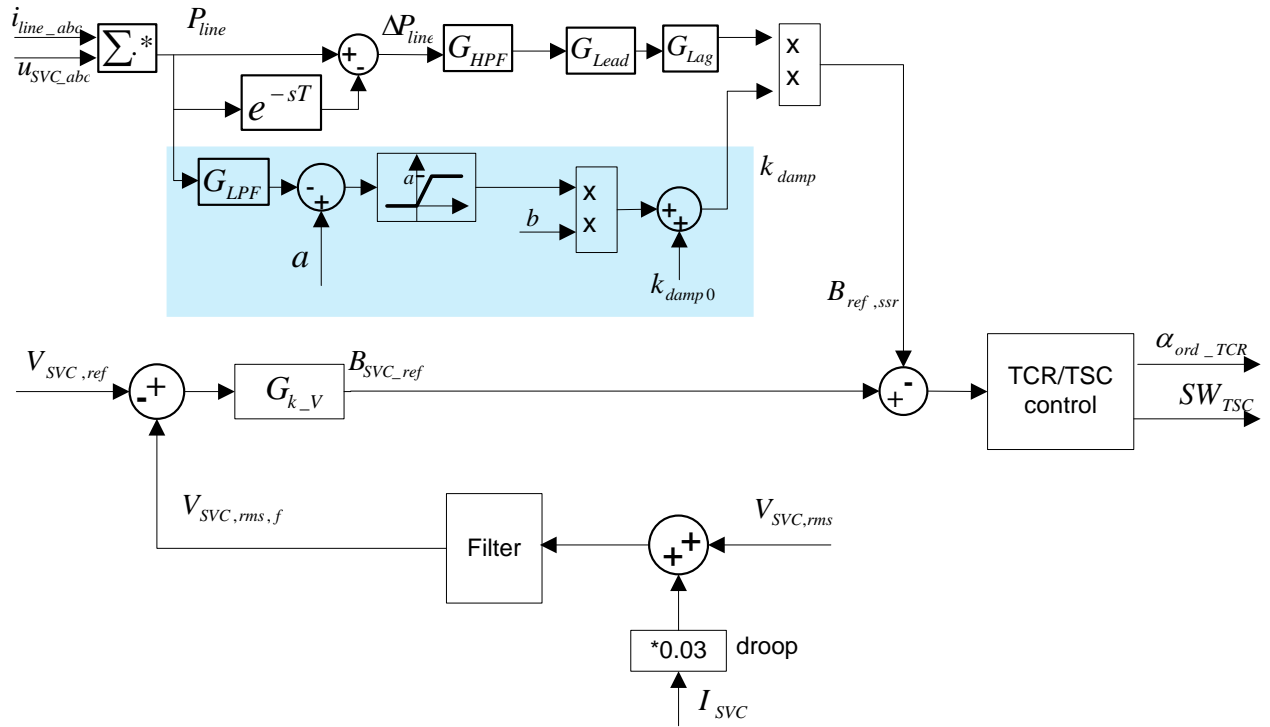


Fig. 6-13. Entire control system of SVC with damping control

### 6.3 Validation of developed SSR damping controller

The controller designed in previous section is for the system with 40% compensation and the reactive power support at wind farm terminal is configured as 140 MVar fixed capacitor bank with -120/100 MVar SVC. The effectiveness of the controller will be investigated in this section.

#### 6.3.1 Effectiveness for SSR damping

Simulations have been done in PSCAD with the controller shown in Fig. 6-13 for validation in the system. In the simulation, the gain adaptation parameters are set to:

$$a = 420 \text{ (MW)}; b = 0.06 \text{ (pu/MW}^2\text{)}; k_{damp0} = 28 \text{ (pu/MW)} \quad (6-7)$$

Fig. 6-14 shows how the SSR was damped out when the SSR situation is the most severe (high DFIG controller gain and lowest wind power output). The oscillation started building up shortly after the damping controller gain was reduced at 1 s. At 2 s, the damping controller gain was increased and the oscillation was damped out shortly.

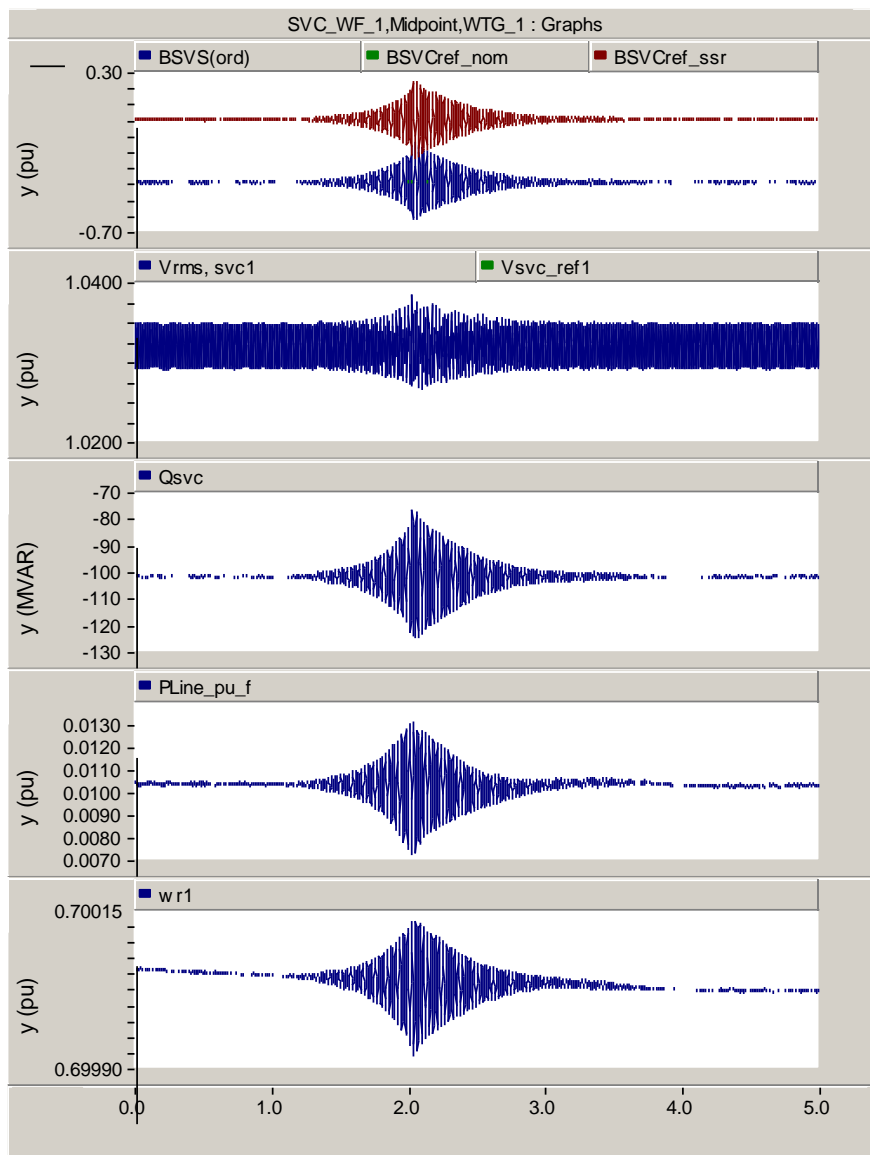


Fig. 6-14. Damping of SSR at the lowest wind generation level (highest SSR risk)

### 6.3.2 Effectiveness for the whole wind generation level range

Fig. 6-15 shows that SSR did not occur for the whole wind generation level range (lowest considered is 0.01 pu). The DFIG controller gain is set to the high value ( $k_{ir}=0.3$ ).

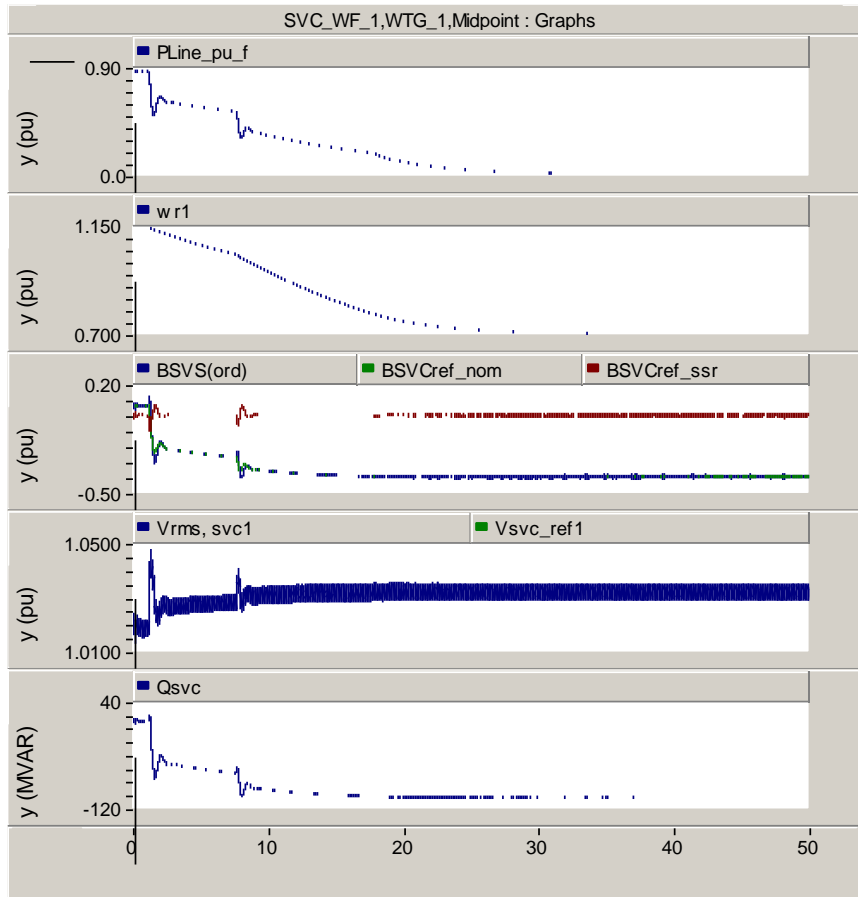


Fig. 6-15. Simulation for whole wind generation range

### 6.3.3 Effectiveness for different compensation levels

The controller is designed for the system with a compensation degree of 40%. Since the SSR problem is more severe with higher compensation degree, SSR damping controller designed for a certain compensation degree will unlikely be equally effective for higher compensation degree. Should higher compensation level be considered, the controller should be designed for the highest compensation level.

Simulation in PSCAD shows that the designed controller works also for less compensated system. Fig. 6-16 shows how the system responded when the compensation degree changed from 40% to 30% and then to 20%. Change of compensation degree caused transients in the system. Oscillations at SSR frequency were stimulated, but were damped out shortly. In this simulation, the compensation degree change happened at high wind generation level. Fig. 6-17 shows the simulation in case the compensation degree changes from 40% to 30% when the wind generation level is the lowest, implying the most severe SSR situation. It can be seen that it takes longer time for the oscillations to be damped out at low wind generation level.

Fig. 6-18 shows that the controller worked with a compensation degree of 30% for the whole wind generation level range. In the first 5 seconds, the compensation degree was changed. At 5 s, the wind speed was reduced from 10.59 m/s to 8 m/s. The wind speed was further reduced to 4 m/s at 10 s.

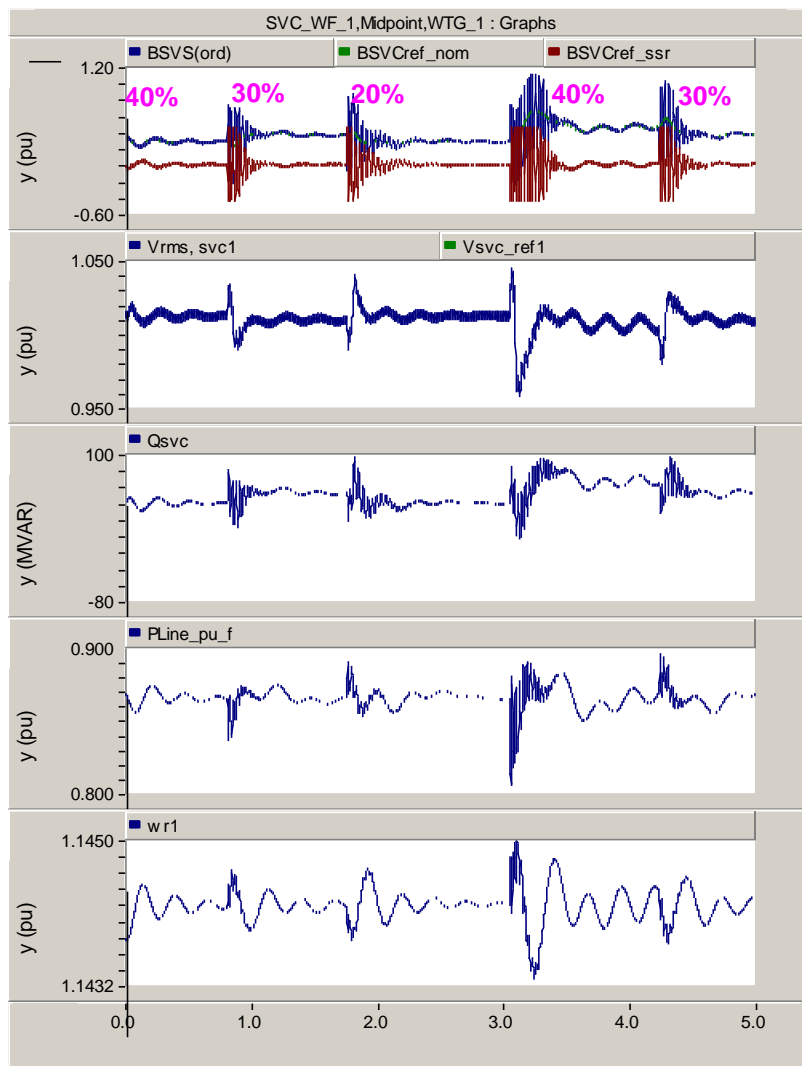


Fig. 6-16. Change of compensation level at high wind generation level (low SSR risk)

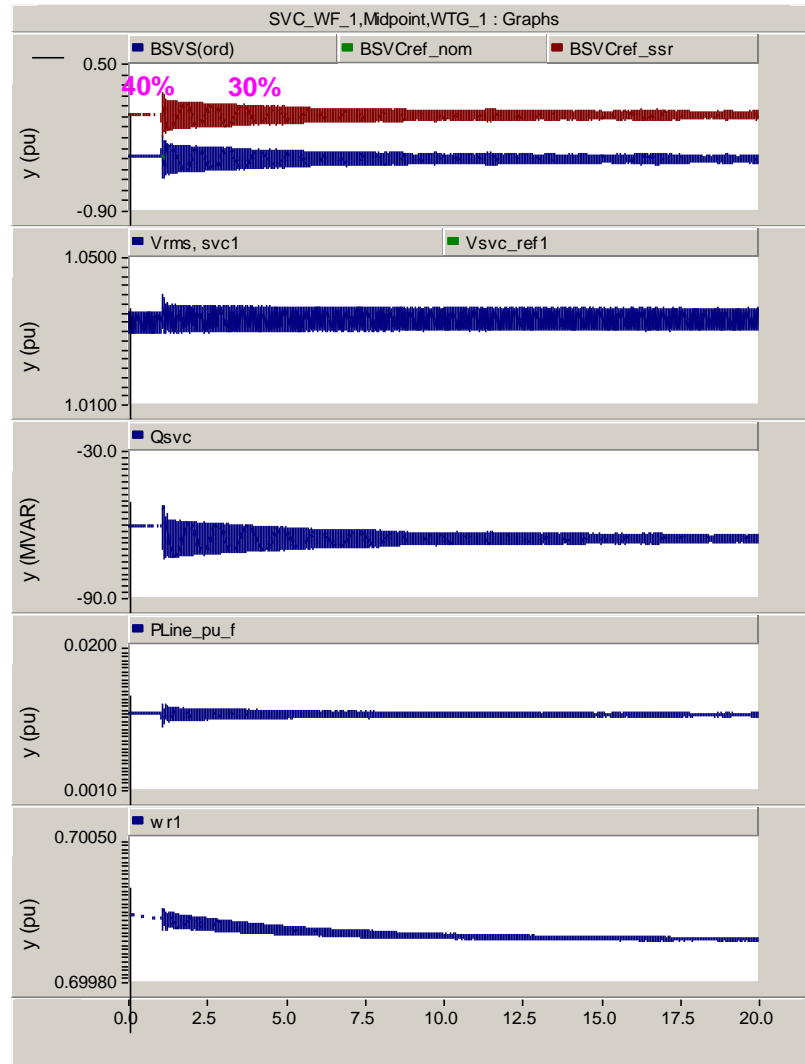


Fig. 6-17. Change of compensation level at low wind generation level (high SSR risk)

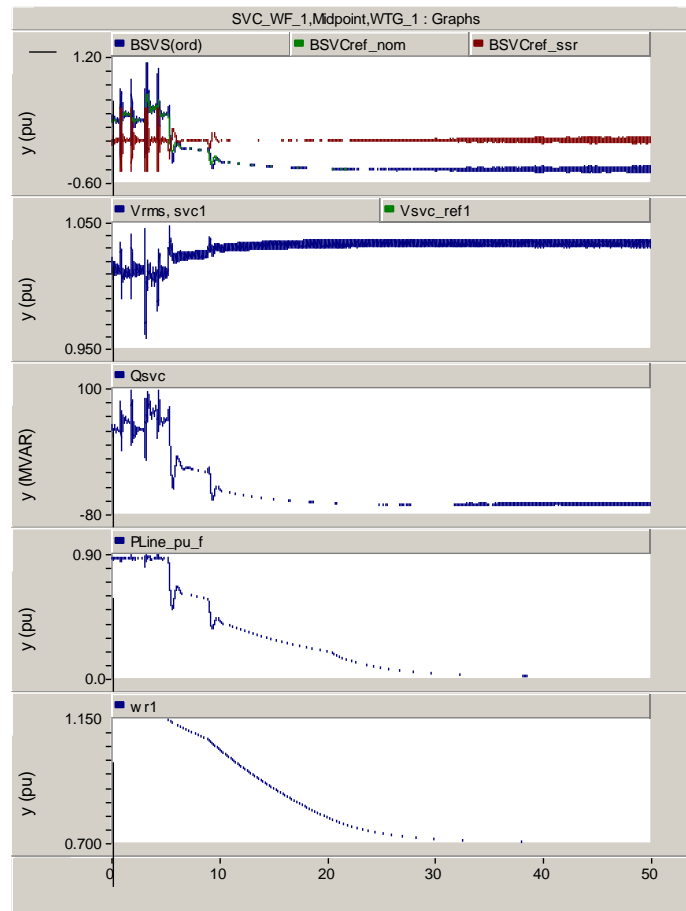


Fig. 6-18. Simulation for whole wind generation level range with a compensation degree of 30%

#### 6.3.4 Effectiveness for DFIGs with different control parameters and operating at different generation levels

As known from the SSR characteristic study, SSR is closely related to DFIG control parameters, especially the control parameter of the rotor-side converter. Therefore, the effectiveness of the controller with respect to the case when the three DFIGs have different control parameters and operate at different generation levels is investigated through simulations in PSCAD. The results plotted in Fig. 6-19 show that it is effective, as expected.

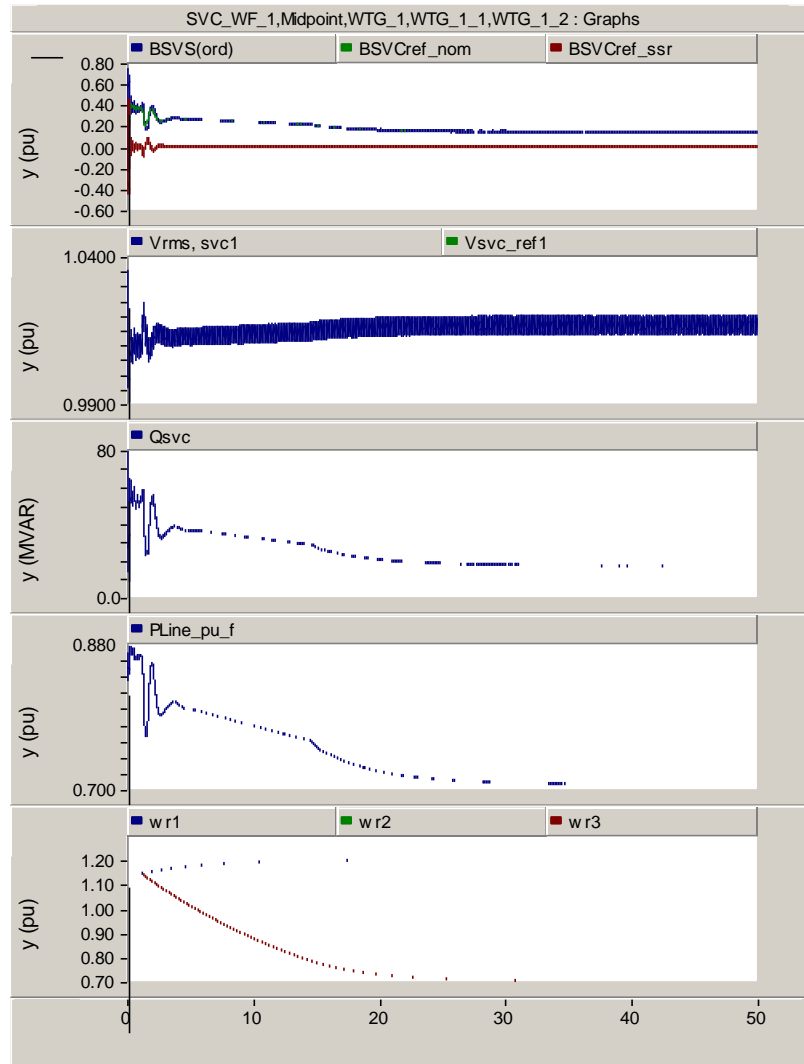


Fig. 6-19 DFIGs with different control parameters ( $k_{ir}=0.1, 0.2, 0.3$  for three DFIGs) and operating at different generation levels (100%, 73%, 1% for three DFIGs)

### 6.3.5 Required rating

The controller design and simulations were based on a reactive power configuration of 140 MVar fixed capacitor with -120/100 MVar SVC. The configuration is reasonable and the rating of SVC is sufficient for SSR damping. It is justified to draw the following conclusion: a reasonable SVC rating that can meet the requirement on reactive power support is sufficient for SSR damping purpose.

## 6.4 Summary

This chapter presents the feasibility of SSR damping by WF-SVC. The following conclusions can be drawn:

- It is feasible to damp SSR by WF-SVC.
- A controller design method is presented.

- The developed controller is verified effective for the whole wind generation level range no matter the three DFIGs are operating at the same or different generation levels and no matter the three DFIGs have the same or different control parameters.
- Gain adaptation is essential for the controller to be effective for the whole wind generation level range.
- Extra measurement (transmission line current) is required for SVC damping control.
- A reasonable SVC rating that meets the requirement on reactive power compensation is sufficient for SSR damping, which is -120/100 Mvar (nominal transmission power: 890 MW)

## 7 SUB-SYNCHRONOUS RESONANCE MITIGATION BY THYRISTOR-CONTROLLED SERIES CAPACITOR

The goals of this chapter are to have a deeper understanding of sub-synchronous resonance phenomena in presence of series compensation and wind farm consisting of DFIGs (double-feed induction generator) and to investigate feasibility of SSR mitigation by thyristor controlled series capacitor (TCSC).

This chapter presents the results from the feasibility study of SSR (sub-synchronous resonance mitigation) mitigation by TCSC. The report is structured as following:

TCSC main circuit and its control system are introduced in Section 7.1. Section 7.2 presents PSCAD modeling of TCSC and transfer function (TF) model of the system with DFIG, fixed capacitor, and TCSC. In Section 7.3, issues in system compensated by pure TCSC are investigated. Section 7.4 investigates system compensated by combined TCSC and FC with SSR risk evaluated and damping control developed. Conclusions are drawn in the last section.

### 7.1 Introduction to TCSC and its control system

#### 7.1.1 TCSC main circuit

A TCSC consists of a capacitor and an inductor in a parallel branch as shown Fig. 7-1 (a). The conduction of the inductor is controlled by two anti-parallel thyristors marked with F (forward) and R (reverse). Typical waveforms of the line current  $i_L$ , valve current  $i_V$ , and TCSC voltage  $u_{TCSC}$  are shown in Fig. 7-1 (b). During the period when  $u_{TCSC}$  is negative and  $i_L$  is positive, the TCSC capacitor is being charged and only the reverse thyristor can be triggered. When the reverse thyristor is conducting, a valve current is circulating within the TCSC circuit, adding an additional charging current to the capacitor. The additional charge causes an additional increase of the capacitor voltage. The net effect as seen from the line side is the TCSC voltage is boosted.

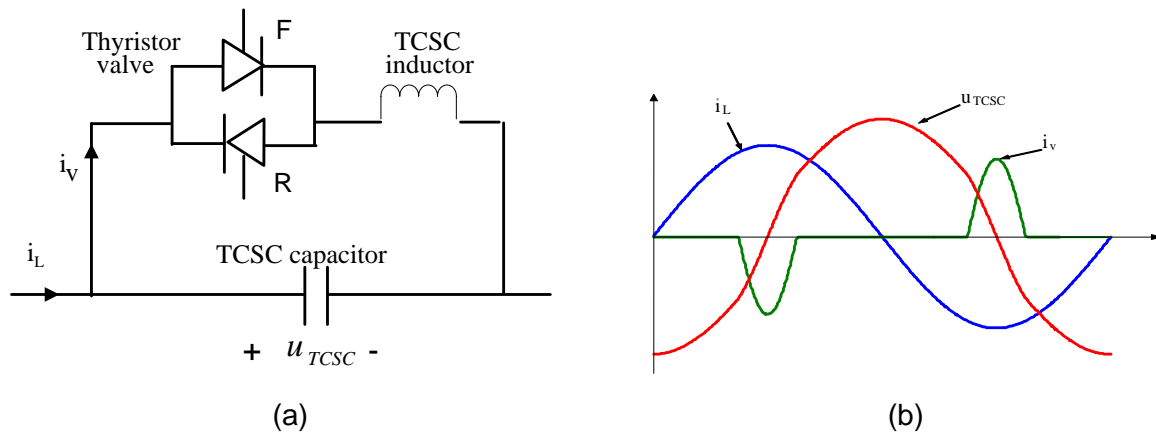


Fig. 7-1 TCSC main circuit and typical waveform

The inductor and the capacitor form a resonance circuit with a resonance frequency of

$$\omega_0 = \frac{1}{\sqrt{L_{TCSC}C_{TCSC}}} \quad (7-1)$$

The ratio of  $\omega_0$  to nominal frequency  $\omega_N$  is a design parameter for TCSC and is defined as

$$\lambda = \frac{\omega_0}{\omega_N} \quad (7-2)$$

For proper operation of TCSC,  $\lambda$  should be larger than 1, typically between 2 and 4. Larger  $\lambda$  will result in larger peak in the valve current and higher distortion in capacitor voltage.

When a TCSC is in operation, the ratio of the boosted reactance  $X_{TCSC}$  (or apparent reactance) at nominal frequency to the non-boosted reactance  $X_{C\_TCSC}$  of TCSC capacitor at nominal frequency is defined as boost factor  $k_B$ :

$$k_B = \frac{X_{TCSC}}{X_{C\_TCSC}} \quad (7-3)$$

### 7.1.2 TCSC control system

The TCSC control scheme adopted in this project is synchronous voltage reversal (SVR) control scheme. The control system is depicted in Fig. 7-2. The control system measures line current and voltage across the TCSC capacitor.

A phase-locked-loop (PLL) is employed working on line current so that the current vector aligns with the d axis of the rotating coordinate system. A phasor estimation (PE) block estimates phasors of line current and capacitor voltage and then the apparent impedance of the TCSC. The imaginary part of the apparent impedance is then divided by the non-boosted reactance of the TCSC capacitor, giving the measured boost factor. The error between the reference and measured boosted factor is delivered to a boost controller. The output of the boost controller is the angular displacement  $\Delta\varphi_c$  (or  $\theta_{k_B\_reg}$ ) of the equivalent instantaneous voltage reversal from their equilibrium positions. The angular displacement together with the PLL angle is sent into the 'SVR triggering pulse generation' block, which calculates the exact triggering time and generates triggering pulses.

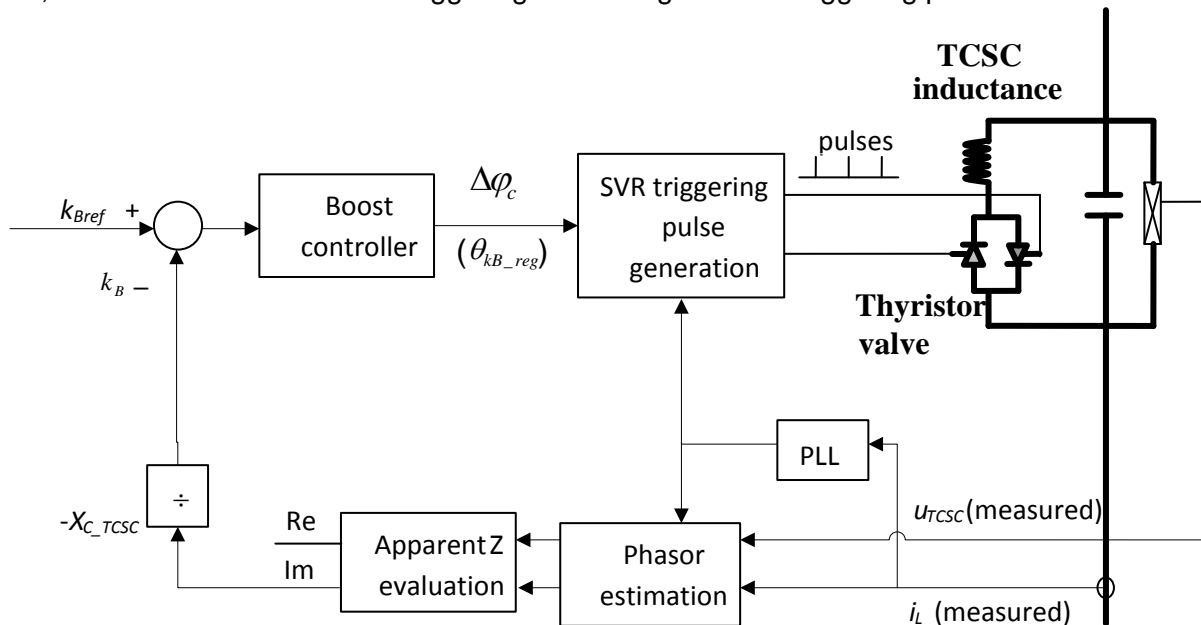


Fig. 7-2 TCSC and its control system

In SVR control, the relation between boost factor and angular displacement can be approximated using TF representation as in (7-4):

$$G_{\theta_{k_B\_reg} k_B}(s) = \frac{k_B(s)}{\theta_{k_B\_reg}(s)} = \frac{16 f_n}{\pi s} \quad (7-4)$$

The main difference between SVR control and conventional control is the output from the boost controller. Boost controller in conventional control gives angle  $\beta$  directly, where  $\beta$  is related to triggering angle  $\alpha$  in the following way:

$$\beta = \pi - \alpha \quad (7-5)$$

$\beta$  is related to boost factor such that:

$$k_B = 1 + \frac{2}{\pi} \frac{\lambda^2}{\lambda^2 - 1} \left[ \frac{2 \cos^2 \beta}{\lambda^2 - 1} (\lambda \tan \lambda \beta - \tan \beta) - \beta - \frac{\sin 2\beta}{2} \right] \quad (7-6)$$

It can be seen that an advantage of SVR control over conventional control is that the relation between boost factor and the angular displacement is linear whereas that between boost factor and angle  $\beta$  is nonlinear.

## 7.2 PSCAD model and transfer function model of TCSC and the compensated system

### 7.2.1 Modeling of TCSC in PSCAD

A TCSC model in PSCAD was developed. The model consists of two blocks for main circuit and control system respectively, as shown in Fig. 7-3. Each block is a component defined with scripts and with Fortran codes provided in separate files. SVR control scheme is implemented in the control system block. The parameters for boost controller, PLL and PE can be defined in the parameter field of the block. There are two entries accessible to users for control purpose: kBref and dphiC. Through kBref entry, the reference value can be modulated. Through dphiC entry, the angular displacement mentioned above can be modulated. In this research it is desired to implement control function of 'dphiC' in the script and Fortran code of the control block.

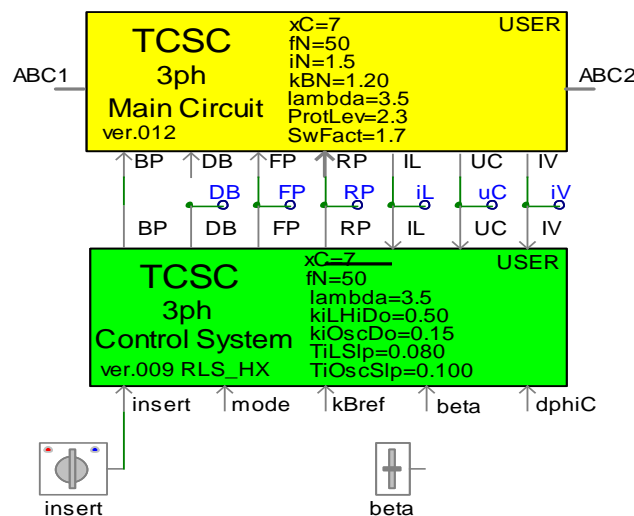


Fig. 7-3 TCSC model in PSCAD

### 7.2.2 Investigated system with TCSC connected

The investigated system defined in Chapter 3 is compensated with FC (fixed capacitor) only. Now assume the system is compensated by TCSC combined with FC. The TCSC is dimensioned so that the sum of the reactance of the FC and the TCSC apparent reactance (at nominal frequency and at nominal boost level) equals to 40% of the line reactance. The diagram of the system with TCSC is shown in Fig. 7-4.

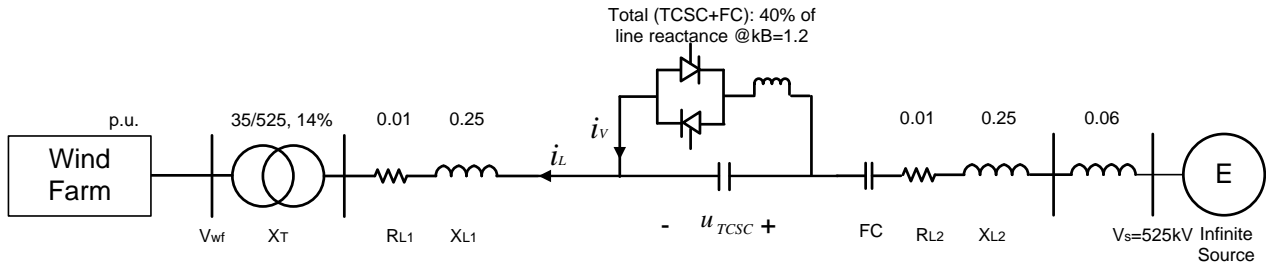


Fig. 7-4 Investigated system compensated by TCSC and FC

The wind farm is modeled as three lumped DFIGs together with three  $\pi$  line segments representing the collection network within the wind farms.

In case of stiff network, i.e., the line current is not affected by TCSC voltage, the boost factor is only dependent on the angular displacement. However, when a TCSC is connected to a system with finite strength, the TCSC voltage will affect the line current, which in turn will affect the TCSC voltage. The line current affects TCSC voltage through two different paths. Firstly, the line current will impact the TCSC voltage directly. Secondly, the PLL angle will be affected by line current and it will impact TCSC voltage in the same way as the angular displacement  $\theta_{k_B,reg}$  commanded by the boost controller. In addition, the line current change will also affect measurement result of  $k_B$ . The whole control system is shown in Fig. 7-5.

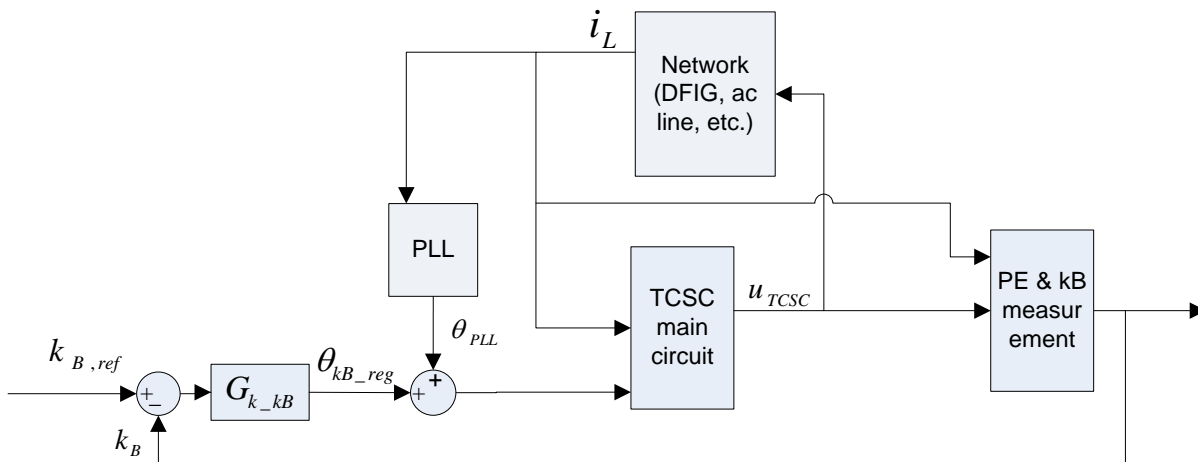


Fig. 7-5 Control system of the investigated system

### 7.2.3 Transfer function model of the investigated system

The whole system including TCSC can be depicted in form of TFs as in Fig. 7-6.

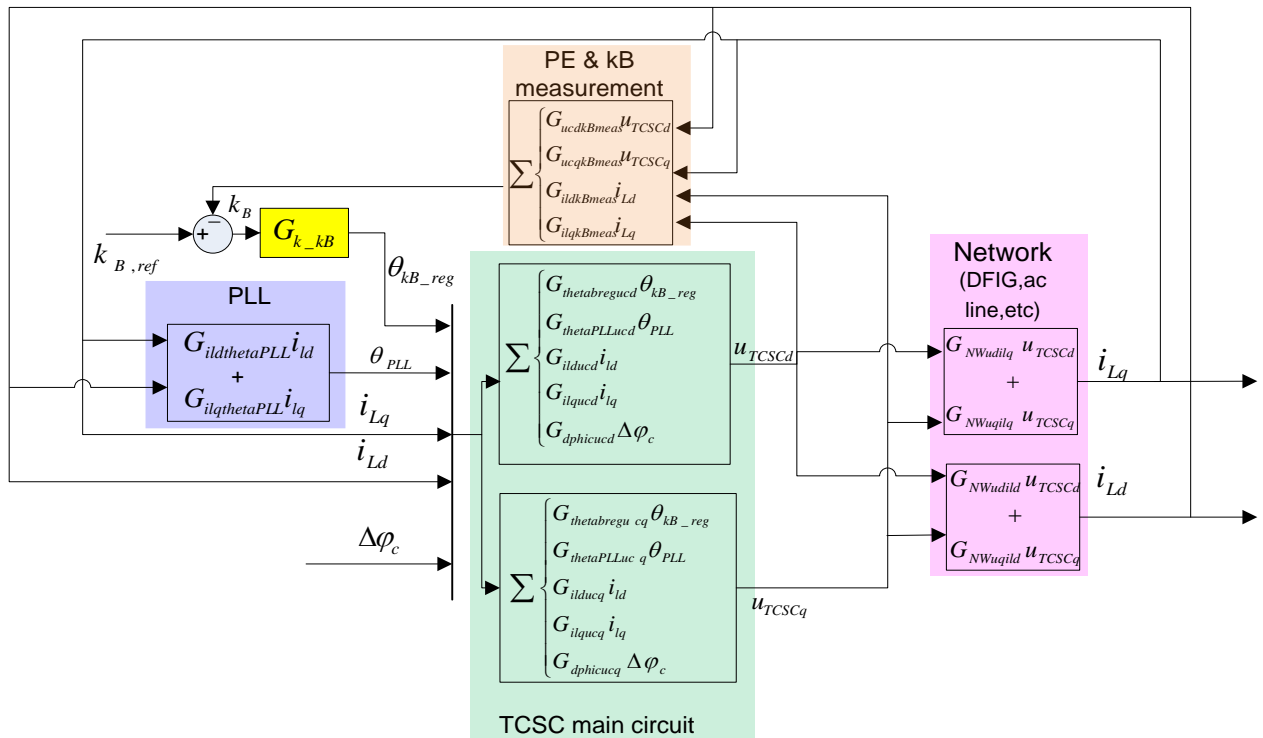


Fig. 7-6 TF model of the investigated system

In the figure, there are five shaded areas: TCSC main circuit in green, network (including DFIG, transmission line, voltage source, etc.) in pink, phasor estimation and kB measurement in orange, PLL in blue and boost controller in yellow. The control blocks are represented in terms of the d and q components in the rotating coordinate system in which the current vector aligns with the d axis.

There is one signal  $\Delta\varphi_c$  (corresponding to  $\phi_c$  in Fig. 7-3) into the TCSC main circuit. It can be set to zero in ordinary application. But this signal adds flexibility for other control purpose for example damping control of SSR, which will be investigated in the following part of the report.

The TFs shown in the blocks of 'PLL', 'PE&kB measurement' and 'TCSC main circuit' in last figure can be derived from the theoretical analysis of the processes. Detailed procedure will not be presented in the report. All the analysis is performed in Matlab.

The TFs (from TCSC voltage to line current) in the block of 'Network' can be derived using the equivalent circuit as shown in Fig. 7-7 for nominal frequency and Fig. 7-8 for sub-synchronous frequency. The difference between these two circuits is the presence of the infinite voltage source in nominal frequency circuit. Since the PLL works on nominal frequency component of the DFIG terminal voltage, signals in the sub-synchronous frequency diagram is non-dc quantities.

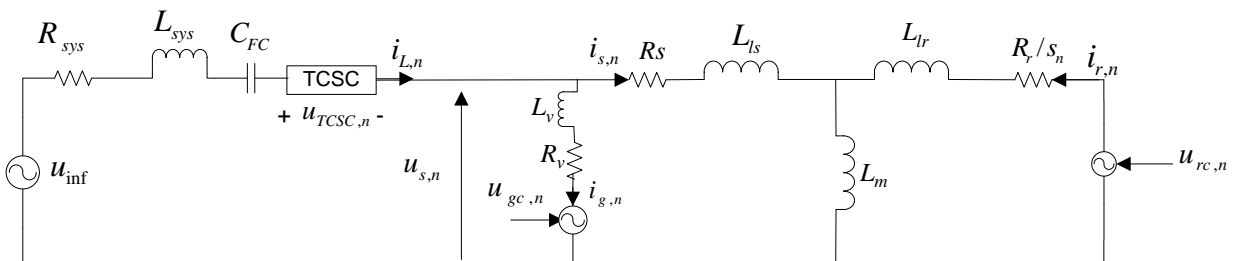


Fig. 7-7 Equivalent circuit of investigated system (nominal frequency)

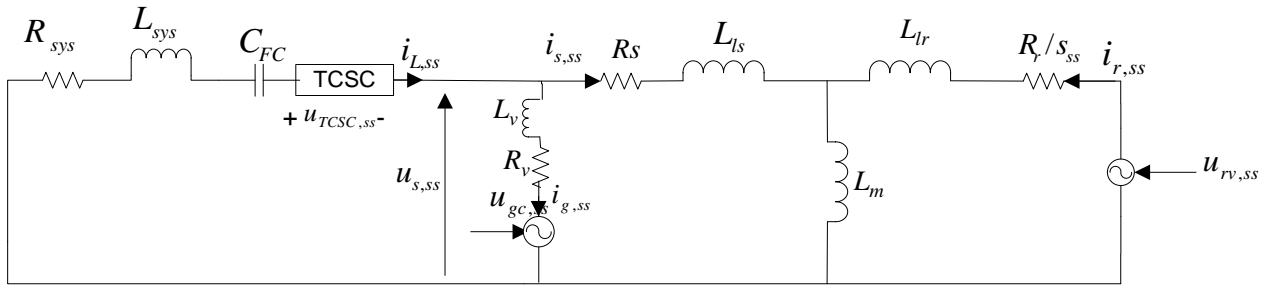


Fig. 7-8 Equivalent circuit of investigated system (sub-synchronous frequency)

### 7.2.4 Connection between TCSC control system and DFIG control system

The control system of DFIG employs a PLL working on the DFIG terminal voltage such that the voltage vector aligns with the d axis. The PLL of TCSC control system works on line current such that the line current vector aligns with the d axis. In real cases, these two coordinate will very unlikely coincide, as shown in Fig. 7-9. If analysis should be performed for such a system, there must be an angle transform between these two coordinate systems:

$$\overline{u_{TCSC}^{Tdq}} = \overline{u_{TCSC}^{dq}} e^{-j\varphi_{iL}} \quad (7-7)$$

Where  $\overline{u_{TCSC}^{Tdq}}$  is the vector of TCSC voltage in the rotating coordinate of TCSC control system,  $\overline{u_{TCSCn}^{dq}}$  is vector of TCSC voltage in the rotating coordinate of the DFIG control system, and  $\varphi_{iL}$  is the phase angle of line current in DFIG rotating coordinate.

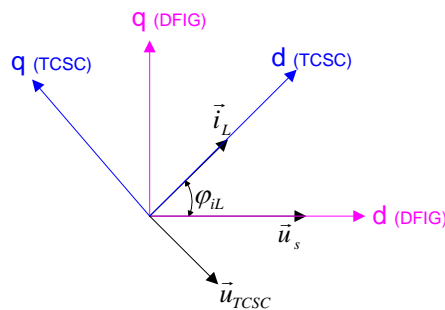


Fig. 7-9 Coordinate systems of DFIG and TCSC control systems

The transformation between these two coordinate systems makes the analysis very complicated. Therefore, when making TF analysis in this project, the following points are assumed:

- The DFIGs are well controlled such that the output reactive power is zero (commonly used strategy for reactive power control)
- The shunt capacitance of the  $\pi$  section is negligible
- There is no reactive power support device installed at wind farm terminal

Based on those assumptions, the line current is pure active with respect to DFIG terminal voltage and these two coordinate systems coincide.

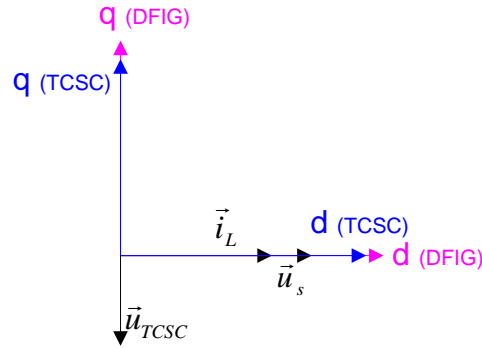


Fig. 7-10 Coordinate systems of DFIG and TCSC control systems based on assumptions

Of course these simplifications will result in certain discrepancy between the theoretical analysis and real application. However, the conclusion from the analysis should reflect the general trends how the control systems interact and how certain variables affect the control performance.

### 7.3 Investigation on System compensated by pure TCSC

#### 7.3.1 Issues identified

For system compensated by pure TCSC, there is no risk of resonance between line reactance and capacitor as in FC case. The reason is that by SVR control, the TCSC apparent reactance in sub-synchronous range is inductive [41-49].

However, interaction between TCSC and DFIG control systems might happen if control speeds in different loops do not match. The interaction may cause power oscillations. The mis-match could be between DFIG and TCSC controllers or among different DFIG control loops. This phenomenon has been observed in PSCAD simulations and can be analyzed using TFs shown in Fig. 7-6 and Fig. 7-7 for the nominal frequency circuit.

#### 7.3.2 Analysis of interaction between DFIG and TCSC control systems

##### 7.3.2.1 Derivation of the closed-loop TF of kB control

From [22], the stator current is determined by terminal voltage and rotor current as shown as follows:

$$\begin{cases} i_{sna}(s) = G_{usndisna}(s)u_{sna}(s) + G_{usnqisna}(s)u_{snq}(s) + G_{irnqisna}(s)i_{rq}(s) + G_{irndisna}(s)i_{rnd}(s) \\ i_{snq}(s) = G_{usndisnq}(s)u_{sna}(s) + G_{usnqisnq}(s)u_{snq}(s) + G_{irndisnq}(s)i_{rq}(s) + G_{irnqisnq}(s)i_{rnq}(s) \end{cases} \quad (7-8)$$

In these equations

$$\left\{ \begin{array}{l}
 G_{usndisnd}(s) = \frac{i_{snd}(s)}{u_{snd}(s)} = \frac{R_s + sL_s}{s^2 L_s^2 + 2sR_s L_s + R_s^2 + \omega^2 L_s^2} \\
 G_{usnqisnd}(s) = \frac{i_{snd}(s)}{u_{snq}(s)} = \frac{\omega L_s}{s^2 L_s^2 + 2sR_s L_s + R_s^2 + \omega^2 L_s^2} \\
 G_{irndisnd}(s) = \frac{i_{snd}(s)}{i_{rnd}(s)} = -\frac{s^2 L_m L_s + sL_m R_s + \omega^2 L_s L_m}{s^2 L_s^2 + 2sR_s L_s + R_s^2 + \omega^2 L_s^2} \\
 G_{irnqisnd}(s) = \frac{i_{snd}(s)}{i_{rnq}(s)} = \frac{\omega L_m R_s}{s^2 L_s^2 + 2sR_s L_s + R_s^2 + \omega^2 L_s^2} \\
 G_{usndisnq}(s) = \frac{i_{snq}(s)}{u_{snd}(s)} = \frac{-\omega L_s}{s^2 L_s^2 + 2sR_s L_s + R_s^2 + \omega^2 L_s^2} = -G_{usnqisnd}(s) \\
 G_{usnqisnq}(s) = \frac{i_{snq}(s)}{u_{snq}(s)} = \frac{R_s + sL_s}{s^2 L_s^2 + 2sR_s L_s + R_s^2 + \omega^2 L_s^2} = G_{usndisnd}(s) \\
 G_{irnqisnq}(s) = \frac{i_{snq}(s)}{i_{rnq}(s)} = -\frac{s^2 L_m L_s + sL_m R_s + \omega^2 L_s L_m}{s^2 L_s^2 + 2sR_s L_s + R_s^2 + \omega^2 L_s^2} = G_{irndisnd}(s) \\
 G_{irndisnq}(s) = \frac{i_{snq}(s)}{i_{rnd}(s)} = -\frac{\omega L_m R_s}{s^2 L_s^2 + 2sR_s L_s + R_s^2 + \omega^2 L_s^2} = -G_{irnqisnd}(s)
 \end{array} \right. \quad (7-9)$$

Since the PLL works on terminal voltage, the impact of disturbances in the grid on the stator current can be seen as impact through the terminal voltage.

From the circuit we can get:

$$u_{sn} = u_{inf} - R_{sys} i_{Ln} - L_{sys} \frac{di_{Ln}}{dt} - u_{TCSC} - u_{FC} \quad (7-10)$$

$$\overrightarrow{\Delta u_{sn}^{dq}} = -\overrightarrow{\Delta u_{TCSC}^{dq}} \quad (7-11)$$

The closed-loop TF from TCSC voltage to stator current can then be derived from the control diagram shown in Fig. 7-11. The TF from d component of TCSC voltage to d component of stator current is denoted as  $G_{NWuTCSCdisd}$ . Similarly, denote the other three as  $G_{NWuTCSCdisq}$ ,  $G_{NWuTCSCqisd}$ , and  $G_{NWuTCSCqisq}$ .

The closed-loop TF from TCSC voltage to rotor current can also be derived from Fig. 7-11. They are denoted as  $G_{NWuTCSCdird}$ ,  $G_{NWuTCSCdirq}$ ,  $G_{NWuTCSCqird}$ , and  $G_{NWuTCSCqirq}$ .

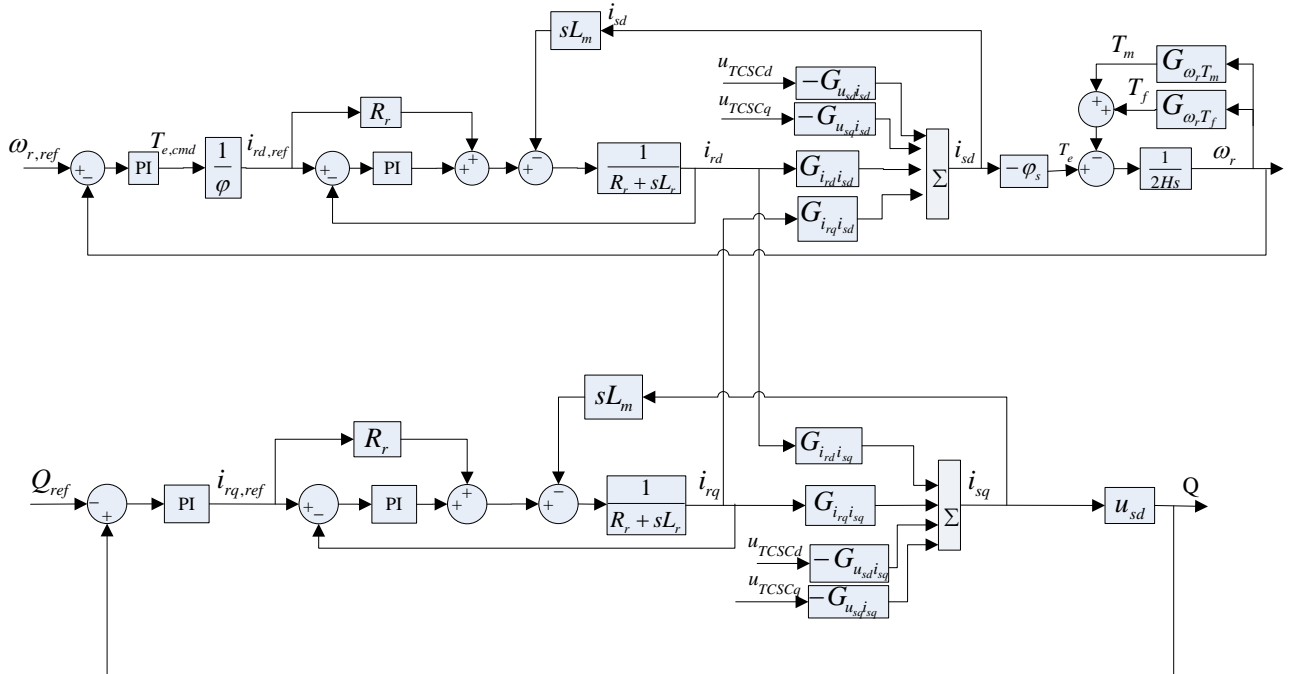


Fig. 7-11 DFIG control system (nominal frequency)

Since the grid-side converter controls the dc link voltage, change in the active current of rotor-side converter will impact on the active current of the grid-side converter. The relation of these two current can be derived from the diagram shown in Fig. 7-12.

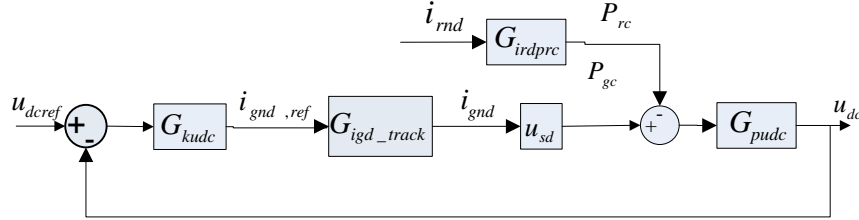


Fig. 7-12 Impact of rotor active current on grid-side converter control

$$i_{gnd}(s) = G_{irdigd}(s)i_{rnd}(s) \quad (7-12)$$

In the figure,  $G_{irdprc}(s)$  can be approximated as:

$$G_{irdprc}(s) = \frac{P_{rc}(s)}{i_{rnd}(s)} \approx \frac{X_m}{X_s} (\omega_n - \omega_r) * u_{sd} \quad (7-13)$$

Since there is no outer loop for reactive current control of the grid-side converter, the reactive current of grid-side converter will not be affected by reactive current of the rotor-side converter and will be kept at its reference (zero).

Finally, the TF from TCSC voltage to line current can be obtained:

$$\begin{cases} G_{NWuTCSCdild} = G_{NWuTCSCdisd} + G_{NWuTCSCdira}G_{irdigd} \\ G_{NWuTCSCqild} = G_{NWuTCSCqisd} + G_{NWuTCSCqird}G_{irdigd} \\ G_{NWuTCSCdilq} = G_{NWuTCSCdisq} \\ G_{NWuTCSCqilq} = G_{NWuTCSCqisq} \end{cases} \quad (7-14)$$

With all the TFs in Fig. 7-6 derived, the closed-loop TF of boost control can be derived. It should be mentioned that model simplification of the TFs has been employed, either by pole-zero cancellation or order reduction, in deriving TFs. Otherwise, the order of TFs will be too high for Matlab to handle and to abstract useful information.

Since the interaction is related to mis-matched control speeds among different loops, the closed-loop TF of kB control will be analyzed with varying control speed.

### 7.3.2.2 Analysis of control interaction with varying DFIG controller gains

Fig. 7-13 shows the pole-zero map of the closed-loop TF of kB control with the current controller gain of rotor-side converter varying from 0.05 to 0.3 and the outer loop controller gains vary accordingly. The part with poles of interest is zoomed in in Fig. 7-14. It can be seen that if the DFIG controller gains are too small, the kB control system will be unstable. Fig. 7-15 shows the poles in case the gain of outer speed control loop doesn't vary accordingly with the variation of the inner current controller gain.

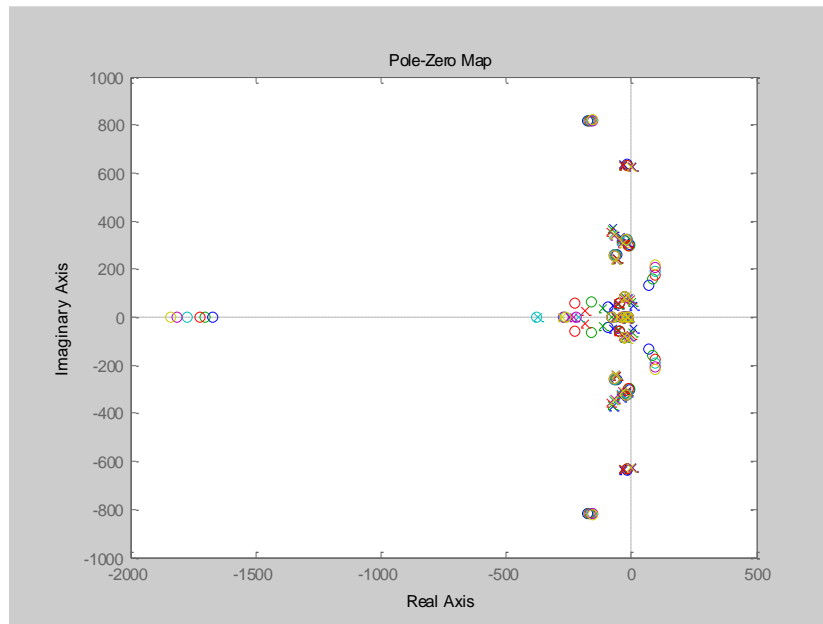


Fig. 7-13 Pole-zero map of closed-loop TF of kB control with  $k_{ir}$  varying from 0.05 to 3 ( $k_Q$  and  $k_{wr}$  vary accordingly)

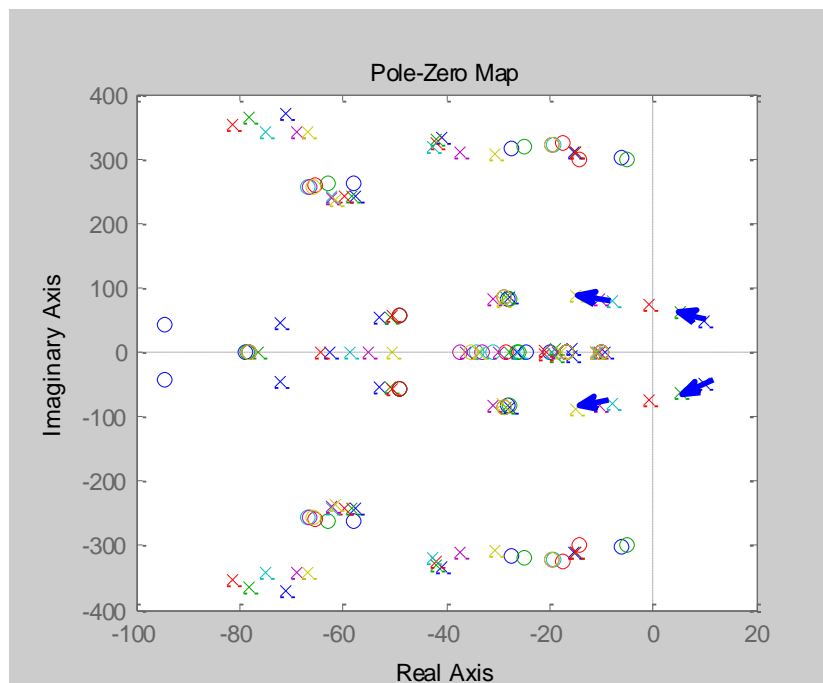


Fig. 7-14 Pole-zero map of closed-loop TF of kB control with  $k_{ir}$  varying from 0.05 to 3 (zoomed in,  $k_Q$  and  $k_{wr}$  vary accordingly)

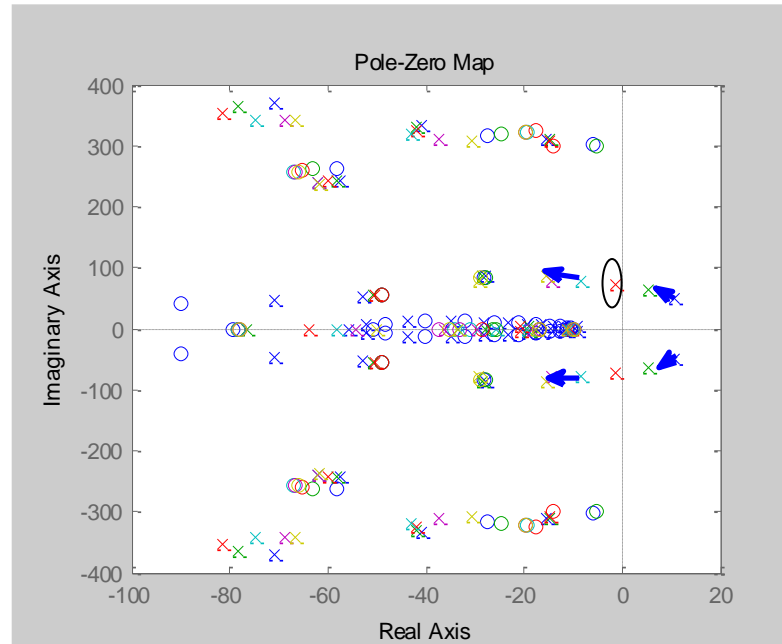


Fig. 7-15 Pole-zero map of closed-loop TF of  $k_Q$  control with  $k_{ir}$  varying from 0.05 to 3 ( $k_Q$  varies accordingly,  $k_{wr}=24$  doesn't change)

Fig. 7-16 shows the bode diagram of the open-loop TF. It can be seen that with the increasing DFIG controller gains, the gain margin and phase margin change from negative to positive.

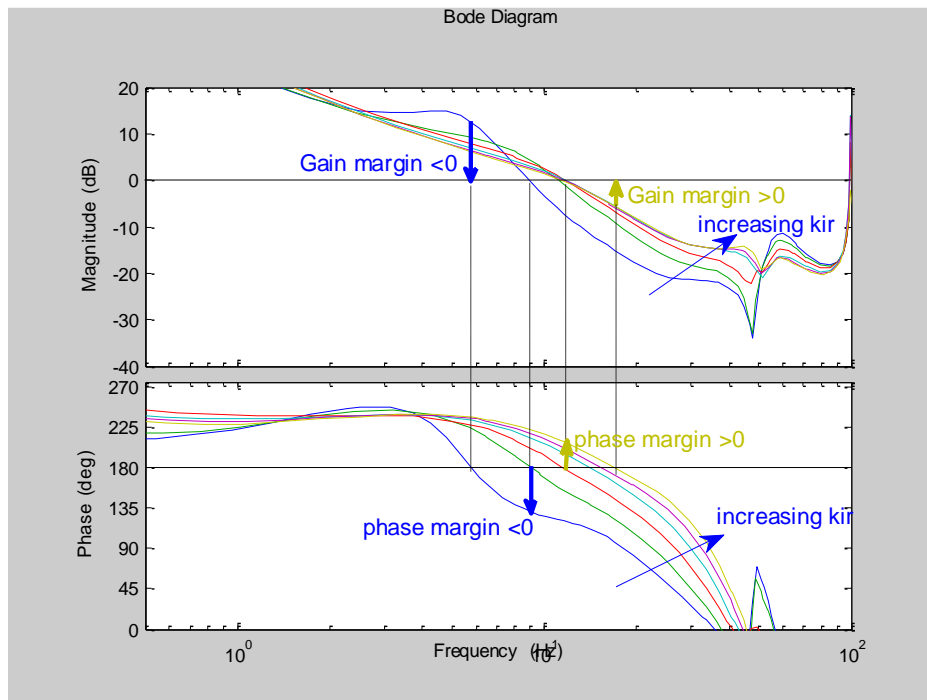


Fig. 7-16 Bode diagram of open-loop TF with  $k_{ir}$  varying from 0.05 to 3

This analysis is verified by PSCAD simulation results shown in Fig. 7-17. At 3s, the controller gains of rotor-side converter were changed from [ $k_{ir}=0.3$ ,  $k_Q=1.5$ ,  $k_{wr}=24$ ] to [ $k_{ir}=0.1$ ,  $k_Q=0.5$ ,  $k_{wr}=24$ ], corresponding to the case marked with ellipse in Fig. 7-15. The frequency of the unstable pole is

63.4 rad/s (10.1 Hz), which is close to the frequency (about 9.4 Hz) of the oscillations shown in Fig. 7-17. The discrepancy might be caused by simplifications made in the theoretical analysis.

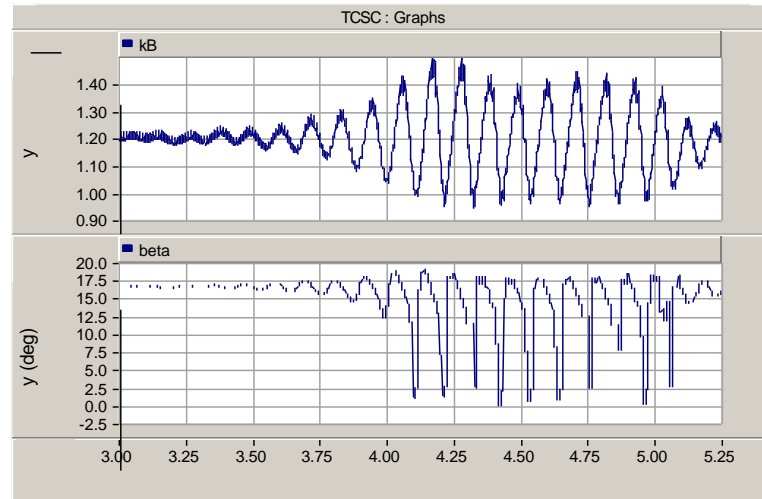


Fig. 7-17 PSCAD simulation results

### 7.3.2.3 Analysis of control interaction with varying TCSC boost controller gain

A straightforward guess is that the oscillation can also be eliminated by reducing  $k_B$  controller gains instead of increasing DFIG controller gain, since the oscillations are caused by interaction of the two control systems.

Fig. 7-18 and Fig. 7-19 shows the pole-zero map of the closed-loop and bode diagram of the open-loop TF of  $k_B$  with  $k_B$  controller gain decreasing from 0.25 to 0.05.

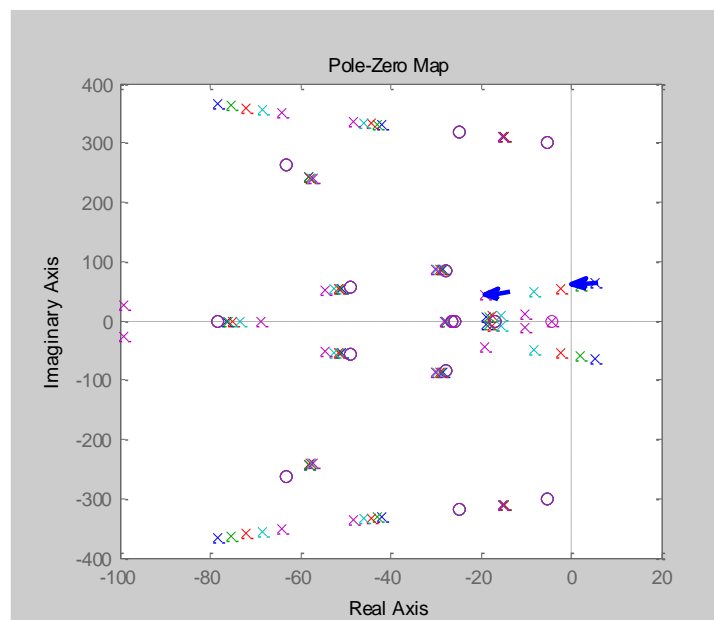


Fig. 7-18 Pole-zero map of closed-loop TF of  $k_B$  control with  $k_p_{k_B}$  varying from 0.25 to 0.05 ( $[k_{ir}=0.1, k_Q=0.5, k_{wr}=8]$ )

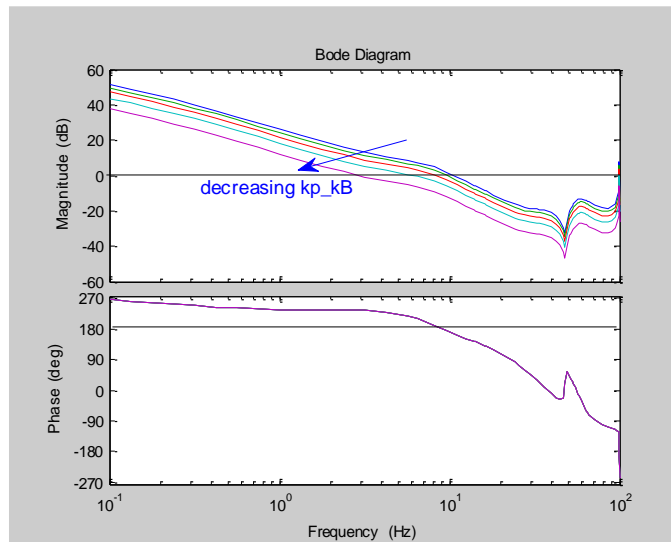
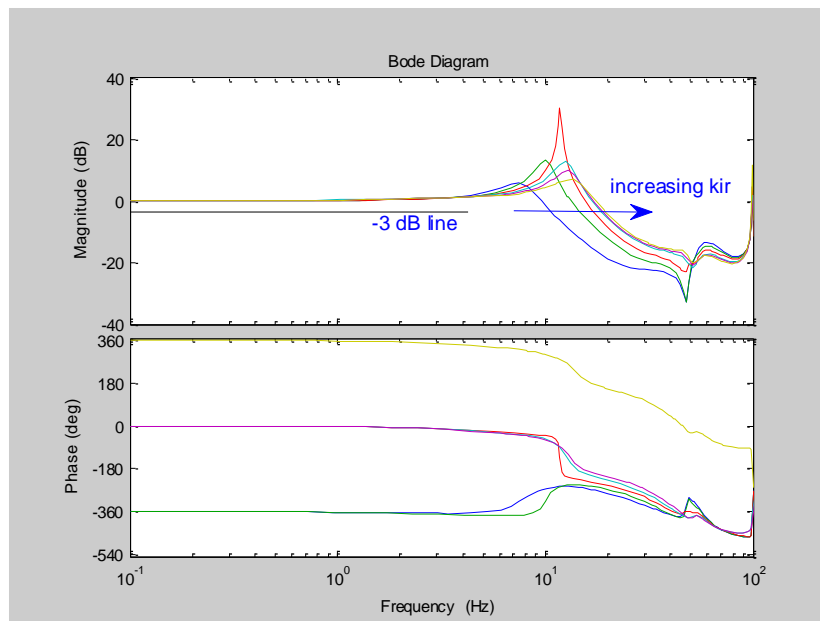
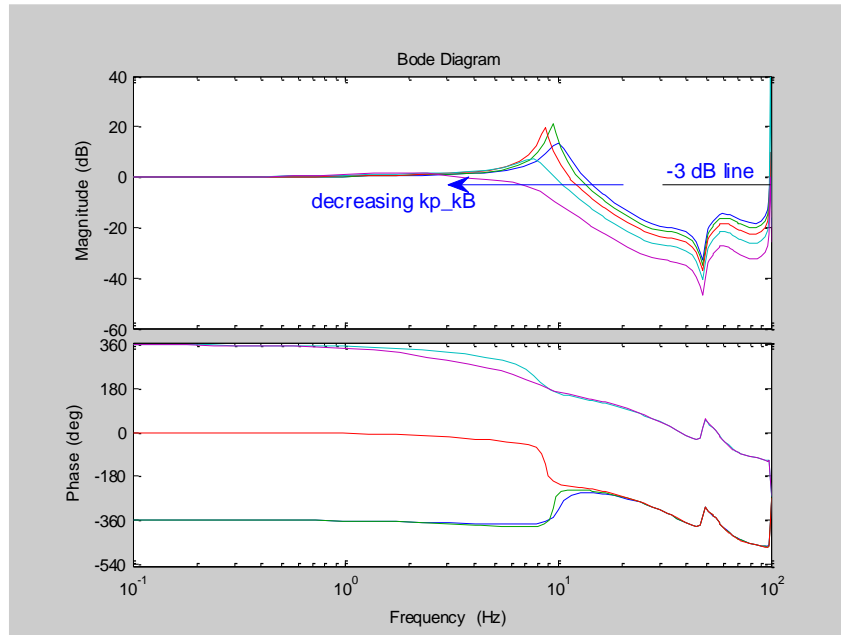


Fig. 7-19 Bode diagram of open-loop TF with varying  $k_p k_B$

Fig. 7-20 compares the bode diagram of the closed-loop TF with increasing  $k_{ir}$  and decreasing  $k_p k_B$ . It can be seen clearly that larger bandwidth can be achieved by increasing  $k_{ir}$ .

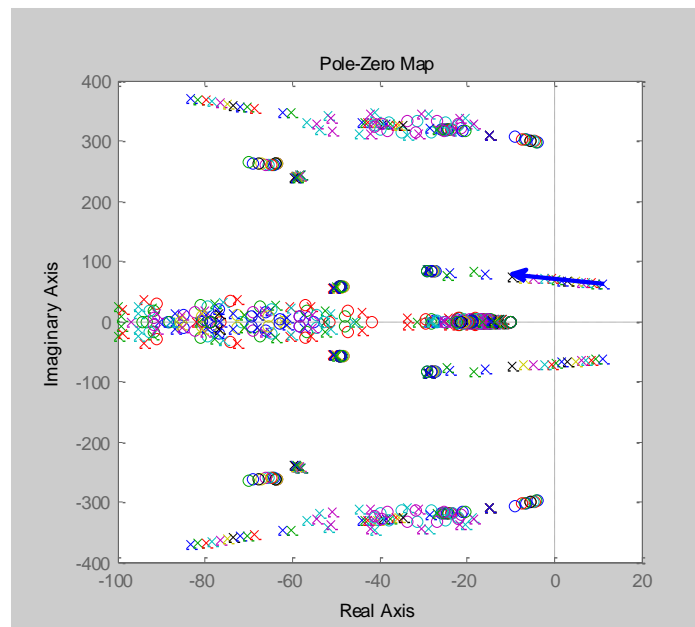


(a) with increasing  $k_{ir}$

(b) with decreasing  $k_p k_B$ Fig. 7-20 Bode diagram of closed-loop TF of  $k_B$ 

#### 7.3.2.4 Impact of TCSC rating on control interaction

Since the oscillations are caused by the interaction between TCSC control and DFIG control, the rating of TCSC will have impact on the oscillations. Fig. 7-21 shows how the critical poles of the closed-loop TF moves from the right-half plane to the left-half plane with the compensation degree of TCSC (ratio of TCSC to line reactance) varies from 40% to 10%. The DFIG controller gains are mis-matched in this case with  $[k_{ir}=0.1; k_Q=0.5; K_{wr}=24]$  and the TCSC controller has a larger gain of 0.25. The boundary degree is 22%.

Fig. 7-21 Pole-zero map of closed-loop TF of  $k_B$  with varying TCSC compensation degree

### 7.3.3 Elimination of control interaction by adding damping control to TCSC control system

Even though the power oscillation caused by control interaction can be eliminated by matching controller gains in different loops, it is desired to design a damping controller in case gain-matching is infeasible or in case gain-matching results in undesired slow control.

#### 7.3.3.1 TF analysis

The power oscillation damping (POD) controller can be added to the TCSC control system as shown in the red-shaded area in the upper-left corner of Fig. 7-22.

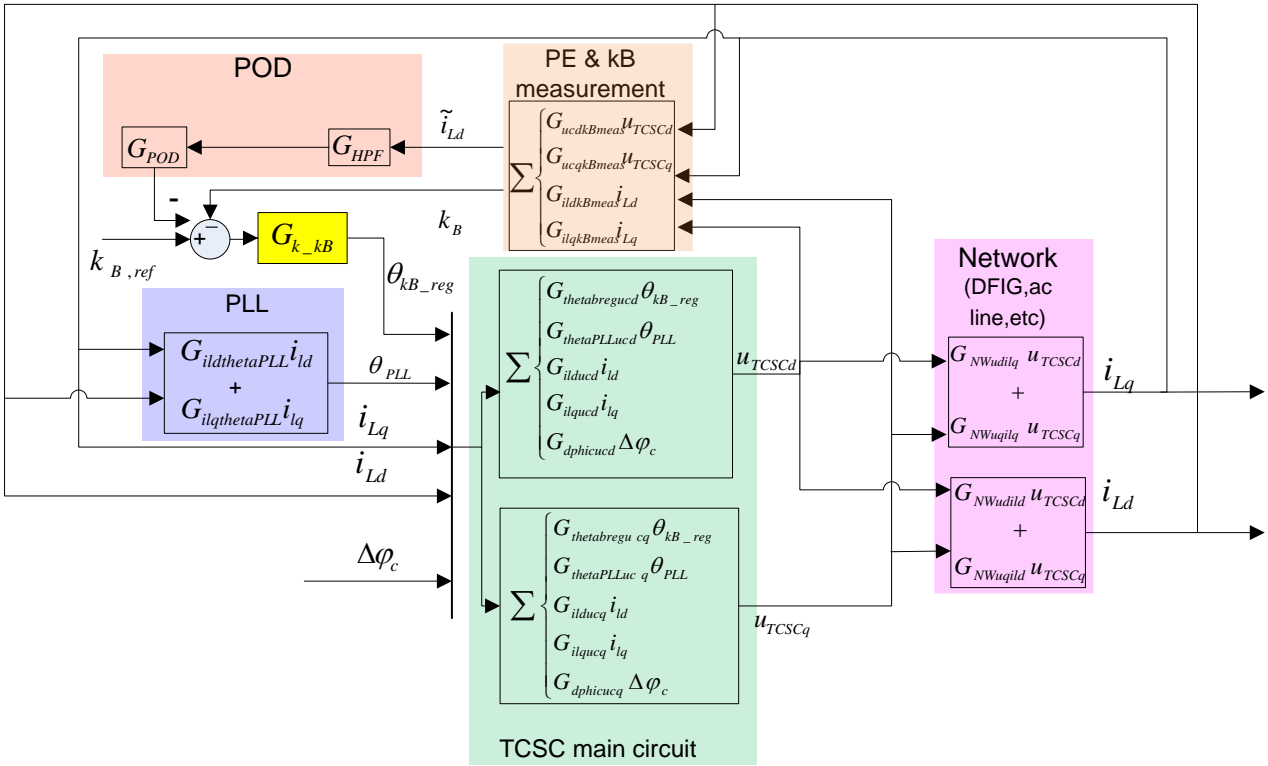


Fig. 7-22 Control system with POD control

The POD controller takes the real part of the estimated line current phasor and passes it to a high pass filter (HPF) to get the oscillation signal. The oscillation signal is then passed through a damping controller to get the modulated signal of the boost factor. The damping controller is a simple phase-lag compensator in the form of

$$G_{POD}(s) = k_{POD} \frac{1+s/\omega_{lead}}{1+s/\omega_{lag}} \quad (7-15)$$

The time constant for HPF is selected as 0.32s, giving a cut-off frequency of 0.5 Hz.

The purposes of using lead-lag compensator is to attenuate open-loop gains at high frequency and meanwhile not to introduce too much phase lag in frequency range close to gain cross-over. Therefore, it is reasonable to choose the frequency  $\omega_m$ , at which the phase lag  $\theta_m$  introduced by the lead-lag compensator is minimum, to be about 10 times smaller than the gain cross-over frequency of the plant. Depending on how big  $\theta_m$  should be,  $\omega_{lead}$  and  $\omega_{lag}$  can be chosen according to (7-16):

$$\omega_{lead} = \sqrt{k_\omega} \omega_m; \omega_{lag} = \omega_m / \sqrt{k_\omega} \quad (7-16)$$

where smaller  $k_\omega$  results in smaller  $\theta_m$ .

From the bode diagram of the open-loop TFs shown in Fig. 7-16, the gain cross-over frequency is in the range of 9-12 Hz when the  $k_{ir}$  varies from 0.05 to 3. If the compensator is in series with the plant, it will be reasonable to choose  $\omega_m = 1 * 2\pi$ . However, since this compensator is not in series with the plant but rather in parallel, it is not straightforward to look at the frequency characteristic of the compensator directly. After fine tuning through simulations in PSCAD,  $\omega_m = 19 \text{ rad/s}$  (3 Hz)  $k_\omega = 2$  gives the best performance.

The frequency characteristics of the HPF, the lead-lag compensator and the product of them are shown in Fig. 7-23.

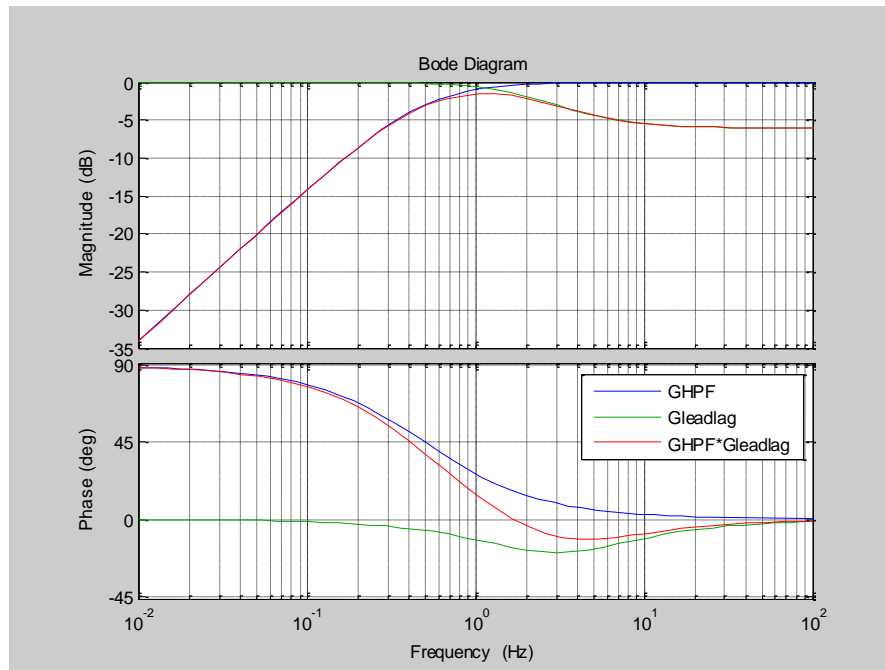


Fig. 7-23 Frequency characteristics of HPF

The base case selected for POD investigation is with the following parameters:  $[k_{ir}=0.1; k_Q=0.5; k_{wr}=24]$ . With  $\omega_m = 19 \text{ rad/s}$  and  $k_\omega = 2$ , the damping factor  $k_{POD}$  is varied from 0 to 3.

Fig. 7-24 shows how the unstable poles of the closed-loop TF of kB control system moves from the left-half plane to right-half plane.

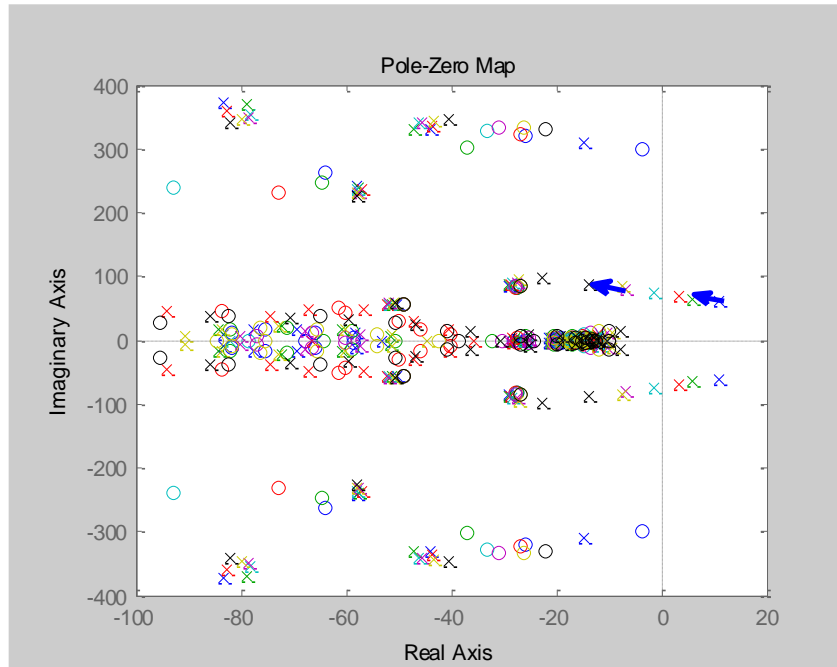


Fig. 7-24 Pole-zero map of closed-loop TF of k<sub>B</sub> control with k<sub>pod</sub> varying from 0 to 6

### 7.3.3.2 PSCAD simulations

Simulation has been done in PSCAD to validate the damping control.

It is worth to describe how the controller is implemented in PSCAD. The control diagram shown in Fig. 7-22 and the TF derived from the figure are based on per unit system. The quantities related to DFIG are per-unitized with wind farm installed capacity and terminal voltage. The quantities related to TCSC are per-unitized with line current peak value and the un-boosted voltage across TCSC capacitor at the corresponding line current. In PSCAD, the control block of the TCSC model outputs line current phasors in kA. Therefore, the real part of the line current phasor  $iphx$  (in kA) is low-pass filtered to get the line current magnitude. The real part of the estimated line current phasor  $\widetilde{i}_{Lq}$  (in pu) shown in Fig. 7-22 is obtained by dividing  $iphx$  (in kA) delivered by TCSC control block with the low-pass filtered  $iphx$ .

The results are plotted in Fig. 7-25. During the simulation, three sets of DFIG control parameters have been used, they are listed in Table 7-1.

Table 7-1 Sets of DFIG control parameter used in PSCAD simulations

	kir	kQ	kwr
Normal gain	0.3	1.5	24
Small gain	0.1	0.5	8
Mis-matched gain	0.1	0.5	24

The damping controller is enabled with k<sub>pod</sub>=6 at time 5s. Fig. 7-25 is enlarged into 6 separate sub-figures for the 6 periods with different combinations of the three sets of parameters and with/without damping controller.

The results show that the damping control works well for various combination of DFIG controller gains. This is valuable since in a real system the controller gains for individual DFIG in a wind farm can use different control parameters or even different control structures.

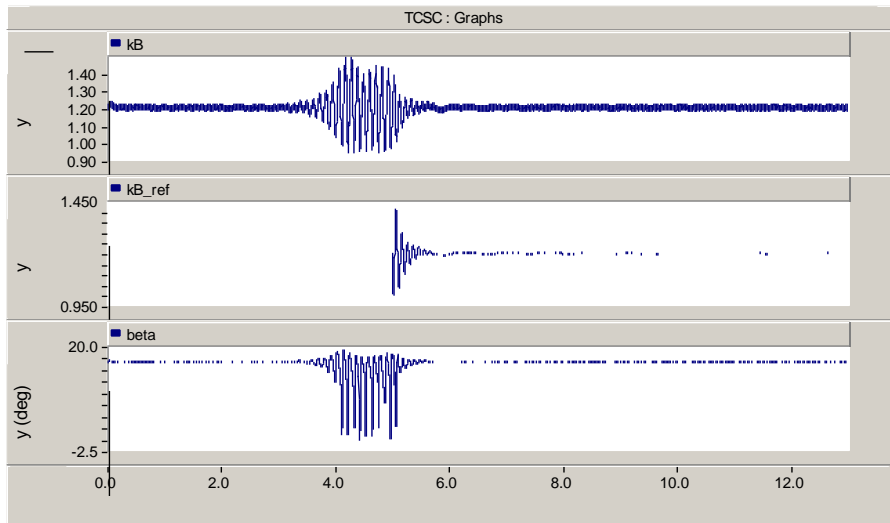
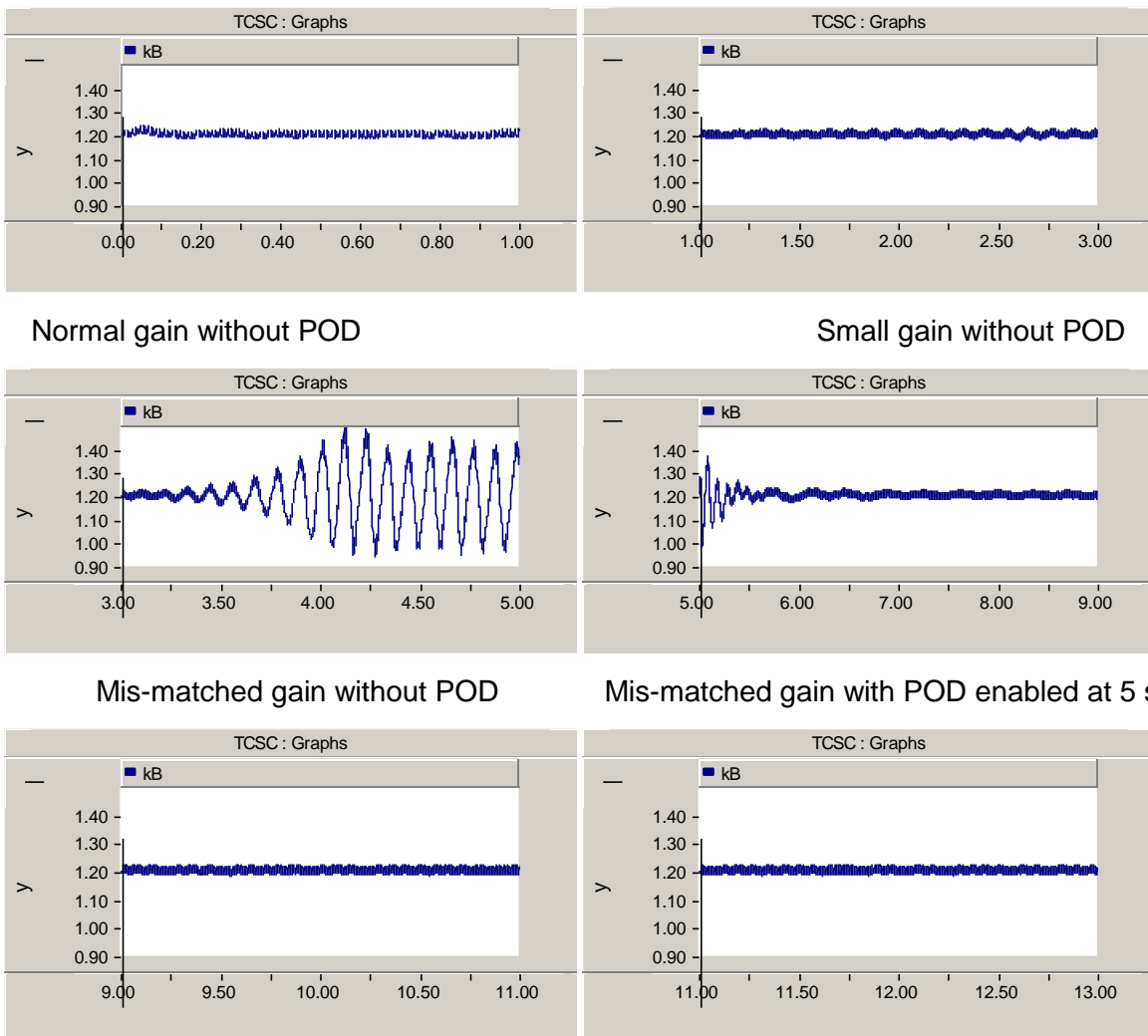


Fig. 7-25 PSCAD simulation showing power oscillation damping



Small gain with POD

Normal gain with POD

Fig. 7-26 PSCAD simulation showing power oscillation damping (enlarged)

## 7.4 Investigation on system compensated by combined TCSC and fixed capacitor

As has been demonstrated, system compensated by FC has high SSR risk whereas system compensated by pure TCSC has no SSR risk. Since TCSC has higher cost than FC, it is desired to compensate the lines by combined TCSC and FC with TCSC portion as small as possible.

In this chapter, the system compensated by combined TCSC and FC will be investigated. The investigation consists of three parts:

- Evaluation of SSR risk with TCSC controlled by SVR control scheme
- Investigation on the impact of TCSC inductance and boost factor on SSR
- Development of SSR damping control to reduce required TCSC portion

### 7.4.1 Evaluation of SSR risk in system with DFIG and TCSC+FC

The objective of SSR risk evaluation is to find out the minimum required portion of TCSC to avoid SSR. The TCSC is controlled with SVR scheme without damping controller at this stage.

As demonstrated in [22], SSR risk is determined by several factors. The most significant ones are: current controller gain  $k_{ir}$  of DFIG rotor-side converter, rotor speed  $w_r$  (corresponding to generation level) and compensation degree. SSR risk will be higher with larger  $k_{ir}$ , smaller  $w_r$ , and higher compensation degree.

The total compensation degree (TCSC+FC) is assumed to be 40% of the line reactance. The considered generation level will be the whole typical generation range; hence the minimum  $w_r$  will be down to 0.7 pu, corresponding to a generation level of 0.01 pu.  $k_{ir}$  will be specified in each evaluated cases later.

The SSR risk will be evaluated through both theoretical analysis and PSCAD simulations. For theoretical analysis, two methods are employed. One method is frequency scanning and the other is TF analysis.

It should be pointed out that fixed capacitor banks are connected at wind farm terminal in evaluation with frequency scanning method. However, no capacitor bank is connected in evaluation with TF analysis for the reason of simplicity as discussed in Section 7.2.4.

#### 7.4.1.1 Evaluation with frequency scanning method and PSCAD simulation

##### 7.4.1.1.1 PSCAD simulation

First, simulations in PSCAD are performed to find out the minimum portion of TCSC to avoid SSR.

In all the simulation studies, the total compensation level is kept at 40%. As a typical value, TCSC boost factor is set to 1.2. The DFIG control parameters are set as [ $k_{ir}=0.3$ ,  $k_Q=1.5$ ,  $k_{wr}=24$ ] in this part of investigation. This set of parameters results in a fast DFIG control, but with high SSR risk.

As the reference scenario, case with 100% (of the 40% total compensation) TCSC is simulated first and then the TCSC portion is decreased by 10% for each simulation. It could be found out the minimum TCSC portion is between 70% and 80%.

In the same way but with a higher resolution (2%) it could be found out that the minimum required TCSC portion is 78%. Below this portion, the system could have SSR risk.

In the simulation shown in Fig. 7-27, the wind speed decreases from 10.59 m/s to 4 m/s at 3s. The step change is not realistic in reality. However, in order to shorten simulation period, such a big step was applied. This will not affect the analysis result. After the system reaches steady state by the end of the simulation, the output power is only 4.5 MW (about 0.01 pu) and the rotor speed is 0.7 pu. Simulation result shows the system with 40% compensation level comprising 78% TCSC and 22% FC doesn't have SSR risk.

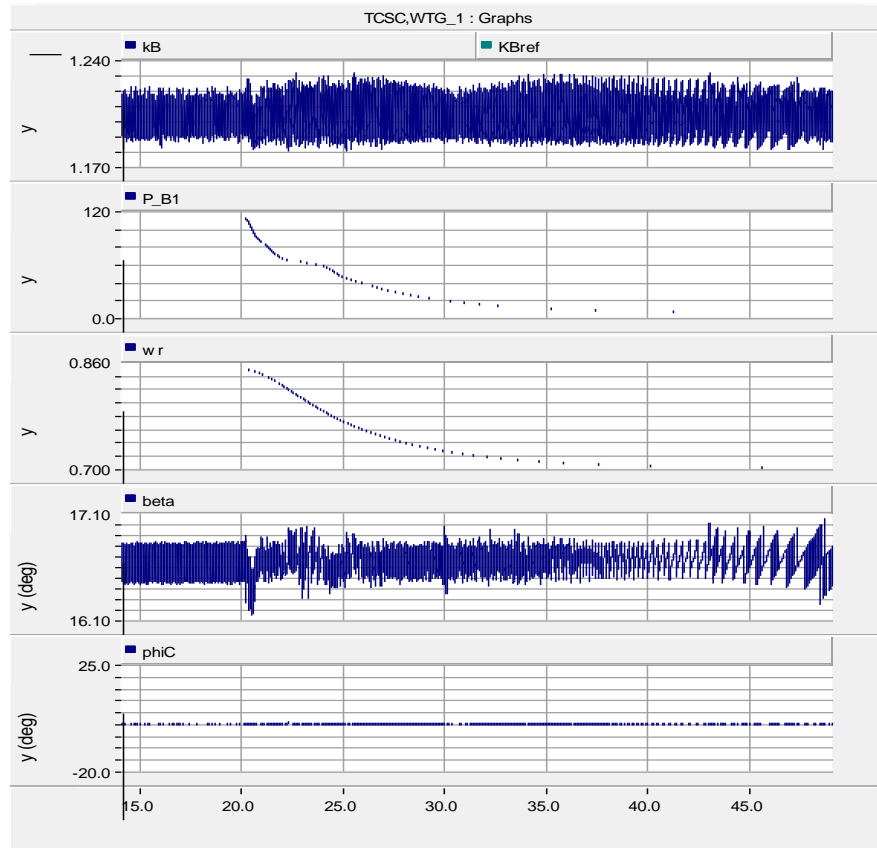


Fig. 7-27 PSCAD simulation with 78% TCSC + 22% FC

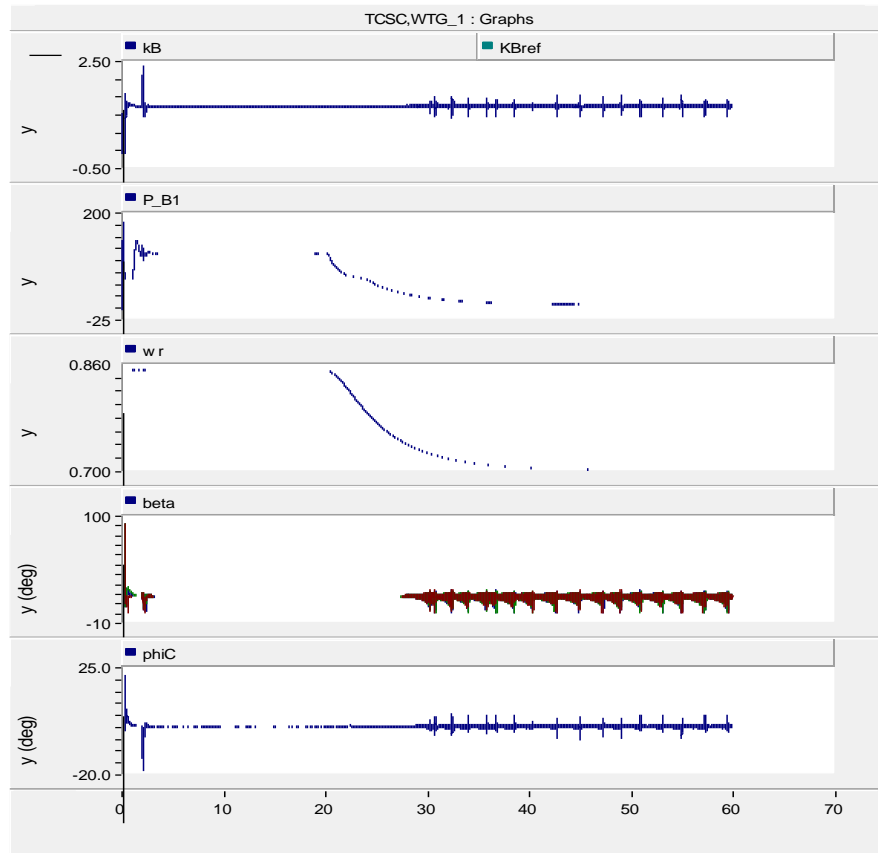


Fig. 7-28 PSCAD simulation with 77% TCSC + 23% FC

But if TCSC portion is decreased to 77%, SSR occurs in system, as shown in Fig. 7-28. That is, the minimum TCSC portion to prevent the system from SSR risk is 78%.

This could be explained through analysis of system impedance with frequency scanning method. First, the wind farm impedance in sub-synchronous frequency range is obtained by frequency scanning. Then TCSC apparent impedance is calculated theoretically. Finally, the system impedance can be obtained and analyzed.

#### 7.4.1.1.2 Frequency scanning of wind farm impedance

Frequency scanning method is introduced to predict whether the system has a SSR risk. Frequency scanning method is approximated linear method, which could calculate the “equivalent” impedance of the tested system. The “equivalent” impedance is not the exact equivalent impedance of system; it is only used to indicate at which frequency the system has a high risk of resonance due to its limited accuracy [23].

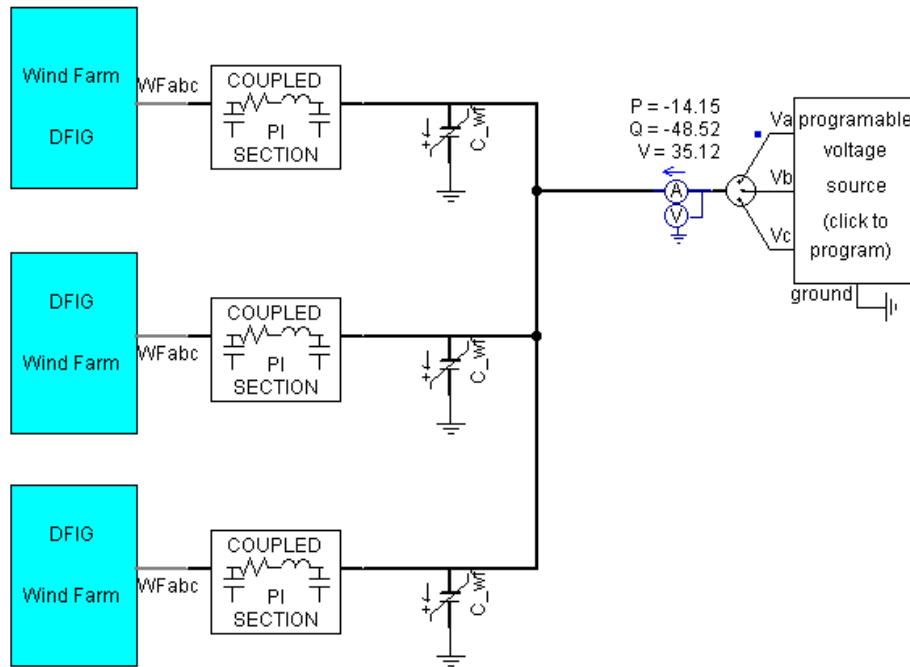


Fig. 7-29 Application of Frequency Scanning Solution

As shown in Fig. 7-29, the output point of wind farm cluster is connected to a voltage source, which could have different frequency at variable time. The wind speed is set to 4 m/s. The reactive power compensation device  $C_{wf}$  is a fixed capacitor. At beginning, voltage source only includes fundamental frequency with amplitude of 35 kV.

After the wind farm cluster reaches its steady state at 4 m/s, voltage source includes not only the original signal, but also a sub-synchronous frequency with small amplitude (e.g. 0.1 kV). This sub-synchronous frequency varies from 0 to 48 Hz with a resolution of 1 Hz. FFT is used to analyze the frequency spectra. With the magnitude and phase of measured current for each frequency, it is feasible to calculate the real and imaginary part of wind farm “equivalent” impedance.

#### 7.4.1.1.3 Calculation of TCSC impedance

The formula for calculation of TCSC apparent reactance in sub-synchronous frequency range could be found in [21] and is shown in (7-17):

$$\zeta = \frac{\omega}{\omega_N}$$

$$Z_{app}(j\zeta\omega_N) = k_Z(\zeta) \frac{1}{\omega_N C}$$

$$k_Z(\zeta) = \frac{(1-D_f)\sin(\zeta\frac{\pi}{2}) + j(1+D_f)[1-\cos(\zeta\frac{\pi}{2})]}{\zeta(1+D_f)\cos(\zeta\frac{\pi}{2}) + j(1-D_f)\sin(\zeta\frac{\pi}{2})}$$
(7-17)

In the equations,  $D_f$  is the loss factor of TCSC. Corresponding to the parameter ‘TCSC inductor quality factor at  $f_N$ ’ of  $QL=100$ , as defined in the simulation model, a loss factor of  $D_f = 0.99$  is used in the calculation [21].

As shown in Fig. 7-30, TCSC portion has a big influence on the apparent impedance of combined TCSC and FC, especially for the imaginary part at lower frequency. The X-axis is normalized

frequency, which is a fraction of the fundamental frequency. The Y-axis is the calculated impedance in Ohm at 500 kV side. If the portion of TCSC is not 100%, the imaginary part of the impedance is below zero at low frequency, which leads to a zero-crossing point. This zero-crossing point of imaginary part will have a big influence on SSR appearance, which will be proved in detail in the following.

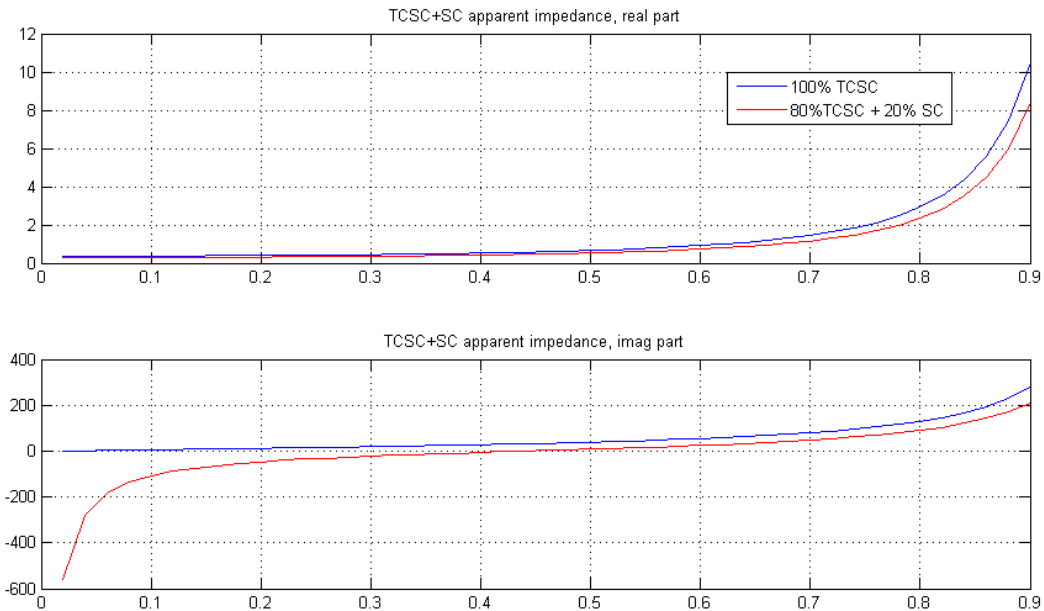


Fig. 7-30 Apparent impedance of TCSC + SC

#### 7.4.1.1.4 Calculation and analysis of system impedance

Finally, the real and imaginary part of the system impedance versus frequency could be plotted. Fig. 7-31 shows the impedance of the system with two different configurations: (a) 78%TCSC+22%FC and (b) 77%TCSC+23%FC. The X-axis is frequency in Hz while Y-axis is the calculated impedance in Ohm at 35 kV side. It can be seen that the imaginary part of system with 77%TCSC+23%FC has a zero-crossing (from negative value to positive value) around 10 Hz while the real part almost also have the same zero-crossing around 10 Hz. That is, the system is very likely to suffer SSR with an oscillation frequency of about 40 Hz, which is complementary frequency of zero-crossing frequency of the impedance. The study based on simulation in PSCAD as shown in Fig. 7-32 proves the result with frequency scanning method performed in Matlab. It is clear that the system suffers SSR with an oscillation frequency of around 40 Hz in wind power output and in DFIG rotor speed.

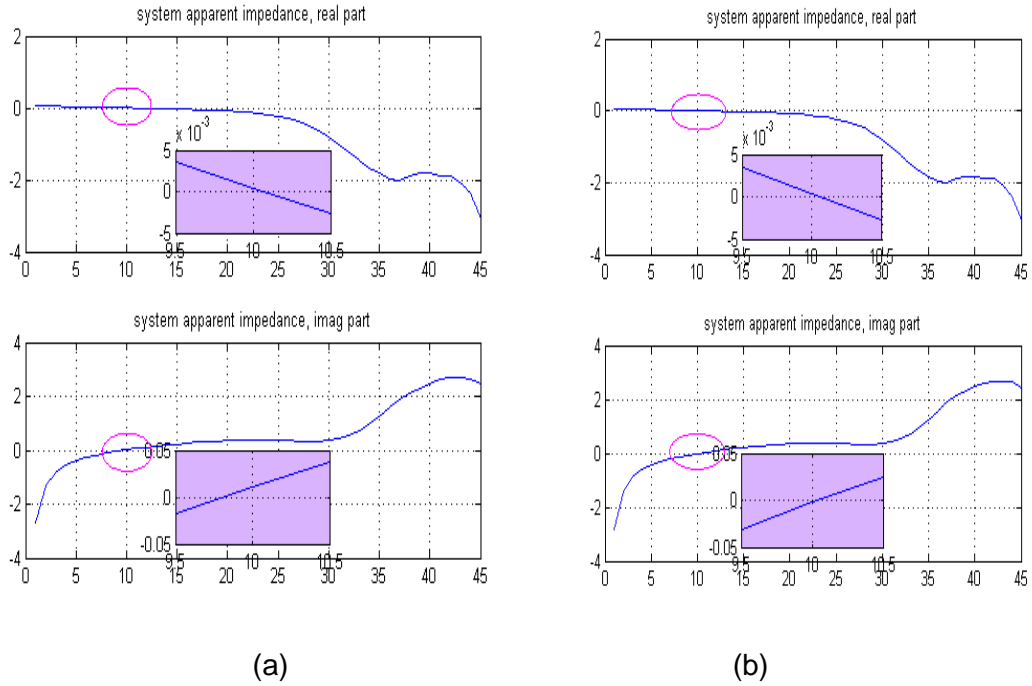


Fig. 7-31 Real and imaginary part of system impedance based on frequency scanning method  
 (a) 78% TCSC+22% FC; (b) 77% TCSC+23% FC

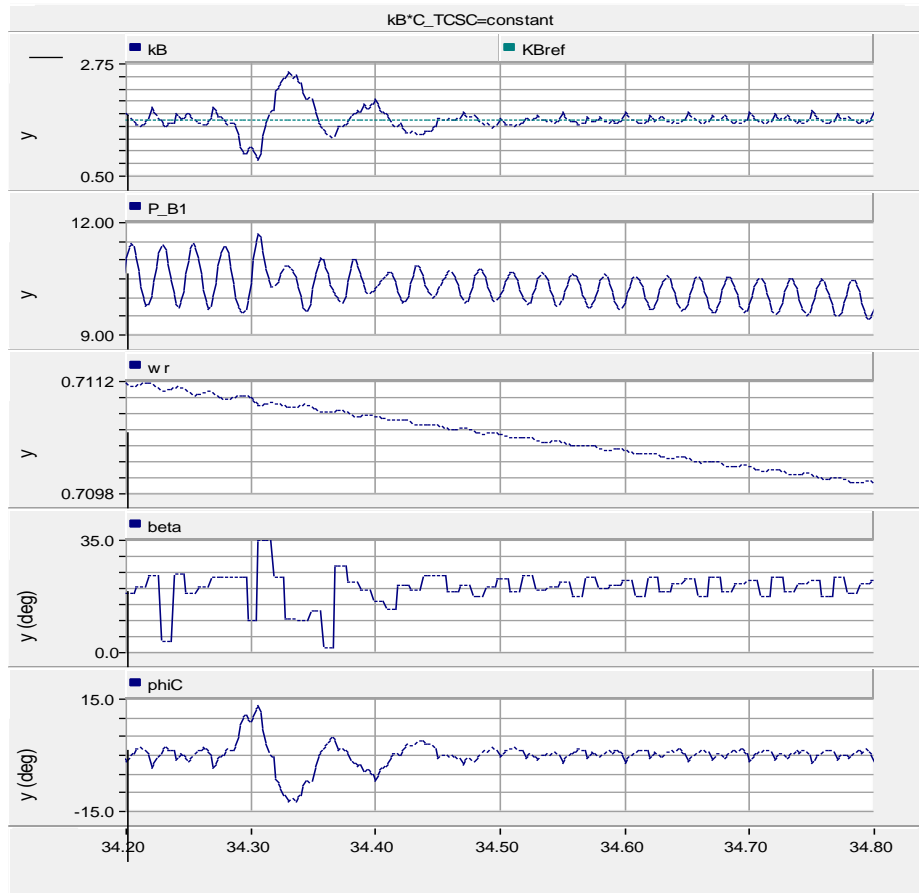


Fig. 7-32 Simulation in PSCAD, TCSC%=77%, kB=1.2

In the same way, the system with different TCSC and FC configuration has also been plotted, as shown in Fig. 7-33. It can be seen that the change of TCSC and FC configuration has little influence on real part of system but a strong influence on imaginary part. As the TCSC portion is decreasing, the zero-crossing of imaginary part moves rightward. Since the real part doesn't have visible change, the possibility of SSR becomes higher.

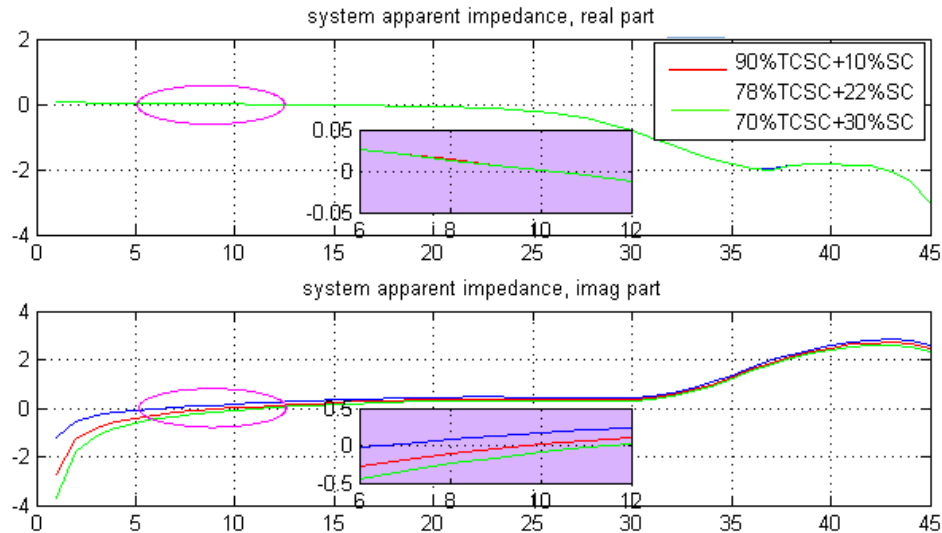


Fig. 7-33 Real and imaginary part of system with different TCSC and FC configuration

#### 7.4.1.2 Evaluation of SSR risk with transfer function analysis and PSCAD simulation

The system used for SSR analysis is shown in Fig. 7-6, which is re-drawn in Fig. 7-34. For SSR analysis, sub-synchronous component of each quantity is considered. Therefore,  $k_{Bref}$  in the figure is zero. The signal flow in pink color represents the closed-loop response of the DFIG control system (line current in response to TCSC voltage), which can be derived from DFIG rotor-side converter control system for sub-synchronous frequency as shown in Fig. 7-35.

The evaluation approach is to analyze the closed-loop TF from disturbance in DFIG stator current to boost response.



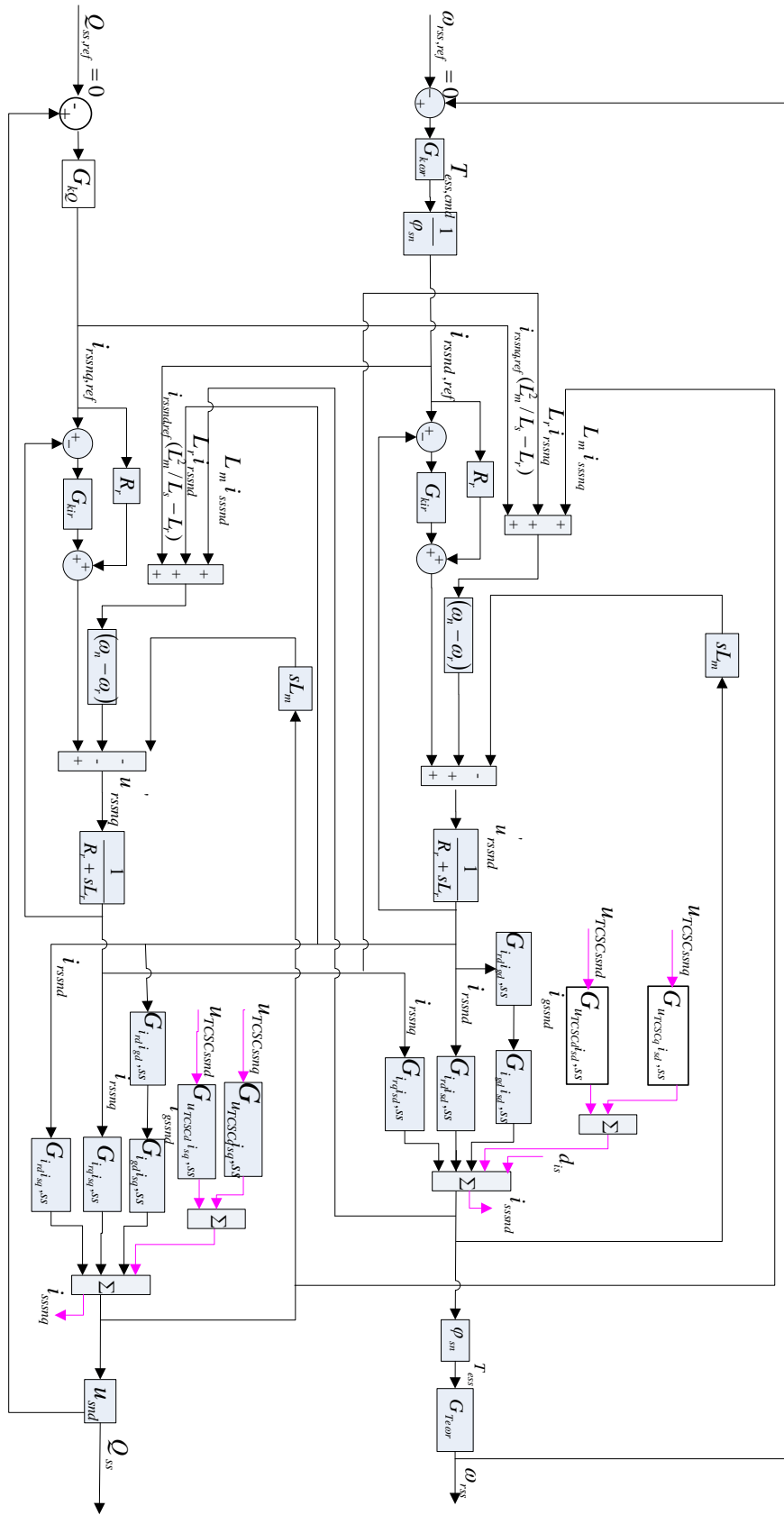


Fig. 7-35 DFIG control system with TCSC voltage as input (sub-synchronous frequency)

### 7.4.1.2.1 Derivation of closed-loop transfer function from line current disturbance to kB

Step 1: Derive closed-loop TF from TCSC voltage to line current (Fig. 7-35)

In the figure, the unknown TFs are the ones from rotor current, grid-side converter current and TCSC voltage to stator current, which can be derived from the equivalent circuit shown in Fig. 7-8. The derivation procedure is similar to that described in [22]. The only difference is the addition of TCSC.

In [22], the derived TFs from line current (the sum of stator current and grid-side converter current) to DFIG terminal voltage without presence of TCSC are:

$$\begin{cases} u_{ssnd}(s) = -\left(R_{sys} + sL_{sys} + \frac{s}{C_{FC}(s^2 + \omega_n^2)}\right) i_{ssnd}(s) + \left(\omega_n L_{sys} - \frac{\omega_n}{C_{FC}(s^2 + \omega_n^2)}\right) i_{ssnq}(s) \\ \quad - \left(R_{sys} + sL_{sys} + \frac{s}{C_{FC}(s^2 + \omega_n^2)}\right) i_{gssnd}(s) + \left(\omega_n L_{sys} - \frac{\omega_n}{C_{FC}(s^2 + \omega_n^2)}\right) i_{gssnq}(s) \\ u_{ssnq}(s) = -\left(R_{sys} + sL_{sys} + \frac{s}{C_{FC}(s^2 + \omega_n^2)}\right) i_{ssnq}(s) - \left(\omega_n L_{sys} - \frac{\omega_n}{C_{FC}(s^2 + \omega_n^2)}\right) i_{ssnd}(s) \\ \quad - \left(R_{sys} + sL_{sys} + \frac{s}{C_{FC}(s^2 + \omega_n^2)}\right) i_{gssnq}(s) - \left(\omega_n L_{sys} - \frac{\omega_n}{C_{FC}(s^2 + \omega_n^2)}\right) i_{gssnd}(s) \end{cases} \quad (7-18)$$

In the above equations, the subscriptions refer to:

*ssnd*, *ssnq*: sub-synchronous component of stator quantities transformed into nominal frequency dq plane

*qssnd*, *gssnq*: sub-synchronous component of grid-side converter quantities transformed into nominal frequency dq plane

With the addition of TCSC, the following can be obtained:

$$\begin{cases} u_{ssnd}(s) = -\left(R_{sys} + sL_{sys} + \frac{s}{C_{SC}(s^2 + \omega_n^2)}\right) i_{ssnd}(s) + \left(\omega_n L_{sys} - \frac{\omega_n}{C_{SC}(s^2 + \omega_n^2)}\right) i_{ssnq}(s) \\ \quad - \left(R_{sys} + sL_{sys} + \frac{s}{C_{SC}(s^2 + \omega_n^2)}\right) i_{gssnd}(s) + \left(\omega_n L_{sys} - \frac{\omega_n}{C_{SC}(s^2 + \omega_n^2)}\right) i_{gssnq}(s) - u_{TCSCssnd}(s) \\ u_{ssnq}(s) = -\left(R_{sys} + sL_{sys} + \frac{s}{C_{SC}(s^2 + \omega_n^2)}\right) i_{ssnq}(s) - \left(\omega_n L_{sys} - \frac{\omega_n}{C_{SC}(s^2 + \omega_n^2)}\right) i_{ssnd}(s) \\ \quad - \left(R_{sys} + sL_{sys} + \frac{s}{C_{SC}(s^2 + \omega_n^2)}\right) i_{gssnq}(s) - \left(\omega_n L_{sys} - \frac{\omega_n}{C_{SC}(s^2 + \omega_n^2)}\right) i_{gssnd}(s) - u_{TCSCssnq}(s) \end{cases} \quad (7-19)$$

The generator circuit equations are:

$$\begin{cases} u_{ssnd}(s) = R_s i_{ssnd}(s) + L_s s i_{ssnd}(s) + L_m s i_{rssnd}(s) - \omega_n L_s i_{ssnq}(s) - \omega_n L_m i_{rssnq}(s) \\ u_{ssnq}(s) = R_s i_{ssnq}(s) + L_s s i_{ssnq}(s) + L_m s i_{rssnq}(s) + \omega_n L_s i_{ssnd}(s) + \omega_n L_m i_{rssnd}(s) \end{cases} \quad (7-20)$$

where  $i_{rssnd}$  and  $i_{rssnq}$  are rotor current induced by sub-synchronous component of air-gap flux and transformed into nominal frequency dq plane.

From the two sets of equations above, the TFs from rotor current, grid-side converter current and TCSC voltage to stator current can be resolved.

$$\begin{cases} i_{ssnd}(s) = i_{rssnd}(s) G_{irdisd,ss}(s) + i_{rssnq}(s) G_{irqisd,ss}(s) + i_{gssnd}(s) G_{igdisd,ss}(s) \\ \quad + i_{gssnq}(s) G_{igqisd,ss}(s) + u_{TCSCssnd}(s) G_{uTCSCdisd,ss}(s) + u_{TCSCssnq}(s) G_{uTCSCqisd,ss}(s) \\ i_{ssnq}(s) = i_{rssnq}(s) G_{irqisq,ss}(s) + i_{rssnd}(s) G_{irdisq,ss}(s) + i_{gssnd}(s) G_{igdisq,ss}(s) \\ \quad + i_{gssnq}(s) G_{igqisq,ss}(s) + u_{TCSCssnd}(s) G_{uTCSCdisq,ss}(s) + u_{TCSCssnq}(s) G_{uTCSCqisq,ss}(s) \end{cases} \quad (7-21)$$

With the derived TFs, closed-loop TF from TCSC voltage to stator current can be derived from the diagram shown in Fig. 7-35.

Step 2: derive the closed-loop TF from line current disturbance to  $k_B$  (Fig. 7-34)

Step 1 only results in the closed-loop TF from TCSC voltage to stator current. In fact, the line current is the sum of stator current and the current from the grid-side converter. As discussed in Section 7.3.2, the active current of the grid-side converter will respond to the active current change of the rotor-side converter due to existence of the dc voltage control loop. However, inclusion of grid-side converter in the derivation will make the system so complicated that Matlab cannot handle the high order. Since the impact of the grid-side converter control is limited, its effect is neglected in this part of analysis for simplicity. Therefore, the closed-loop TFs from TCSC voltage to line current in Fig. 7-35 will be approximated as the closed-loop TFs from TCSC voltage to DFIG stator current derived in step 1.

With these TFs derived, the closed-loop TF from line current disturbance to  $k_B$  can be derived from the diagram shown in Fig. 7-34.

#### 7.4.1.2.2 SSR risk evaluation with TF analysis

With the TF derived in previous section, the SSR risk can be evaluated. The target is to find out the minimum portion of TCSC that can avoid SSR. Here the TCSC is controlled with SVR scheme without any damping control.

In Matlab calculation, it is found the minimum rotor speed with which the calculation converges is 0.75 pu. Below this value, no reasonable solution can be returned. The possible reason could be computational problems or no solution existing. Hence, 0.75 pu will be used as the minimum rotor speed for SSR evaluation. This makes the result optimistic since with smaller rotor speed, e.g., 0.7 pu, the SSR risk is higher.

The total compensation degree is 40% of line reactance. Assume no reactive power support is deployed at wind farm terminal for simplicity, as discussed in Section 7.2.4.

As mentioned earlier, the current controller gain  $k_{ir}$  of DFIG rotor-side converter has significant impact on SSR risk. First, assume a fast DFIG control speed that can be achieved with larger  $k_{ir}=0.3$  and at the same time with higher SSR risk.

Fig. 7-36 shows Pole-zero map of closed-loop TF from line current disturbance to  $k_B$  with TCSC portion (out of the total 40% compensation) varying from 20% to 90% with a step of 10%. The part with critical poles is zoomed in shown in Fig. 7-37. With the increase of TCSC portion, the unstable poles move from the right-half plane toward the left-half plane. The boundary portion falls between 80% and 90%. For case with TCSC portion close to the boundary, Matlab could not return reasonable calculation results. Therefore, it's hard to obtain exact boundary portion.

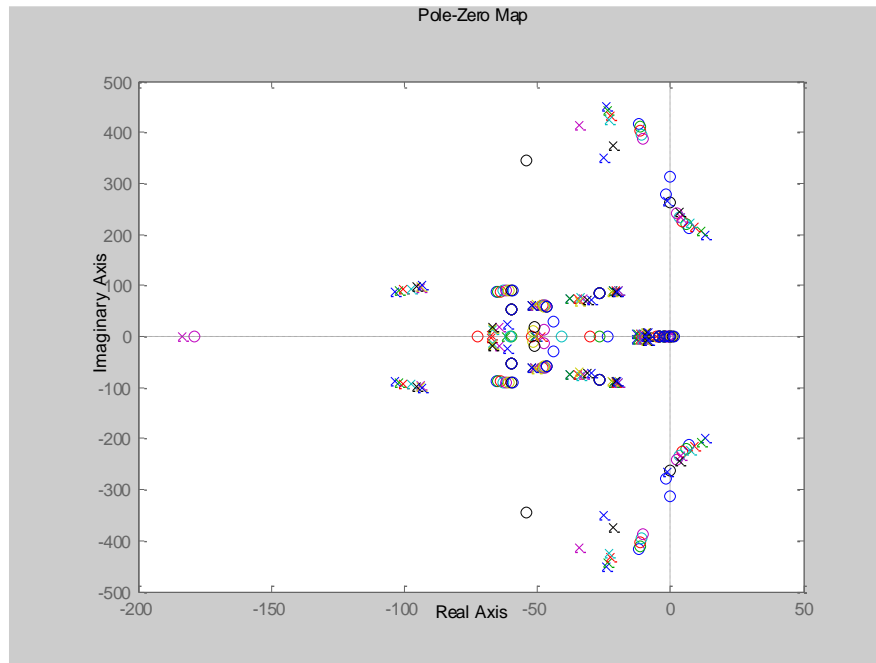


Fig. 7-36 Pole-zero map of closed-loop TF from line current disturbance to kB with TCSC portion varying from 20% to 90%

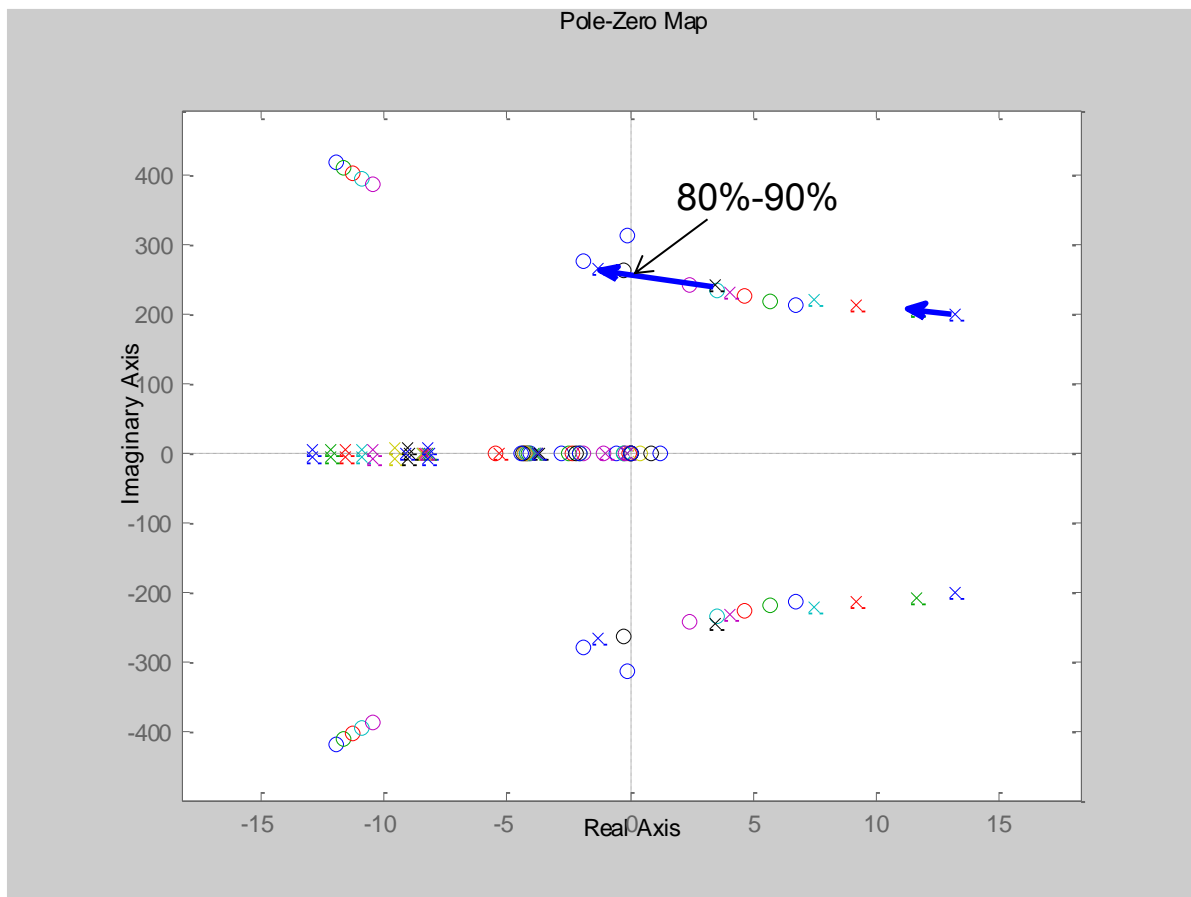
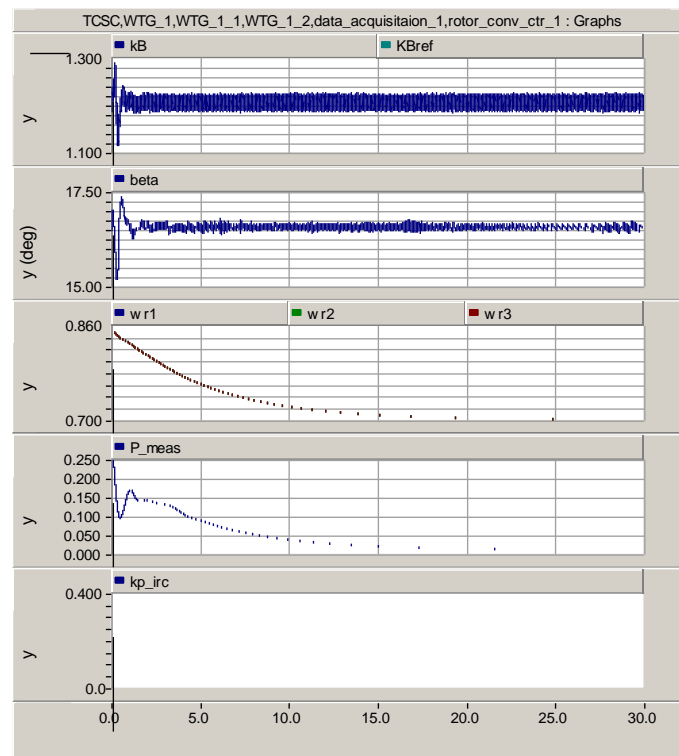
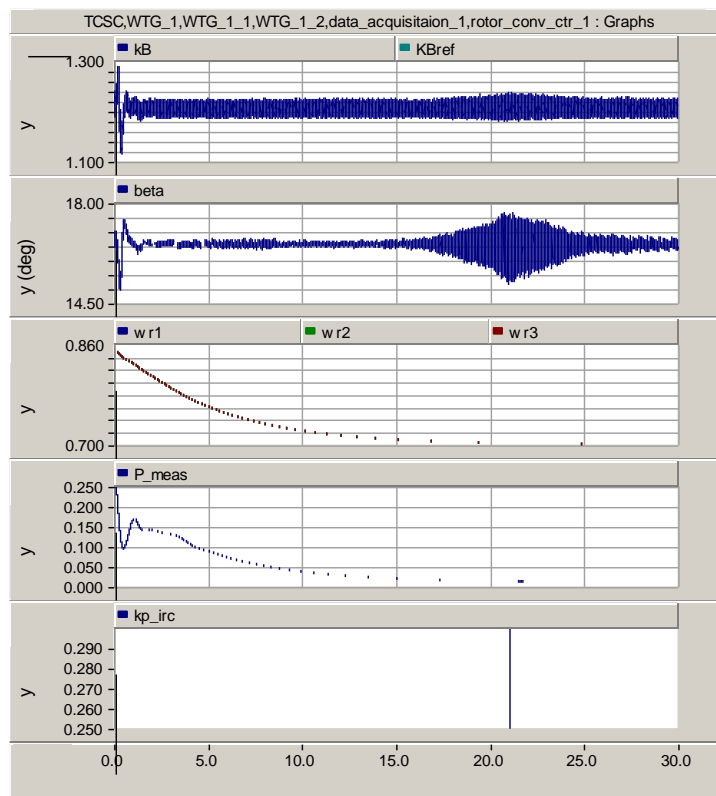


Fig. 7-37 Pole-zero map of closed-loop TF from line current disturbance to kB with TCSC portion varying from 20% to 90% (zoomed in)

Simulations have been performed in PSCAD with rotor speed down to 0.7 pu (corresponding to 1% generation level). The TCSC portion is varied with 5% resolution. The results show that the boundary portion of TCSC to avoid SSR is between 85% and 90% if  $k_{ir}$  is set to 0.3.



(a) TCSC portion = 90%;  $k_{ir}=0.3$



(b) TCSC portion = 85%; kir changes from 0.3 to 0.25 at 22s

Fig. 7-38 PSCAD simulation

Similarly, boundary portion with smaller kir can be found out from both Matlab TF analysis and PSCAD simulations. The results are listed in Table 7-2 together with the bandwidth of DFIG closed-loop control.

Table 7-2 Boundary portion (out of the 40% total compensation) of TCSC to avoid SSR

Rotor-side converter controller gains [ kir, kQ, kwr]	[0.2, 1, 16]	[0.25, 1.25, 20]	[0.3, 1.5, 24]
Corresponding DFIG control bandwidth (rad/s)	[283, 41, 3.9]	[348, 52, 4.3]	[358, 67, 4.5]
Boundary portion from TF analysis in Matlab (10% resolution ; wr down to 0.75pu)	70%-80%;	80%-90%	80%-90%;
Boundary portion from PSCAD simulation (5% resolution; wr down to 0.7 pu)	75%-80%	80%-85%	85%-90%

#### 7.4.1.3 Summary of SSR risk evaluation

With frequency scanning method result, the following conclusion could be derived: with kir=0.3 and fixed shunt capacitor bank installed at wind farm terminal for reactive power support, the boundary portion of TCSC to avoid SSR is about 78%.

With TF analysis, the results are as follows: with kir=0.3 and no reactive power support at wind farm terminal, the boundary portion of TCSC to avoid SSR is between 85%-90%. With smaller kir, the required TCSC portion to avoid SSR is reduced.

The comparison of the results from these two method (kir=0.3) is as follows: due to the shunt capacitor bank at the wind farm terminal, SSR risk is mitigated. Therefore, required TCSC portion is reduced from 85%-90% to 78%. This is in agreement with the statement from literature that SSR risk is higher when DFIGs are connected radially to series compensated transmission lines. Shunt paths help with mitigation of SSR.

#### 7.4.2 Investigation on impact of boost factor and TCSC inductance on SSR

##### 7.4.2.1 Impact of TCSC inductance on SSR

As discussed in Section 7.1.1, TCSC inductance determines the design parameter  $\lambda$ . Therefore, it makes sense to investigate the impact of TCSC inductance on SSR potential.

Since the typical value of  $\lambda$  falls in the range of 2~4, simulation studies have been performed in the following way: in the 1st simulation  $\lambda$  is set to be 2 and then increase  $\lambda$  step by step (0.5 for each time) until it reaches 4. From the simulation results it could be concluded that  $\lambda$  has almost no impact on the SSR potential. For compactness, only the simulation results with  $\lambda = 2.5$  and  $\lambda = 4$  are illustrated in Fig. 7-39.

This could be proved from theoretical point of view. The apparent impedance of TCSC has nothing to do with  $\lambda$ . The change of  $\lambda$  could not affect the system impedance. Therefore, the TCSC inductance doesn't have impact on SSR potential.

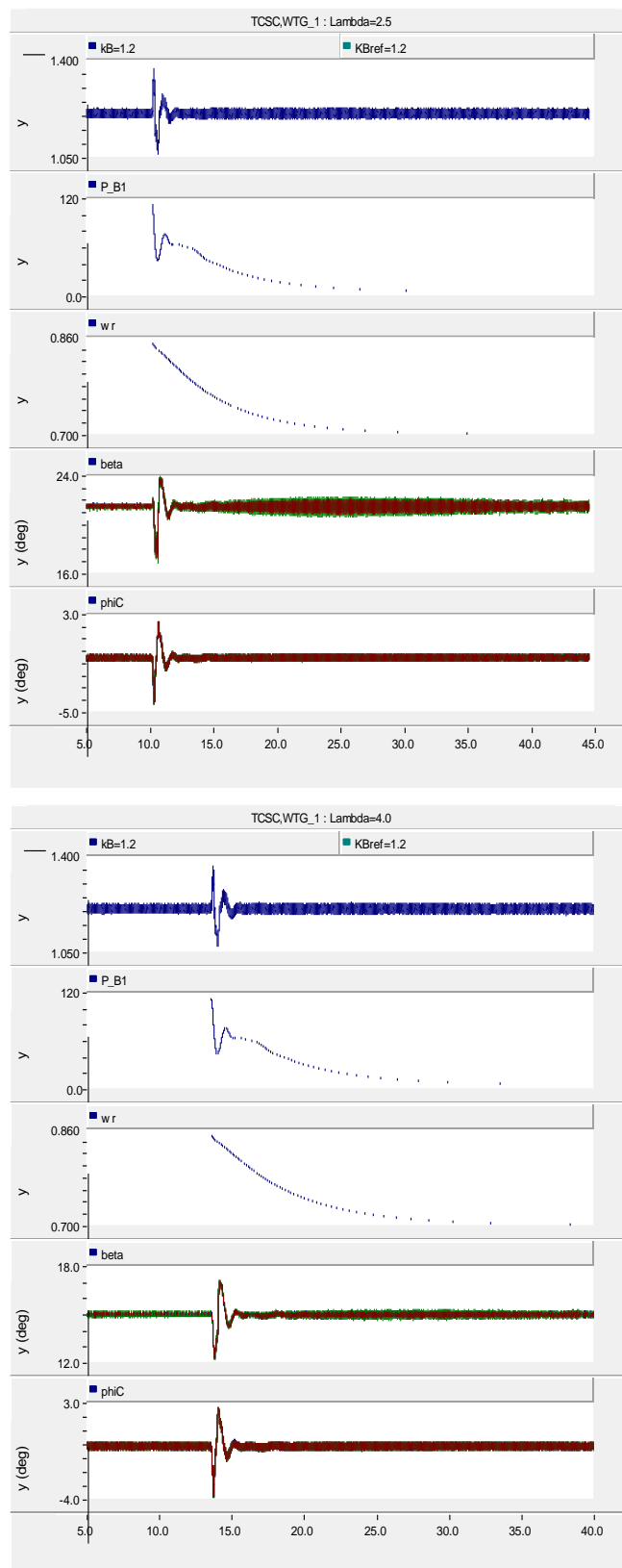


Fig. 7-39 Impact of TCSC reactance on SSR mitigation, upper  $\lambda = 2.5$ , lower  $\lambda = 4.0$

#### 7.4.2.2 Impact of boost factor on SSR potential

Since TCSC can be operated with a boost factor in a certain range, e.g., 1.2 to 3, it is valuable to investigate if nominal boost factor has any impact on SSR potential. The impact is analyzed under two conditions:

- TCSC apparent reactance is kept constant
- TCSC capacitance is kept constant

#### 7.4.2.2.1 Impact of boost factor on SSR potential with constant TCSC apparent reactance

The total compensation level is set to 40% with 22% FC and 78% TCSC. The apparent reactance of TCSC is kept constant. That means when  $k_B$  is varying, the capacitance of TCSC is changed accordingly. The reason why the TCSC portion is set to its boundary portion of 78% is as follows: the impact of  $k_B$  is small and it is difficult to observe any impact with a portion far away from the boundary portion.

With frequency scanning method, the system impedance is calculated and illustrated in Fig. 7-40. From the figure it is clear that  $k_B$  could affect the real and imaginary part of system impedance. As the boost factor is increasing (TCSC capacitance decreasing), the zero-crossing of real part moves leftward whereas the zero-crossing of imaginary part moves rightward. However, the change of real part is very small. In case of  $k_B \geq 1.7$ , the system is likely to suffer SSR. In normal operation,  $k_B$  is usually set to be in range between 1.2 and 3. In the simulation studies, three typical values have been tested: 1.2, 1.7 and 2.2. From the results illustrated in Fig. 7-40, it is clear that the influence of  $k_B$  on zero-crossing of imaginary part of system impedance is much lower than the one of TCSC portion shown in Fig. 7-33.

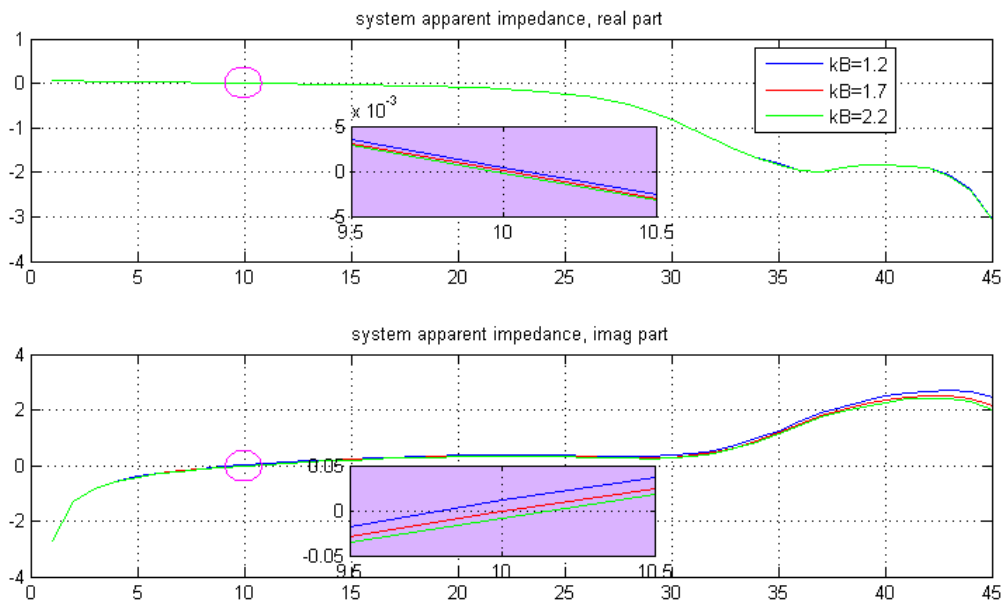


Fig. 7-40 Investigation on  $k_B$  impact

Similar investigation has also been performed with simulations in PSCAD.  $k_B$  is increased from 1.2 by 0.1 for each simulation study. Accordingly, capacitance of TCSC is also changed in order to keep TCSC portion the same. The simulation result proves that SSR will occur if  $k_B \geq 1.3$ . This is different from the result with frequency scanning method. The possible reason is that  $k_B$  has little impact on

the zero-crossing point and the resolution of FFT analysis in frequency scanning is 1 Hz. With such a low FFT resolution it is possible to have errors at the point of zero-crossing of both real and imaginary part of system impedance.

#### 7.4.2.2.2 Impact of boost factor on SSR with constant TCSC capacitance

In this section, the TCSC capacitance is kept constant. With variable boost factor  $k_B$  the apparent reactance changes, thus the compensation level changes. In order to make a good comparison, it is better to set the operation point with  $k_B = 1.2$  according to 40% compensation level (78% TCSC + 22% FC) as reference.

With the strategy described above, simulation studies have been done and the results show the boost factor doesn't have visible influence on SSR potential. As shown in Fig. 7-41, different  $k_B$  reference values have been applied: 1.2, 1.6, 2.0 and 3.0. There is no visible difference shown in the figure except the error band between reference value and real value. This can be easily explained from (7-1).  $k_B$  does not show up in the formula calculating apparent impedance in sub-synchronous range.

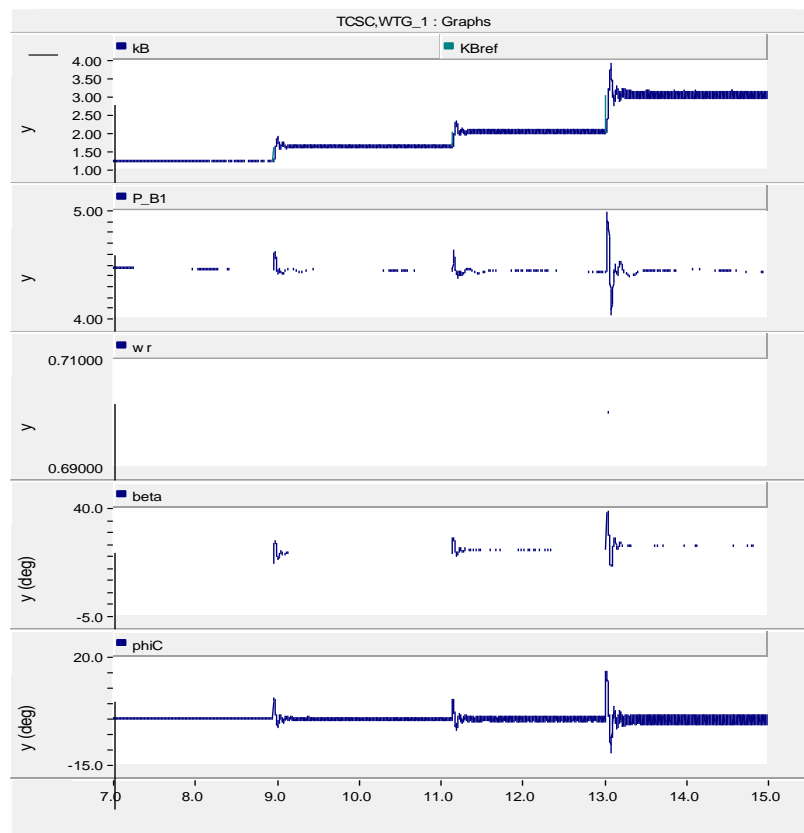


Fig. 7-41 impact of  $k_B$  on SSR mitigation with variable compensation level

### 7.4.3 Development of SSR damping control for system with DFIG and TCSC+FC

As demonstrated in Section 7.4.1.2, the minimum required TCSC portion to avoid SSR is 85%-90% of the total 40% compensation if TCSC is controlled with SVR control scheme without damping control. In order to lower cost, it is desired to design a damping controller so that smaller portion of TCSC can be used.

#### 7.4.3.1 Development of SSR damping control

### 7.4.3.1.1 Design procedure

The SSR damping control system designed is shown in the part in red color in Fig. 7-42. The damping control takes the imaginary part of the line current phasor delivered from the phasor estimation block and passes it to a high pass filter (HPF) to get the oscillation signal. The oscillation signal is then passed through a damping controller to get the modulated angular displacement of the equivalent, instantaneous voltage reversal.

The damping controller is a lead-lag compensator in the form of

$$G_{damp}(s) = k_{damp} \frac{1+s/\omega_{lead}}{1+s/\omega_{lag}} \quad (7-22)$$

The time constant for HPF is selected as 0.32s, giving a cut-off frequency of 0.5 Hz.

It can be seen that the damping control affects both the nominal and sub-synchronous frequency responses. Moreover, it is not an ordinary compensator in series with controlled plant. These features make it difficult to design in a direct analytical way. Therefore, a design approach with the following procedures is adopted:

1. Choose a controller intuitively.
2. Analyze how closed-loop TF is affected by damping controller parameters (gain and pole-zero position) in Matlab.
3. Identify controller parameters resulting in good performance.
4. Simulate in PSCAD with selected control parameters and identify possible improvement.
5. Improve controller.



- In deriving the coupling between d and q components ( $i_{rq}$  and  $i_{sq}$  induced by  $i_{rd}$ ,  $i_{sd}$  and  $i_{gq\_damp}$ ), the outer control loops (Q and  $w_r$ ) are disconnected. This simplification is justified considering the response of the outer loops is much slower than the inner loops.
- The response from TCSC voltage to grid-side converter current is neglected. The line current response is approximated as the stator current only. This approximation has larger impact than the two above.

Certainly, these simplification and approximation will affect the accuracy of the analysis results. Nevertheless, the analysis provides information about the general trends of how the controller affects the sub-synchronous response of the system.

In the following an example will be given to design a damping control for a system with the following specifications:

- 40% total compensation with 20% TCSC (without damping control, 85%-90% TCSC is required)
- TCSC boost factor:  $k_B=1.2$
- DFIG controller gain:  $k_{ir}=0.3$  (SSR risk is high)

The controller selected is a phase-lag compensator in the form of (7-6). Fig. 7-43 shows Pole-zero map of closed-loop TF from line current disturbance to  $k_B$  with varying damping controller gain  $k_{damp}$ . Since the controller affects both of sub-synchronous frequency response and nominal frequency response, both responses are evaluated with rotor speed of 0.75 pu and 1.2 pu considered. In this case, the pole and zero position of the lead-lag compensator is chosen as:

$$k_\omega = \frac{\omega_{lead}}{\omega_{lag}} = 4, \quad \omega_m = \sqrt{\omega_{lead}\omega_{lag}} = 19 \text{ rad/s } (\sim 3 \text{ Hz}) \quad (7-23)$$

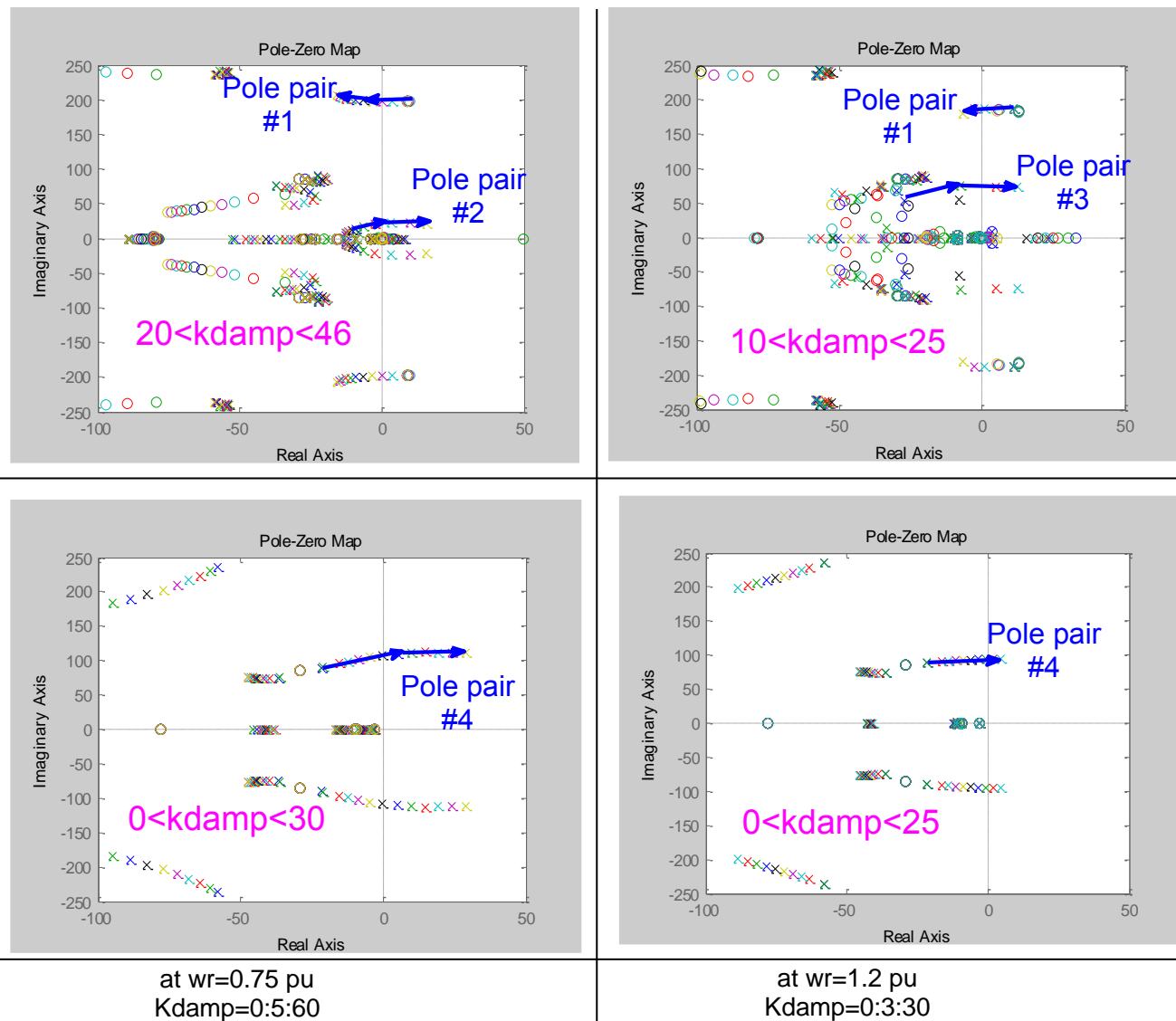


Fig. 7-43 Pole-zero map of closed-loop TF with varying damping controller gain  $k_{damp}$  (left-top: sub-synchronous response at  $w_r=0.75$  pu, TF from line current disturbance to  $k_B$ ; right-top: sub-synchronous response at  $w_r=1.2$  pu, TF from line current disturbance to  $k_B$ ; left-bottom: nominal frequency response at  $w_r=0.75$  pu, TF of  $k_B$  control; right-bottom: nominal frequency response at  $w_r=1.2$  pu, TF of  $k_B$  control)

From the figure, following trends can be observed:

- Four pairs of poles are affected by damping controller. #1 is the pair of SSR poles and the other 3 are related to TCSC control system.
- Impact of the damping controller on sub-synchronous frequency response depends on rotor speed to a large extent
- Impact of the damping controller on nominal frequency response depends on rotor speed to a small extent.
- Nominal frequency response does not exert extra limitation on gain selection (other than the limitation by sub-synchronous response)

- Damping controller gain that can be used is limited to a certain range due to consideration of stability of all four pairs of poles.
- At low generation level (small rotor speed), usable gain is larger than at high generation level.

The pole-zero maps are from controller design for system with 20% TCSC (out of 40% total compensation). For this design, the available gain range is 20-25. Further reduction of TCSC portion might have no solution due to the gain range constraints.

During controller tuning process, different pole and zero positions for the lead-lag compensator have been applied as described in the following.

Step 1:

Keep  $k_\omega = 4$  and vary  $\omega_m$ . The usable gain ranges are listed in as follows:

Table 7-3 Usable gain range for different  $\omega_m$

$\omega_m$ (corresponding Hz)	~1 Hz	~3 Hz	~5 Hz	~7 Hz	~11 Hz
usable gain range	20-25	20-25	20-22	No solution	No solution

The following can be concluded:

- if  $\omega_m$  is too big, e.g. 44 rad/s (~7 Hz), there will be no solution due to constraints on usable gain range.
- For  $\omega_m < 19$  rad/s (~3 Hz), there is no significant difference in usable gain range.

Step 2:

Keep  $\omega_m = 19$  rad/s (~3 Hz) and vary  $k_\omega$ . The usable gain ranges are listed in Table 7-4.

Table 7-4 Usable gain range for different  $k_\omega$

$k_\omega$	2	4	9
Usable gain range	10-11	20-25	45-47

Based on the analysis above, pole and zero positions with  $k_\omega = 4$  and  $\omega_m = 19$  rad/s (~3 Hz) are selected for lead-lag compensator.

#### 7.4.3.2.1 Impact of kB on damping control

TF analysis shows that with higher kB, the damping control is more effective with the same damping gain. However, the limitation on range of usable gain still exists. For example, the usable gain range is 20-25 with kB=1.2 and is 17-22 with kB=1.8.

Even though higher kB brings no obvious advantage to SSR damping control, TCSC operating at higher kB can withstand larger power variation without being tripped by its protection system. For this consideration, it is better to run TCSC at higher kB in case the transmitted power changes as in the case of wind power transmission.

#### 7.4.3.2.2 Simulation results in PSCAD

Simulations have been done in PSCAD with the controller selected from Matlab.

It is worth to describe how the controller is implemented in PSCAD. The control diagram shown in Fig. 7-42 and the TF derived from the figure are based on per unit system. The quantities related to DFIG are per-unitized with wind farm installed capacity and terminal voltage. The quantities related to TCSC are per-unitized with line current peak value and the un-boosted voltage across TCSC capacitor at the corresponding line current. In PSCAD, the control block of the TCSC model outputs line current phasors in kA. Therefore, the real part of the line current phasor  $i_{phx}$  (in kA) is low-pass filtered to get the line current magnitude. The imaginary part of the estimated line current phasor  $\widetilde{i}_{Lq}$  (in pu) shown in Fig. 7-42 is obtained by dividing the  $i_{phy}$  (in kA) delivered by TCSC control block with the low-pass filtered  $i_{phx}$ .

Simulations show that the controller is effective to damp SSR. However, the damping factor  $k_{damp}$  should be adjusted accordingly when the generation level (hence rotor speed) varies. Table 7-5 shows the usable gain range for three different TCSC portions at rotor speed 0.7 pu and 1.1445 pu. The reason why rotor speed of 1.1445 pu is considered is that this speed corresponds to the typical maximum power output from a GW-level wind farm cluster. Rotor speed of 0.7 pu corresponds to a generation level of 1%, which is considered as the minimum possible output power from the wind farms.

Table 7-5 usable gain range identified from PSCAD simulation for various TCSC portion (of the total 40% compensation)

TCSC portion	10%	15%	20%
Usable gain range at $w_r=0.70$ pu	43-58	37-40	27-39
Usable gain range at $w_r=1.145$ pu	10-18	4.5-8	4-7

It can be seen that there is a discrepancy between Matlab analysis and PSCAD simulation in the usable gain range, especially at high rotor speed. Possible reason for discrepancy could be simplifications and approximations used in Matlab analysis. Moreover, the rotor speed considered is also different.

The simulation results in Table 7-5 show that there is no overlap in the usable gain range at the highest and lowest generation level considered. Further improvement is required.

### 7.4.3.2.3 Further improvement of the damping controller

Adaptive method is proposed to adjust damping controller gain according to generation level. The gain  $k_{damp}$  is multiplied by an adaption factor in form of:

$$k_{adapt} = \frac{1}{\frac{i_{Ld\_LPF\_+b}}{a}} \quad (7-24)$$

By adjusting adaptation parameters  $a$  and  $b$ , different adaptation level can be achieved. At very low power generation, the line current will be very small and  $k_{adapt}$  will be  $1/b$ . The adaptation can be seen as adaptation to rotor speed rather than to line current.

It is important to note that the adaptation is different from per-unitizing described in previous section. It can be deemed that the damping control adapts to the line current twice, one for per-unitizing of TCSC control and the other for adaption to generation level.

**7.4.3.2.4 Final simulation results**

Simulations in PSCAD have been done with the damping controller selected in Section 7.4.3.2 and the adaptation parameters tuned. Boost factor set in the simulation is 1.5. The parameters are listed in Table 7-6. The results show that a minimum TCSC portion 10% (of the total 40% compensation) is required to damp SSR. The damping control reduces the minimal required TCSC portion from 85%-90% to 10%.

In the simulation, the wind speed is reduced at 0s and reduced further at 5s such that the rotor speed drops from typical maximal speed (1.1445 pu) to minimal speed (0.7 pu, corresponding to output power of 0.01 pu). The simulation result shows that SSR doesn't occur for the whole typical generation range.

Table 7-6 Parameters used in the simulation

TCSC portion	Nominal kB	Boost controller gain kp_kB	Damping controller gain	Damping gain adaptation	DFIG rotor-side converter current controller gain kir
10%	1.5	0.25	18	a=1.32 b=0.33	0.3 for all three DFIGs

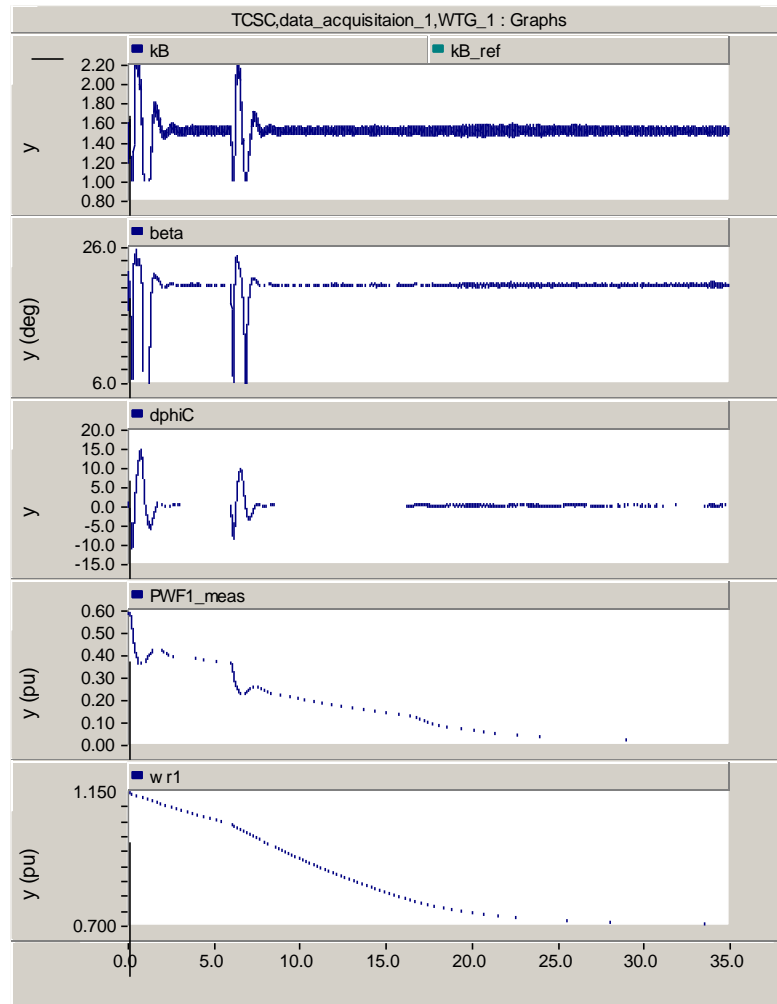


Fig. 7-44 PSCAD simulation results for whole generation range

Fig. 7-45 shows how the SSR is damped when the rotor speed is the minimum (0.7 pu). At 0.3s, the damping controller gain is set to 0. The oscillation starts to build up. At 0.5s, the gain is set to 20, the oscillation is damped out shortly. The gain is set to 20 instead of 18 as in previous simulation just to show the process in a short time period. A gain of 18 also works in this case, but it takes longer time to damp the oscillations.

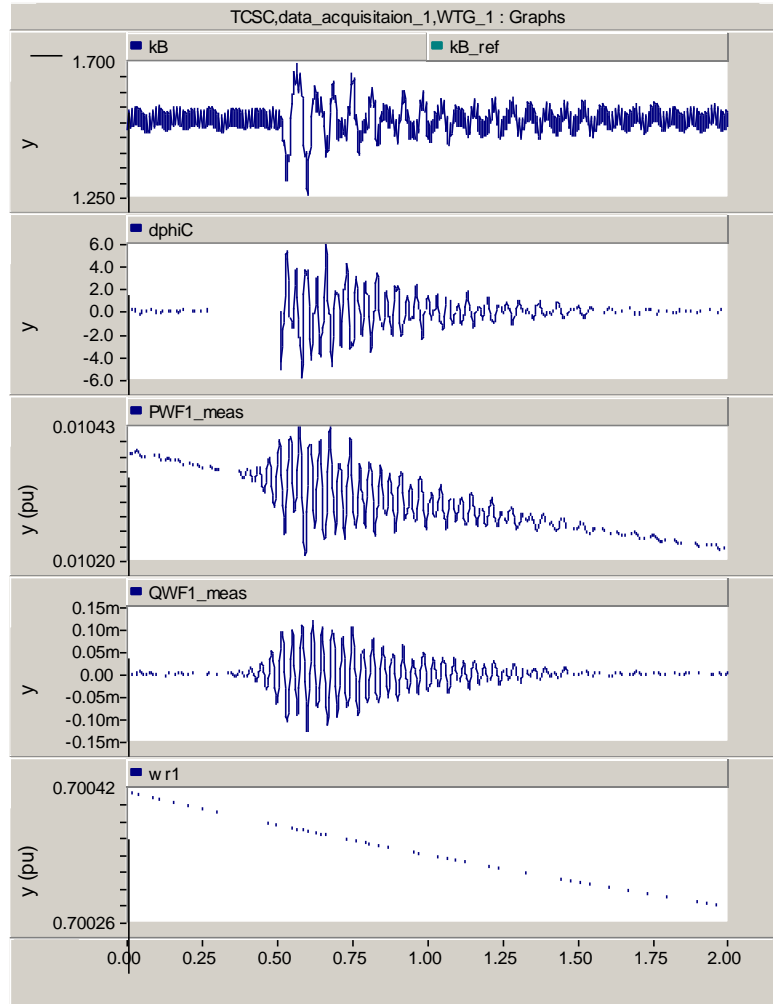


Fig. 7-45 Damping of SSR

It has also been observed that the damping controller must be activated before the oscillation grows too much. Otherwise, the oscillation cannot be damped.

### 7.4.3.3 Evaluation of effectiveness and limitations

#### 7.4.3.3.1 For system with DFIGs with different control speeds

The controller is designed for system with faster DFIG controller ( $k_{ir}=0.3$ ), which means SSR risk is higher. SSR risk is lower with slower DFIG control. However, as discussed in Chapter 7.3, interaction between nominal frequency response of DFIG control and TCSC control might happen if the control speeds in different loops don't match. Therefore, it is necessary to investigate if the controller designed for system with fast DFIG control works for system with slow DFIG control.

As the first step of the investigation, the DFIG controller gain  $k_{ir}$  is decreased while TCSC control parameters (damping controller and boost controller) is kept the same. The results from TF analysis and PSCAD simulation show that if  $k_{ir}$  is too small, e.g.,  $k_{ir}=0.1$ , there will be no usable gain for SSR damping controller to achieve stable operation. The main limitation on controller gain is the nominal frequency response. With such a smaller gain, whether the gain can be used is limited to a small value in order to avoid interaction in nominal frequency response and this gain is too small to damp out SSR.

One solution to this problem is to adjust the TCSC boost controller gain accordingly. Simulations and Matlab analysis show it is possible to tune the TCSC controller and SSR damping controller to adapt to different DFIG control speeds. The simulation results shown in Fig. 7-46 are obtained with the set of parameters listed in Table 7-7.

Table 7-7 Parameter used in simulation with different DFIG controller gains

TCSC portion	Nominal $k_B$	Boost controller gain $k_{p\_k_B}$	Damping controller gain	Damping gain adaptation	DFIG rotor-side converter current controller gain $k_{ir}$
10%	1.5	0.125	18	$a=1.32$ $b=0.45$	0.1, 0.2, 0.3 for three DFIGs respectively

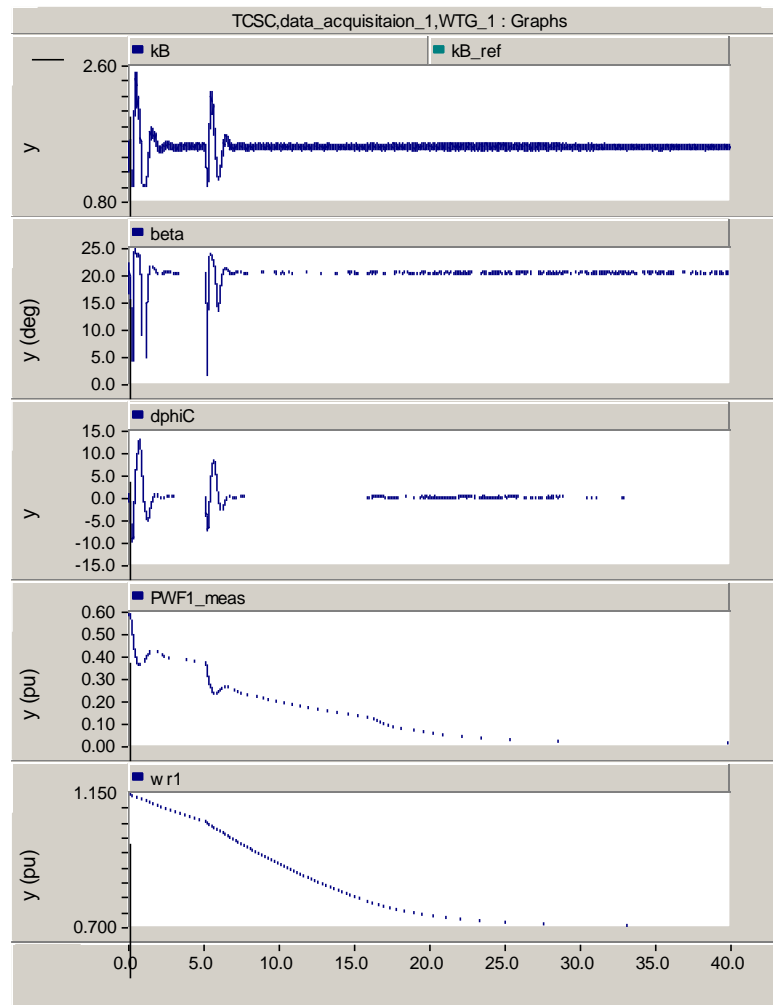
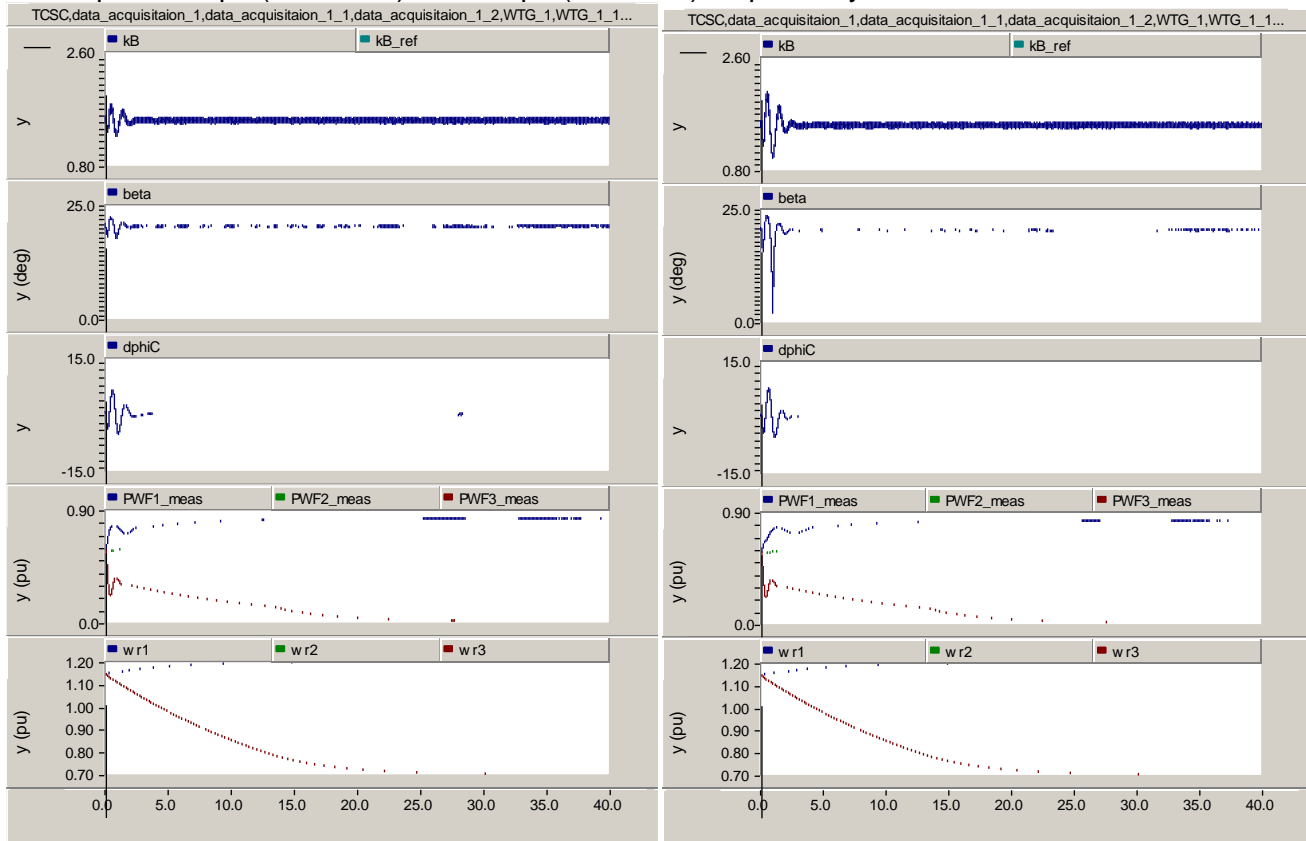


Fig. 7-46 Simulation results for whole typical generation range with DFIGs with different controller gains

#### 7.4.3.3.2 For system with DFIGs operating at different generation levels

Simulations are also performed to investigate if the damping controller works for system with DFIGs operating at different generation levels. Fig. 7-47 shows the simulation results with same DFIG controller gains (a) and different DFIG controller gains (b) respectively. In the simulations, the wind speed is changed so that the rotor speed of DFIG1 and DFIG 3 changes from 1.1445 pu to 1.2 pu (maximum) and 0.7 pu (minimum) respectively.



(a) Use parameters in Table 7-6  
(same kir for all DFIGs)

(b) Use parameters in Table 7-7  
(different kir)

Fig. 7-47 Simulation results for whole typical generation range with DFIGs operating at different generation levels

## 7.5 Conclusions

This report describes TCSC main circuit and its control system. Modeling of TCSC in PSCAD, derivation of TFs describing TCSC and the compensated system with DFIG are also presented. Systems compensated by pure TCSC and by combined TCSC and FC are investigated with following conclusions.

1. Wind power transmission system compensated by pure TCSC
  - There is no SSR risk in such a system

- Control interaction may occur if control speeds in different control loops do not match, resulting in power oscillations.
  - Interaction risk is lower at lower TCSC compensation degree.
  - A POD (power oscillation damping) controller is developed and it works well for various control speeds combinations.
2. Wind power transmission system compensated by combined TCSC and FC
- Evaluation of SSR risk in system by theoretical analysis and PSCAD simulations
    - Minimum portion of TCSC is between 85%-90% of the total compensation to avoid SSR (with fast DFIG control and without reactive power support installed at wind farm terminal).
    - Minimum portion of TCSC is 78% of the total compensation to avoid SSR (with fast DFIG control and with reactive power support installed at wind farm terminal).
  - Investigation of the impact of boost factor and TCSC inductance on SSR
    - TCSC inductance has no impact on SSR potential.
    - Boost factor has no impact on SSR potential; however it has certain impact on SSR mitigation.
  - Development of SSR damping control
    - Developed SSR damping controller reduces required TCSC portion from 85%-90% to 10%.
    - The effectiveness of the damping controller is verified with respect to different DFIG control speeds and different generation levels for three DFIGs.

## 8 COMPARISON OF DIFFERENT MITIGATION SOLUTIONS

The various SSR mitigation solutions by FACTS devices developed in this thesis are compared in this chapter. Table 8-1 gives an overview of the comparison. Some of the items will be explained in detail.

Table 8-1 Comparison of SSR mitigation solutions by FACTS devices

SSR mitigation solution	Suitable application Scenario	Performance ranking	Rating requirement	Extra cost in addition to control system modification
Temporal bypass of SC	Moderate or slow DFIG control speed in radial connection	NA	NA	Extra measurement (bus voltage)
WF-StatCom	WF-StatCom installed for reactive power; independent of DFIG control speed	1	Reasonable rating meeting requirement on reactive power support is sufficient	Extra measurement (transmission line current)
TCSC	Newly planned series compensation; independent of DFIG control speed	2	10% of total compensation (4% of line reactance)	Cost difference between TCSC and FC rated at 4% line reactance
WF-SVC	WF-SVC installed for reactive power; independent of DFIG control speed	3	Reasonable rating meeting requirement for reactive power support is sufficient	Extra measurement (transmission line current)

### 8.1 Comparison regarding applicable scenarios

The solutions by temporal bypass of SC cannot be applied to systems where DFIGs have very fast control speed. Since with fast control speed, SSR might occur even at high generation level. If they are applied in such a system, SC will be bypassed due to SSR oscillations while it is needed for high power transmission. SSR in such kind of systems should be mitigated by other three FACTS devices, e.g., TCSC, WF-StatCom, WF-SVC. The solutions by temporal bypass of SC are suitable for systems where DFIGs have moderate or slow control speed, especially where wind farms are radially connected (or become radially connected under some conditions) to one end of the ac transmission line.

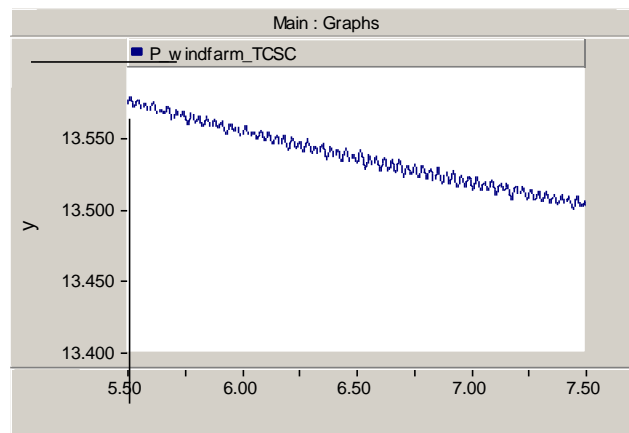
In the investigation of solutions by TCSC, WF-StatCom and WF-SVC, the system configuration and DFIG control parameters used are the same. There is no difference in applicable scenarios for these three solutions. However, the damping performances are slightly different, as will be compared in the following.

### 8.2 Comparison regarding SSR damping performance

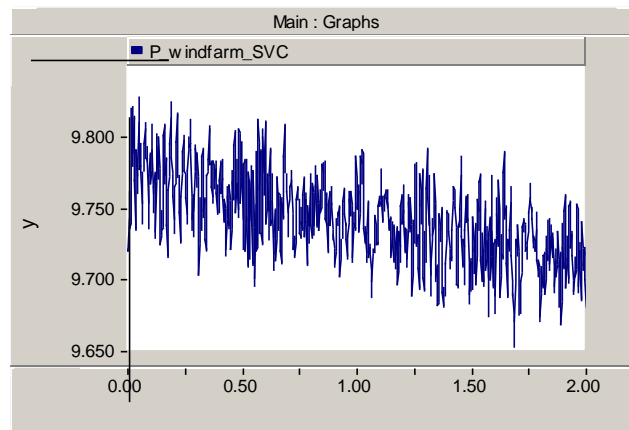
Solutions by temporal bypass of SC will not be compared, since the DFIG control speed is set much slower than it is in the other three solutions and it's unfair to make a comparison. Therefore, the damping performances will be compared among solutions by TCSC, WF-StatCom and WF-SVC.

As presented in the chapters above, all the solutions are effective to damp SSR even in the most severe situation (lowest wind generation level). In steady state at the lowest generation level, there are ripples in the signals in the system in case of SSR damping by TCSC, WF-StatCom, and WF-SVC. The system is said to be in steady state since these ripples are sustained without growing in magnitude.

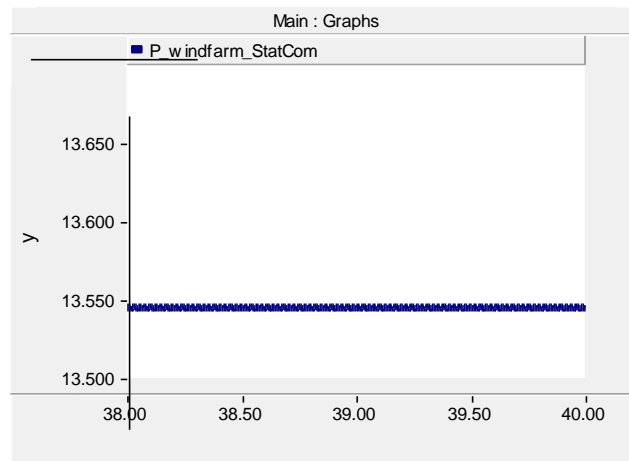
It is found the magnitudes with different solutions are different, as shown in Fig. 8-1. Since the curves are plotted with the same scale, it is obvious that the ripple magnitude with StatCom is the smallest and magnitude with SVC is the largest. This comparison result is reasonable, since StatCom uses IGBTs as switching devices and can give the fastest response among these three devices. Comparing the two thyristor-based solutions, the series solution with TCSC is better than shunt solution with SVC. This is also reasonable since series compensator influences line current or line power in a more direct way than shunt compensator. If the ripple magnitude is used as an indicator for SSR damping performance, the performances with these three solutions can be ranked as shown in the last table.



(a): with solution by TCSC



(b): with solution by WF-SVC



(a): with solution by WF-StatCom

Fig. 8-1 Steady state ripples in signal of total wind power.

Comparison regarding rating requirement and extra cost is easy to be understood in the table. Hence no more detailed discussion will be given.

## 9 CONCLUSIONS

This dissertation gives an overview of SSR (sub-synchronous resonance mitigation) phenomenon in presence of DFIG (double-feed induction generator) and SC (series compensation), which covers the mechanism causing SSR, impact of various factors on SSR and solutions to mitigate SSR. The following conclusions can be drawn.

### 1) SSR Mechanism

SSR is caused by the electrical interaction between DFIG and series capacitor. The series capacitor and the combined inductance in the system (including line inductance, source inductance, lumped DFIG inductance, etc.) determine the resonance frequency which is in sub-synchronous range. The DFIG rotor winding presents a negative resistance at the resonance frequency. The negative resistance is a combined effect of the negative slip and DFIG control system. If the combined resistance of the system (including the negative rotor resistance and other lumped system resistance) is smaller than zero at the resonance frequency, there will be a negative damping in the system, causing oscillations at the resonance frequency.

### 2) SSR characteristics

SSR characteristics have been investigated with main factors affecting SSR identified. The main factors and their impact are summarized in the table below:

Table 9-1 SSR characteristics

Variable	Impact on SSR
Compensation degree	SSR risk higher with higher compensation degree
$\omega_r$ Rotor speed (steady state)	SSR risk higher with lower generation level
$R_r$ (rotor winding resistance)	SSR risk higher with higher resistance
$K_{ir}$ (rotor-side converter current controller gain)	SSR risk higher with larger controller gains
$k_Q$ (rotor-side converter reactive power controller gain)	insignificant impact
$K_{\omega r}$ (rotor-side converter rotor speed controller gain)	Almost no impact
$K_{ig}$ (grid-side converter current controller gain)	Almost no impact
$K_{udc}$ (grid-side converter dc voltage controller gain)	Almost no impact

### 3) SSR mitigation

SSR can be mitigated with various solutions, which can be described briefly in the following. A comparison of these solutions has been made. All the investigations are based on a total compensation degree of 40% of the line reactance unless otherwise stated.

- SSR mitigation by DFIG control modification

It's feasible to mitigate SSR by individual DFIGs. Damping control can be added either to the grid-side converter or the rotor-side converter. The developed controllers have been validated with three wind farms consisting of three DFIGs.

- SSR mitigation by temporal bypass of series compensation

Control algorithms have been developed to bypass the SC (series compensation) either upon detection of SSR or predictively. Since SSR risk is high at low wind generation level, bypassing SC will not create significant impact on system operation due to the low transmitted power. The control algorithms will also control the re-insertion of SC when SSR risk is low, which is indicated by low line voltage level. Simulation analysis proves the reinsertion of SC doesn't bring SSR back to the system. The developed control algorithms are validated under different wind power generation levels and system strengths.

- SSR mitigation by Static Synchronous Compensator in wind farm

Damping control strategy has been developed as an added function to the WF-StatCom (wind farm Static Synchronous Compensator), which is assumed to be installed at the wind farm terminal for dynamic reactive power support. Two controllers have been developed, one is based on generator speed and the other based on active power. Since the former needs external signal communication channel, the latter is preferred. In order to investigate the economy of this solution, the required StatCom rating is estimated. As the rating that meets the requirement for reactive power support is sufficient for SSR damping, it is feasible to add the developed SSDC to WF-StatCom controller to achieve SSR mitigation. The novelty of the damping control strategy is the gain adaption in the designed controller. By introducing the adaptive concept, the developed controller could adjust the gain automatically according to wind power generation level. Research shows gain adaption could help to reduce the required StatCom capacity from SSR mitigation point of view.

- SSR mitigation by static VAR compensator in wind farm

Damping control strategy has been developed as an added function to the WF-SVC (wind farm static VAR compensator), which is assumed to be installed at the wind farm terminal for dynamic reactive power support. A reasonable rating that meets the requirement for reactive power support is sufficient for SSR damping.

- SSR mitigation by thyristor controlled series capacitor

In case the transmission line is compensated by pure TCSC (thyristor controlled series capacitor), there is no SSR risk. However, control interaction may occur if control speeds in different control loops do not match, resulting in power oscillations. Interaction risk is lower at lower TCSC compensation degree. A POD (power oscillation damping) controller has been developed and it works well for various control speeds combinations.

In case the transmission line is compensated by combined TCSC and fixed capacitor banks, there will be SSR risk if the portion of TCSC is not big enough. SSR damping control has been developed and added to TCSC control system. With damping control, the required TCSC portion to avoid SSR can be reduced from 85% to 10% of the total compensation (40% of line reactance).

A comparison between various solutions has been made regarding their performance, rating and cost requirement, and suitable application cases.

## LIST OF FIGURES

Fig. 1-1. Overview of various solutions to SSR mitigation .....	1-9
Fig. 2-1 DFIG diagram .....	2-10
Fig. 2-2 Schematic diagram of the DFIG model .....	2-10
Fig. 2-3. Control structure of the grid side converter.....	2-11
Fig. 2-4 Control structure of the rotor side converter .....	2-12
Fig. 2-5 Pitch control and mechanical torque calculation.....	2-12
Fig. 2-6 System used for analysis .....	2-13
Fig. 2-7 Simplified model of the system.....	2-13
Fig. 2-8 System equivalent circuit .....	2-14
Fig. 2-9 system equivalent circuit of nominal frequency .....	2-15
Fig. 2-10 system equivalent circuit of frequency fss .....	2-15
Fig. 2-11 Control system of the grid-side converter .....	2-16
Fig. 2-12 Inner control loop of the grid-side converter .....	2-17
Fig. 2-13 Simplified inner active current control loop of grid-side converter.....	2-17
Fig. 2-14 Grid-side converter control system.....	2-18
Fig. 2-15 Step response of the inner current control system (red: simulation with DFIG model, green: simulation with transfer function).....	2-19
Fig. 2-16 Step response of the inner current control system (red: DFIG model; green: transfer function).....	2-20
Fig. 2-17 Step response of the dc voltage control system (red: reference; green: DFIG model; blue: transfer function) .....	2-20
Fig. 2-18 Response of dc voltage to step change in active power from rotor converter .....	2-21
Fig. 2-19 Inner current control system of the rotor converter .....	2-23
Fig.2-20 Simplified inner current control system of the rotor converter .....	2-24
Fig. 2-21 Simplified inner current control system of the rotor converter.....	2-24
Fig. 2-22 Structure of reactive power control.....	2-25
Fig. 2-23 Structure of the rotor speed control system.....	2-25
Fig. 2-24 Step response of the inner current control system (top: reactive power; bottom: rotor speed; blue: reference; red: DFIG model; green: transfer function).....	2-27
Fig. 2-25 control system of the inner current loop at sub-synchronous frequency .....	2-31
Fig.2-26 Comparison between DFIG model and the derived transfer functions in case of SSR (top: reactive power from DFIG, bottom: DFIG rotor speed; blue: results from system built with transfer functions, red: results from system with DFIG model) .....	2-32
Fig. 2-27 Impedance Characteristics of the system at sub-synchronous frequencies.....	2-33
Fig. 2-28 Pole-zero map of the closed inner current control loop of the rotor-side converter ....	2-34
Fig. 2-29 Pole-zero map of closed loop transfer functions of rotor speed in response to stator current disturbances with $k_{ig}$ varying from 0.5 to 5.....	2-35
Fig. 2-30 Pole-zero map of closed loop transfer functions of rotor speed in response to stator current disturbances with $k_{udc}$ varying from 0 to 10 .....	2-35
Fig. 2-31 Pole-zero map of closed loop transfer functions of rotor speed in response to stator current disturbances with $k_{udc}$ varying from 0 to 10 (zoomed) .....	2-36
Fig. 2-32 Pole-zero map of closed loop transfer functions of rotor speed in response to stator current disturbances with compensation degree varying from 10% to 70%.....	2-37
Fig. 2-33 Pole-zero map of closed loop transfer functions of rotor speed in response to stator current disturbances with $k_{ir}$ varying from 0.1 to 0.4 .....	2-37
Fig. 2-34 Pole-zero map of closed loop transfer functions of rotor speed in response to stator current disturbances with $\omega_r$ varying from 0.8 pu to 1.2 pu.....	2-38

Fig. 2-35 Pole-zero map of closed loop transfer functions of rotor speed in response to stator current disturbances with $k\omega_r$ varying from 0 to 50.....	2-38
Fig. 2-36 Pole-zero map of closed loop transfer functions of rotor speed in response to stator current disturbances with $R_r$ varying from 0 to 0.1 pu .....	2-39
Fig. 2-37 Pole-zero map of closed loop transfer functions of rotor speed in response to stator current disturbances with $KQ$ varying from 0.4 to 1.6 .....	2-39
Fig. 2-38 Identification of the closed-loop poles .....	2-41
Fig. 2-39 Pole-zero map with varying $k_{ir}$ for system with 75% compensation and 0.8pu rotor speed.....	2-42
Fig. 2-40 Addition of voltage magnitude control loop.....	2-42
Fig. 2-41 Voltage control loop of sub-synchronous system .....	2-43
Fig. 2-42 Sub-synchronous control system with the addition of voltage magnitude control loop.....	2-44
Fig. 2-43 Pole-zero map of closed loop transfer function with varying voltage magnitude controller gain.....	2-46
Fig. 2-44 SSR damping by enabling voltage magnitude control (top: current rating 0.8 pu, enabled at 0.085 s; middle: current rating 0.25 pu, enabled at 0.085 s; bottom: current rating 0.25 pu, enabled at 0.059 s) .....	2-47
Fig. 2-45 Root locus of the closed-loop voltage magnitude control.....	2-48
Fig. 2-46 Root locus of the closed-loop voltage magnitude control (zoomed).....	2-48
Fig. 2-47 Change of oscillation frequency .....	2-49
Fig. 2-48 Simulation results (zoomed).....	2-50
Fig. 2-49 Damping controller .....	2-51
Fig. 2-50 Whole control system with addition of damping control .....	2-52
Fig. 2-51 Pole-zero map with varying damping factor.....	2-53
Fig. 2-52 SSR damping by damping control (top: current rating 0.8 pu, enabled at 0.14s; middle: current rating 0.25 pu, enabled at 0.14 s; bottom: current rating 0.25 pu, enabled at 0.1s) .....	2-55
Fig. 2-53 Change of oscillation frequency .....	2-55
Fig. 2-54 SSR mitigation by damping controller with a three-DFIG system and single DFIG system (from top to bottom: DFIG terminal voltage, DFIG output current, DFIG output reactive power and active power, DFIG rotor speed, DFIG reactive current from grid-side converter) .....	2-56
Fig. 3-1. Sketch map of the research network in the project - IEEE (first) benchmark model for computer simulation of SSR.....	3-59
Fig. 3-2. Research network in project 10556 adapted from IEEE (first) benchmark model for computer simulation of SSR.....	3-59
Fig. 3-3. Modeling of wind farm cluster.....	3-60
Fig. 3-4. Modeling of each phase of the series compensation system.....	3-60
Fig. 4-1 Model used for solution based on proper SC control .....	4-63
Fig. 4-2 Block diagram of bypass control .....	4-64
Fig. 4-3 Structure of reinserting process .....	4-65
Fig. 4-4 Signal process in bypass control.....	4-66
Fig. 4-5 Lock period of the system .....	4-66
Fig. 4-6 simulation results of temporally bypass SC .....	4-67
Fig. 4-7 bypass process .....	4-68
Fig. 4-8 reinserting process.....	4-68
Fig. 4-9 system with $X_{line}=0.75$ pu instead of 0.5 pu .....	4-70
Fig. 4-10 system with $X_{line}=0.25$ pu .....	4-71
Fig. 4-11 Effectiveness in case DFIGs operating at different generation levels .....	4-72
Fig. 4-12 SSR mitigation solution with prediction ability .....	4-73
Fig. 4-13 bypass SC without SSR appearance .....	4-74
Fig. 5-1 IEEE first bench mark model for SSR research with wind farm and StatCom.....	5-76
Fig. 5-2 Structure of StatCom model.....	5-77
Fig. 5-3 diagram of StatCom control .....	5-77

Fig. 5-4 StatCom step response.....	5-78
Fig. 5-5 introduced modulating signal.....	5-79
Fig. 5-6 SSDC controller structure .....	5-79
Fig. 5-7 Bode diagram of designed SSDC based on generator speed .....	5-80
Fig. 5-8 Effectiveness of designed SSDC over whole power range.....	5-81
Fig. 5-9 Effectiveness of designed controller under the lowest power generation level .....	5-82
Fig. 5-10 SSDC effect under different compensation level .....	5-83
Fig. 5-11 SSDC effectiveness under different wind speed, scenario 1 .....	5-84
Fig. 5-12 SSDC effectiveness under different wind speed, scenario 2 .....	5-85
Fig. 5-13 SSDC based on reactive power .....	5-86
Fig. 5-14 Effectiveness of SSDC based on active power .....	5-87
Fig. 5-15 Modified SSDC based on active power .....	5-88
Fig. 5-16 Effect of modified SSDC .....	5-88
Fig. 5-17 Bode diagram of modified SSDC based on active power .....	5-89
Fig. 5-18 Effectiveness of modified SSDC based on active power over whole power range.....	5-90
Fig. 5-19 performance of SSDC with active power delay .....	5-91
Fig. 5-20 Effectiveness of modified SSDC based on active power, different compensation level .	5-92
Fig. 5-21 Effectiveness of SSDC with minimized StatCom capacity .....	5-93
Fig. 5-22 Gain adaption .....	5-94
Fig. 6-1. Single line diagram of the investigated system.....	6-96
Fig. 6-2. Main circuit model of the SVC.....	6-97
Fig. 6-3. SVC voltage control system .....	6-98
Fig. 6-4. Step responses with different integral gains: (a) 100; (b) 150. Green: voltage reference; blue: measured RMS value of the voltage; red: the filtered RMS value of the voltage with the droop considered.....	6-98
Fig. 6-5. Processing of power signal .....	6-99
Fig. 6-6. SVC control system with the addition of damping controller .....	6-99
Fig. 6-7. Sinusoidal signal injection for obtaining frequency response of line power to SVC susceptance .....	6-100
Fig. 6-8. Frequency response characteristic of line power to SVC susceptance.....	6-101
Fig. 6-9. damping control system .....	6-101
Fig. 6-10. Bode diagram of the damping controller (blue, bold) and its components ( $kdamp = 1$ )	6-102
Fig. 6-11. Bode plot of loop transfer function with damping controller ( $kdamp = 1$ ).....	6-103
Fig. 6-12. Gain adaptation curve .....	6-103
Fig. 6-13. Entire control system of SVC with damping control .....	6-104
Fig. 6-14. Damping of SSR at lowest wind generation level (highest SSR risk).....	6-105
Fig. 6-15. Simulation for whole wind generation range.....	6-106
Fig. 6-16. Change of compensation level at high wind generation level (low SSR risk) .....	6-107
Fig. 6-17. Change of compensation level at low wind generation level (high SSR risk) .....	6-108
Fig. 6-18. Simulation for whole wind generation level range with a compensation degree of 30%	6-109
Fig. 6-19. DFIGs with different control parameters ( $k_{ir}=0.1, 0.2, 0.3$ for three DFIGs) and operating at different generation levels (100%, 73%, 1% for three DFIGs).....	6-110
Fig. 7-1 TCSC main circuit and typical waveform .....	7-112
Fig. 7-2 TCSC and its control system.....	7-113
Fig. 7-3 TCSC model in PSCAD .....	7-114
Fig. 7-4 Investigated system compensated by TCSC and FC .....	7-115
Fig. 7-5 Control system of the investigated system .....	7-115
Fig. 7-6 TF model of the investigated system.....	7-116
Fig. 7-7 Equivalent circuit of investigated system (nominal frequency).....	7-117

Fig. 7-8 Equivalent circuit of investigated system (sub-synchronous frequency) .....	7-117
Fig. 7-9 Coordinate systems of DFIG and TCSC control systems .....	7-117
Fig. 7-10 Coordinate systems of DFIG and TCSC control systems based on assumptions....	7-118
Fig. 7-11 DFIG control system (nominal frequency) .....	7-120
Fig. 7-12 Impact of rotor active current on grid-side converter control.....	7-120
Fig. 7-13 Pole-zero map of closed-loop TF of kB control with kir varying from 0.05 to 3 (kQ and kwr vary accordingly) .....	7-121
Fig. 7-14 Pole-zero map of closed-loop TF of kB control with kir varying from 0.05 to 3 (zoomed) (kQ and kwr vary accordingly).....	7-121
Fig. 7-15 Pole-zero map of closed-loop TF of kB control with kir varying from 0.05 to 3 (kQ varies accordingly, kwr=24 doesn't change) .....	7-122
Fig. 7-16 Bode diagram of open-loop TF with kir varying from 0.05 to 3.....	7-122
Fig. 7-17 PSCAD simulation results .....	7-123
Fig. 7-18 Pole-zero map of closed-loop TF of kB control with kp_kB varying from 0.25 to 0.05 ([kir=0.1, kQ=0.5, kwr=8]) .....	7-123
Fig. 7-19 Bode diagram of open-loop TF with varying kp_kB .....	7-124
Fig. 7-20 Bode diagram of closed-loop TF of kB .....	7-125
Fig. 7-21 Pole-zero map of closed-loop TF of kB with varying TCSC compensation degree ..	7-125
Fig. 7-22 Control system with POD control .....	7-126
Fig. 7-23 Frequency characteristics of HPF .....	7-127
Fig. 7-24 Pole-zero map of closed-loop TF of kB control with kpod varying from 0 to 6.....	7-128
Fig. 7-25 PSCAD simulation showing power oscillation damping .....	7-129
Fig. 7-26 PSCAD simulation showing power oscillation damping (enlarged) .....	7-130
Fig. 7-27 PSCAD simulation with 78% TCSC + 22% FC.....	7-131
Fig. 7-28 PSCAD simulation with 77% TCSC + 23% FC.....	7-132
Fig. 7-29 Application of Frequency Scanning Solution .....	7-133
Fig. 7-30 Apparent impedance of TCSC + SC .....	7-134
Fig. 7-31 Real and imaginary part of system impedance based on frequency scanning method (a) 78% TCSC+22% FC; (b) 77% TCSC+23% FC .....	7-135
Fig. 7-32 Simulation in PSCAD, TCSC%=77%, kB=1.2 .....	7-135
Fig. 7-33 Real and imaginary part of system with different TCSC and FC configuration.....	7-136
Fig. 7-34 TCSC control system with DFIG control system embedded.....	7-137
Fig. 7-35 DFIG control system with TCSC voltage as input (sub-synchronous frequency) .....	7-138
Fig. 7-36 Pole-zero map of closed-loop TF from line current disturbance to kB with TCSC portion varying from 20% to 90%.....	7-141
Fig. 7-37 Pole-zero map of closed-loop TF from line current disturbance to kB with TCSC portion varying from 20% to 90% (zoomed) .....	7-141
Fig. 7-38 PSCAD simulation .....	7-143
Fig. 7-39 Impact of TCSC reactance on SSR mitigation, left $\lambda = 2.5$ , right $\lambda = 4.0$ .....	7-144
Fig. 7-40 Investigation on kB impact .....	7-145
Fig. 7-41 impact of kB on SSR mitigation with variable compensation level .....	7-146
Fig. 7-42 SSR damping control .....	7-148
Fig. 7-43 Pole-zero map of closed-loop TF with varying damping controller gain kdamp (left-top : sub-synchronous response atwr=0.75 pu, TF from line current disturbance to kB; right-top : sub-synchronous response atwr=1.2 pu, TF from line current disturbance to kB; left-bottom : nominal frequency response atwr=0.75 pu, TF of kB control; right-bottom: nominal frequency response atwr=1.2 pu, TF of kB control) .....	7-150
Fig. 7-44 PSCAD simulation results for whole generation range .....	7-154
Fig. 7-45 Damping of SSR .....	7-154
Fig. 7-46 Simulation results for whole typical generation range with DFIGs with different controller gains.....	7-156

Fig. 7-47 Simulation results for whole typical generation range with DFIGs operating at different generation levels.....	7-156
Fig. 8-1 Steady state ripples in signal of total wind power. ....	8-160

## LIST OF TABLES

Table 2-1 System specifications.....	2-13
Table 2-2 controller parameters for grid-side converter.....	2-19
Table 2-3 Parameters for rotor converter control system.....	2-27
Table 2-4 Variables used in study of closed-loop transfer functions.....	2-34
Table 2-5. Impact of variables on SSR.....	2-40
Table 3-1 System Parameters.....	3-60
Table 3-2. Evaluation of SSR risk with slower DFIG control.....	3-61
Table 7-1 Sets of DFIG control parameter used in PSCAD simulations.....	7-128
Table 7-2 Boundary portion (out of the 40% total compensation) of TCSC to avoid SSR.....	7-143
Table 7-3 Usable gain range for different $\omega m$ .....	7-151
Table 7-4 Usable gain range for different $k\omega$ .....	7-151
Table 7-5 Usable gain range identified from PSCAD simulation for various TCSC portion (of the total 40% compensation).....	7-152
Table 7-6 Parameters used in the simulation.....	7-153
Table 7-7 Parameter used in simulation with different DFIG controller gains.....	7-155
Table 8-1 Comparison of SSR mitigation solutions by FACTS devices.....	8-158

## REFERENCES

- 
- [1] Global Wind Energy Outlook 2018, <http://www.gwec.net/index.php?id=181&L=0%2Findex.php%3Fi%EF%BF>
- [2] IEEE Committee Report, "First Supplement to a Bibliography for the Study of Subsynchronous Resonance Between Rotating Machines and Power Systems", IEEE Trans. PAS, Vol. PAS-98, No. 6 Nov./Dec. 1979, pp.1872-1875.
- [3] P.Kurdur, Power System Stability and Control, New York:McGraw-Hill, 1994.
- [4] Junyong Wu, Shijie Cheng, Deshu Chen, "Research Status and trend of subsynchronous resonance and torsional amplification in power system", Power System Automation, Vol. Z1, 1991.
- [5] C. F. Wagner, "Self-Excitation of Induction Motors with Series Capacitors", AIEE Transactions, pp. 1241-1247, Vol. 60, 1941.
- [6] Yong Qin, Fen Cai, "Sub synchronous Resonance and its mitigation solution of induction machines", Electric Machine Engineering, Vol. 4, No.2, May 1984.
- [7] G. D. Irwin, "Sub-Synchronous Interactions with Wind Turbines," Technical Conference - CREZ System Design and Operation, January 26, 2010, Taylor, Texas, USA.
- [8] <http://www.fenglifadian.com/fenglifadianji/51406A344.html>
- [9] IEEE Subsynchronous Resonance Task Force of the Dynamic System Performance Working Group Power System Engineering committee, "First Benchmark Model for Computer simulation of Subsynchronous Resonance", IEEE Transaction on Power Apparatus and Systems, Vol. PAS-96, no.5, September/October 1977
- [10] SongXu Xin, Jianhua Bai, etc. "Study on wind power characteristics of JiuQuan wind power base" , Energy technology and economics, Vol.22, No.12, Dec. 2010.
- [11] GB/T 19963, "technical rule for connecting wind farm to power system".
- [12] M. S. El-Moursi, B. Bak-Jensen, M. H. Abdel-Rahman "Novel STATCOM Controller for Mitigating SSR and Damping Power System Oscillations in a Series Compensated Wind Park," IEEE Trans. Power Delivery., vol. 25, no. 2, pp. 429–441, Feb 2010.
- [13] S.Golshannavaz, M.Mokhtari, and D.Nazarpour, "SSR Suppression via STATCOM in Series Compensated Wind Farm Integrations", Electrical Engineering (ICEE), 2011 19th Iranian Conference.
- [14] B.k. Keshaven, N. Prabhu, "Damping of Subsynchronous Oscillations Using STATCOM -A FACTS Controller", 2002 Int. Conference on Power system Technology (POWERCON 2004), Singapore, Nov. 21-24, 2004.
- [15] A.F. Abdou, A. Abu-Siada, H.R. Pota, "Damping of Subsynchronous Oscillations and Improve Transient Stability for Wind farms", 2011 IEEE PES Innovative Smart Grid Technologies, ISGT Asia 2011, Nov. 13-16, Perth, Australia.
- [16] A. Moharana, R. Varma, R. Seethapathy, "SSR mitigation in wind farm connected to SC transmission line using StatCom", Power Electronics and Machines in wind applications (PEMWA) 2012.
- [17] R.M. Mathur and R.K. Varma, "Thyristor-Based FACTS Controllers for Electrical Transmission Systems", IEEE Press and Wiley Interscience, New York, USA, Feb. 2002.
- [18] E.H. Camm, M.R. Behnke, "Reactive Power Compensation for Wind Power Plants", Power & Energy Society General Meeting, 2009. PES '09. IEEE.

- 
- [19] ZHANG Zhi-qiang, XIAO Xiang-ning, "Analysis and Mitigation of SSR Based on SVC in Series Compensated System" in International Conference on Energy and Environment Technology, ICEET '09. Beijing, China, 16-18 Oct. 2009.
- [20] Nazarpour, D. ; Ghahramani, H., "Novel Methods with Fuzzy Logic and ANFIS Controller Based SVC for Damping Sub-Synchronous Resonance and Low-Frequency Power Oscillation" in 20th Iranian Conference on Electrical Engineering (ICEE), 15-17 May 2012.
- [21] Rajiv K. Varma, Soubhik Auddy, and Ysni Semsedini, "Mitigation of Subsynchronous Resonance in a Series-Compensated Wind Farm Using FACTS Controllers" in IEEE TRANSACTIONS ON POWER DELIVERY, VOL. 23, NO. 3, JULY 2008.
- [22] PSCAD Manual.
- [23] S. Viek, V. Seve, "SSR mitigation and damping power system oscillation in a series compensated wind generation system", 2014 IEEE National Conference on Emerging Trends In New & Renewable Energy Sources And Energy Management (NCET NRES EM), 16-17 Dec. 2014.
- [24] Cecil L. Smith, *Advanced Process Control: Beyond Single Loop Control*, page 69, Chapter 2.
- [25] Amit K. Jindal, Garth D. Irwin and Dennis A. Woodford, in "The 9th International Workshop on Large-Scale Integration of Wind Power into Power Systems", Oct. 18-19, 2010 in Québec City, Canada.
- [26] Warren Lasher (ERCOT/USA), Cathey Carter (ERCOT/USA), John Daniel (ABB/USA), Rodolfo Koessler (ABB/USA), Don Martin (ABB/USA), Wille Wong (ABB/USA), in "The 9th International Workshop on Large-Scale Integration of Wind Power into Power Systems", Oct. 18-19, 2010 in Québec City, Canada.
- [27] Xin,S., Bai,J., Guo,Y., "Study on wind power characteristics of JiuQuan wind power base", *Energy Technol. Econ.*, 2010, 22, (12), pp. 16–20.
- [28] L. Fan, Z. Miao, 'Modal analysis of a DFIG-based wind farm interfaced with a series compensated network', *IEEE Trans. Energy, Convers.*, 2011, 26, (4), pp. 1010–1020.
- [29] L. Fan, Z. Miao, 'Nyquist-stability-criterion-based SSR explanation for type-3 wind generators', *IEEE Trans. Energy Convers.*, 2012, 27, (3), pp. 807–809.
- [30] L. Fan, Z. Miao, 'Mitigating SSR using DFIG-based wind generation', *IEEE Trans. Sustain. Energy*, 2012, 3, (3), pp. 349–358.
- [31] Rajiv K. Varma, Reza Salehi, "SSR Mitigation With a New Control of PV Solar Farm as STATCOM (PV-STATCOM)", *IEEE Transactions on Sustainable Energy*, Volume: 8, Issue: 4, Oct. 2017, P. 1473 – 1483.
- [32] Chinnari Eswar Prasad , Shelly Vadhera , "Mitigation of sub synchronous resonance using STATCOM controlled by PID and FL controllers", 2014 IEEE 6th India International Conference on Power Electronics (IICPE), 8-10 Dec. 2014.
- [33] Akshaya Moharana, , Rajiv K. Varma , "SSR Alleviation by STATCOM in Induction-Generator-Based Wind Farm Connected to Series Compensated Line", *IEEE Transactions on Sustainable Energy* ( Volume: 5, Issue: 3, July 2014 ), P. 947 – 957.
- [34] Gajanan V. Gotmare, Vasudeo B. Virulkar , "Remote signal STATCOM controller for mitigation of sub-synchronous resonance in series compensated type 3 wind farm", 2017 International Conference on Energy, Communication, Data Analytics and Soft Computing (ICECDS), 1-2 Aug. 2017.
- [35] Siddhartha Mozumder, Arunima Dhar, Shriram S Rangarajan, S. Prabhakar Karthikeyan, "Coordinated operation of multiple inverter based renewable distributed generators as an active

- 
- power injector and reactive power compensator”, 2014 International Conference on Computation of Power, Energy, Information and Communication (ICCPEIC), 16-17 April 2014.
- [36] S. Vivek, V. Selve, “SSR mitigation and damping power system oscillation in a series compensated wind generation system”, 2014 IEEE National Conference on Emerging Trends In New & Renewable Energy Sources And Energy Management (NCET NRES EM), 16-17 Dec. 2014.
- [37] R. Gunasekari, R. Dhanalakshmi , P.C Kishore Raja, “Power flow stability improvement in renewable hybrid power system using SVPWM technique”, 2016 Biennial International Conference on Power and Energy Systems: Towards Sustainable Energy (PESTSE), 21-23 Jan. 2016.
- [38] J. Sreeranganayakulu, G.V. Marutheswar, K.S.R. Anjaneyulu, “Mitigation of sub synchronous resonance oscillations using static var compensator”, 2016 International Conference on Electrical, Electronics, and Optimization Techniques (ICEEOT), 3-5 March 2016.
- [39] H. Xie, Marcio M. de Oliveira, “Mitigation of SSR in presence of wind power and series compensation by SVC”, 2014 International Conference on Power System Technology, 20-22 Oct. 2014.
- [40] Akbar Lak, Daryoush Nazarpour, Hasan Ghahramani, “Novel methods with Fuzzy Logic and ANFIS controller based SVC for damping Sub-Synchronous Resonance and low-frequency power oscillation”, 20th Iranian Conference on Electrical Engineering (ICEE2012), 15-17 May 2012.
- [41] Ankita Singh, Neeraj Verma, Atul Kumar, “Mitigation technique and measurement of subsynchronous resonance”, 2016 International Conference on Innovation and Challenges in Cyber Security (ICICCS-INBUSH), 3-5 Feb. 2016.
- [42] M. H. Abardeh, J. Sadeh, “Effects of TCSC parameters and control structure on damping of sub-synchronous resonance”, 2010 4th International Power Engineering and Optimization Conference (PEOCO), 23-24 June 2010
- [43] Anvar Yarahmadi, Akbar Lak, Hasan Gahramani, “Novel methodologies with Fuzzy Logic and ANFIS controller based TCSC for mitigating sub-synchronous resonance and low-frequency power oscillations”, 2012 Proceedings of 17th Conference on Electrical Power Distribution, 2-3 May 2012.
- [44] X. Zhang, Y. Song, D. Wang, Z. Zheng, G. Li, “Simulation of SSR evoked by TCSC for UHVAC transmission system from Yimin to fengtun on RTDS”, International Conference on Sustainable Power Generation and Supply (SUPERGEN 2012), 8-9 Sept. 2012.
- [45] R. Zheng, T. Joseph, S. Wang, J. Liang, “A control strategy for TCSC to mitigate SSR with local measurements”, 14-16 Feb. 2017.
- [46] Hossein Ali Mohammadpour, Enrico Santi, “Sub-synchronous resonance analysis in DFIG-based wind farms: Mitigation methods — TCSC, GCSC, and DFIG controllers — Part II”, 2014 IEEE Energy Conversion Congress and Exposition (ECCE), 14-18 Sept. 2014.
- [47] Federico Bizzarri, Angelo Brambilla, Federico Milano, “Analytic and Numerical Study of TCSC Devices: Unveiling the Crucial Role of Phase-Locked Loops”, IEEE Transactions on Circuits and Systems I: Regular Papers, Volume: 65, Issue: 6, June 2018.
- [48] Hossein Ali Mohammadpour, Jonathan Siegers, Enrico Santi, “Controller design for TCSC using observed-state feedback method to damp SSR in DFIG-based wind farms”, 2015 IEEE Applied Power Electronics Conference and Exposition (APEC), 15-19 March 2015

- 
- [49] Dillip Kumar Mishra, Asit Mohanty, Prakash Ray, "MATLAB/Simulink based FA for optimizing TCSC controller in a power system", 2017 4th International Conference on Advanced Computing and Communication Systems (ICACCS), 6-7 Jan. 2017.